UNCLASSIFIED

AD NUMBER

AD893334

NEW LIMITATION CHANGE

TO

Approved for public release, distribution unlimited

FROM

Distribution authorized to U.S. Gov't. agencies only; Test and Evaluation; AUG 1971. Other requests shall be referred to Air Force Flight Dynamics Laboratory, ATTN: FY, Wright-Patterson AFB, OH 45433.

AUTHORITY

AFWAL notice dtd 27 Feb 1980

THIS PAGE IS UNCLASSIFIED

AFFDL-TR-71-108, PART I

AD893334

PREDICTION OF UNSTEADY AERODYNAMIC LOADINGS OF NON-PLANAR WINGS AND WING-TAIL CONFIGURATIONS IN SUPERSONIC FLOW

Part I Theoretical Development, Program Usage, and Application

JACK MORITO II
CHRISTOPHER J. BORLAND
JOHN R. HOGLEY

THE BOEING COMPANY
COMMERCIAL AIRPLANE GROUP

DDC
RECEIVED
APR 17 1972
C

FILE COPY

TECHNICAL REPORT AFFDL-TR-71-108, PART I

MARCH 1972

Distribution limited to U.S. Government agencies only; test and evaluation; statement applied August 1971. Other requests for this document must be referred to AF Flight Dynamics Laboratory (FY), Wright-Patterson AFB, Ohio 45433.

AIR FORCE FLIGHT DYNAMICS LABORATORY
AIR FORCE SYSTEMS COMMAND
WRIGHT-PATTERSON AIR FORCE BASE, OHIO

NOTICE

When Government drawings, specifications, or other data are used for any purpose other than in connection with a definitely related Government procurement operation, the United States Government thereby incurs no responsibility nor any obligation whatsoever; and the fact that the government may have formulated, furnished, or in any way supplied the said drawings, specifications, or other data, is not to be regarded by implication or otherwise as in any manner licensing the holder or any other person or corporation, or conveying any rights or permission to manufacture, use, or sell any patented invention that may in any way be related thereto.

ACCESSION for

CFSTI WHITE SECTION ☐

DDC BUFF SECTION ☑

UNANNOUNCED ☐

JUSTIFICATION .....

BY .....

DISTRIBUTION/AVAILABILITY CODES

DIST.	AVAIL. and/or SPECIAL
B	

Copies of this report should not be returned unless return is required by security considerations, contractual obligations, or notice on a specific document.

AIR FORCE: 30-3-72/150

PREDICTION OF UNSTEADY AERODYNAMIC LOADINGS OF NON-PLANAR WINGS AND WING-TAIL CONFIGURATIONS IN SUPERSONIC FLOW

Part I Theoretical Development, Program Usage, and Application

JACK MORITO II
CHRISTOPHER J. BORLAND
JOHN R. HOGLEY

Distribution limited to U.S. Government agencies only; test and evaluation; statement applied August 1971. Other requests for this document must be referred to AF Flight Dynamics Laboratory (FY), Wright-Patterson AFB, Ohio 45433.

FOREWORD

This report was prepared under USAF Contract No. F33615-70-C-1126, "Unsteady Aerodynamics and Flutter of Wing Horizontal Tail Configurations in Supersonic Flow", as a part of Project No. 1370, "Dynamic Problems in Military Flight Vehicles" and Task No. 137003, "Prevention of Dynamic Aeroelastic Instabilities in Advanced Military Aircraft". The work was performed by the Flutter Research Group of The Boeing Company, Commercial Airplane Group, Renton, Washington, for the Aerospace Dynamics Branch, Vehicle Dynamics Division, Air Force Flight Dynamics Laboratory, Wright-Patterson Air Force Base, Ohio. The computer program was prepared and documented by Mr. Gordon D. Kramer and Mr. George F. Keylon of Boeing Computer Services, Inc. The overall program management was provided by Mr. William S. Rowe of The Boeing Company. Mr. Lawrence J. Huttsell of the Aerospace Dynamics Branch (FYS) monitored the contract for the Air Force.

This document constitutes the first part of a two-part final report. Part II containing the computer program listing is available upon request from the Air Force Flight Dynamics Laboratory (FY), Wright-Patterson AFB, Ohio 45433.

This report covers work performed from December 1969 to April 1971.

The manuscript was released by the authors Dr. Jack Morito II, Mr. Christopher J. Borland and Mr. John R. Hogley of the Flutter Research Group of Commercial Airplane Group for publication as an AFFDL technical report. This report is also known as Boeing Document D6-24860.

This technical report has been reviewed and is approved.

Walter J. Mykytow

WALTER J. MYKYTOW
Assistant for Research & Technology
Vehicle Dynamics Division
Air Force Flight Dynamics Laboratory

ABSTRACT

A three-dimensional extension of the Mach Box technique has been developed for the unsteady aerodynamic analysis of non-planar wings and wing-tail configurations in supersonic flow. Various refinement procedures have been included to improve the accuracy of the results.

A general purpose computer program has been written for the CDC 6600. The program is capable of treating wing tail combinations with or without vertical separation, longitudinal separation and dihedral on either surface. A non-intersecting wing-vertical tail combination may be examined. If a wing alone is treated, perturbation velocity components in the flow field may be found.

The program has been used to obtain pressure distributions and generalized forces on several wing-tail configurations. In addition, correlations with experimental flutter results have been performed for several models tested in the low supersonic Mach number range at Cornell Aeronautical Laboratory.

TABLE OF CONTENTS

Section		Page
I	INTRODUCTION	1
II	THEORETICAL DEVELOPMENT	3
	1. A Brief Summary of the Theory	3
	2. Thin Airfoil Theory in Supersonic Flow	4
	3. Numerical Computation in the Mach Box Grid System	9
	4. Evaluation of Aerodynamic Influence Coefficients	15
	5. Velocity Potential and Perturbation Velocity Calculations	22
	6. Pressure Distributions, Generalized Forces, and Generalized Aerodynamic Coefficients	39
	7. Refinements of the Mach Box Method	44
III	COMPUTER PROGRAM USAGE	60
	1. Machine and Operating System Requirements	60
	2. Timing and Output Estimates	60
	3. Program Limits and Restrictions	65
	4. Deck Setup	66
	5. Card Input Data	68
	6. Diagnostics	84
	7. Output Description	89
IV	APPLICATIONS	91
	1. Introduction	91
	2. Program Limitations	91
	3. Preliminary Comments on Program Characteristics	91
	4. Preliminary Checkout of the Program	94
	5. Flutter Model Correlation	96
	6. Unsteady Aerodynamic Applications	117
V	CONCLUSIONS AND RECOMMENDATIONS	123
REFERENCES		181

LIST OF ILLUSTRATIONS

Figure		Page
1	Coordinate Systems for a Right Wing	xxvi
2	Coordinate Systems for a Right Tail	xxviii
3	Distributed Singularities on a Planar Surface with Supersonic Leading Edge	5
4	Receiving Point Coordinate System Corresponding to a Right Wing Sending Surface	10
5	Receiving Point Coordinate System in Wing-Tail Configuration	13
6	Mach Box Grid Systems on Sending Surfaces and Their Boundaries	14
7	Values of (τ, θ) Corresponding to $(\bar{\xi}, \bar{\eta})$	16
8	Integration Limits on Partial Edge Box	17
9	Zones in Wing-Tail Configuration	23
10	Interacted Flow Field in Wing-Tail Configuration in Steady Case	25
11	Box Arrangement on a Wing With Dihedral	27
12	Normal Wash on Upper and Lower Surfaces of Wing	29
13	Irregularities in Distorted Jagged Leading Edges	44
14	Refinement of Jagged Leading Edges	46
15	Avoidance of Irregular Point Effects by Subdivision in Odd Number Increments	47
16	Subdivision of Box Grid System in Effective Area Zone	48
17	Summary of Polynomial Terms	55
18	Thickness Distribution About Wing Mean Surface	57
19	Timing of AIC Calculations	62
20	Sample Timing of Velocity Potential Calculations with Subdivision	63
21	Velocity Potential Timing, Unsubdivided	64
22	Determination of Box Pattern Limits	65
23	Definition of Sampling Locations	78
24	Boxes Needed for Trailing Edge Velocity Potential Calculations	88
25	Planform Edge Definition, Wing or Tail	126

LIST OF ILLUSTRATIONS (cont.)

Figure		Page
26	Allowable Wing/Tail Configurations	127
27	Additional Allowable Wing/Tail Configurations	128
28	Dihedral Combination Not Allowed	129
29	Tail Overlap Restriction	130
30	Other Configurations Not Allowed	131
31	Mach Box Grid System Without Subdivision	132
32	Mach Box Grid System With Subdivision	133
33	Method of Evaluating $\alpha^{n,m}$ used in Subdivision	134
34	Effect of Subdivision on Chordwise Loading	135
35	Effect of Subdivision on Velocity Potentials	136
36	Velocity Potential Smoothing Process	137
37	Non-Dimensional Lift Distribution	138
38	Analysis Planform of Chordwise Loadings-Gap Study	139
39	Chordwise Loadings for Various Wing-Tail Separations in Wing Tip Region	140
40	Chordwise Loadings Near Root Section	141
41	Velocity Potential Smoothing and Resulting Chordwise Loadings for Configuration 15 $M = 1.238$, $k_s = 0.338$, $\eta = 0.85$	142
42	Application of CRDFT = .TRUE. and Resulting Chordwise Loadings at $\eta = 0.85$	143
43	Wing Deflection Shape, Mode No. 3, Cornell Configuration 15	144
44	Wing Deflection Shape, Mode No. 4, Cornell Configuration 15	145
45	Downwash Distribution in Wing Wake, Mode No. 3, $M = 1.238$, $k_s = .3425$	146
46	Normalwash Distribution in Wing Wake, Mode No. 4, $M = 1.238$, $k_s = 0.3425$	147
47	Spatial Variation in Vertical Wash, Configuration 15 $M = 1.238$, $k_s = 0.338$, $\eta = 0.85$	148
48	45° Swept Model Assembly	149
49	60° Swept Model Assembly	150
50	Comparison of Calculated and Experimental Node Lines, Test Configuration 15	151

LIST OF ILLUSTRATIONS (cont.)

Figure		Page
51	Comparison of Calculated and Experimental Node Lines, Test Configuration 22	152
52	Comparison of Calculated and Experimental Node Lines, Test Configuration 23	153
53	Flutter Speed and Frequency vs. Horizontal Separation for Configuration 15, 45° Swept Model, M = 1.238, $\frac{z}{b_s} = 0$	154
54	Flutter Speed and Frequency vs. Vertical Separation for Configuration 15, 45° Swept Model, M = 1.238, $x/b_s = 0.505$	155
55	Flutter Speed and Frequency vs. Mach Number for Configuration 15, 45° Swept Model, $z/b_s = 0$, $x/b_s = 0.166$	156
56	Flutter Speed and Frequency vs. Mach Number for Configuration 22, 60° Swept Model, $z/b_s = 0$, $x/b_s = 0.19$	157
57	Flutter Speed and Frequency vs. Mach Number for Configuration 23, 60° Swept Model, $z/b_s = 0$, $x/b_s = 0.19$	158
58	Flutter Speed vs. Mach Number, 45° Swept Models	159
59	Flutter Speed vs. Mach Number, 60° Swept Models	160
60	AGARD Wing-Tail Configuration	161
61	Longitudinal Wash on A Sampling Chord, $y/_s = 0.72$, $z/s = 0.2$, $k_s = 0.75$, M = 1.56	162
62	Longitudinal Wash on a Sampling Chord, $y/_s = 0.72$, $z/s = 0.2$, $k_s = 1.5$, M = 1.56	162
63	Sidewash on a Sampling Chord, $y/_s = 0.72$, $z/s = 0.2$, $k_s = 0.75$, M = 1.56	163
64	Sidewash on a Sampling Chord, $y/_s = 0.72$, $z/s = 0.2$, $k_s = 1.5$, M = 1.56	163
65	Upwash on a Sampling Chord, $y/_s = .056$, $z/s = 0.5$, $k_s = 0.75$, M = 1.56	164
66	Upwash on a Sampling Chord, $y/_s = .056$, $z/s = 0.5$, $k_s = 1.5$, M = 1.56	164
67	Pressure Distribution Along Chord No. 1, $y/_s = .056$, $k_s = 0.75$, M = 1.56, Mode 1	165
68	Pressure Distribution Along Chord No. 1, $y/_s = .056$, $k_s = 0.75$, M = 1.56, Mode 2	165
69	Pressure Distribution Along Chord No. 1, $y/_s = .056$, $k_s = 1.5$, M = 1.56, Mode 1	166
70	Pressure Distribution Along Chord No. 1, $y/_s = .056$, $k_s = 1.5$, M = 1.56, Mode 2	166

LIST OF ILLUSTRATIONS (cont.)

Figure		Page
71	Pressure Distribution Along Chord No. 7, $y/s = 0.72$, $k_s = 0.75$, $M = 1.56$, Mode 1	167
72	Pressure Distribution Along Chord No. 7, $y/s = 0.72$, $k_s = 0.75$, $M = 1.56$, Mode 2	167
73	Pressure Distribution Along Chord No. 7, $y/s = 0.72$, $k_s = 1.5$, $M = 1.56$, Mode 1	168
74	Pressure Distribution Along Chord No. 7, $y/s = 0.72$ $k_s = 1.5$, $M = 1.56$, Mode 2	168
75	Chordwise Pressure Distribution, AGARD Planform, Small Separation, Wing Pitch Mode, $M = 1.414$, $k_s = 0.75$	169
76	Chordwise Pressure Distribution, AGARD Planform, Small Separation, Wing Pitch Mode, $M = 1.414$ $k_s = 1.5$	170
77	Chordwise Pressure Distribution, AGARD Planform, Small Separation, Wing Pitch Mode, $M = 3.162$, $k_s = 0.75$	171
78	Chordwise Pressure Distribution, AGARD Planform, Small Separation, Wing Pitch Mode, $M = 3.162$, $k_s = 1.50$	172
79	Chordwise Pressure Distribution, AGARD Planform, Moderate Separation, Wing Pitch Mode, $M = 1.56$, $k_s = 0.75$	173
80	Chordwise Pressure Distribution, AGARD Planform, Moderate Separation, Wing Pitch Mode, $M = 1.56$, $k_s = 1.5$	174
81	Source of Load Irregularities due to L. E. Definition	175
82	Recommended Revised Subdivision Pattern	176
83	Solution Extension to Remove Modal Dependency	177
84	Flutter Speed and Air Density vs. Flow Mach Number for Cornell Configuration No. 15	178
85	Flutter Speed and Air Density vs. Flow Mach Number for Cornell Configuration No. 22	179

LIST OF TABLES

No.	Title	Page
1	Order of All Optional Output	90
2	Measured Cantilever Coupled-Mode Frequencies	103
3	Mass Properties of Configuration 15	104
4	Mass Properties of Configurations 22 & 23	105
5	Roll Inertia of Fuselage of Cornell Wing-Horizontal Tail Flutter Models	106
6	Uncoupled Cantilever Mode Shapes of Configuration 15	107
7	Uncoupled Cantilever Mode Shapes of Configurations 22 & 23	108
8	Uncoupled Rigid Body Roll and Fuselage Torsion Mode Shapes of the Cornell Wing-Horizontal Tail Flutter Models	109
9	Generalized Coordinate Transformation Matrix for Configuration 15	110
10	Generalized Coordinate Transformation Matrix for Configuration 22	111
11	Generalized Coordinate Transformation Matrix for Configuration 23	112
12	Analytical Flutter Results on Configuration 15 (Original Modes, 45° Swept Models, ω_θ/ω_h = 1.765)	113
13	Analytical & Test Flutter Results on Configuration 22 (Original Modes, 60° Swept Models, ω_θ/ω_h = 1.428)	114
14	Analytical & Test Flutter Results on Configuration 23 (Original Modes, 60° Swept Models, ω_θ/ω_h = 1.775)	115
15	Analytical & Test Flutter Results on Configurations 15,22,23 (Modified Modes, 45° and 60° Swept Models)	116
16	Summary of AGARD Configuration Cases	118
17	Generalized Unsteady Aerodynamic Coefficients for AGARD Case 1-1 (M= 1.56)	119
18	Generalized Unsteady Aerodynamic Coefficients for AGARD Case 2-1 (M = 1.414)	120
19	Generalized Unsteady Aerodynamic Coefficients for AGARD Case 2-2 (M = 3.162)	121
20	Generalized Unsteady Aerodynamic Coefficients for AGARD Case 2-3 (M = 1.56)	122
21	Analytical Flutter Results v.s. Flow Mach Number	180

NOMENCLATURE

Mathematical Symbol	FORTRAN Symbol	Dimension	Definition
a		length/time	Speed of Sound = U/M
$A(n,m)$		area	Integration area of box n,m
b_1	B1	length	Chordwise dimension of Mach box.
b_{1S}	B1S	length	b_1/N_S = chordwise dimension of a subdivided box.
$C_{\bar{\nu}\bar{\mu}\bar{\lambda}}$	C	non-dimensional	Velocity potential spatial aerodynamic influence coefficient (AIC).
$C_{\bar{\nu}\bar{\mu}\bar{\lambda}}^{\binom{xy}{ab}}$	C	non-dimensional	Spatial AIC giving velocity potential at a point on surface "xy" due to constant outward normal wash over a box on surface "ab"; possible values for superscripts are x or a $\begin{cases}\text{R-right}\\ \text{L-left}\end{cases}$ y or b $\begin{cases}\text{W-wing}\\ \text{T-tail}\end{cases}$
$C_{\bar{\nu}\bar{\mu}o}$, $C_{\bar{\nu},\bar{\mu}}$	PKERNL	non-dimensional	Velocity potential planar AIC
$C_{\bar{\nu}\bar{\mu}o}^{S}$	SKERNL	non-dimensional	Planar AIC defined for subdivided sending boxes.
$\Delta\bar{C}_{p_j}^{n,m}$	DELCP	1/length	Pressure coefficient difference at box n,m for the jth mode (program output)
l_c, c	--	length	Local reference chord

NOMENCLATURE

Mathematical Symbol	FORTRAN Symbol	Dimension	Definition
$C^m_{\ell_j}$	--	1/length	Local lift coefficient per unit span for the jth mode
$C^m_{m_j}$	SECMOM	$1/(\text{length})^2$	Local moment coefficient per unit span for the jth mode
$\left.\begin{matrix} c_{rW} \\ c_{rT} \end{matrix}\right\}$	---	length	$\left\{\begin{matrix}\text{Wing} \\ \text{Tail}\end{matrix}\right\}$ root section chord length.
$\frac{D}{Dt}$	--	1/time	Substantial derivative; $\frac{D}{Dt} = \frac{\partial}{\partial t} + U \frac{\partial}{\partial x}$
$f_j(x,y)$	DEFSL(1,L)	non-dimensional	j^{th} mode shape deflection at location (X,Y).
f_{ij}	---	non-dimensional	Deflection of ith lumped mass in mode j
$\frac{\partial f_j(x,y)}{\partial x}$	DEFSL(2,L)	1/length	Slope of jth mode shape function.
$\bar{f}_j^{n,m}$	---	time	Scaled modal displacement at box n,m $\bar{f}_j^{n,m} = \frac{b_1}{U} f_j^{n,m}$
g_j		1/length	j^{th} mode shape deflection / s
I_i	---	mass x length^2	Moment of inertia about the elastic axis of the ith lumped mass
K_{ij}	---	force/length	Generalized stiffness
k_s	XKS	Non-dimensional	Reduced frequency based on leading planform semi-span, $k_s = \frac{\omega s}{U}$

NOMENCLATURE

Mathematical Symbol	FORTRAN Symbol	Dimension	Definition
k_1	XKI,K1	non-dimensional	Reduced frequency based on the chordwise dimension of the Mach box $k_1 = \frac{\omega b_1}{U}$
$\bar{k}_1$	K1BAR	non-dimensional	$k_1 M^2/\beta^2$
L	CAPL	non-dimensional	Vertical separation of the center lines of the 2 surfaces, positive upward measuring from the wing to the tail.
$L_j^{n,m}$	--	force/length	lift on box n,m for the jth mode
L_j^{m}	--	force/length	lift on the mth chordwise strip of boxes for the jth mode.
L_j	--	force/length	lift on a complete half-surface or half-airplane for the jth mode.
$\bar{L}_j^{n,m}$	--	force/length	amplitude of box lift $L_j^{n,m}$
$\bar{L}_j^{m}$	--	force/length	amplitude of section lift L_j^{m}
$\bar{L}_j$	--	force/length	amplitude of total lift L_j
$\bar{\bar{L}}_j^{n,m}$	BXL1FT	non-dimensional	Non-dimensional amplitude of box lift (program output) $L_j^{n,m} = \bar{L}_j^{n,m} e^{i\omega t} = q\left(\frac{b_1}{\beta}\right) \bar{\bar{L}}_j^{n,m} e^{i\omega t}$

NOMENCLATURE

Mathematical Symbol	FORTRAN Symbol	Dimension	Definition
$\bar{\bar{L}}_j^m$	SLIFT	non-dimensional	nondimensional amplitude of section lift (program output) $L_j^n = \bar{L}_j^n e^{i\omega t} = q\left(\frac{b_1}{\beta}\right) \bar{\bar{L}}_j^n e^{i\omega t}$
$\bar{\bar{L}}_j$	TLIFT	non-dimensional	Nondimensional amplitude of total lift (program output) $L_j = \bar{L}_j e^{i\omega t} = q\left(\frac{b_1}{\beta}\right) \bar{\bar{L}}_j e^{i\omega t}$
ℓ	EL	non-dimensional	The ℓ_c coordinate location of a pulse receiving point, i.e., the perpendicular distance from the sending plane to receiving point.
M	XMACH	non-dimensional	Mach number
M_{jj}	--	mass	Generalized mass for the jth mode
m	--	non-dimensional	The m_c coordinate location of a pulse receiving point.
m_i	--	mass	i^{th} lumped mass
$N_{xyz}^{n,m}$	ENRUS ENRLS, EN, ENSUBD	non-dimensional	Normal wash at box n,m on surface "xyz" due to local source strength, where possible subscript values are; $x = \begin{cases} \text{R-right} \\ \text{L-left} \end{cases}$ $y = \begin{cases} \text{U-upper} \\ \text{L-lower} \end{cases}$ $z = \begin{cases} \text{W-wing} \\ \text{T-tail} \end{cases}$ e.g. $N_{RUW}^{n,m}$ means normal wash on the right upper wing at box n,m

NOMENCLATURE

Mathematical Symbol	FORTRAN Symbol	Dimension	Definition
$\hat{N}^{n,m}_{xyz\,abc}$	ENRULU, ENRLLL, ENRURW, ENRULW	non-dimensional	Normal wash at box n,m on surface "xyz" due to remote source strengths on surface "abc", where possible subscript values for a,b, and c are the same as for x,y, and z, respectively, defined above; e.g. $\hat{N}^{n,m}_{RUT\,LLW}$ means normal wash at box n,m on the right upper tail due to source strengths on the left lower wing.
N_s	NSUBDV	non-dimensional, odd integer	No. of "sub-boxes" (chordwise and spanwise) to be used in the subdivision improvement technique.
n	--	non-dimensional	the n_c coordinate location of a pulse receiving point.
n_c, m_c, ℓ_c	---	---	Sending Surface Coordinate System
$\bar{n}_c, \bar{m}_c, \bar{\ell}_c$	---	---	Receiving Point Coordinate System
$p, p(x,y,t)$	---	force/area	local static pressure
p_∞	---	force/area	Free stream static pressure
$\Delta p(x,y,t)$	---	force/area	pressure difference between upper and lower surfaces at point (x,y) at time t $\Delta p(x,y,t) = p(x,y,t)_{upper} - p(x,y,t)_{lower}$

NOMENCLATURE

Mathematical Symbol	FORTRAN Symbol	Dimension	Definition
$\Delta\bar{p}(x,y)$	--	force/area	Amplitude of pressure difference: $\Delta p(x,y,t) = \Delta\bar{p}(x,y)e^{i\omega t}$
Q_{ij}		force/length	Generalized force due to the deformation in the ith elastic mode and loading for the jth modal deflections
$\bar{Q}_{ij}$	--	force/length	Amplitude of generalized force
$\bar{\bar{Q}}_{ij}$	GENAF	non-dimensional	Non-dimensional generalized force (program output); $Q_{ij} = \bar{Q}_{ij}e^{i\omega t} = q\frac{b_1}{\beta}\bar{\bar{Q}}_{ij}e^{i\omega t}$
$\hat{Q}_{ij}$	QAGARD	$1/(\text{length})^2$	Generalized force in the AGARD notation
Q'_{ij}, Q''_{ij}	GENAFC	$1/(\text{length})^2$	Real and imaginary parts of $\hat{Q}_{ij}$ in the AGARD definition (program output)
q	--	force/area	dynamic pressure
$q_j(t)$	--	length	Generalized coordinate relating physical deflection to j^{th} modal deflections: $Z(x,y,t) = \sum_j f_j(x,y)\,q_j(t)$
$\bar{q}_j$	--	length	Amplitude of jth generalized coordinate
s	S	length	Wing semi-span.

NOMENCLATURE

Mathematical Symbol	FORTRAN Symbol	Dimension	Definition
S	--	length^2	Area of integration. Bounded by edge of planform plus diaphragm and lying inside the forward Mach cone of the receiving point.
t	--	time	Time
U	--	length/ time	Free stream velocity.
$U_{\bar{\nu}\bar{\mu}\bar{\lambda}}$	---	non-dimensional	Velocity spatial AIC for perturbation velocity parallel to the free stream.
u	---	length/ time	Perturbation velocity in the streamwise direction, positive downstream.
$V_{\bar{\nu}\bar{\mu}\bar{\lambda}}$	V	non-dimensional	Velocity spatial aerodynamic influence coefficient (AIC) for velocity normal to the free stream and parallel to the sending surface.
$V^{\binom{xy}{ab}}_{\bar{\nu}\bar{\mu}\bar{\lambda}}$	V	non-dimensional	Spatial AIC giving velocity normal to the free stream and parallel to surface "ab" at a point on surface "xy" or in the flowfield (FF), due to constant normal wash over a box on surface "ab"
v		length/ time	Perturbation velocity in the spanwise direction, positive right (looking upstream).
$W_{\bar{\nu}\bar{\mu}\bar{\lambda}}$	W	non-dimensional	Velocity spatial aerodynamic influence coefficient (AIC) for velocity normal to the sending plane.

NOMENCLATURE

Mathematical Symbol	FORTRAN Symbol	Dimension	Definition
$W_{\overline{\nu\mu\lambda}}^{\binom{xy}{ab}}$	W	non-dimensional	Spatial AIC giving velocity normal to surface "ab" at a point on surface "xy" or in the flow field (FF) due to a constant normal wash over a box on surface "ab".
w		length/ time	Perturbation velocity in the vertical direction, positive upward.
X,Y,Z		length	Reference (global) coordinate system, X positive aft, Y positive right, Z positive upward.

NOMENCLATURE

Mathematical Symbol	FORTRAN Symbol	Dimension	Definition
X_w, Y_w, Z_w			Wing local coordinate system.
X_T, Y_T, Z_T			Tail local coordinate system
X_{WLE}	XWLE	length	The location of a leading edge definition point of the wing planform, measured along the X_w co-ordinate.
X_{TLE}	XTLE	length	Same as above for the tail planform, measured along the X_T coordinate.
X_{WTE}	XWTE	length	The location of a trailing edge definition point of the wing planform.
X_{TTE}	XTTE	length	Same as above for the tail, measured along the X_T co-ordinate.
$\left\{ \begin{matrix} X_F \\ X_c \end{matrix} \right\}$	$\left\{ \begin{matrix} \text{XEDGE} \\ \text{XCENTR} \end{matrix} \right\}$	length	Location of the $\left\{ \begin{matrix} \text{edge} \\ \text{center} \end{matrix} \right\}$ of a Mach box used for the placement of the box pattern, measured along the X_W coordinate.
$\left\{ \begin{matrix} X_{CW} \\ X_{CT} \end{matrix} \right\}$			The location of the most upstream row of boxes on the $\left\{ \begin{matrix} \text{wing} \\ \text{tail} \end{matrix} \right\}$ measured along the $\left\{ \begin{matrix} X_W \\ X_T \end{matrix} \right\}$ co-ordinate.

NOMENCLATURE

Mathematical Symbol	FORTRAN Symbol	Dimension	Definition
$\begin{Bmatrix} Y_{WLE} \\ Y_{TLE} \end{Bmatrix}$	$\begin{Bmatrix} YWLE \\ YTLE \end{Bmatrix}$	length	The location of a leading edge definition point of the $\begin{Bmatrix} \text{wing} \\ \text{tail} \end{Bmatrix}$ planform measured along coordinate $\begin{Bmatrix} Y_W \\ Y_T \end{Bmatrix}$.
$\bar{y}$	YBAR	non-dimensional	Offset of receiving chord from the nearest sending chord.
$\begin{Bmatrix} Z_u \\ Z_L \end{Bmatrix}(x,y,t)$	--	length	$\begin{Bmatrix} \text{Upper} \\ \text{Lower} \end{Bmatrix}$ surface deflection at (x,y) as a function of time
$Z_m(x,y,t)$	--	length	mean surface deflection: $Z_M(x,y,t) = f_j(x,y)e^{i\omega t}$
$Z_\tau(x,y)$	--	length	Local thickness at (x,y)
$\frac{\partial Z_\tau}{\partial x}(x,y)$	TSLFN	non-dimensional	Local thickness slope at (x,y)
$\bar{\bar{Z}}_\tau$	--	non-dimensional	Thickness slope piston theory correction; $\bar{\bar{Z}}_\tau = 1 + \frac{\gamma+1}{2} M \frac{\partial Z_\tau}{\partial x}$
$\alpha^{n,m}$	ALPHA	non-dimensional	Edge box area ratio for box(n,m).
β	BETA	non-dimensional	$\sqrt{M^2 - 1}$

NOMENCLATURE

Mathematical Symbol	FORTRAN Symbol	Dimension	Definition
b_1/β	BIBETA	length	Spanwise dimension of the Mach box.
b_{1_s}/β	BIBTAS	length	Spanwise dimension of a subdivided Mach box.
γ	GAMMA	non-dimensional	Ratio of specific heats, = 1.4
ζ	ZETA	non-dimensional	Dummy variable in the Z_w or Z_T coordinate.
$\bar{\eta}$	ETABAR	non-dimensional	Dummy variable of integration in the $\bar{m}_c$ coordinate.
θ	THETA	radians	$\sin^{-1}\frac{\bar{\eta}}{\tau} = \sin^{-1}\frac{\bar{\eta}}{\sqrt{\bar{\zeta}^2 - \bar{\lambda}^2}}$
θ_{ij}	--	radians/length	Torsion of ith lumped mass in mode j.
$\bar{\lambda}$	--	non-dimensional	$\bar{l}_c$ coordinate location of a pulse sending box.
μ	MU, YMU	non-dimensional	m_c coordinate location of a pulse sending box.
$\bar{\mu}$	YMUBAR	non-dimensional	$\bar{m}_c$ coordinate location of a pulse sending box.

NOMENCLATURE

Mathematical Symbol	FORTRAN Symbol	Dimension	Definition
ν	NU,XNU	non-dimensional	n_c coordinate location of a pulse sending box.
$\bar{\nu}$	XNUBAR	non-dimensional	$\bar{n}_c$ coordinate location of a pulse sending box.
ξ	XI	non-dimensional	Dummy variable of integration in the X_w or X_T coordinate.
$\bar{\xi}$	XIBAR	non-dim dimensional	Dummy variable of integration in the $\bar{n}_c$ coordinate.
ρ, ρ_∞	--	Mass/volume	Free stream density.
τ	TAU	non-dimensional	$\sqrt{\bar{\xi}^2 - \bar{\lambda}^2}$
$\phi(x,y,t)$	--	length^2/time	Disturbance velocity potential at point (x,y) and time t, defined so that $\frac{\partial \phi}{\partial x_i}$ is velocity, positive in positive x_i direction, where x_i = X, Y, or Z
$\Delta\phi(x,y,t)$	--	length^2/time	Disturbance velocity potential difference between the top and bottom side of the surface at point (x,y) and time t: $\Delta\phi(x,y,t) = \phi_{upper} - \phi_{lower}$

NOMENCLATURE

Mathematical Symbol	FORTRAN Symbol	Dimension	Definition
$\Delta\bar{\phi}_j(x,y)$	--	length / time	Amplitude of velocity potential difference at point (x,y) or for box n,m for the jth mode
$\left.\begin{array}{l}\Delta\bar{\bar{\phi}}_j(x,y)\\ \Delta\bar{\bar{\phi}}_j^{n,m}\end{array}\right\}$	DELPHI	non-dimensional	Non-dimensional velocity potential difference due to the unit j^{th} generalized coordinate (program output); $\Delta\phi_j^{n,m} = \Delta\bar{\phi}_j^{n,m} e^{i\omega t} = \frac{U}{b_1}\left(\frac{b_1}{\beta}\right)\Delta\bar{\bar{\phi}}_j^{n,m} e^{i\omega t}$
$\left.\begin{array}{l}\Delta\bar{\bar{\phi}}_j(X_{TE},y)\\ \Delta\bar{\bar{\phi}}_j^{m}{}_{TE}\end{array}\right\}$	TVP	non-dimensional	Trailing edge velocity potential difference.
$\left\{\begin{array}{l}\psi_W\\ \psi_T\end{array}\right\}$	$\left\{\begin{array}{l}\text{PSIW}\\ \text{PSIT}\end{array}\right\}$	degrees	Dihedral angle of $\left\{\begin{array}{l}\text{wing}\\ \text{tail}\end{array}\right\}$, radians, positive upwards from horizontal.
ω	---	radians/ time	Circular frequency
ω_j	---	radians/ time	Circular frequency of mode j

Superscripts

$\left.\begin{array}{l}(n,m)\\ (\nu,\mu)\end{array}\right\}$ Box location

Subscripts

L	Lower limit of Integration; Left-hand surface; Lower surface
R	Right-hand Surface
S	Subdivided
T	Tail
U	Upper limit of Integration; Upper Surface
W	Wing
FF	Flowfield

GLOSSARY OF TERMINOLOGY

Aftmost Box - Each chord on each planform and diaphragm combination has one such box. It is the aftmost box on that chord for which AIC arrays must be calculated and may be on the planform or diaphragm.

AIC - Aerodynamic Influence Coefficient

Area Ratio - On-planform fraction of a box which is cut by the planform boundary.

Apex Box - The box on the sending surface which encloses the apex of the Mach hyperbola associated with the receiving box.

Box Grid - Non-dimensionalized geometric array of boxes whose extent is determined by the geometric properties of the planforms. The term "grid" embraces the arrays on both surfaces.

Control Point - The location at which a receiving box is deemed to be influenced by other boxes. In general, the center of the receiving box.

Effective Area - A concept which relates entirely to the sub-division technique. It is composed of those boxes sufficiently close to the receiving box that their influence on it is large enough for the subdivision refinement to affect results significantly. The size has been arbitrarily set to include the N_{BOX}/N_S rows immediately ahead of the receiving box.

Global Co-ordinate System - An overall reference system of co-ordinates. For example, the airplane co-ordinate system X ~ aft, Y~right, Z~up. Y = 0 at centerline of airplane.

Leading Edge Diaphragm - All diaphragms on which $\Delta\phi = 0$.

Local Co-ordinate System - A co-ordinate system lying in the plane of the surface. x~aft, y~root to right tip. y = 0 at center line of airplane.

Longitudinal Separation - Streamwise distance between the trailing edge of the wing and the leading edge of the tail, measured along the centerline.

GLOSSARY OF TERMINOLOGY

Mach Asymptote - The asymptote of the Mach hyperbola.

Mach Hyperbola - The intersection of the sending plane and the forward Mach cone of the receiving point. Since this is always non-dimensionalized, it is a rectangular hyperbola.

Map - A condensed description of a large amount of data which can be used to locate any desired data element. A map of a banded sparse matrix might consist of two numbers per row, the first being the first non-zero column of that row and the second being the band width for that row. The matrix itself could then be stored as band elements only.

Normal Offset - The l_c distance between the sending box and the receiving point.

Parallel Offset - The m_c distance between the sending box center and the receiving point.

Partial Box - A sending box which is cut by the Mach hyperbola but which is neither an apex box nor an edge box.

Planar A.I.C.- An A.I.C defined by the geometric relation between a sending box and receiving box which lies in the same plane. $C_{\bar{\nu},\bar{\mu},0}$ only.

Receiving Box - In defining the relationship between two boxes the receiving box is the box which can be influenced by the other box.

Receiving Chord - Those receiving boxes which lie on the same chord. The receiving chord is significant in that all the boxes lying on it use AIC arrays which are a subset of those for the aftmost box lying on that chord.

Sending Box - In defining the relationship between two boxes, the sending box is the box which influences the other box (c.f. Receiving Box).

Spatial A.I.C. - An AIC defined by the geometrical relationship between two boxes which do not lie in the same plane. $C_{\bar{\nu}\bar{\mu}\bar{\lambda}}$, $V_{\bar{\nu}\bar{\mu}\bar{\lambda}}$, $W_{\bar{\nu}\bar{\mu}\bar{\lambda}}$.

GLOSSARY OF TERMINOLOGY

Sub-box - A member of the array of boxes formed when the grid of sending boxes is subdivided. Note it refers to the small box which is a fraction of the large box, and not to a large box which has been subdivided.

Tail - The downstream surface.

Vertical Separation - The vertical distance between the center lines of the two surfaces. Positive if the second surface is above the first.

Wake Diaphragm - That part of the diaphragm where $\Delta P = 0$ due to the influence of a surface.

Wing - Upstream Surface - (E.g. a Canard could be referred to as a wing)

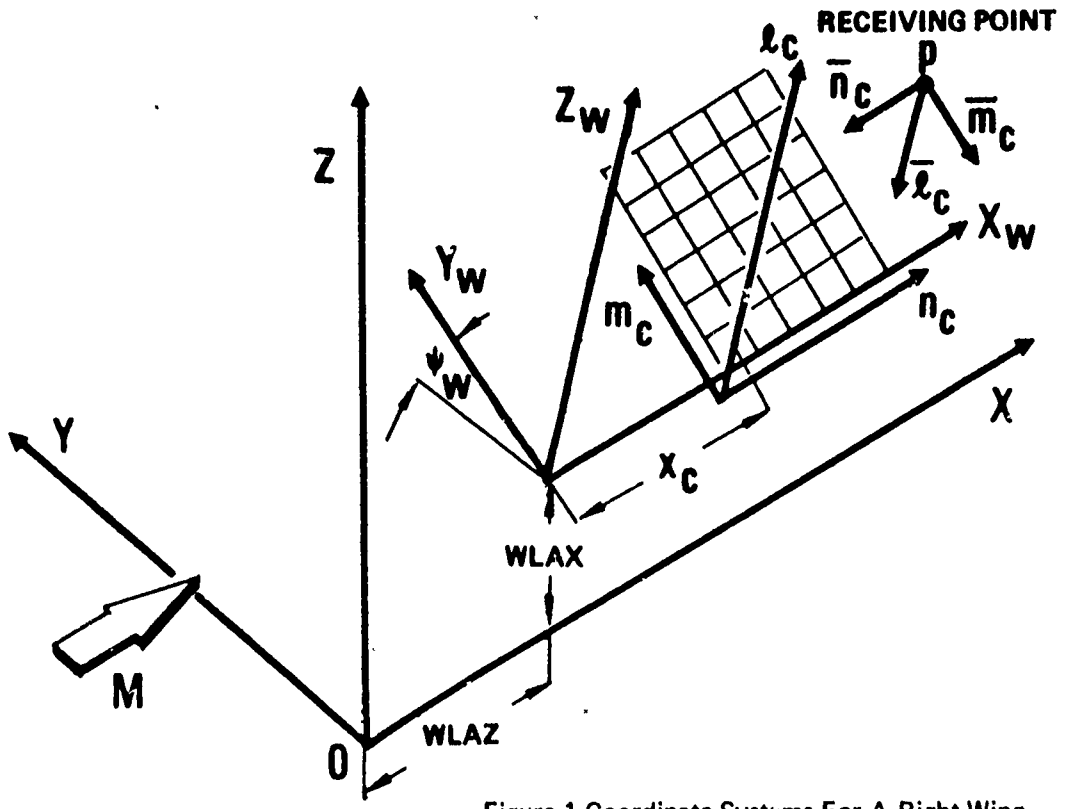

Figure 1 Coordinate Systems For A Right Wing

Symbol	Transformation	Definition	Dimension
X Y Z	Global or Reference Coordinate System. X positive Aft, Y positive Right, Z positive Upward		Length
X_w Y_w Z_w	$X - WLAX$ $Y\cos\psi_w + (Z - WLAZ)\sin\psi_w$ $(Z - WLAZ)\cos\psi_w - Y\sin\psi_w$	Wing Local Coordinate System, used to define wing leading and trailing edges. X_T, Y_T, Z_T are similarly defined for the tail local axes	Length
n_c m_c ℓ_c	$(X_w - X_c)/b_1 + 1$ $Y_w/(b_1/\beta) + 1/2$ $Z_w/(b_1/\beta)$	Sending Surface Coordinate System used to define box grid. The (n_c, m_c) plane lies within the plane of the sending surface, in this case the right wing.	Non-dimensional

Figure 1 (Cont'd)

Symbol	Transformation	Definition	Dimension
$\bar{n}_c$ $\bar{m}_c$ $\bar{l}_c$	$-(n_c-n)$ $-(m_c-m)$ $-(l_c-l)$	Receiving Point Coordinate System parallel to the n_c, m_c, l_c coordinates but opposite in sign and having their origin at the pulse receiving point (n,m,l in the n_c, m_c, l_c coordinates).	non-dimensional

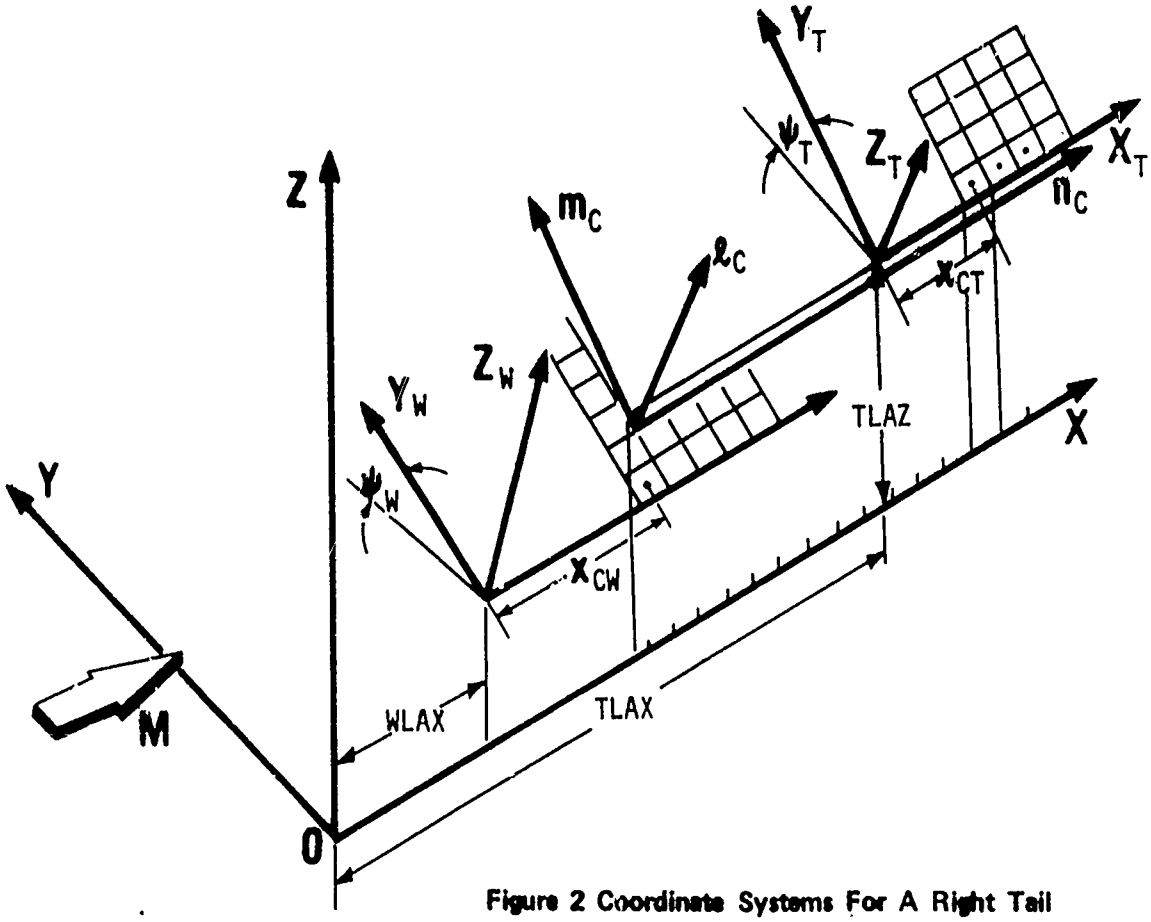

Figure 2 Coordinate Systems For A Right Tail

SYMBOL	TRANSFORMATION	DEFINITION	DIMENSION
X_T Y_T Z_T	X-TLAX $Y\cos\psi_T+(Z-TLAZ)\sin\psi_T$ $(Z-TLAZ)\cos\psi_T-Y\sin\psi_T$	Tail Local Coordinate System used to define tail leading and trailing edges.	length
n_c m_c ℓ_c	$\{X_T+TLAX-(WLAX+X_C)\}/b_1+1$ $Y_T/(b_1/\beta) + 1/2$ $Z_T/(b_1/\beta)$	Sending Surface Coordinate System. In this case the right tail is shown as the sending surface.	non-dimensional

SECTION I

INTRODUCTION

This report describes the development of a method for predicting the unsteady aerodynamics of flexible aircraft with non-planar wing and tail surfaces. The aerodynamic interference between the wing and tail has been taken into account. The method is based on a three-dimension extension and refinements of the well-known "Mach Box" method, first developed in Ref. (1). The refinements consist of a subdivision technique for improving the accuracy of the pressure distributions, a velocity potential smoothing technique, and a thickness-correction procedure based on second-order piston theory. The theoretical developments are described in Section II.

A general purpose computer program for implementing the theory has been written for the Control Data Corporation 6600. All information necessary for operation of the program is contained in Section III of the report. Detailed information on the computer program, including flow charts and listings, is contained in Part II.

The program has been tested by obtaining results on several typical configurations. Unsteady aerodynamic results, in the forms of pressure distributions, generalized forces, and perturbation velocities in the flow field, have been obtained for a standard AGARD wing-tail configuration for several Mach numbers, reduced frequencies, and geometrical arrangements. The program has also been used for comparison of experimental and analytical flutter results of several wing-horizontal tail configurations tested in the low supersonic Mach number range at Cornell Aeronautical Laboratory (Ref. (2)).

The possible configurations which may be analysed by the use of the program described herein may be summarized as follows:

a) Single Planar Wings (flow field sampling permitted);

b) Single Wings with Dihedral up to $\pm 45°$ (flow field sampling permitted);

c) Coplanar wing and tail;

d) Planar wing and tail with vertical separation;

e) Non planar wing and tail, dihedral on either surface up to $\pm 45°$, with or without vertical separation;

f) Wing, single vertical tail, non-intersecting

The planforms of either surface are entirely general, being specified by linear boundaries between points, for up to ten (x,y) coordinates on either leading or trailing edge. Segments of the leading edge may not be swept forward. Either subsonic or supersonic leading or trailing edges are permitted. Tips may be streamwise or raked. The surfaces are not permitted to have "mutual interaction" i.e., where the tail directly affects the wing as well as vice-versa, except in the case where the dihedral angles of the two surfaces are equal and there is no vertical separation. This includes the coplanar case.

Structural modal or rigid body deflections may be input at arbitrary points on the lifting surfaces, as polynomial coefficients, or at the control points of a previously determined Mach box grid. The program is capable of recycling on Mach number and reduced frequency without reinput of mode shapes or geometry. New mode shapes may be input without reinput of geometry information. The reverse may also be accomplished if it is desired, for example, to change the fineness of the Mach box grid.

The applicable Mach number range of the program is greater than 1.0 to less than 5.0. However, because of the limitations of linearized theory, results obtained for Mach numbers of less than 1.2 or greater than 3.0 should be used with extreme caution.

SECTION II

THEORETICAL DEVELOPMENT

1. A BRIEF SUMMARY OF THE THEORY

The motion of the configuration under consideration is assumed to be simple harmonic motion of sufficiently small amplitude that the perturbation velocity potential $\phi(x,y,z,t)$ satisfies the linearized differential equation of invicid fluid motion (Ref. 3):

$$(1 - M^2)\ \phi_{xx} + \phi_{yy} + \phi_{zz} = \frac{2M}{a}\phi_{xt} + \frac{1}{a^2}\phi_{tt}$$

where U is the free stream velocity and is parallel to the x-direction and M is the free stream Mach Number.

In order to determine the pressure distributions on the planform, and from thence the generalized forces, the method of Aerodynamic Influence Coefficients is used. As is described in References 3 and 4 the disturbances of the flow are reproduced by distributing pulsating sources related to the amplitudes of the modal displacements over each surface of each planform and over artificial "diaphragm regions" where necessary to isolate the upper and lower surfaces of the planform. There results an integral expression for $\phi(x,y,z)$ which is dependent upon the distribution of sources and the location of the point (x,y,z). This equation is developed in sub-section 2 below.

This integral expression cannot, in general, be evaluated analytically. The numerical approach used divides the surface into a grid of rectangular Mach Boxes whose diagonals lie along Mach Rays, and which are sufficiently small that the source distribution may be considered constant within them. The expression for ϕ then becomes a summation over the Mach Boxes. Each element of the summation is the source strength at the box center multiplied by an Aerodynamic Coefficient which is dependent only on the relative locations of the box and the point (x,y,z). This expression is derived in sub-sections 3 and 4.

The velocity potentials and, where unknown, the source distributions are then evaluated at each surface of each planform and diaphragm, taking into account the boundary conditions at the surfaces (section 5). The pressure distributions and generalized aerodynamic forces are then calculated from the difference between the velocity potential distributions on the upper and lower surfaces of the planform, as

$$r' = \{(x' - \xi')^2 + (y' - \eta')^2 + (z' - \zeta')^2\}^{1/2} \tag{4}$$

The potential in the original coordinates will be

$$\phi\ (x,y,z,t) = \frac{F}{r}\ \{f(t - \tau_1) + f(t - \tau_2)\} \tag{5}$$

where

$$r = \frac{1}{\beta^2}\sqrt{(x - \xi)^2 + \beta^2\ \{(y - \eta)^2 + (z - \zeta)^2\ \}}$$

$$\tau_1 = \frac{M}{a}\ \frac{x - \xi}{\beta^2} - \frac{r}{a}$$

$$\tau_2 = \frac{M}{a}\ \frac{x - \xi}{\beta^2} + \frac{r}{a}$$

and

$$\beta^2 = M^2 - 1$$

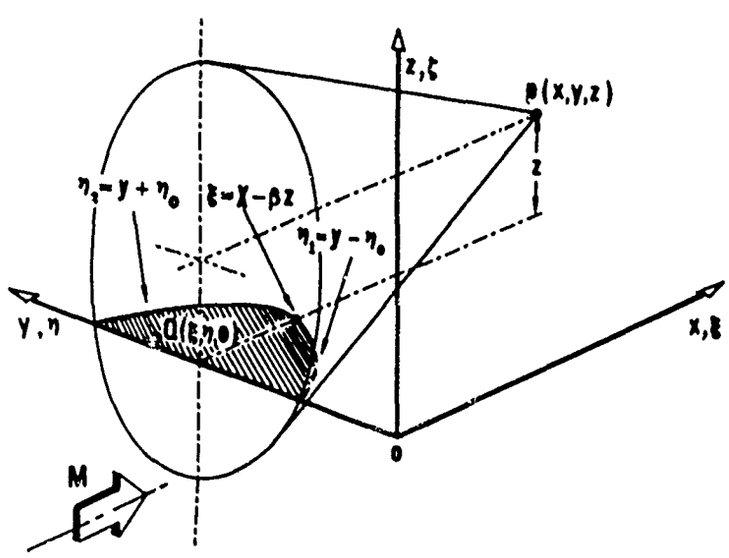

Figure 3 Distributed Singularities On A Planar Surface With Supersonic Leading Edge

described in sub-section 6.

It is well known that the Mach Box method produces pressure distributions which contain inaccuracies in the form of irregular fluctuations. Two refining techniques to reduce the fluctuations are used in this computer program. Of prime importance is the subdivision refinement in which the sending Mach Box grid is divided into an even finer grid while the receiving grid of control points remains unchanged. This refinement reduces the magnitude of the pressure distribution fluctuations substantially. A second refinement is the application of a least squares surface or chordwise polynomial, fitted to the velocity potential distribution, which smoothes the pressure distributions.

The pressure distributions are further refined by applying to them a thickness correction based on second order piston theory. All these optional refinements are described in sub-section 7.

2. THIN AIRFOIL THEORY IN SUPERSONIC FLOW

Thin airfoil or small perturbation theory is applied to describe the flow patterns that result when small disturbances are superposed on parallel uniform flow. When coordinate axes are fixed on a thin body placed in uniform flow, the perturbation velocity potential satisfies the differential equation.

$$(1 - M^2)\,\phi_{xx} + \phi_{yy} + \phi_{zz} = \frac{2\,M}{a}\,\phi_{xt} + \frac{1}{a^2}\,\phi_{tt} \qquad (1)$$

The linearized equation (1) can be transformed into the canonical wave equation through the mixed Lorentz-Galilean transformations, which does not involve any spacial rotation but is concerned only with a uniformly moving system, and which preserves the speed of sound in both coordinate systems (Refs. 4 and 5).

Then equation (1) will be transformed into

$$\phi_{x'x'} + \phi_{y'y'} + \phi_{z'z'} - \frac{1}{a^2}\,\phi_{t't'} = 0 \qquad (2)$$

One form of the general solution of equation (2) is

$$\phi(x',y',z',t') = \frac{F(x',y',z')}{r'}\,\{f(t' - \frac{r'}{a}) + f(t' + \frac{r'}{a})\}$$

which signifies a pulsing source singularity moving with a speed of U (Ref. 6), and where $F(x',y',z')$ is independent of time and is related only to the spacial coordinates, and

Consider a lifting surface whose leading edge is supersonic (for convenience the y -axis is placed on the leading edge), so that there is no communication between the upper and lower surfaces (see Figure 3). The potential at P(x,y,z) and at time t is computed from a source singularity distribution over the x,y plane and is

$$\phi(x,y,z,t) = \int_0^{x-\beta z} d\xi \int_{y-\eta_o}^{y+\eta_o} \frac{F(\xi,\eta,\zeta)}{r} \{f(t-\tau_1) + f(t-\tau_2)\} d\eta \quad (7)$$

where

$$\eta_o = \sqrt{\frac{(x-\xi)^2}{\beta^2} - (z-\zeta)^2}$$

The non-time dependent function F is determined by letting $z \to 0+$ and $\zeta \to 0+$. The result is

$$F(\xi,\eta,0+) = -\frac{1}{2\pi\beta^2} W_o(\xi,\eta,0+) \quad (8)$$

where W_o is the amplitude of the upwash w.

If the time variation f(t) of the source singularity is harmonic, that is,

$$f(t) = e^{i\omega t}$$

then, by applying the identities (6) the following can be obtained:

$$f(t-\tau_1) + f(t-\tau_2) = e^{i\omega(t-\tau_1)} + e^{i\omega(t-\tau_2)} = e^{i\omega t}\, e^{-i\omega\frac{M(x-\xi)}{a\beta^2}}\, 2\cos\omega\frac{r}{a} \quad (9)$$

Therefore, substitution of Equations (8) and (9) into (7) yields

$$\phi(x,y,z,t) = -\frac{e^{i\omega t}}{\pi} \int_0^{x-\beta z} d\xi \int_{y-\eta_o}^{y+\eta_o} W_o(\xi,\eta,0+) \frac{e^{-i\omega\frac{M(x-\xi)}{a\beta^2}}}{R_h} \cos\omega\frac{R_h}{a\beta^2} d\eta \quad (10)$$

where

R_h = Hyperbolic radius = $\beta^2 r = [(x-\xi)^2 - \beta^2\{(y-\eta)^2 + z^2\}]^{1/2}$

and 0+ indicates the upper surface of the pulse-sending box.

From the previous discussion, Equation (10) is only valid for harmonically oscillating source singularities in which the wing leading edges are supersonic.

The time-independent part of Equation (10) may be written a little more generally as

$$\phi(x,y,z) = -\frac{1}{\pi}\iint_S W_o(\xi,\eta,0+)\,\frac{e^{-i\omega\frac{M(x-\xi)}{a\beta^2}}\cos\frac{\omega R_h}{a\beta^2}}{R_h}\,dS \qquad (11)$$

For a planform with a supersonic leading edge, S indicates that portion of the planform which lies inside the forward Mach cone emanating from (x,y,z). If the planform has a subsonic leading edge, or trailing edge, or a streamwise edge at its tip, "diaphragms" are introduced using the "Evvard concept" as described in Ref. 7. The diaphragms are artificial "surfaces" which present no barrier to the flow, across which there can be no pressure discontinuity, and through which continuity of mass is maintained. They are introduced so that sources may be distributed upon them to account for the effects on the upper surface of the planform induced by the source distribution on the lower surface. The upper and lower surfaces of the planform plus diaphragm can now be considered non-communicative. Thus, S in Equation (11) is presumed to include any diaphragm regions needed to isolate the upper and lower surfaces, but is again restricted to that part of the planform and diaphragm contained inside the forward Mach cone emanating from (x,y,z).

The source distribution that is placed on the diaphragm is initially unknown, and is evaluated using the boundary condition $\Delta p = 0$ at all points not on the wing surface. This condition may be expressed as

$$\frac{\partial}{\partial t}\Delta\phi + U\frac{\partial}{\partial x}\Delta\phi = 0 \qquad (12)$$

Thus $\Delta\phi = 0$ for an off-wing diaphragm and

$$\Delta\phi(x,y,0,t) = \Delta\phi(x_{TE},y,0,\ t - \frac{x - x_{TE}}{U})$$

for a diaphragm that lies in the wake of the wing. For simple harmonic motion, this latter expression may be stated thus:

$$\Delta\phi(x,y,0,t) = \Delta\phi(x_{TE},y,0)\, e^{ik_1 \frac{(x-x_{TE})}{b_1}}\, e^{i\omega t} \tag{13}$$

The wake may have an effect on the wing (if the trailing edge is subsonic) or on the tail. Considerations have so far been based upon purely linearized theory, where the wake coincided with the mean plane of the lifting surface. However, the actual wake deforms in the direction of disturbed free flow and, as is known, tends to roll up. The distortion depends on the spanwise station, initial angle of attack, flow Mach number, reduced frequency, etc. The interaction effects on a tail surface with elevated vertical position is exaggerated by the wing with a positive initial angle of attack due to this distortion phenomenon. This effect can approximately be taken into account by assuming the actual position of the tail surface relative to the steady wake position to be the effective vertical position to which the unsteady wake will be superimposed, (Ref. 8).

The pressure due to the jth mode of oscillation is found from the usual linearized expression in the x,y,z, coordinate system.

$$P_j(x,y,0+,t) - p_\infty = \rho_\infty \frac{D\,\phi_j}{D\,t}$$

Thus, the airloads L_j are evaluated by an integration of the pressure over the area of interest. The generalized force over the area A due to deformation in the i-th elastic or rigid body mode and loadings of the j-th mode is

$$Q_{ij} = \iint_A f_i \Delta p_j \, ds$$

where Δp_j = Pressure difference between upper and lower surfaces at point (x,y) at time t due to a unit generalized deflection of j-th mode.

Further discussion of the computation of pressures and generalized forces will be found in Section 6.

3. NUMERICAL COMPUTATION IN THE MACH BOX GRID SYSTEM

If the integration area may be split into sufficiently small elementary areas, one may make approximations in the evaluation of the double integral in Equation (10).

The form of elementary areas presently available for practical computation are squares, the so-called Mach Boxes whose diagonals are parallel to the Mach lines, and the so-called characteristic boxes which are rhombuses with sides parallel to the Mach lines. Due to the fact that the Mach Box appears to be the most useful and versatile of the elementary shapes proposed to date, the numerical scheme for evaluating the aerodynamic forces used in this report is based on the Mach Box method (Refs. 1, 9).

In order to establish a convenient counting system for the grid of sending boxes a transformation is made from the dimensional coordinate system to a non-dimensional coordinate system (n_c, m_c, ℓ_c) in which the sending boxes are located at (ν, μ, 0) where ν, and μ are integers. This transformation, with the wing as sending surface is:

$$n_c = (X_W - X_{CW})/b_1 + 1$$

$$m_c = \beta Y_W/b_1 + 1/2$$

$$\ell_c = \beta Z_W/b_1$$

where X_{CW} is the location of the first box on the sending surface (see Figure 2) and (X_W, Y_W, Z_W) in the wing local coordinate system.

A similar transformation is used when the tail is the sending surface, with X_W, Y_W, Z_W, X_{WC} replaced by X_T, Y_T, Z_T, X_{CT} respectively.

The location of the receiving point, (x,y,z) in the local coordinate system), is designated (n,m,ℓ) in the (n_c, m_c, ℓ_c) coordinate system, as shown in Figure 4.

It is assumed that each box in the grid is sufficiently small that the upwash within it, $w_{o_{\nu\mu}}$ is constant. Thus, Equation (11) may be expressed in the form

$$\phi_o(x,y,z) = -\frac{1}{\pi}\sum_{\nu}\sum_{\mu} w_{o_{\nu\mu}} \iint_{A(\nu,\mu)} \frac{e^{-\frac{ik_1M^2}{\beta^2 b_1}(x-\xi)}}{R_h} \cos\frac{k_1 M}{\beta^2 b_1} R_h \, d\xi d\eta \qquad (14)$$

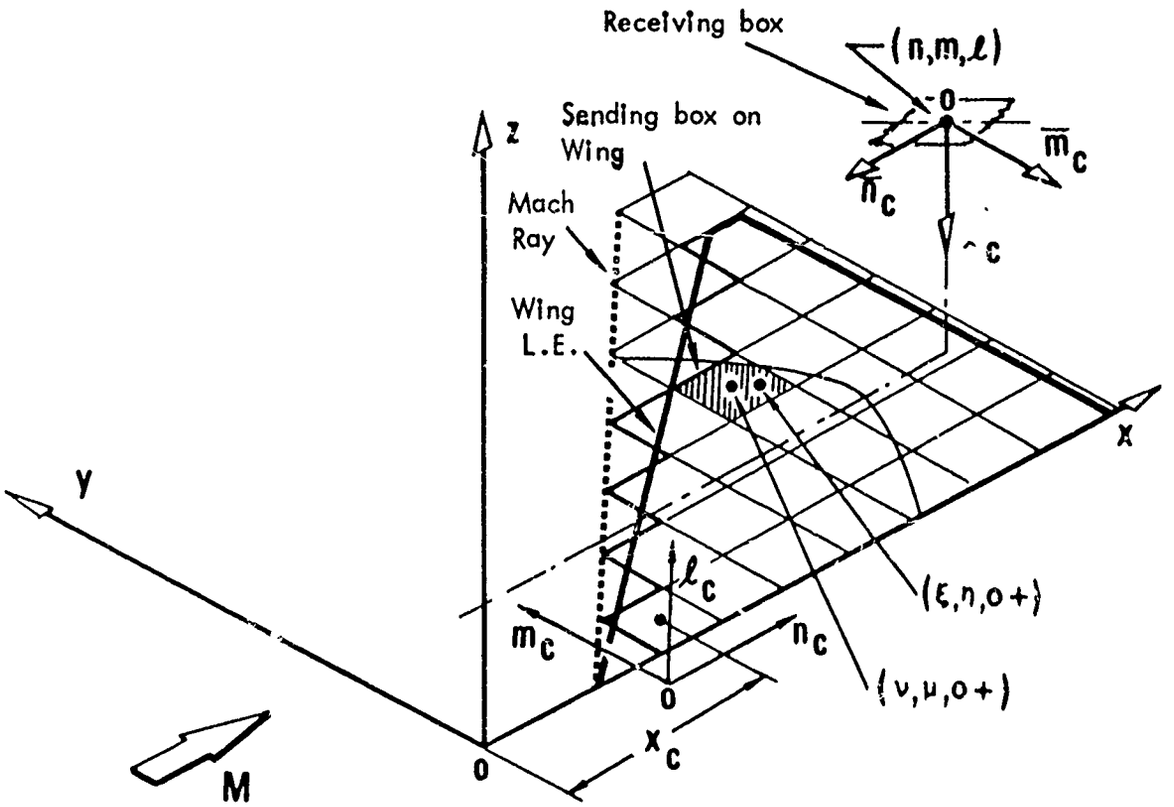

Figure 4 Receiving Point Coordinate System Corresponding To A Right Wing Sending Surface

where $$k_1 = \frac{\omega b_1}{U}$$

$A(\nu,\mu)$ denotes integration over box(ν,μ) and b_1 is the streamwise dimension of a Mach box

A final transformation, which is

$$\begin{cases} \overline{n}_c = -(n_c - n) \\ \overline{m}_c = -(m_c - m) \\ \overline{\ell}_c = -(\ell_c - \ell) \end{cases}$$

establishes a non-dimensional coordinate system centered on the receiving point, (Figure 4). The location of a sending box is $(\overline{\nu},\overline{\mu},\overline{\lambda})$ in this receiving coordinate system.

The expression for the perturbation velocity potential (Equation 14) may now be expressed as

$$\phi_o(0,0,0) = \sum_{\bar{\nu}} \sum_{\bar{\mu}} w_{\nu\mu} \, C_{\bar{\nu}\bar{\mu}\bar{\lambda}} \tag{15}$$

where

$$C_{\bar{\nu}\bar{\mu}\bar{\lambda}} = -\frac{1}{\pi} \int_{\bar{\xi}_L}^{\bar{\xi}_U} \int_{\bar{\eta}_L}^{\bar{\eta}_U} \frac{e^{-i\bar{k}_1\bar{\xi}} \cos\left(\frac{\bar{k}_1}{M}\sqrt{\bar{\xi}^2 - \bar{\eta}^2 - \bar{\lambda}^2}\right)}{\sqrt{\bar{\xi}^2 - \bar{\eta}^2 - \bar{\lambda}^2}} \, d\bar{\xi} d\bar{\eta} \tag{16}$$

and is known as an "Aerodynamic Influence Coefficient" or AIC. Also, $\bar{\xi}$, $\bar{\eta}$ are dummy variables of integration

$\bar{\xi}_u$, $\bar{\xi}_L$, $\bar{\eta}_u$, $\bar{\eta}_L$ are the limits of integration associated with the Mach Box whose center is at $\bar{\nu},\bar{\mu},\bar{\lambda}$ and are in general functions of $\bar{\nu},\bar{\mu},\bar{\lambda}$

Also,

$$\bar{k}_1 = \frac{M^2 k_1}{\beta^2}$$

$$\bar{\nu} = n-\nu$$

$$\bar{\mu} = m-\mu$$

$$\bar{\lambda} = \ell-\lambda = \ell \text{ since } \lambda \text{ must be } 0.$$

and

$$\bar{\xi} = (x - \xi)/b_1 \qquad \bar{\eta} = \beta(y - \eta)/b_1$$

The AIC for velocity potential, $C_{\bar{\nu},\bar{\mu},\bar{\lambda}}$, in Equations (15) and (16) may be interpreted as the velocity potential induced at an origin of the $\bar{n}_c$, $\bar{m}_c$, $\bar{\ell}_c$ coordinate system due to a unit upwash distributed over unit "pulse-sending" Mach Box whose center is located at $(\bar{\nu},\bar{\mu},\bar{\lambda})$. The "pulse-sending" Mach Box lies wholly or partially inside the forward Mach cone associated with the point (0,0,0).

Three more forms of Aerodynamic Influence Coefficients are required by this three-dimensional analysis. They are the AIC's associated with the upwash, sidewash, and longitudinal wash generated at the receiving point and are related to $C_{\bar{\nu},\bar{\mu},\bar{\lambda}}$ as shown below.

If the perturbation velocity potential at a point (x,y,z) in the local coordinate system of a surface is $\phi(x,y,z)$, the upwash is defined as the z - component of this velocity and is therefore

$$w(x,y,z) = \frac{\partial \dot{\phi}}{\partial z}(x,y,z)$$

This may be expressed in the numerical computation scheme, in the $(\bar{n}_c, \bar{m}_c, \bar{\ell}_c)$ coordinate system using Equation (15)

$$\frac{\partial \phi}{\partial z} = \frac{\beta}{b_1}\frac{\partial \phi}{\partial \bar{\lambda}} = \frac{\beta}{b_1}\sum_{\bar{\nu}}\sum_{\bar{\mu}} w_{o_{\nu\mu}} \frac{\partial}{\partial \bar{\lambda}} C_{\bar{\nu}\bar{\mu}\bar{\lambda}}(\bar{\nu},\bar{\mu},\bar{\lambda}) \tag{17}$$

The AIC for upwash is therefore defined as

$$W_{\bar{\nu}\bar{\mu}\bar{\lambda}} = \frac{\partial}{\partial \bar{\lambda}} C_{\bar{\nu}\bar{\mu}\bar{\lambda}} \tag{18}$$

which may be defined as the upwash induced at the pulse-receiving point due to a unit upwash distributed over the pulse-sending box.

Similarly for the sidewash,

$$v(0,0,0) = \frac{\beta}{b_1}\sum_{\bar{\nu}}\sum_{\bar{\mu}} w_{o_{\nu\mu}} \frac{\partial}{\partial \bar{\mu}} C_{\bar{\nu}\bar{\mu}\bar{\lambda}} \tag{19}$$

and the AIC for sidewash is

$$V_{\bar{\nu}\bar{\mu}\bar{\lambda}} = \frac{\partial}{\partial \bar{\mu}} C_{\bar{\nu}\bar{\mu}\bar{\lambda}} \tag{20}$$

For completesess, the longitudinal wash is

$$u(0,0,0) = \frac{1}{b_1}\sum_{\bar{\nu}}\sum_{\bar{\mu}} w_{o_{\nu\mu}} \frac{\partial}{\partial \bar{\nu}} C_{\bar{\nu}\bar{\mu}\bar{\lambda}} \tag{21}$$

and the AIC for longitudinal wash is

$$U_{\bar{\nu}\bar{\mu}\bar{\lambda}} = \frac{\partial}{\partial \bar{\nu}} C_{\bar{\nu}\bar{\mu}\bar{\lambda}} \tag{22}$$

The symmetry of the general wing-tail configuration allows the assumption that the receiving point is on the right hand side of the configuration. Furthermore ϕ need only be evaluated at a planform or diaphragm, and consequently the receiving points of interest will be only the centers of Mach boxes on the right wing and right tail. The possible combinations of receiving points and sending boxes may therefore be summarized as follows:

Receiving point lies on:	Sending box lies on:
1) Right Wing	Right wing
2) Right wing	Left wing
3) Right tail	Right wing
4) Right tail	Left wing
5) Right tail	Right tail
6) Right tail	Left tail

Each of these combinations gives rise to a distinct coordinate system, $(\bar{n}_c, \bar{m}_c, \bar{\ell}_c)$, with its origin at the receiving point, and with the $(\bar{n}_c, \bar{m}_c)$ plane lying paralled to the sending box plane. Thus, in Equations (15) to (22) $\bar{\nu}$ is always an integer, $\bar{\lambda}$ is the same for every sending box, and $\bar{\mu}$ is a real number, In cases 1) and 5) above $\bar{\lambda} = 0$.

Consider now case 3), the influence of the right wing on the right tail. The wing and its diaphragm are the sending surface; the receiving points are the centers of the Mach Boxes on the tail. Figure 5 shows the general relationship between the surfaces.

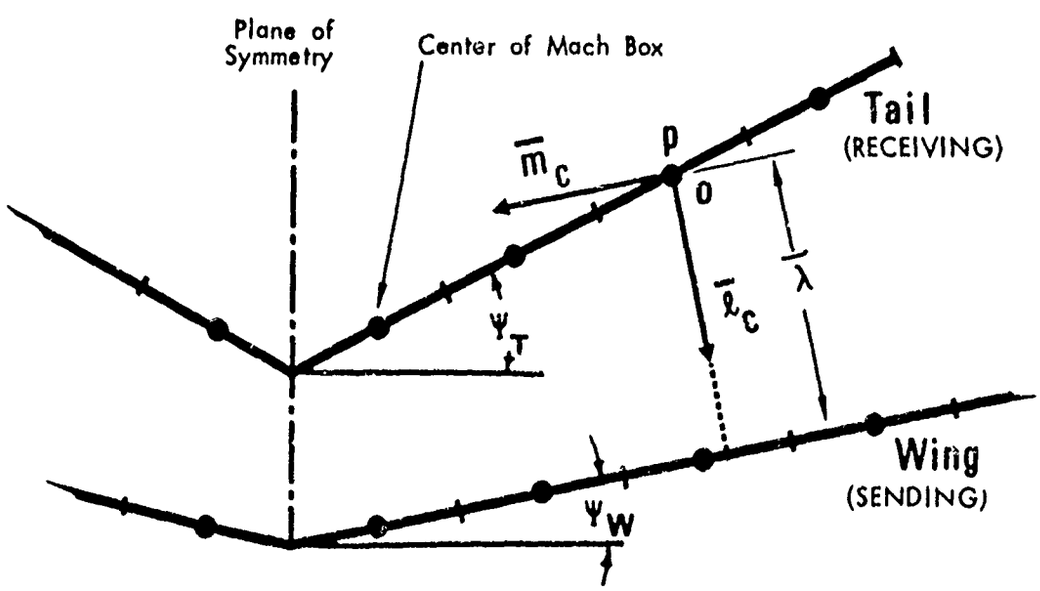

Figure 5. Receiving Point Coordinate System In Wing-Tail Configuration

If P is the center of a receiving box on the tail, $(\bar{n}_c, \bar{m}_c, \bar{\ell}_c)$ forms the coordinate system for the analysis where $\bar{n}_c$ disappears into the paper in Figure 5. Figure 6 shows how the wing looks from P.

A box is considered to be a sending box if its center lies on the wing, and if the box lies wholly or partially inside the Mach hyperbola $\bar{\xi}^2 = \bar{\eta}^2 + \bar{\lambda}^2$, which is defined as the intersection of the wing plane with the forward Mach cone emanating from P.

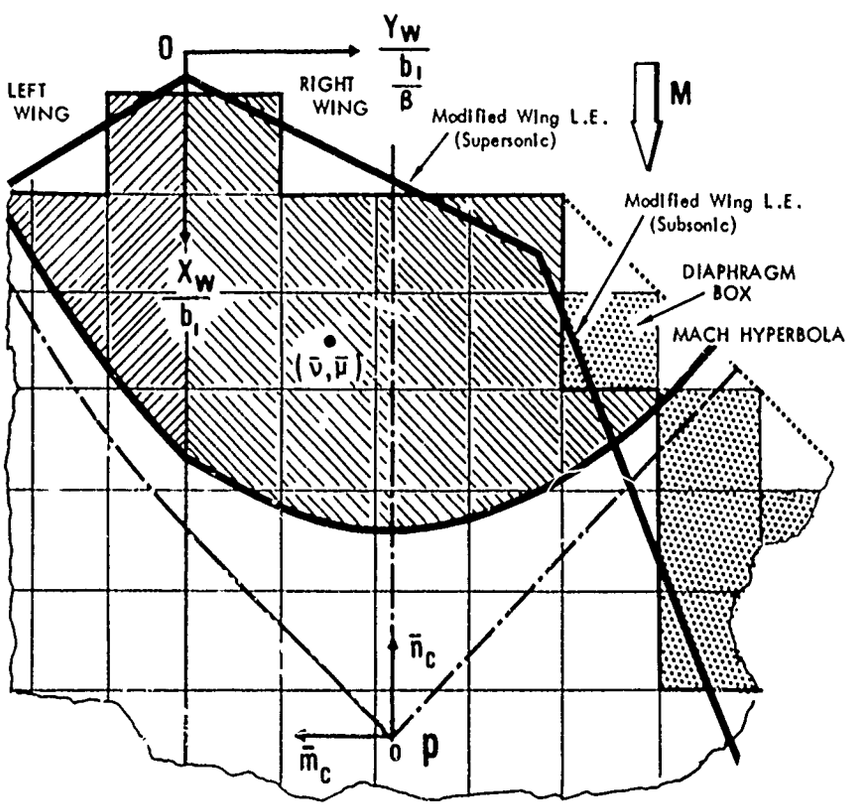

Figure 6. Mach Box Grid Systems On Sending Surfaces And Their Boundaries

The size of each AIC array is determined by how many boxes on the sending surface can influence the receiving box. Receiving boxes at different spanwise locations on the receiving surface will, in general, require different AIC arrays. However, receiving boxes which lie on the same chord of the receiving surface use the same AIC's, and consequently, an AIC array that is large enough to satisfy the requirements of the aftmost box on that surface can be used for all boxes on that chord. Note again that "surface" includes any diaphragm areas needed in the solution of the problem.

When the receiving surface lies in the plane of the sending surface, the AIC arrays $V_{\bar{\nu}\bar{\mu}\bar{\lambda}}$ and $W_{\bar{\nu}\bar{\mu}\bar{\lambda}}$ are not required.

4. EVALUATION OF AERODYNAMIC INFLUENCE COEFFICIENTS

a. Evaluation of $C_{\bar{\nu}\bar{\mu}\bar{\lambda}}$

The analysis in the previous section has formulated the aerodynamic influence coefficients in the Mach Box grid system with reference to the receiving point coordinate system. Since the integrand of $C_{\bar{\nu}\bar{\mu}\bar{\lambda}}$ in Equation (16) becomes singular at the Mach hyperbola some manipulation of $C_{\bar{\nu}\bar{\mu}\bar{\lambda}}$ is needed to render it amenable to numerical integration. To this end, the function $G(\bar{\xi},\bar{\eta},\bar{\lambda})$ is introduced, where

$$G(\bar{\xi},\bar{\eta},\bar{\lambda}) = \frac{\cos[\,\bar{k}_1/M\ (\bar{\xi}^2-\bar{\eta}^2-\bar{\lambda}^2)^{1/2}]}{(\,\bar{\xi}^2-\bar{\eta}^2-\bar{\lambda}^2)^{1/2}} = \frac{\partial}{\partial\bar{\eta}}F(\tau,\bar{\eta}) \tag{23}$$

where F is the Bessel function series expressed by

$$F(\tau,\bar{\eta}) = J_o\ (k_1\tau/M)\ \theta + \sum_{r=1}^{\infty} \frac{(-1)^r}{r}\ J_{2r}\ (\bar{k}_1\tau/M)\ \sin(2r\theta) \tag{24}$$

where

$$\tau = (\,\bar{\xi}^2-\bar{\lambda}^2)^{1/2} \geqslant 0$$

and

$$\theta = \sin^{-1}\bar{\eta}\ /\ \tau$$

The significance of τ and θ is illustrated in Figure 7.

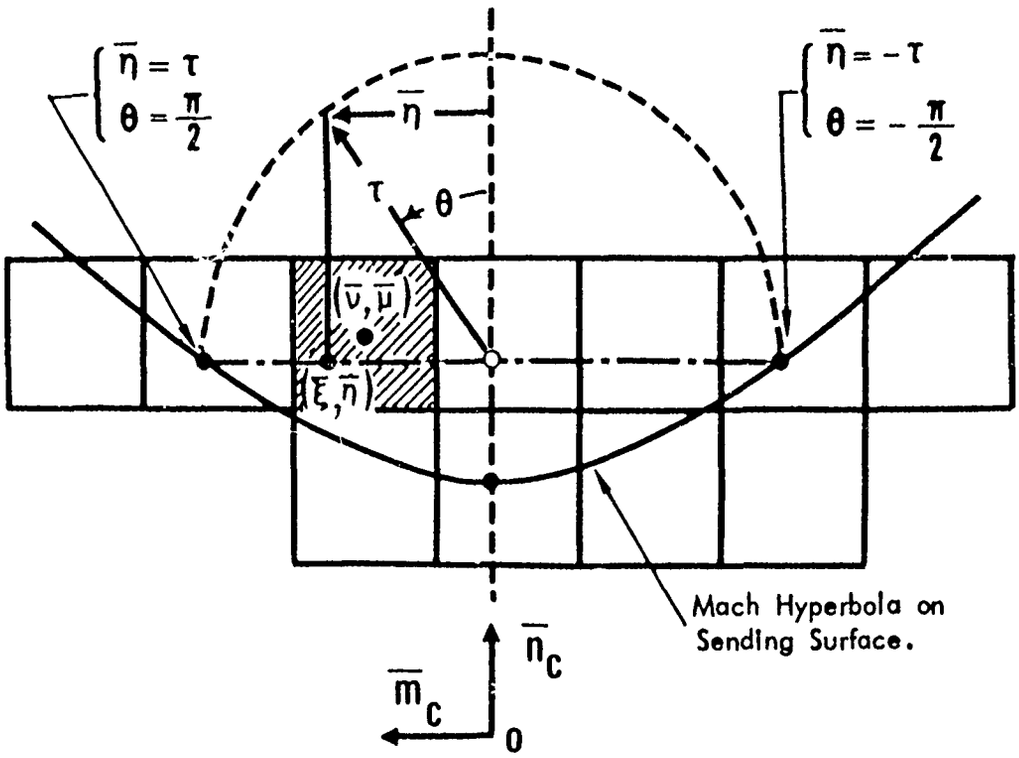

Figure 7. Values Of (τ, θ) Corresponding To $(\bar{\xi}, \bar{\eta})$

Substitution of Equations (23) and (24) into Equation (16) yields

$$C_{\bar{\nu}\bar{\mu}\bar{\lambda}} = -\frac{1}{\pi} \int_{\bar{\xi}_L}^{\bar{\xi}_U} e^{-i\bar{k}_1\bar{\xi}} \left[F(\tau, \bar{\eta}_U) - F(\tau, \bar{\eta}_L) \right] d\bar{\xi} \tag{25}$$

$C_{\bar{\nu}\bar{\mu}\bar{\lambda}}$ can be evaluated from this expression using numerical integration techniques, since F is closely approximated by the first few terms of the infinite summation in Equation (24).

The limits of integration $\bar{\xi}_u$, $\bar{\xi}_L$, $\bar{\eta}_u$, $\bar{\eta}_L$ are determined by the location of the box with respect to the Mach hyperbola (see Figure 7). If the box is cut by the Mach hyperbola, only that part of the box upstream of the Mach hyperbola contributes to the value of the AIC.

In general the integration limits may be summarized in the following way:

$$\bar{\eta}_u = \text{Minimum of } (\bar{\mu} + 1/2) \text{ or } \sqrt{\bar{\xi}^2 - \bar{\lambda}^2}$$

$$\bar{\eta}_L = \text{Maximum of } (\bar{\mu} - 1/2) \text{ or } -\sqrt{\bar{\xi}^2 - \bar{\lambda}^2}$$

$$\bar{\xi}_u = \bar{\nu} + 1/2 \tag{26}$$

$$\bar{\xi}_L = \begin{cases} \text{Maximum of } (\bar{\nu} - 1/2) \text{ or } \sqrt{[|\bar{\mu}| - 1/2]^2 + \bar{\lambda}^2} & \text{if } |\bar{\mu}| \geq 1/2 \\ \text{Maximum of } (\bar{\nu} - 1/2) \text{ or } \bar{\lambda} \text{ if } |\bar{\mu}| < 1/2 \end{cases}$$

Figure 8 shows a typical partial box, with these limits applied to it.

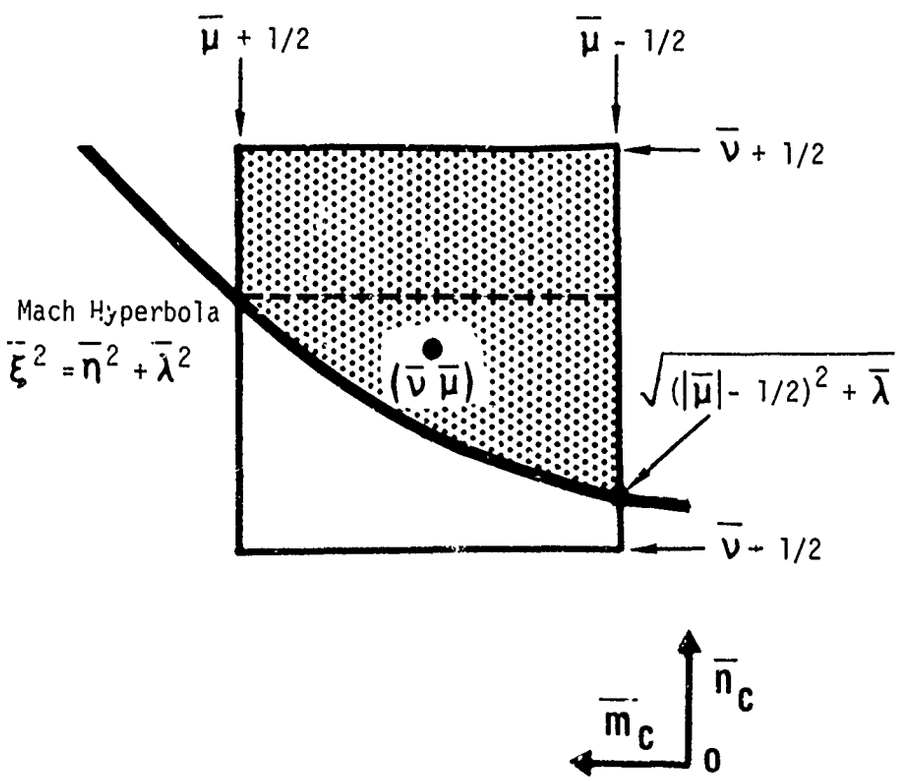

Figure 8. Integration Limits On Partial Edge Box

b. Development of $W_{\bar{\nu}\bar{\mu}\bar{\lambda}}$, $V_{\bar{\nu}\bar{\mu}\bar{\lambda}}$, and $U_{\bar{\nu}\bar{\mu}\bar{\lambda}}$

As written, Equations (18),(20) and (22) imply that $W_{\bar{\nu}\bar{\mu}\bar{\lambda}}$, $V_{\bar{\nu}\bar{\mu}\bar{\lambda}}$ and $U_{\bar{\nu}\bar{\mu}\bar{\lambda}}$ are obtained by differentiating $C_{\bar{\nu}\bar{\mu}\bar{\lambda}}$. $C_{\bar{\nu}\bar{\mu}\bar{\lambda}}$ however, is a numerically evaluated approximation, and is not suitable for differentiation; furthermore, differentiation tends to increase the effects of rounding errors and approximations. Therefore, the expressions for $W_{\bar{\nu}\bar{\mu}\bar{\lambda}}$, $V_{\bar{\nu}\bar{\mu}\bar{\lambda}}$ and $U_{\bar{\nu}\bar{\mu}\bar{\lambda}}$ are manipulated to a form which requires only integration.

Normal Wash

Substituting Equation (25) into Equation (18) yields:

$$W_{\bar{\nu}\bar{\mu}\bar{\lambda}} = -\frac{1}{\pi}\frac{\partial}{\partial\bar{\lambda}}\int_{\bar{\xi}_L}^{\bar{\xi}_U} e^{-i\bar{k}_1\bar{\xi}}\,[\,F(\tau,\bar{\eta}_U) - F(\tau,\bar{\eta}_L)\,]\,d\bar{\xi} \tag{27}$$

Applying Leibnitz Theorem for differentiation of an integral

$$W_{\bar{\nu}\bar{\mu}\bar{\lambda}} = -\frac{1}{\pi}\left[\int_{\bar{\xi}_L}^{\bar{\xi}_U}\frac{\partial}{\partial\bar{\lambda}}\{\,e^{-i\bar{k}_1\bar{\xi}}\,[F(\tau,\bar{\eta}_U) - F(\tau,\bar{\eta}_L)]\}\,d\bar{\xi} + \{\,e^{-i\bar{k}_1\bar{\xi}}\,[F(\tau,\bar{\eta}_U) - F(\tau,\bar{\eta}_L)\,\frac{\partial\bar{\xi}}{\partial\bar{\lambda}}\}\Big|_{\bar{\xi}_L}^{\bar{\xi}_U}\right] \tag{28}$$

Now, $\tau = [\,\bar{\xi}^2 - \bar{\lambda}^2\,]^{1/2}$ Therefore, $\frac{\partial\tau}{\partial\bar{\lambda}} = -\frac{\bar{\lambda}}{\tau}$ and $\frac{\partial\tau}{\partial\bar{\xi}} = \frac{\bar{\xi}}{\tau}$

Thus, $\frac{\partial\tau}{\partial\bar{\lambda}} = -\frac{\bar{\lambda}}{\bar{\xi}}\frac{\partial\tau}{\partial\bar{\xi}}$

In Equation (28), since $\bar{\eta}_U$ and $\bar{\eta}_L$ are function of τ, one may obtain:

$$\frac{\partial F(\tau,\bar{\eta}_U)}{\partial\bar{\lambda}} = -\frac{\bar{\lambda}}{\bar{\xi}}\frac{\partial F(\tau,\bar{\eta}_U)}{\partial\bar{\xi}}$$

$$\frac{\partial F(\tau,\bar{\eta}_L)}{\partial\bar{\lambda}} = -\frac{\bar{\lambda}}{\bar{\xi}}\frac{\partial F(\tau,\bar{\eta}_L)}{\partial\bar{\xi}} \tag{29}$$

Equation (28) can be integrated by parts as follows:

$$U = \frac{e^{-i\bar{k}_1\bar{\xi}}}{\bar{\xi}} \qquad dU = -\frac{1 + i\bar{k}_1\bar{\xi}}{\bar{\xi}^2}\, e^{-i\bar{k}_1\bar{\xi}}\, d\bar{\xi} \quad \text{and} \quad V = F \qquad dV = \frac{\partial F}{\partial \bar{\xi}}\, d\bar{\xi}$$

$$W_{\bar{\nu}\bar{\mu}\bar{\lambda}} = \frac{1}{\pi}\Bigg[\bar{\lambda}\int_{\bar{\xi}_L}^{\bar{\xi}_U} e^{-i\bar{k}_1\bar{\xi}}\frac{(1 + i\bar{k}_1\bar{\xi})}{\bar{\xi}^2}\{F(\tau,\bar{\eta}_U) - F(\tau,\bar{\eta}_L)\}\, d\bar{\xi}$$

$$+ \bar{\lambda}\left\{\frac{1}{\bar{\xi}}\, e^{-i\bar{k}_1\bar{\xi}}[F(\tau,\bar{\eta}_U) - F(\tau,\bar{\eta}_L)]\right\}\Bigg|_{\bar{\xi}_L}^{\bar{\xi}_U} + \left\{e^{-i\bar{k}_1\bar{\xi}}[F(\tau,\bar{\eta}_U) - F(\tau,\bar{\eta}_L)\frac{\partial\bar{\xi}}{\partial\bar{\lambda}}\right\}\Bigg|_{\bar{\xi}_L}^{\bar{\xi}_U}\Bigg] \tag{30}$$

Since $\bar{\xi}_U = \bar{\nu} + 1/2$ so $\dfrac{\partial\bar{\xi}_U}{\partial\bar{\lambda}} = 0$

If $\bar{\xi}_L = \bar{\nu} - 1/2$ then $\partial\bar{\xi}_L/\partial\bar{\lambda} = 0$

If $\bar{\xi}_L = [(|\bar{\mu}| - 1/2)^2 - \bar{\lambda}^2]^{1/2}$ or $\bar{\lambda}$

so that $$\frac{\partial\bar{\xi}}{\partial\bar{\lambda}}[F(\tau,\bar{\eta}_U) - F(\tau,\bar{\eta}_L)]\Bigg|_{\bar{\xi}_L}^{\bar{\xi}_U} = 0$$

Therefore, Equation (30) can be written

$$W_{\bar{\nu}\bar{\mu}\bar{\lambda}} = \frac{\bar{\lambda}}{\pi}\Bigg[\int_{\bar{\xi}_L}^{\bar{\xi}_U} e^{-i\bar{k}_1\bar{\xi}}\frac{(1 + i\bar{k}_1\bar{\xi})}{\bar{\xi}^2}\{F(\tau,\bar{\eta}_U) - F(\tau,\bar{\eta}_L)\}\, d\bar{\xi}$$

$$+ \left\{\frac{e^{-i\bar{k}_1\bar{\xi}}}{\bar{\xi}}[F(\tau,\bar{\eta}_U) - F(\tau,\bar{\eta}_L)]\right\}\Bigg|_{\bar{\xi}_L}^{\bar{\xi}_U}\Bigg] \tag{31}$$

Sidewash

Combining Equations (20),(24) and (25) yields

$$V_{\bar{\nu}\bar{\mu}\bar{\lambda}} = -\frac{1}{\pi}\frac{\partial}{\partial\bar{\mu}}\int_{\bar{\eta}_L}^{\bar{\eta}_U}\int_{\bar{\xi}_L}^{\bar{\xi}_U} G(\bar{\xi},\bar{\eta},\bar{\lambda})\, e^{-i\bar{k}_1\bar{\xi}}\, d\bar{\xi}\, d\bar{\eta} \tag{32}$$

Since $\bar{\xi}_L$ and $\bar{\xi}_U$ can not be functions of $\bar{\mu}$, the inner integral is not a function of $\bar{\mu}$. Therefore by applying Leibnitz's Theorem, we have,

$$V_{\bar{\nu}\bar{\mu}\bar{\lambda}} = -\frac{1}{\pi}\{\frac{\partial\,\bar{\eta}_U}{\partial\,\bar{\mu}}\int_{\bar{\xi}_L}^{\bar{\xi}_U} G(\bar{\xi},\bar{\eta}_U,\bar{\lambda})\, e^{-i\bar{k}_1\bar{\xi}}\, d\bar{\xi} - \frac{\partial\bar{\eta}_L}{\partial\bar{\mu}}\int_{\bar{\xi}_L}^{\bar{\xi}_U} G(\bar{\xi},\bar{\eta}_L,\bar{\lambda})\, e^{-i\bar{k}_1\bar{\xi}}\, d\bar{\xi}\,\} \tag{33}$$

Since

$$\frac{\partial}{\partial\bar{\xi}}\sin\left(\frac{\bar{k}_1}{M}\left[\bar{\xi}^2-\bar{\eta}^2-\bar{\lambda}^2\right]^{1/2}\right) = \frac{\bar{k}_1}{M}\bar{\xi}G(\bar{\xi},\bar{\eta},\bar{\lambda}) \tag{34}$$

Equation (33) integrated by parts gives:

$$V_{\bar{\nu}\bar{\mu}\bar{\lambda}} = -\frac{M}{\pi\,\bar{k}_1}\Bigg[\Bigg\{\frac{e^{-i\bar{k}_1\bar{\xi}}}{\bar{\xi}}\left(\frac{\partial\bar{\eta}_U}{\partial\bar{\mu}}\sin\frac{\bar{k}_1}{M}[\bar{\xi}^2-\bar{\eta}_U^2-\bar{\lambda}^2]^{1/2}-\frac{\partial\bar{\eta}_L}{\partial\mu}\sin\frac{\bar{k}_1}{M}[\bar{\xi}^2-\bar{\eta}^2-\bar{\lambda}^2]^{1/2}\right)\Bigg|_{\bar{\xi}_L}^{\bar{\xi}_U}$$
$$+\int_{\bar{\xi}_L}^{\bar{\xi}_U}\Bigg\{\left(\frac{\partial\bar{\eta}_U}{\partial\mu}\sin\frac{\bar{k}_1}{M}[\bar{\xi}^2-\bar{\eta}^2-\bar{\lambda}^2]^{1/2}-\frac{\partial\bar{\eta}_L}{\partial\bar{\mu}}\sin\frac{\bar{k}_1}{M}[\bar{\xi}^2-\bar{\eta}^2-\bar{\lambda}^2]^{1/2}\right)\frac{1+\bar{k}_1\bar{\xi}}{\bar{\xi}^2}e^{-i\bar{k}_1\bar{\xi}}\Bigg\}d\bar{\xi} \tag{35}$$

The limit of integration for this expression are summarized in Equation (26). They will yield $\partial\bar{\eta}_U/\partial\bar{\mu} = 1$ when $\bar{\eta}_U$ does not lie on the Mach hyperbola, and $\partial\bar{\eta}_U/\partial\bar{\mu} = 0$ when $\bar{\eta}_U$ lies on the Mach hyperbola. It is similar for $\partial\bar{\eta}_L/\partial\bar{\mu}$. It will be seen that evaluation of Equation (35) will be troublesome when $\bar{k}_1=0$. Consequently, Equation (35) is remanipulated in the limit as $\bar{k}_1 \rightarrow 0$.

$$\lim_{\bar{k}_1 \to 0} V_{\bar{\nu}\bar{\mu}\bar{\lambda}} = \lim_{\bar{k}_1 \to 0} \Bigg[- \frac{M}{\pi} \Bigg[\frac{\exp(-i\bar{k}_1\bar{\xi})}{\bar{\xi}} \Bigg\{ \frac{\sin \frac{\bar{k}_1}{M} (\bar{\xi}^2 - \bar{\eta}_U^2 - \bar{\lambda}^2)^{1/2}}{\bar{k}_1} \frac{\partial \bar{\eta}_U}{\partial \bar{\mu}}$$

$$- \frac{\sin \frac{\bar{k}_1}{M} (\bar{\xi}^2 - \bar{\eta}_L^2 - \bar{\lambda}^2)^{1/2}}{\bar{k}_1} \frac{\partial \bar{\eta}_L}{\partial \bar{\mu}} \Bigg\} \Bigg] \Bigg|_{\bar{\xi}_L}^{\bar{\xi}_U} + \int_{\bar{\xi}_L}^{\bar{\xi}_U} \Bigg[\frac{1 + i\bar{k}_1\bar{\xi}}{\bar{\xi}^2} \exp(-i\bar{k}_1\bar{\xi}) \tag{36}$$

$$\Bigg\{ \frac{\sin \frac{\bar{k}_1}{M} (\bar{\xi}^2 - \bar{\eta}_U^2 - \bar{\lambda}^2)^{1/2}}{\bar{k}_1} \frac{\partial \bar{\eta}_U}{\partial \bar{\mu}} - \frac{\sin \frac{\bar{k}_1}{M} (\bar{\xi}^2 - \bar{\eta}_L^2 - \bar{\lambda}^2)^{1/2}}{\bar{k}_1} \frac{\partial \bar{\eta}_L}{\partial \bar{\mu}} \Bigg\} \Bigg] d\bar{\xi} \Bigg]$$

Applying L'Hospital's rule yields

$$\lim_{\bar{k}_1 \to 0} V_{\bar{\nu}\bar{\mu}\bar{\lambda}} = - \frac{1}{\pi} \Bigg[\Bigg\{ \frac{(\bar{\xi}^2 - \bar{\eta}_U^2 - \bar{\lambda}^2)^{1/2}}{\bar{\xi}} \frac{\partial \bar{\eta}_U}{\partial \bar{\mu}} - \frac{(\bar{\xi}^2 - \bar{\eta}_L^2 - \bar{\lambda}^2)^{1/2}}{\bar{\xi}} \frac{\partial \bar{\eta}_L}{\partial \bar{\mu}} \Bigg\}_{\bar{\xi}_L}^{\bar{\xi}_U}$$

$$+ \int_{\bar{\xi}_L}^{\bar{\xi}_U} \Bigg\{ \frac{(\bar{\xi}^2 - \bar{\eta}_U^2 - \bar{\lambda}^2)^{1/2}}{\bar{\xi}^2} \frac{\partial \bar{\eta}_U}{\partial \bar{\mu}} - \frac{(\bar{\xi}^2 - \bar{\eta}_L^2 - \bar{\lambda}^2)^{1/2}}{\bar{\xi}^2} \frac{\partial \bar{\eta}_L}{\partial \bar{\mu}} \Bigg\} d\bar{\xi} \Bigg] \tag{37}$$

Noticing that $\partial\bar{\eta}_U/\partial\bar{\mu}$ and $\partial\bar{\eta}_L/\partial\bar{\mu}$ are constant and by applying:

$$\int \frac{(x^2 - a^2)^{1/2}}{x^2} dx = - \frac{(x^2 - a^2)^{1/2}}{x} + \log \left| x - (x^2 - a^2)^{1/2} \right|$$

$$\lim_{\bar{k}_1 \to 0} V_{\bar{\nu}\bar{\mu}\bar{\lambda}} = - \frac{1}{\pi} \log \frac{\left| \bar{\xi} + (\bar{\xi}^2 - \bar{\eta}_U^2 - \bar{\lambda}^2)^{1/2} \right| \frac{\partial \bar{\eta}_U}{\partial \bar{\mu}}}{\left| \bar{\xi} + (\bar{\xi}^2 - \bar{\eta}_L^2 - \bar{\lambda}^2)^{1/2} \right| \frac{\partial \bar{\eta}_L}{\partial \bar{\mu}}} \Bigg|_{\bar{\xi}_L}^{\bar{\xi}_U} \tag{38}$$

Equation (38) is used to calculate $V_{\bar{\nu}\bar{\mu}\bar{\lambda}}$ for the case when $\bar{k}_1$ is very small.

<u>Longitudinal Wash</u>

Combining Equations (22),(24) and (25) gives

$$U_{\bar{\nu}\bar{\mu}\bar{\lambda}} = \frac{\partial}{\partial \bar{\nu}} \int_{\bar{\xi}_L}^{\bar{\xi}_U} \int_{\bar{\eta}_L}^{\bar{\eta}_U} G(\bar{\xi}, \bar{\eta}, \bar{\lambda}) \, e^{-i\bar{k}_1\bar{\xi}} \, d\bar{\eta} \, d\bar{\xi} \tag{39}$$

Since $\bar{\eta}_u$ and $\bar{\eta}_L$ are not a function of $\bar{\nu}$, the inner integral is not a function of $\bar{\nu}$. Thus, applying Leibnitz's Theorem yields

$$U_{\bar{\nu}\bar{\mu}\bar{\lambda}} = -\frac{1}{\pi}\left[\frac{\partial\bar{\xi}_U}{\partial\bar{\nu}}\int_{\bar{\eta}_L}^{\bar{\eta}_U} G(\bar{\xi}_U,\bar{\eta},\bar{\lambda})\, e^{-ik_1\xi_U}\, d\bar{\eta}\right.$$

$$\left. - \frac{\partial\bar{\xi}_L}{\partial\bar{\nu}}\int_{\bar{\eta}_L}^{\bar{\eta}_U} G(\bar{\xi}_L,\bar{\eta},\bar{\lambda})\, e^{-i\bar{k}_1\bar{\xi}_L}\, d\bar{\eta}\right] \tag{40}$$

Using $G(\bar{\xi},\bar{\eta},\bar{\lambda}) = \frac{\partial}{\partial\bar{\eta}} F(\tau,\bar{\eta})$ from Equation (23)

$$U_{\bar{\nu}\bar{\mu}\bar{\lambda}} = -\frac{1}{\pi}\left[\frac{\partial\bar{\xi}_U}{\partial\bar{\nu}}\{F(\tau,\bar{\eta}_U) - F(\tau,\bar{\eta}_L)\}_{\bar{\xi}=\bar{\xi}_U} e^{-i\bar{k}_1\bar{\xi}_U} - \frac{\partial\bar{\xi}_L}{\partial\bar{\nu}}\right.$$

$$\left.\times\{F(\tau,\bar{\eta}_U) - F(\tau,\bar{\eta}_L)\}_{\bar{\xi}=\bar{\xi}_L} e^{-i\bar{k}_1\bar{\xi}_L}\right] \tag{41}$$

It should be noted that use of Equation (41) in Equation (21) yields the perturbation longitudinal wash. The free stream velocity should be added to it to give the total longitudinal wash.

5. VELOCITY POTENTIAL AND PERTURBATION VELOCITY CALCULATIONS

a. Zones of Influence in Wing-Wing and Wing-Tail Interaction

The basic process of solving an interference flow problem as described in Ref. 13, is one of calculating the flow field induced at one surface by a source distribution on another surface, cancelling this flow field by modifying the boundary condition of the "interfered" surface, and solving for the unknown quantities by treating the interfered surface as though it were in an undisturbed uniform flow.

This process may be more fully explained by consideration of the various "non-communicative zones" or disturbed regions of the flow field and their bounding surfaces, and the various physical conditions to be satisfied by source distributions on these surfaces. Figure 9 shows a wing and tail combination with subsonic leading edges, both having positive dihedral with the tail centerline located above the wing centerline. (In our analysis, the tail may not be located directly above the wing, but must be located far enough aft to prevent mutual interference).

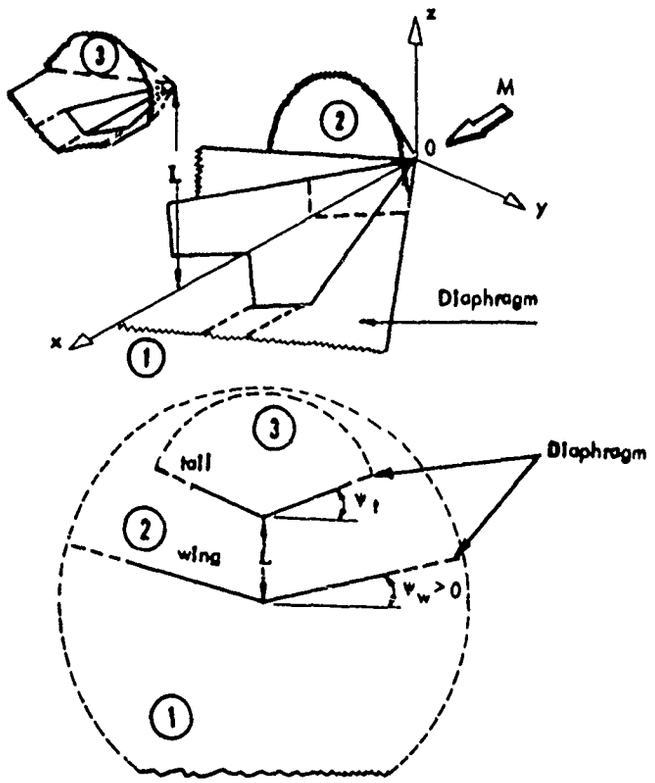

Figure 9. Zones In Wing-Tail Configuration

The region of disturbed flow may be divided into three zones, as shown in Figure 9. Zone (1) lies below the wing and its diaphragm, and inside the Mach Cone emanating from the apex of the wing. It is disturbed only by the sources placed on the lower surface of the wing and wing-diaphragm.

Zone (2) lies between the wing and the tail, is inside the wing Mach Cone. It is disturbed by the sources placed upon the upper surface of the wing and wing diaphragm and the lower surface of the tail and tail diaphragm.

Zone (3) lies above the tail, and inside the tail Mach Cone.

The complete solution of the flow field, then, would consist of separately finding the velocity potential in these three zones. It may be seen however, that the tail Mach Cone lies at least partially inside the wing Mach Cone. This has the important implication that the flow conditions ahead of the tail Mach Cone are non-uniform. Hence, the usual methods of

linearized theory cannot be used to find the flow field inside zone (3), which includes the upper surface of the tail. An alternate formulation of the problem, using modified boundary conditions, is thus used to allow for this non-uniformity.

The boundary conditions used for the various surfaces and diaphragms may be described as follows:

a)	Wing surface:	The tangency condition of flow parallel to the surface;
b)	Wing diaphragm:	Zero pressure difference and continuity of normal wash across the diaphragm;
c)	Tail diaphragm:	Zero pressure difference and continuity of normal wash across the diaphragm;
d)	Tail surface:	A modified form of the boundary condition which permits the tail to be examined as if it were in a uniform flow.

We may note that since the non-uniform flow affects both the upper and lower tail surfaces, the modified boundary conditions are to be applied to both surfaces, whereas in the zonal picture the upper tail surface is isolated from the upper wing surface.

A further illustration of this replacement of non-uniform flow effects by modified boundary conditions, showing how the tail diaphragms should be treated, is given in Figure 10.

The upper part of Figure 10 shows a wing which is pitched at an angle α, and a tail which is parallel to the undisturbed flow. The influence of the wing creates a pressure distribution on the tail because the tail is now placed in a non-uniform flow. This pressure distribution could be reproduced on the tail by removing the wing and deforming the tail surface appropriately. The appropriate deformation could then be represented by a source distribution on the tail planform upper and lower surfaces which would cancel exactly the flow disturbance caused by the wing, thus satisfying the boundary condition on the tail. This source distribution would in turn give rise to a distribution on the tail diaphragm so that the upper and lower tail surfaces can be considered non-communicative. There would, however, be no direct influence on the tail diaphragm from the wing.

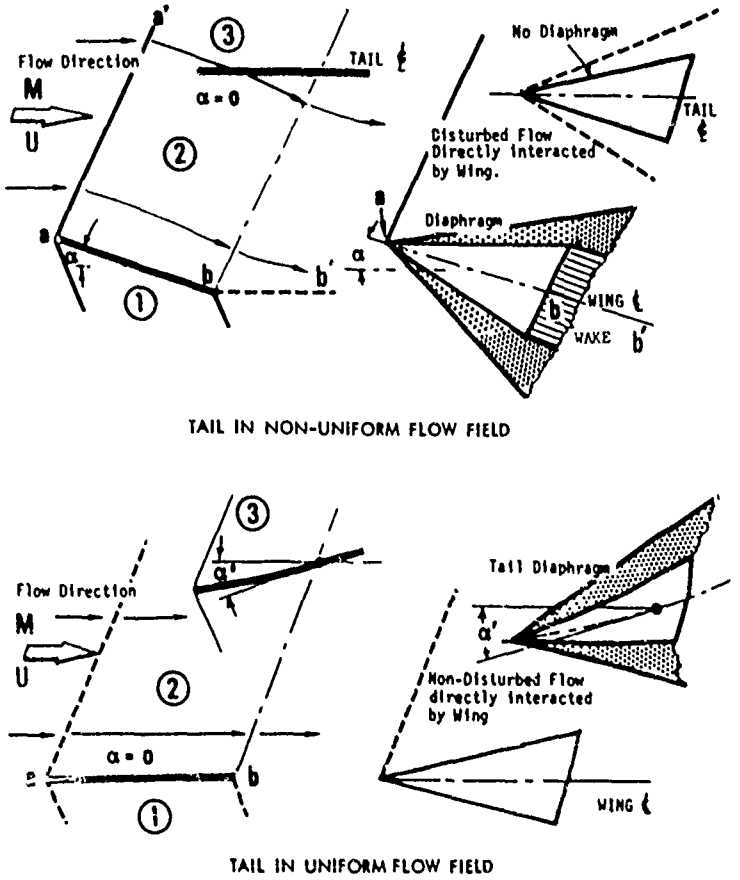

Figure 10. Interacted Flow Field in Wing-Tail Configuration In Steady Case

Once the appropriate regions of influence have been determined, and the necessary AIC's calculated as described in the previous section, the strength of the source distribution and the local velocity potential differences may be determined. Since the application of this process to the general configuration is rather complex it will be described for three distinct problems.

1) The velocity potential distribution $\Delta\phi$ will be evaluated for a single wing with dihedral.

2) The distributions will then be evaluated for a wing and tail where neither surface has dihedral, and the tail does not lie in the plane of the wing.

3) These solutions will be combined to give distributions in the case of the general configuration.

b. Solution for Single Wing with Dihedral

This problem requires only one receiving surface - the right wing, and two sending surfaces - the left wing and the right wing. The AIC arrays required are consequently:

1) The velocity potential array representing the influence of the right wing upon itself, $C_{\bar{\nu},\bar{\mu},\bar{0}}$.

2) Velocity potential arrays representing the influence of the left wing upon the right wing, $C_{\bar{\nu},\bar{\mu},\bar{\lambda}}^{\binom{RW}{LW}}$. A separate array is required for each chordwise row of receiving boxes (a receiving chord) on the right wing;

3) Sidewash arrays, left wing upon right wing $V_{\bar{\nu},\bar{\mu},\bar{\lambda}}^{\binom{RW}{LW}}$, one for each receiving chord;

4) Upwash arrays, left wing upon right wing $W_{\bar{\nu},\bar{\mu},\bar{\lambda}}^{\binom{RW}{LW}}$, one for each receiving chord.

The solution process begins by considering the innermost box on the most upstream row of the right wing, box (1,1) in the (n_c, m_c, ℓ_c) coordinate system (see Figure 11). Since the wing leading edge may not be swept forward, this box must be on the wing, and is not influenced by any other box on the wing or its diaphragm. Consequently the source strength on the upper and lower surfaces of box (1,1) are given by

$$N_{RUW}^{1,1} = \frac{D\,\bar{f}_j^{1,1}}{D\,t}$$

$$N_{RLW}^{1,1} = -\frac{D\,\bar{f}_j^{1,1}}{D\,t} \qquad (42)$$

where $N_{RUW}^{n,m}$ and $N_{RLW}^{n,m}$ denotes the complex outward normal wash due to the source distribution on the upper and lower surfaces respectively of box (n,m) on the right wing.

$\bar{f}_j^{n,m}$ is the scaled modal deflection at box (n,m) in mode j and

$$\frac{D\,\bar{f}_j^{n,m}}{D\,t} = \frac{b_1}{U}\frac{D\,f_j^{n,m}}{D\,t} = \left[\, ik_1 f_j^{n,m} + b_1 \frac{\partial\, f_j^{n,m}}{\partial\, x} \,\right]$$

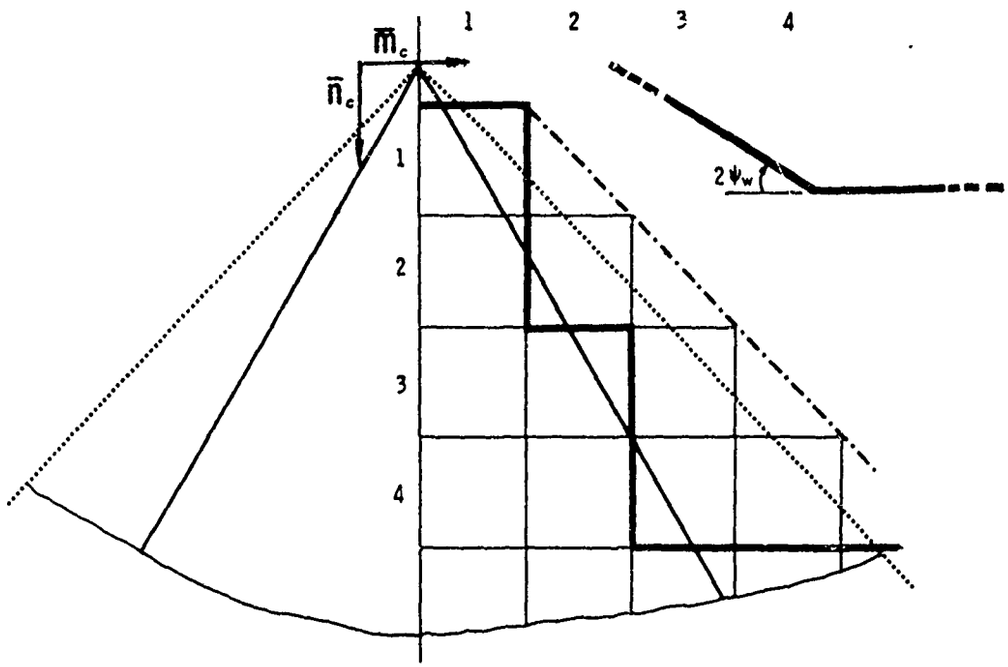

Figure 11. Box Arrangement On A Wing With Dihedral

where $k_1 = \dfrac{\omega\, b_1}{U}$ and $\bar{f}_j^{n,m} = \dfrac{b_1}{U}\, f_j^{n,m}$

If the leading edge of the wing is at least partially supersonic there may be more than one box on the first row; Equation (42) holds for all such boxes.

Since the configurations are symmetric about the center line, and the modes are either symmetric or antisymmetric, the source strengths on the left wing can be found as

$$N_{LUW}^{n,m} = \left\{ \begin{matrix} + \\ - \\ 0 \end{matrix} \right\} N_{RUW}^{n,m} \tag{43}$$

and

$$N_{LLW}^{n,m} = \left\{ \begin{matrix} + \\ - \\ 0 \end{matrix} \right\} N_{RLW}^{n,m} \tag{44}$$

Here the positive sign is taken for symmetric modes, the negative for antisymmetric modes, and the zero factor for the cases where the left hand surface contributions are to be ignored.

When $N_{RUW}^{n,m}$ has been calculated for all boxes in the first row, the solution process proceeds to the second row, then the third and subsequent rows. Each row is influenced only by boxes on the rows upstream of it. Any row other than the first may include diaphragm boxes, and all rows except the first will be influenced by the left hand side of the planform and diaphragm.

Let us suppose that box (n,m) lies on the upper surface of the right wing planform. The source strength placed on box (n,m) must include the effect of the modal deflection at (n,m), and also the influence of the sources on the upper surface of the left wing (planform and diaphragm) at that box.

The tangency condition must still be satisfied on box (n,m), i.e. the complex normal wash due to modal deflection and slope must equal the sum of normal washes induced by both local and remote source strength. (The only remote sources inducing normal wash are on the left hand surface.) The boundary condition may thus be expressed as

$$\frac{D\bar{f}_j^{n,m}}{Dt} = \left(N_{RUW}^{n,m} + \hat{N}_{\substack{RUW\\LUW}}^{n,m}\right) \tag{45}$$

where $\hat{N}_{\substack{RUW\\LUW}}^{n,m}$ is the complex outward normal wash at (n,m) induced by the source distribution over the upper surface of the left wing, given by:

$$\hat{N}_{\substack{RUW\\LUW}}^{n,m} = \sum_{\substack{\text{left wing}\\+\text{ diaphragm}}} \left\{ \left[W\frac{\binom{RW}{LW}}{\nu\mu\lambda}\cos 2\psi_W - V\frac{\binom{RW}{LW}}{\nu\mu\lambda}\sin 2\psi_W \right] N_{LUW}^{\nu\mu} \right\}$$

The local source strength is then found by solution of Equation (45).

$$N_{RUW}^{n,m} = \frac{D\bar{f}^{n,m}}{Dt} - \hat{N}_{\substack{RUW\\LUW}}^{n,m} \tag{46}$$

It should be noted that for any given box (n,m) all the quantities on the right hand side of Equation (45) and hence of Equation (46) are known, since the sum of Equation (45) includes only boxes in rows ahead of the row under consideration, where the source strengths have been found previously.

A similar argument is used to show that if (n,m) is a box on the lower surface of the right wing

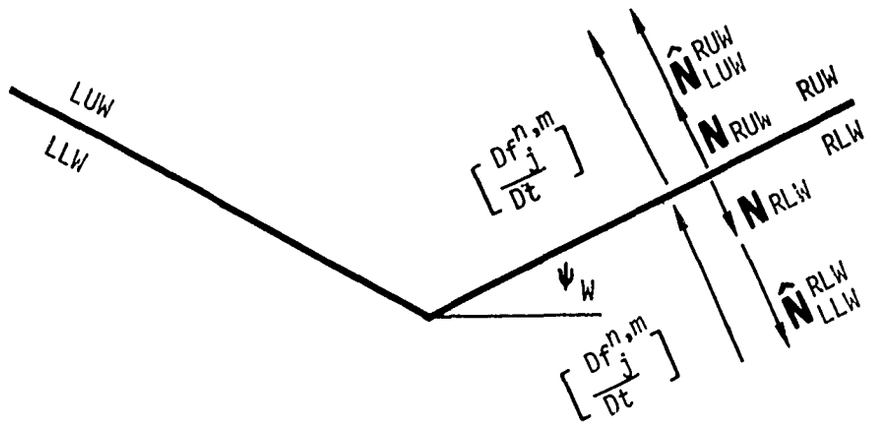

Figure 12. Normal Wash On Upper And Lower Surfaces Of Wing

$$N^{n,m}_{RLW} = -\frac{Df_j}{Dt} - \hat{N}^{n,m}_{\substack{RLW\\LLW}} \tag{47}$$

where

$$\hat{N}^{n,m}_{\substack{RLW\\LLW}} = -\sum_{\substack{\text{left wing}\\+\text{ diaphragm}}} \left\{\left[W_{\nu\mu\lambda}^{\binom{RW}{LW}} \cos 2\Psi_W - V_{\nu\mu\lambda}^{\binom{RW}{LW}} \sin 2\Psi_W\right] N^{\nu\mu}_{LLW}\right\} \tag{48}$$

Figure 12 illustrates the reason for the negative signs appearing in in Equations (47) and (48). It must be noted, that $f_j^{n,m}$ is here defined by motion of the upper surface.

If the box (n,m) is located off the planform i.e in a leading or trailing edge diaphragm, a different boundary condition must be applied in order to find the unknown source strength. Since the diaphragm is incapable of supporting a pressure difference;

$$\Delta p_j^{n,m} = 0 \tag{49}$$

for boxes in any diaphragm, where $\Delta p_j^{n,m}$ is the pressure difference at box (n,m) resulting from the motion of mode j.

The relation between pressure and velocity potential difference, $\Delta\phi_j^{n,m}$, is

$$\Delta p_j^{n,m} = \rho \frac{D\Delta\phi_j^{n,m}}{Dt}$$

$$= \rho\left(i\omega + U\frac{\partial}{\partial x}\right) \Delta\phi_j^{n,m}$$

$$= \frac{\rho U}{b_1}\left(ik_1 \Delta\bar{\phi}_j^{n,m} + b_1\frac{\partial}{\partial x} \Delta\bar{\phi}_j^{n,m}\right) e^{i\omega t} \tag{50}$$

$$= \frac{\rho U^2}{b_1\beta} \left(ik_1 \Delta\bar{\bar{\phi}}_j^{n,m} + b_1\frac{\partial}{\partial x}\Delta\bar{\bar{\phi}}_j^{n,m}\right)e^{i\omega t}$$

where $\Delta\bar{\bar{\phi}}_j^{n,m}$ is the non-dimensionalized velocity potential difference at box (n,m) due to a unit generalized deflection of the jth mode. The actual value of the perturbation velocity potential is then

$$\Delta\phi_j^{n,m} = \frac{U}{b_1} \left(\frac{b_1}{\beta}\right) \Delta\bar{\bar{\phi}}_j^{n,m} e^{i\omega t} \tag{51}$$

Setting the pressure difference to zero, and solving Equation (44) as an ordinary differential equation subject to initial conditions at x_o:

$$\Delta\bar{\bar{\phi}}_j^{n,m} = \Delta\bar{\bar{\phi}}(x_o)\left[e^{-ik_1 \frac{x_n - x_o}{b_1}}\right] \tag{52}$$

For leading edge diaphragms, the initial value for velocity potential is that at the foremost Mach line, i.e. zero. Thus for leading edge diaphragm boxes

$$\Delta\bar{\bar{\phi}}_j^{n,m} = 0 \tag{53}$$

For trailing edge diaphragm boxes, the initial velocity potential is the value at the trailing edge of the wing for that spanwise location.

Thus:

$$\Delta \overset{=}{\phi}{}^{n,m}_{j} = \Delta \overset{=}{\phi}{}^{m}_{TE} \exp\left[-ik_1 (x_n - x_{TE_m})/b_1 \right] \tag{54}$$

The value at the trailing edge is found by extrapolation from previously calculated values as

$$\Delta \overset{=}{\phi}{}^{m}_{TE} = \left[(x_{TE,m} - x_{n'})/b_1\right]\left(\Delta \overset{=}{\bar{\phi}}{}^{n',m}_{j} - \Delta \overset{=}{\bar{\phi}}{}^{n'-1,m}_{j}\right) + \Delta\overset{=}{\bar{\phi}}{}^{n',m}_{j} \tag{55}$$

Where n' is the index of the last complete box on chord m. If there is only a single box on the chord, as in the case of a pointed wing tip the extrapolation is performed along a Mach line.

The non-dimensional velocity potential distribution is related to the local normal washes (source strength) through

$$\Delta \overset{=}{\phi}{}^{n,m}_{j} = \sum_{\substack{\text{right wing} \\ + \text{ diaphragm}}} C_{\bar{\nu}\bar{\mu}0} \left(N^{\nu\mu}_{RUW} - N^{\nu\mu}_{RLW}\right) + \sum_{\substack{\text{left wing} \\ + \text{ diaphragm}}} C_{\bar{\nu}\bar{\mu}\bar{\lambda}} \begin{Bmatrix} + \\ - \\ 0 \end{Bmatrix} \left(N^{\nu\mu}_{RUW} - N^{\nu\mu}_{RLW}\right) \tag{56}$$

The source strength difference at box (n,m) on the diaphragm can now be found by solving Equation (56). All the source strengths ahead of box (n,m) are known, and the velocity potential is given by either Equation (53) or Equation (54).

$$\left(N^{n,m}_{RUW} - N^{n,m}_{RLW}\right) = \frac{1}{C_{ooo}} \Bigg[\Delta \overset{=}{\bar{\phi}}{}^{n,m}_{j} - \Bigg[\sum_{\substack{\text{right wing ahead} \\ + \text{ diaphragm}}} C_{\bar{\nu}\bar{\mu}0} \left(N^{\nu\mu}_{RUW} - N^{\nu\mu}_{RLW} \right)$$

$$+ \sum_{\substack{\text{left wing} \\ + \text{ diaphragm}}} C_{\bar{\nu}\bar{\mu}\bar{\lambda}} \begin{Bmatrix} + \\ - \\ 0 \end{Bmatrix} \left(N^{\nu\mu}_{RUW} - N^{\nu\mu}_{RLW} \right) \Bigg] \Bigg] \tag{57}$$

An additional condition to be solved is the continuity of total normal wash across the diaphragm. This may be expressed as

$$\left(N^{n,m}_{RUW} + \hat{N}^{n,m}_{\substack{RUW \\ LUW}} \right) = -\left(N^{n,m}_{RLW} + \hat{N}^{n,m}_{\substack{RLW \\ LLW}} \right) \tag{58}$$

or rearranging:

$$\left(N^{n,m}_{RUW} + N^{n,m}_{RLW} \right) = -\left(\hat{N}^{n,m}_{\substack{RUW \\ LUW}} + \hat{N}^{n,m}_{\substack{RLW \\ LLW}} \right) \tag{59}$$

Equations (57) and (59) can now be solved simultaneously to give the source strength on the upper and lower surfaces of box (n,m).

The source strengths found on the upper and lower surfaces are in general, different in magnitude. (For the case of zero dihedral, they will differ in sign but not in magnitude, in which case only the upper surface need be considered.)

For boxes on the planform, the velocity potential difference is found by application of Equation (56).

c. Solution for Flat Wing-Flat Tail with Vertical Separation

Discussion of the case of a flat wing and tail with positive vertical separation will lend some insight into the process of performing the solution with two separated lifting surfaces, without the complicating features of the dihedral solution discussed above.

The solution may be divided conceptually into three parts: 1) Performing the solution for the isolated wing and its wake; 2) finding the interference field over the tail and cancelling it; and 3) performing the solution for the isolated, but modified tail surface. Actually, however, the second and third parts are performed simultaneously.

The complete solution for the wing is performed first. Since there is no dihedral, the velocity potential difference is just given by:

$$\Delta\bar{\bar{\phi}}_j^{n,m} = 2\left[\sum_{\substack{\text{right wing}\\ +\text{diaphragm}}} C_{\bar{\nu}\bar{\mu}0}\, N_{RUW}^{\nu\mu} + \sum_{\substack{\text{left wing}\\ +\text{diaphragm}}} C_{\bar{\nu}\bar{\mu}0} \begin{Bmatrix} + \\ - \\ 0 \end{Bmatrix} N_{RUW}^{\nu\mu}\right] \quad (60)$$

where the source strength is found directly from the modal deflections and slopes

$$N_{RUW}^{n,m} = \frac{D\bar{f}_j^{n,m}}{Dt} = \left[ik_1 f_j^{n,m} + b_1 \frac{\partial f_j^{n,m}}{\partial x}\right] \quad (61)$$

For leading and trailing edge diaphragm boxes, the zero pressure difference and continuity conditions are applied, and Equation (60) is solved for unknown source strengths.

The solution for the tail is performed in a similar manner. The strength of the sources on the tail surface are given by

$$N_{RUT}^{n,m} = \frac{D\bar{f}_j^{n,m}}{Dt} - \hat{N}_{\substack{RUT\\RW}}^{n,m} - \hat{N}_{\substack{RUT\\LW}}^{n,m} \quad (62)$$

where for a tail located above the wing

$$\hat{N}_{\substack{RUT\\RW}}^{n,m} = \sum_{\substack{\text{right wing}\\ +\text{diaphragm}}} W_{\bar{\nu}\bar{\mu}\bar{\lambda}}^{\binom{RT}{RW}}\, N_{RUW}^{\nu\mu} \quad (63)$$

and

$$\hat{N}_{\substack{RUT\\RW}}^{n,m} = \sum_{\substack{\text{left wing}\\ +\text{diaphragm}}} W_{\bar{\nu}\bar{\mu}\bar{\lambda}}^{\binom{RT}{LW}}\, N_{LUW}^{\nu\mu} \quad (64)$$

where

$$N_{LUW}^{\nu\mu} = \begin{Bmatrix} + \\ - \\ 0 \end{Bmatrix} N_{RUW}^{\nu\mu} \quad (65)$$

The velocity potential difference is then

$$\Delta \bar{\phi}_j^{n,m} = 2\left[\sum_{\substack{\text{right tail}\\ +\text{ diaphragm}}} C_{\bar{\nu}\bar{\mu}o}\, N_{RUT}^{\nu\mu} + \sum_{\substack{\text{left tail}\\ +\text{diaphragm}}} C_{\bar{\nu}\bar{\mu}o}\begin{Bmatrix}+\\-\\0\end{Bmatrix} N_{RUT}^{\nu\mu}\right] \quad (6$$

For tail diaphragm boxes, the zero pressure difference and continuity conditions are applied, and the unknown source strength found as for the wing. It must be noted here, that the sources on the tail diaphragm do <u>not</u> include effects directly from the wing, as these are accounted for by the influence of the wing on the tail surface itself. In the absence of effective motion on the tail (i.e. in the case where the interference normal wash just cancels the modal induced normal wash) the source strength on the tail would be zero. Hence there would be no tail diaphragm, since it is necessary only to isolate the upper and lower tail surfaces in the presence of a finite source strength. The case of wing dihedral is dissimilar since the interference normal washes on the upper and lower surfaces are generally of different magnitudes while the modal deflections are the same. Thus a diaphragm is always necessary to isolate the upper and lower surfaces, and it is affected by the opposite surface.

d. Solution for Wing and Tail with Dihedral and Vertical Separation

The general case is found by combining the wing with dihedral and wing tail solutions described above. First the complete wing with dihedral solution is performed as described in Section (a), complete with a sufficient wake region to permit tail interference effects to be considered. The source strength difference used to satisfy the boundary condition of tangential flow for boxes on the tail surface is given

$$N_{RUT}^{n,m} - N_{RLT}^{n,m} = 2\frac{D\bar{f}^{n,m}}{Dt} + \left(\hat{N}_{\substack{RLT\\LLT}}^{n,m} - \hat{N}_{\substack{RUT\\LUT}}^{n,m}\right) - 2\hat{N}_{\substack{RUT\\RW}}^{n,m} - 2\hat{N}_{\substack{R\cdots\\LW}}^{n,m} \quad (67)$$

where

$$\hat{N}_{\substack{RUT\\LUT}}^{n,m} = \sum_{\substack{\text{left tail}\\ +\text{diaphragm}}} \left[\cos 2\psi_T\, W_{\bar{\nu},\bar{\mu},\bar{\lambda}}^{\binom{RT}{LT}} - \sin 2\psi_T\, V_{\bar{\nu},\bar{\mu},\bar{\lambda}}^{\binom{RT}{LT}}\right] N_{LUT}^{\nu\mu} \quad (68)$$

and

$$N^{n,m}_{\substack{RLT\\LLT}} = - \sum_{\substack{\text{Left tail}\\+\text{ diaphragm}}} \left[\cos 2\Psi_T \, W^{\binom{LT}{RT}}_{\nu\mu\lambda} - \sin 2\Psi_T \, V^{\binom{RT}{LT}}_{\nu\mu\lambda} \right] N^{\nu\mu}_{LLT} \tag{69}$$

where

$$\begin{bmatrix} N^{\nu\mu}_{LUT} \\ \\ N^{\nu\mu}_{LLT} \end{bmatrix} = \begin{Bmatrix} + \\ - \\ 0 \end{Bmatrix} \begin{bmatrix} N^{\nu\mu}_{RUT} \\ \\ N^{\nu\mu}_{RLT} \end{bmatrix} \tag{70}$$

Also

$$\hat{N}^{n,m}_{\substack{RUT\\LW}} = \sum_{\substack{\text{left wing}\\+\text{ diaphragm}}} \left[\cos (\Psi_T + \Psi_W) \, W^{\binom{RT}{LW}}_{\nu\mu\lambda} - \sin (\Psi_T + \Psi_W) \, V^{\binom{RT}{LW}}_{\nu\mu\lambda} \right] N^{\nu\mu}_{LW} \tag{71}$$

where

$$N^{\nu\mu}_{LW} = \begin{Bmatrix} + \\ - \\ 0 \end{Bmatrix} \begin{Bmatrix} N^{\nu\mu}_{RUW} & \text{if } (L > 0) \text{ or } (L = 0 \text{ and } \Psi_T - \Psi_W > 0) \\ N^{\nu\mu}_{RLW} & \text{if } (L < 0) \text{ or } (L = 0 \text{ and } \Psi_T - \Psi_W < 0) \end{Bmatrix} \tag{72}$$

and

$$\hat{N}^{n,m}_{\substack{RUT\\RW}} = \sum_{\substack{\text{right wing}\\+\text{ diaphragm}}} \left[\cos (\Psi_T - \Psi_W) \, W^{\binom{RT}{RW}}_{\nu\mu\lambda} - \sin (\Psi_T - \Psi_W) \, V^{\binom{RT}{RW}}_{\nu\mu\lambda} \right] N^{\nu\mu}_{RW} \tag{73}$$

where

$$N^{\nu\mu}_{RW} = \begin{cases} N^{\nu\mu}_{RUW} & \text{if } (L > 0) \text{ or } (L = 0 \text{ and } \Psi_T - \Psi_W > 0) \\ N^{\nu\mu}_{RLW} & \text{if } (L < 0) \text{ or } (L = 0 \text{ and } \Psi_T - \Psi_W < 0) \end{cases} \tag{74}$$

Then the velocity potential difference is found in the usual manner,

$$\Delta\bar{\bar{\phi}}_j^{n,m} = \sum_{\substack{\text{right tail}\\ +\text{diaphragm}}} C_{\overline{\nu\mu o}} \left(N_{RUT}^{\nu\mu} - N_{RLT}^{\nu\mu}\right) + \sum_{\substack{\text{left tail}\\ +\text{diaphragm}}} C_{\overline{\nu\mu\lambda}}^{\binom{RT}{LT}} \begin{Bmatrix} + \\ - \\ 0 \end{Bmatrix} \left(N_{RUT}^{\nu\mu} - N_{RLT}^{\nu\mu}\right) \qquad (75)$$

For diaphragm boxes:

$$N_{RUT}^{n,m} - N_{RLT}^{n,m} = \Big[\Delta\bar{\bar{\phi}}_j^{n,m} - \Big\{\sum_{\substack{\text{right}\\ \text{tail}}} C_{\overline{\nu\mu\lambda}} \left(N_{RUT}^{\nu\mu} - N_{RLT}^{\nu\mu}\right) + \sum_{\substack{\text{left}\\ \text{tail}}} C_{\overline{\nu\mu\lambda}}^{\binom{RT}{LT}} \begin{Bmatrix} + \\ - \\ 0 \end{Bmatrix} \left(N_{RUT}^{\nu\mu} - N_{RLT}^{\nu\mu}\right)\Big\}\Big] \qquad (76)$$

and

$$N_{RUT}^{n,m} + N_{RLT}^{n,m} = -\left(\hat{N}_{\substack{RUT\\ LUT}}^{n,m} + \hat{N}_{\substack{RLT\\ LLT}}^{n,m}\right) \qquad (77)$$

which may be solved for the unknown source strength on the tail. It may be seen that the tail surface boundary condition (Equation 67) includes direct wing contributions, but the diaphragm boundary condition (76) does not.

e. Special Cases

When the dihedral angle of either surface is zero, or when the dihedral angles of both surfaces are equal, or when the tail lies in the plane of the wing, some simplifications of the procedure can be made. There are special cases which occur quite often in practice and are discussed briefly below.

Flat Coplanar Wing-Tail

In this case, the two lifting surfaces may almost be treated as one surface and the source strength and velocity potential found in the same way as for a flat wing alone. The sole difference is that there exists a diaphragm between the wing and the tail which is handled in the usual manner of a wake. It may be theoretically demonstrated that the three-dimensional solution just reaches this limit as $L \to 0$ and the tail surface merges into the wing plane. One additional feature of this case is that the "mutual interaction" condition, i.e. where there is direct influence of the tail on the wing, may be

handled, since the computational scheme works with a single box pattern and can conveniently switch from wing to tail and back again as required. This case would occur with highly swept coplanar wing-tail combinations in close proximity at low Mach number.

Coplanar Wing-Tail with Dihedral

This case is similar to that described above, but both the wing and tail have dihedrals, which are equal. In this case, the two surfaces are treated as a single wing with dihedral, and the above diaphragm between the two planforms apply.

Wing Tail with Equal Dihedral and Vertical Separation

This case is similar to the general case. Since the dihedrals are equal, some saving can be effected by using the same AIC arrays for the effect of the wing on itself and the tail on itself. Separate arrays for the wing-tail interaction effect must be computed, however, Mutual interaction is not permitted in this case.

Wing with Vertical Tail

This case is another variant of the general case. The tail dihedral is set equal to 90° and the contribution of the left tail surface is ignored. This case is meaningful only for anti-symmetric mode shapes. Overlap between wing and tail surfaces is not permitted, so that a T-tail cannot be analyzed.

f. Wing - Flowfield Sampling Calculations

The method of interference flow fields described above can be used to sample the perturbation velocity components in the flow-field, resulting from the motions of the wing. The upwash and sidewash perturbation velocity components at a point (n,m) are found by:

$$\left(\frac{w}{U}\right)^{n,m,\ell} = \frac{1}{b_1} \left\{ \sum_{\substack{\text{right wing} \\ +\text{diaphragm}}} \left[\cos\psi_w \, W_{\nu\mu\lambda}^{\binom{FF}{RW}} + \sin\psi_w \, V_{\nu\mu\lambda}^{\binom{FF}{RW}} \right] N_{RW}^{\nu\mu} \right.$$

$$\left. + \sum_{\substack{\text{left wing} \\ +\text{diaphragm}}} \left[\cos\psi_w \, W_{\nu\mu\lambda}^{\binom{FF}{LW}} - \sin\psi_w \, V_{\nu\mu\lambda}^{\binom{FF}{LW}} \right] N_{LW}^{\nu\mu} \right\} \qquad (78)$$

$$\left(\frac{v}{U}\right)^{n,m,\ell} = \frac{1}{b_1}\left\{ \sum_{\substack{\text{right wing}\\ +\text{diaphragm}}} \left[\cos\psi_w \, V_{\frac{\binom{FF}{RW}}{\nu\mu\lambda}} - \sin\psi_w \, W_{\frac{\binom{FF}{RW}}{\nu\mu\lambda}}\right] N_{RW}^{\nu\mu} \right.$$

$$\left. + \sum_{\substack{\text{left wing}\\ +\text{diaphragm}}} \left[\cos\psi_w \, V_{\frac{\binom{FF}{LW}}{\nu\mu\lambda}} + \sin\psi_w \, W_{\frac{\binom{FF}{RW}}{\nu\mu\lambda}}\right] N_{LW}^{\nu\mu} \right\} \tag{79}$$

where $N_{RW}^{\nu\mu}$, $N_{LW}^{\nu\mu}$ are defined above for the general case, and the AIC's are the same as those for the wing-tail effect with $\psi_T = 0$.

The longitudinal wash is found from the velocity potential in the flow field

$$\left(\frac{u}{U}\right)^{n,m} = \frac{1}{b_1\beta} \left[\bar{\bar{\phi}}^{TE} - \bar{\bar{\phi}}^{LE}\right]^{n,m} \tag{80}$$

where

$$\bar{\bar{\phi}}^{TE} = \frac{1}{2}\left\{\bar{\bar{\phi}}^{n,m} + \bar{\bar{\phi}}^{n+1,m}\right\}$$

$$\bar{\bar{\phi}}^{LE} = \frac{1}{2}\left\{\bar{\bar{\phi}}^{n-1,m} + \bar{\bar{\phi}}^{n,m}\right\} \tag{81}$$

and

$$\bar{\bar{\phi}}^{n,m} = \sum_{\substack{\text{right wing}\\ +\text{diaphragm}}} C_{\frac{\binom{FF}{RW}}{\nu\mu\lambda}} N_{RW}^{\nu\mu} + \sum_{\substack{\text{left wing}\\ +\text{diaphragm}}} C_{\frac{\binom{FF}{LW}}{\nu\mu\lambda}} N_{LW}^{\nu\mu} \tag{82}$$

Note that it is most convenient to find the values of the perturbation velocities at the centers of "pseudo-boxes" located in the flow field, rather than at artibrary points. Interpolation to different points could be performed, of course.

6. PRESSURE DISTRIBUTIONS, GENERALIZED FORCES AND GENERALIZED AERODYNAMIC COEFFICIENTS

a. Pressure Distributions

Once the velocity potential difference is evaluated over a surface, the pressure distribution for the jth mode is found from the usual linearized expression (ref. 3)

$$\Delta p_j(x,y,t) = p_{j_{UPPER}}(x,y,t) - p_{j_{LOWER}}(x,y,t) \tag{83}$$

or

$$\Delta p_j(x,y,t) = \rho U \left[\frac{1}{U}\frac{\partial}{\partial t} + \frac{\partial}{\partial x}\right]\Delta\phi_j(x,y,t) \tag{84}$$

The complex amplitude of the pressure for simple harmonic motion is then

$$\Delta\bar{p}_j(x,y) = \frac{\rho U}{b_1}\left[ik_1 + b_1\frac{\partial}{\partial x}\right]\Delta\bar{\phi}_j(x,y) \tag{85}$$

In terms of the nondimensionalized velocity potential difference for box (n,m), the local pressure coefficient difference is

$$\Delta\bar{C}^{n,m}_{p_j} = \frac{\Delta\bar{p}_j}{q} = \frac{2}{\alpha^{n,m}b_1\beta}\left[\Delta\bar{\bar{\phi}}_j(x,y)\Big|_{x_{LE}}^{x_{TE}} + i\alpha^{n,m}k_1\Delta\bar{\bar{\phi}}_j^{n,m}\right] \tag{86}$$

where the velocity potential difference $\Delta\bar{\bar{\phi}}_j(x,y)$ is evaluated at the leading and trailing edges of box (n,m) by interpolation between the value for box (n,m) and the values for boxes directly ahead or behind. The on-planform area of each box is

$$\alpha^{n,m}\frac{b_1^2}{\beta}$$

where $\alpha^{n,m}$ is an area factor used to adjust the basic box area along planform edges and equals the proportion of box (n,m) that lies on the planform. For interior boxes, $\alpha^{n,m}$ is always unity.

The lift on each box due to a unit generalized deflection of jth mode is given by

$$\bar{L}^{n,m} = q\left(\frac{b_1}{\beta}\right) \bar{\bar{L}}_j^{n,m} \tag{87}$$

where the $\bar{\bar{L}}_j^{n,m}$ is the machine output and is

$$\bar{\bar{L}}_j^{n,m} = \frac{2}{\beta}\left[\left[\Delta\bar{\bar{\phi}}_j(x,y)\right]\Big|_{x_{LE}}^{x_{TE}} + i\,\alpha^{n,m}\,k_1\bar{\bar{\Delta\phi}}_j^{n,m}\right] \tag{88}$$

The lift on a chordwise section (chordwise row of boxes) is given by

$$\bar{\bar{L}}_j^{m} = \sum_n \bar{\bar{L}}_j^{n,m} \tag{89}$$

The total lift for half the airplane is

$$\bar{\bar{L}}_j = \sum_m \sum_n \bar{\bar{L}}_j^{n,m} \tag{90}$$

If the section or total lift for the wing or tail alone is desired, the sums of Equation (89) or (90) are taken only over the appropriate on-planform boxes.

The lift and moment coefficients per unit span C_ℓ and C_m, which take account of three dimensional interaction effects, may be found directly from the sectional lift and generalized force by the following relationships:

$$\alpha C_{\ell_j}^{m} = \frac{\bar{L}_j^{m}}{q\left(\frac{b_1}{\beta}\right)} = \bar{\bar{L}}_j^{m} \qquad \text{and} \qquad c^2 C_{m_j}^{m} = \frac{\bar{Q}_{ij}^{m}}{q\left(\frac{b_1}{\beta}\right)} = \bar{\bar{Q}}_{ij}^{m} \tag{91}$$

where c is the local chord and $\bar{Q}_{ij}^{m}$ is the sectional generalized force due to i-th pitching mode about a specified axis and loading for j-th mode. (see the following section). The values $\bar{\bar{L}}_j^{m}$ and $\bar{\bar{Q}}_{ij}^{m}$ are optional machine outputs.

b. Generalized Forces

The presence of the differentiation with respect to x in the pressure expression (Equation 85) makes it preferable to calculate the generalized forces directly from the velocity potential, rather than by integration of the pressure distributions weighted by the various modal functions. This may be accomplished as follows. If $f_i(x,y)$ is the i-th modal deflection in non-dimensional form, the associated generalized force due to

the pressure for the jth mode is

$$Q_{ij} = \overline{Q}_{ij}\, e^{i\omega t} \tag{92}$$

$$\overline{Q}_{ij} = \iint_A f_i(x,y)\Delta\overline{p}_j(x,y)\, dxdy \tag{93}$$

The applicable sign convention is that a positive generalized force is in the direction opposing the motion (restoring force).

The generalized force associated with each box (n,m) is therefore

$$\overline{Q}_{ij}^{n,m} = \iint_{A(n,m)} f_i(x,y)\Delta\overline{p}_j(x,y)dxdy \tag{94}$$

Or, substituting Equation (85) into Equation (94)

$$\overline{Q}_{ij}^{n,m} = \frac{\rho V}{b_1}\iint_{A(n,m)} f_i(x,y)\ [ik_1 + b_1\frac{\partial}{\partial x}]\ \Delta\overline{\phi}_j(x,y)dxdy \tag{95}$$

In terms of the nondimensionalized velocity potential difference

$$\overline{Q}_{ij}^{n,m} = \frac{\rho V^2}{\beta b_1}\iint_{A(n,m)} f_i(x,y)\ [\frac{\partial\overline{\overline{\phi}}_j(x,y)}{\partial(\frac{x}{b_1})} + ik_1\Delta\overline{\overline{\phi}}_j(x,y)]\ dxdy \tag{96}$$

Integration by parts and rearrangement of terms yields

$$\overline{Q}_{ij}^{n,m} = \frac{\rho V^2}{\beta b_1}\{ik_1\iint_{A(n,m)} f_i(x,y)\Delta\overline{\overline{\phi}}_j(x,y)dxdy + b_1\int_{\substack{\text{Box}\\ \text{Span}}} [f_i(x,y)\Delta\overline{\overline{\phi}}_j(x,y)]\Big|_{x_{LE}}^{x_{TE}} dy$$

$$- b_1\iint_{A(n,m)} \Delta\overline{\overline{\phi}}_m(x,y)\ \frac{\partial}{\partial x}[f_i(x,y)]\ dxdy\} \tag{97}$$

Equation (97) is integrated by assuming at most linear variation of the parameters over each box. The box generalized load is thus

$$\bar{Q}_{ij}^{n,m} = 2q\left(\frac{b_1^2}{\beta}\right)\frac{\alpha^{n,m}}{b_1\beta}\left\{ik_1 f_i^{n,m}\Delta\bar{\bar{\phi}}_j^{n,m} + \frac{1}{\alpha^{n,m}}\left[f_i(x,y)\Delta\bar{\bar{\phi}}_j(x,y)\right]\Big|_{x_{LE}}^{x_{TE}}\right.$$

$$\left. - b_1\Delta\bar{\bar{\phi}}^{n,m}\frac{\partial f_i^{n,m}}{\partial x}\right\} \tag{98}$$

The total generalized force in the ith mode due to a unit generalized deflection of the jth mode is thus

$$\bar{Q}_{ij} = q\frac{b_1}{\beta}\bar{\bar{Q}}_{ij} \tag{99}$$

where

$$\bar{\bar{Q}}_{ij} = \frac{2}{\beta}\sum_m\sum_n \left[f_i^{n,m}\Delta\bar{\bar{\phi}}_j^{n,m}\right]\Big|_{x_{LE}}^{x_{TE}} - b_1\Delta\bar{\bar{\phi}}_j^{n,m}\alpha^{n,m}\frac{\partial f_i^{n,m}}{\partial x} + ik_1\alpha^{n,m}f_i^{n,m}\Delta\bar{\bar{\phi}}_j^{n,m} \tag{100}$$

C. Generalized Aerodynamic Coefficients

In order to be able to compare results of the methods of this report to experimental values or other theoretical methods, it is desirable to have a standard notation and nondimensionalization for deflections and generalized forces. Such a standard has been established by the Advisory Group for Aeronautical Research and Development (AGARD).

This standard is based primarily on a nondimensionalization by semi-span, s . In the AGARD notation system the total generalized force is given by

$$\hat{Q}_{ij} = -\int_{y'=-1}^{y'=+1}\int_{x'=x'_{le}}^{x'=x'_{te}} g_i(x',y')\lambda_j(x',y')\,dx'dy' \tag{101}$$

where

$$\lambda_j(x',y') = \frac{\Delta P_j}{2q} \qquad g_i(x',y') = \frac{f_i(x',y')}{s} \qquad x' = \frac{x}{s} \qquad y' = \frac{y}{s}$$

In our notation, then

$$\hat{Q}_{ij} = -\frac{1}{qs^3}\iint_A f_i(x,y)\overline{\Delta p}_j(x,y)dxdy = -\frac{1}{qs^3}\overline{Q}_{ij} \text{ ***} \tag{102}$$

where A is the area of a half-airplane. But since

$$\overline{Q}_{ij} = q\frac{b_1}{\beta}\bar{\bar{Q}}_{ij} \tag{103}$$

then

$$\hat{Q}_{ij} = -\frac{b_1}{s^3\beta}[\bar{\bar{Q}}_{ij}] \tag{104}$$

Furthermore, in the AGARD system, the real and imaginary parts are separated as

$$\hat{Q}_{ij} = Q'_{ij} + ik_s Q''_{ij} \tag{105}$$

with reduced frequency given as

$$k_s = \frac{s\omega}{V} \tag{106}$$

In our notation, then AGARD generalized aerodynamic coefficients are given by:

$$Q'_{ij} = -\frac{b_1}{s^3\beta} \text{ Re } [\bar{\bar{Q}}_{ij}] \tag{107}$$

$$Q''_{ij} = -\frac{b_1^2}{k_1 s^4\beta} \text{ Im } [\bar{\bar{Q}}_{ij}] \tag{108}$$

NOTE - To obtain generalized aerodynamic coefficients in the correct AGARD notation the planform and mode shapes must be normalized. The planform must have a semi-span of 1.0 and the mode functions must correspond to the normalized planform.

7. REFINEMENTS OF THE MACH BOX METHOD

a. Subdivision

It is well known that the Mach Box Method may produce inaccurate pressures. The inaccuracies take the form of irregular fluctuations in the chordwise and spanwise pressure distributions. These pressure fluctuations are more pronounced for a planform which has subsonic leading edges, due to the inaccurate representation of the singular upwash distribution on the diaphragm region. It has appeared in the past that, in spite of these pressure fluctuations, generalized airforces have been acceptable.

As discussed in subsection 3 above, the true leading edge of the planform is replaced by the edges of boxes in the Mach Box Grid, to form an artificial leading edge. Unless the true leading edge is parallel or perpendicular to the stream flow the artificial leading edge will be "jagged", as in Figure 13.

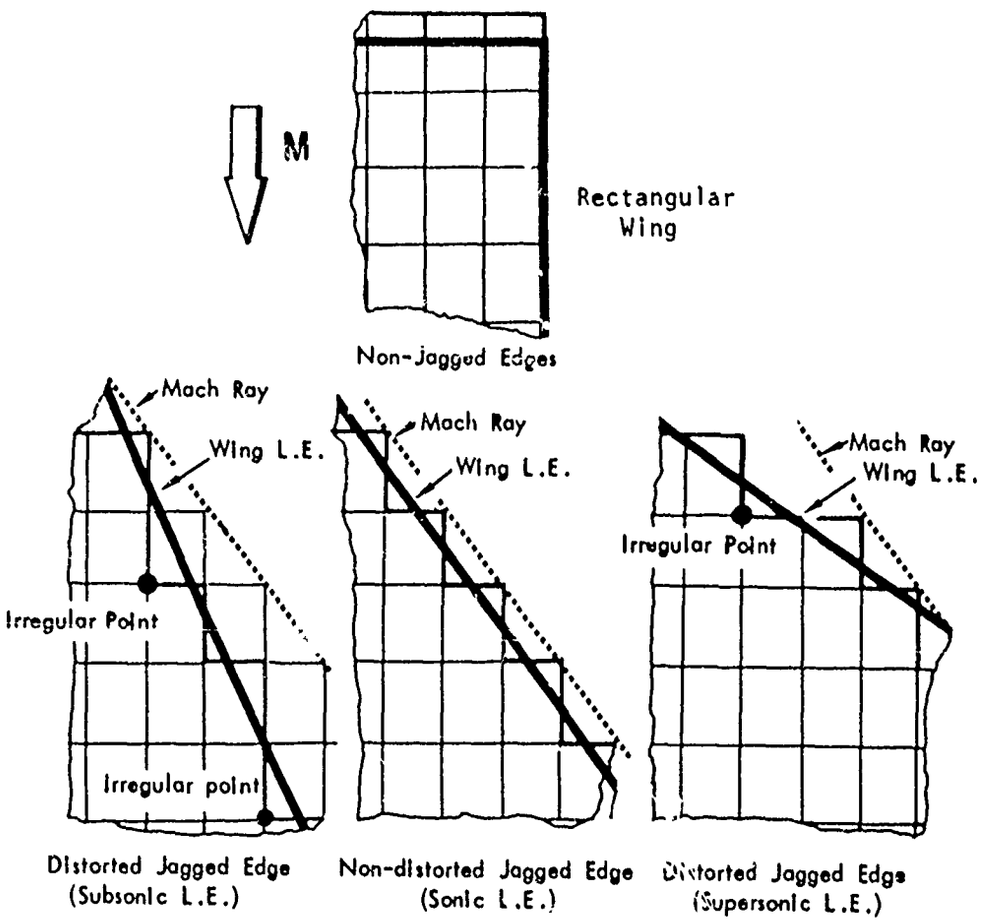

Figure 13. Irregularities in Distorted Jagged Leading Edges

As may be seen from Figure 13 , leading edges which are not parallel to the Mach rays are represented by an irregular pattern of Mach boxes. It is this irregularity which is the primary cause of the pressure fluctuation.

The concept of "distortion" may be introduced to quantify the irregularity in the relationship between the true and artificial leading edges. This distortion is defined as the maximum distance between the true and artificial leading edges, measured either spanwise or chordwise (whichever is the larger), divided by the box dimension, b_1 or b_1/β, respectively. If the distortion does not exceed 1, the planform is "non-distorted". Clearly if a finer box grid is chosen, the distortion is unchanged; this corresponds to the finding that a finer box grid merely increases the spatial frequency of the pressure fluctuations, but does not reduce their amplitudes (Figure 14).

This phenomenom has been reported on extensively in References 10 & 11 which found that the pressure fluctuations are principally caused by (a) the singular nature of the AIC's along the forward Mach lines emanating from the receiving point, (b) the strong upwash which is discontinuous at a subsonic leading edge and in the opposite direction on the diaphragm ahead of the edge, and (c) the irregular points * produced by the jagged leading edge of a grid of boxes. These effects combine to cause noticeable fluctuations in the velocity potential distributions which when differentiated cause the pressure distribution to fluctuate unrealistically over the wing planform.

It is the aim of the subdivision technique to reduce the distortion of the leading edge. This is achieved by decreasing the minimum unit scale of the sending box grid system, i.e. the box dimension, without changing the dimension of the receiving box, as shown in Figure 14.

---

* The "irregular points" are defined as the down-stream corners of regions where the leading edge cuts more than one box on the chordwise or spanwise strips.

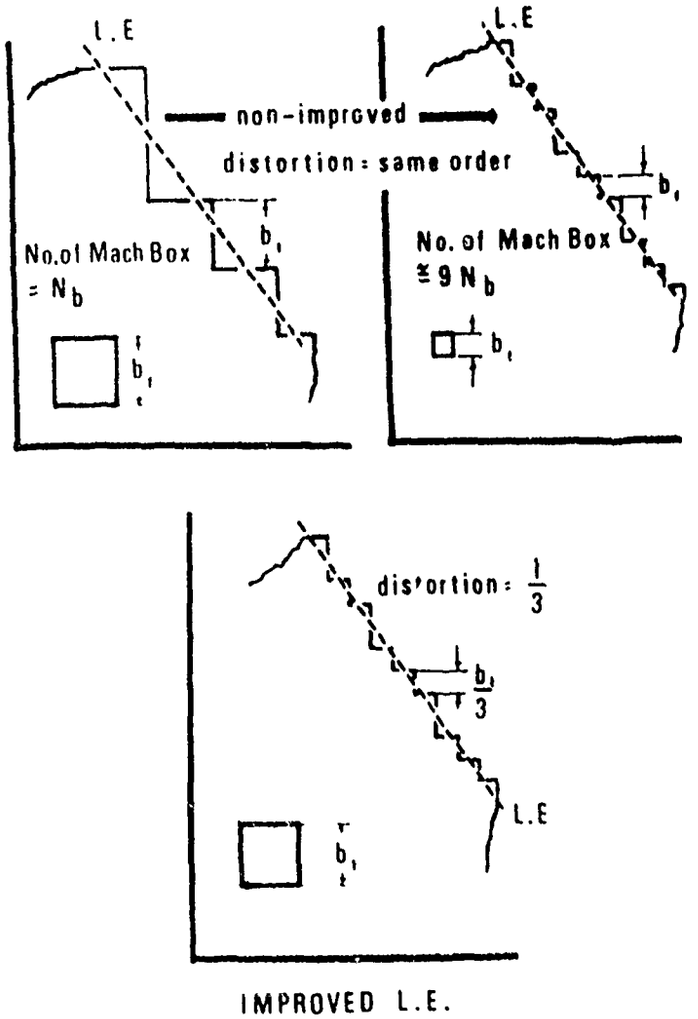

Figure 14 Refinement Of Jagged Leading Edges

Each box in the sending box grid is divided into N_S^2 "sub-boxes" where N_S is an odd integer. The receiving boxes remain unchanged, their centers forming the "control points" of the system. Clearly, each control point will be at the center of the central "sub-box". Figure 15 shows that the distortion is reduced by a factor N_S, and that the effects of the irregular points on the control points are effectively reduced.

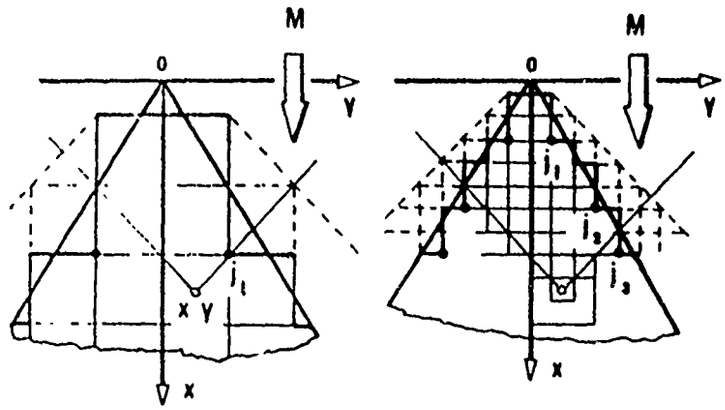

Figure 15 Avoidance Of Irregular Point Effects By Subdivision

In Odd Number Increments

Principles for Application of the Subdivision Scheme

The subdivision refinement is applied using the following assumptions and techniques:

1) Subdivision may be used only when the receiving and sending boxes lie in the same plane. This means that, in the general configuration, subdivision may be applied only to the calculation of the effect of the right wing on itself and of the left wing on itself. If the wing dihedral is zero, subdivision may be used in calculating the effect of the left wing on the right wing.

2) Subdivision is not applied to the whole surface. A receiving box is influenced primarily by sending boxes which are close to it. Therefore, there is introduced the concept of "effective area" shown in Figure 16. The effective area may contain more or

fewer subdivided boxes than the total number of ordinary boxes required in the solution. The influence of sending boxes which lie inside the effective area on the receiving point will be determined using subdivision; the influence of those boxes on the planform which lie outside the effective area will be calculated in the usual way. For off planform boxes outside the effective area, an average value of upwash will be used.

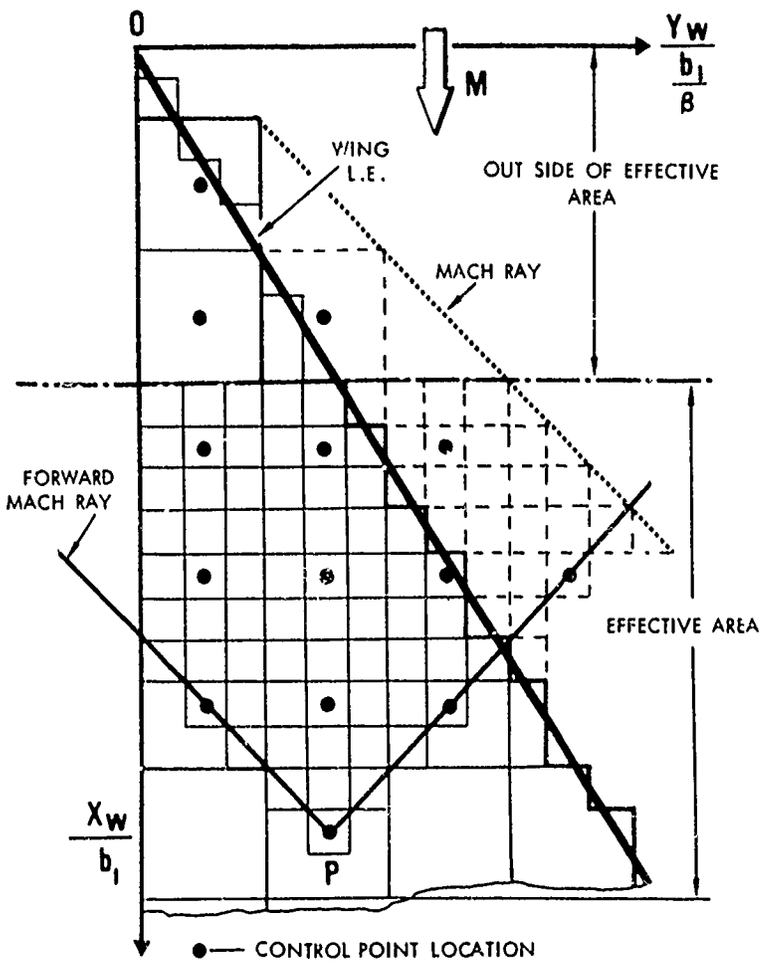

Figure 16 Subdivision Of Box Grid System In Effective Area Zone

3) The modal deflection and slope is calculated at the center of each unsubdivided box that lies on the planform. The deflection at the center of each sub-box that lies on the planform is determined by point slope extrapolation from the center of the unsubdivided box within which it lies.

4) The upwash at the center of each sub-box which does not lie on the planform is calculated using the boundary condition of zero pressure difference. The upwash associated with any unsubdivided box that includes a diaphragm sub-box is calculated as the average of the upwashes of the sub-boxes which lie within the unsubdivided box.

5) Only the velocity potentials at the unsubdivided box centers are used to calculate the generalized forces and pressure distributions.

Application of Subdivision to Flat Wings-or-Coplanar Wing Tails

The subdivision refinement may be applied only in cases where the sending and receiving boxes lie in the same plane. If such a case were analized without subdivision an array of AIC's for velocity potential, $C_{\bar{\nu},\bar{\mu},o}$, would be used where $C_{\bar{\nu},\bar{\mu},o}$ is given

$$C_{\bar{\nu},\bar{\mu},o} = -\frac{1}{\pi}\int_{\bar{\xi}_L}^{\bar{\xi}_u}\int_{\bar{\eta}_L}^{\bar{\eta}_u} \frac{e^{-i\bar{k}_1\bar{\xi}} \cos\left(\frac{\bar{k}_1}{M}\sqrt{\bar{\xi}^2-\bar{\eta}^2}\right)}{\sqrt{\bar{\xi}^2-\bar{\eta}^2}}\, d\bar{\xi}\, d\bar{\eta} \tag{109}$$

for $\bar{\nu} = o, 1, \ldots N_A$ where N_A = number of rows in the array
and $\bar{\mu} = 0, 1, 2, \ldots \bar{\nu}$

When subdivision is used a second array of AIC's is needed. The subdivided AIC array for velocity potential differs from the unsubdivided array only in the value of frequency, k_1 being replaced by k_1/N_S. Thus some saving can be affected when multiple frequencies are considered by choosing them in multiples of N_S. Some differences in the necessary sizes of the array may be found, however, due to the finer breakdown of the planform geometry into a box pattern.

The nondimensional velocity potential difference at the receiving box, when subdivision is applied, is

$$\Delta\bar{\phi}^{n,m} = 2\left[\sum_{\substack{\text{right wing}\\ \text{"effective area"}}} C^{s}_{\bar{\nu}\bar{\mu}o}\; N^{(\nu\mu)^{s}}_{RUW} + \sum_{\substack{\text{right wing}\\ \text{ahead}}} C_{\bar{\nu}\bar{\mu}o}\; N^{\nu\mu}_{RUW}\right.$$

$$\left. + \sum_{\substack{\text{left wing}\\ \text{"effective area"}}} C^{s}_{\bar{\nu}\bar{\mu}o} \begin{Bmatrix} + \\ - \\ o \end{Bmatrix} N^{(\nu\mu)^{s}}_{RUW} + \sum_{\substack{\text{left wing}\\ \text{ahead}}} C_{\bar{\nu}\bar{\mu}o} \begin{Bmatrix} + \\ - \\ o \end{Bmatrix} N^{\nu\mu}_{RUW}\right] \tag{110}$$

This equation is used to evaluate the source strength $N^{(\nu\mu)^{s}}$ on the diaphragm by applying the boundary conditions Eq. (53) or (54) for each of the subdivided boxes on the diaphragm.

Application of Subdivision to a Wing with Dihedral

If the small (subdivided) box center corresponds to a large (unsubdivided) box center, the unknown source strength for the small box may be found directly from the value for the large box;

$$N^{(n,m)^{s}}_{RUW} = \frac{1}{N_s}\left(N^{n,m}_{RUW}\right) \tag{111}$$

where N_s is the subdivision factor.

It can be shown that, since both the mode shapes and interference normal washes are obtained for large box centers only, that the unknown source strength for small boxes on the planform which do not correspond to large box centers may be found directly from the values at large box centers by a point-slope extrapolation. Assuming the complex source strength represents the normal wash produced by a pseudo mode shape,

$$N^{(n,m)^{s}}_{RUW} = \frac{1}{N_s}\left\{ \mathrm{Re}\left[N^{n,m}_{RUW}\right] + i\left[\mathrm{Im}\left[N^{n,m}_{RUW}\right] + \frac{k_1}{b_1}(x_s - x)\,\mathrm{Re}\left[N^{n,m}_{RUW}\right]\right]\right\} \tag{112}$$

where x_s is the X coordinate of the sub-box center. A similar expression can be deduced for $N_{RLW}^{(n,m)^S}$ on the lower surface.

If the small box is not contained within a large box on the planform:

$$N_{RUW}^{(n,m)^S} = \frac{1}{N_S}\left[\mathrm{Re}\ [N_{RUW}^{n+p,m}] + i\left\{\mathrm{Im}\ [N_{RUW}^{n+p,m}] + \frac{k_1}{b_1}(x_s - x)\,\mathrm{Re}\ [N_{RUW}^{n+p,m}]\right\}\right] \tag{113}$$

where n + p is the index of the nearest on-planform large box, upstream or downstream.

The velocity potential for on-planform unsubdivided boxes is then found as:

$$\Delta\,\bar{\bar{\phi}}_j^{\,n,m} = \sum_{\substack{\text{right wing + diaphragm}\\ \text{"effective area"}}} C^S_{\nu\mu o}\,(N_{RUW}^{(\nu\mu)^S} - N_{RLW}^{(\nu\mu)^S})$$

$$+ \sum_{\substack{\text{right wing + diaphragm}\\ \text{outside the effective area}}} C_{\nu\mu o}\,(N_{RUW}^{\nu\mu} - N_{RLW}^{\nu\mu}) \tag{114}$$

$$+ \sum_{\text{left wing + diaphragm}} C_{\nu\mu\lambda}^{\binom{RW}{LW}} \left\{\begin{matrix} + \\ - \\ 0 \end{matrix}\right\} (N_{RUW}^{\nu\mu} - N_{RLW}^{\nu\mu})$$

For subdivided boxes in leading or trailing edge diaphragms, the local source strength is found by satisfying the zero pressure difference and continuity conditions explicitly at every point (rather than extrapolating from large box values). Thus in the diaphragm region

$$N_{RUW}^{(n,m)^s} - N_{RLW}^{(n,m)^s} = \frac{1}{C_{ooo}^s} \left\{ \Delta\bar{\phi}^{(n,m)^s} - \left[\sum_{\substack{\text{effective}\\ \text{area}}} C_{\overline{\nu\mu\lambda}}^s \left(N_{RUW}^{(\nu\mu)^s} - N_{RLW}^{(\nu\mu)^s}\right) + \sum_{\substack{\text{right wing}\\ \text{ahead}}} C_{\overline{\nu\mu}o} \left(N_{RUW}^{\nu\mu} - N_{RLW}^{\nu\mu}\right) + \sum_{\text{left wing}} C_{\overline{\nu\mu\lambda}}^{\binom{RW}{LW}} \begin{Bmatrix} + \\ - \\ o \end{Bmatrix} \left(N_{RUW}^{\nu\mu} - N_{RLW}\right) \right] \right\} \tag{115}$$

and

$$N_{RUW}^{(n,m)^s} + N_{RLW}^{(n,m)^s} = -\left(\hat{N}_{\substack{RUW\\LUW}}^{(n,m)^s} + \hat{N}_{\substack{RLW\\LLW}}^{(n,m)^s} \right) \tag{116}$$

Here the interference normal wash values are again found by the point-slope extrapolation method from large box center values.

$$\hat{N}_{\substack{RUW\\LUW}}^{(n,m)^s} = \frac{1}{N_s} \left\{ \mathrm{Re}\left[\hat{N}_{\substack{RUW\\LUW}}^{\nu\mu}\right] + i\left[\mathrm{Im}\left[\hat{N}_{\substack{RUW\\LUW}}^{\nu\mu}\right] + \frac{k_1}{b_1}(x_s - x)\ \mathrm{Re}\left[\hat{N}_{\substack{RUW\\LUW}}^{\nu\mu}\right] \right] \right\} \tag{117}$$

and

$$\hat{N}_{\substack{RLW\\LLW}}^{(n,m)^s} = \frac{1}{N_s} \left\{ \mathrm{Re}\left[\hat{N}_{\substack{RLW\\LLW}}^{\nu\mu}\right] + i\left[\mathrm{Im}\left[\hat{N}_{\substack{RLW\\LLW}}^{\nu\mu}\right] + \frac{k_1}{b_1}(x_s - x)\ \mathrm{Re}\left[\hat{N}_{\substack{RLW\\LLW}}^{\nu\mu}\right] \right] \right\} \tag{118}$$

The velocity potential difference for subdivided diaphragm boxes is found in a similar manner. For leading edge diaphragm boxes:

$$\Delta\bar{\bar{\phi}}_j^{(n,m)^S} = 0 \tag{119}$$

for trailing edge diaphragm boxes:

$$\Delta\bar{\bar{\phi}}_j^{(n,m)^S} = \Delta\bar{\bar{\phi}}_{TE}^{(m)^S} \; e^{-ik_1\left(\frac{X_n^S - X_{TE_m}^S}{b_1}\right)} \tag{120}$$

where

$$\Delta\bar{\bar{\phi}}_{TE}^{(m)^S} = \left(\frac{X_{TE_m}^S - X_{n'}}{b_1}\right)\left(\Delta\bar{\bar{\phi}}^{n',m} - \Delta\bar{\bar{\phi}}_j^{n'-1,m}\right) + \Delta\bar{\bar{\phi}}_j^{n',m} \tag{121}$$

where n' is the index of the last complete box on chord m.

Once all the on-planform and diaphragm subdivided source strengths are determined, the velocity potential for unsubdivided boxes is found from Eq. (114).

b. Velocity Potential Smoothing

The subdivision technique described above reduces substantially the fluctuation in the velocity potential and pressure distributions. Some fluctuations still occur however, for the subdivision technique is still a finite element approach. These smaller fluctuations may be eliminated through the application of a least squares surface fitting technique to the velocity potential distribution. The method is described as follows.

The function chosen to represent the velocity potential is

$$\Delta\bar{\bar{\phi}}(\bar{x},\bar{y}) = \left[\sum_n \sum_m f_{nm}^{(R)} \bar{x}^n \bar{y}^m\right] + i\left[\sum_n \sum_m f_{nm}^{(I)} \bar{x}^n \bar{y}^m\right] \tag{122}$$

where

$$\bar{x} = \frac{x}{b_1}$$

$$\bar{y} = \frac{y}{b_1/\beta}$$

$$n,m = \text{integers} \; ; \; n + m \leqslant 5$$

and

$f_{nm}^{(R)}$, $f_{nm}^{(I)}$ = sets of least squares polynomial coefficients used to fit the real and imaginary parts, respectively, of the velocity potential function.

Application of the least-square surface fit to the velocity potential functions is performed separately over each lifting surface. The number of control points required (including the leading edge points where the velocity potential is zero or determined from the wake) is

$$\text{Number of Control Points} > \sum_{i=1}^{k+1} i \qquad \text{for a } k\text{-th order polynomial}$$

In practice, however, the control points used for a given order polynomial should exceed these theoretical limits by at least

$$1/2 \sum_{i=1}^{k+1} i \qquad \text{in order to obtain a smooth fit.}$$

The following sketch summarizes the term actually used in the various assummed polynomials.

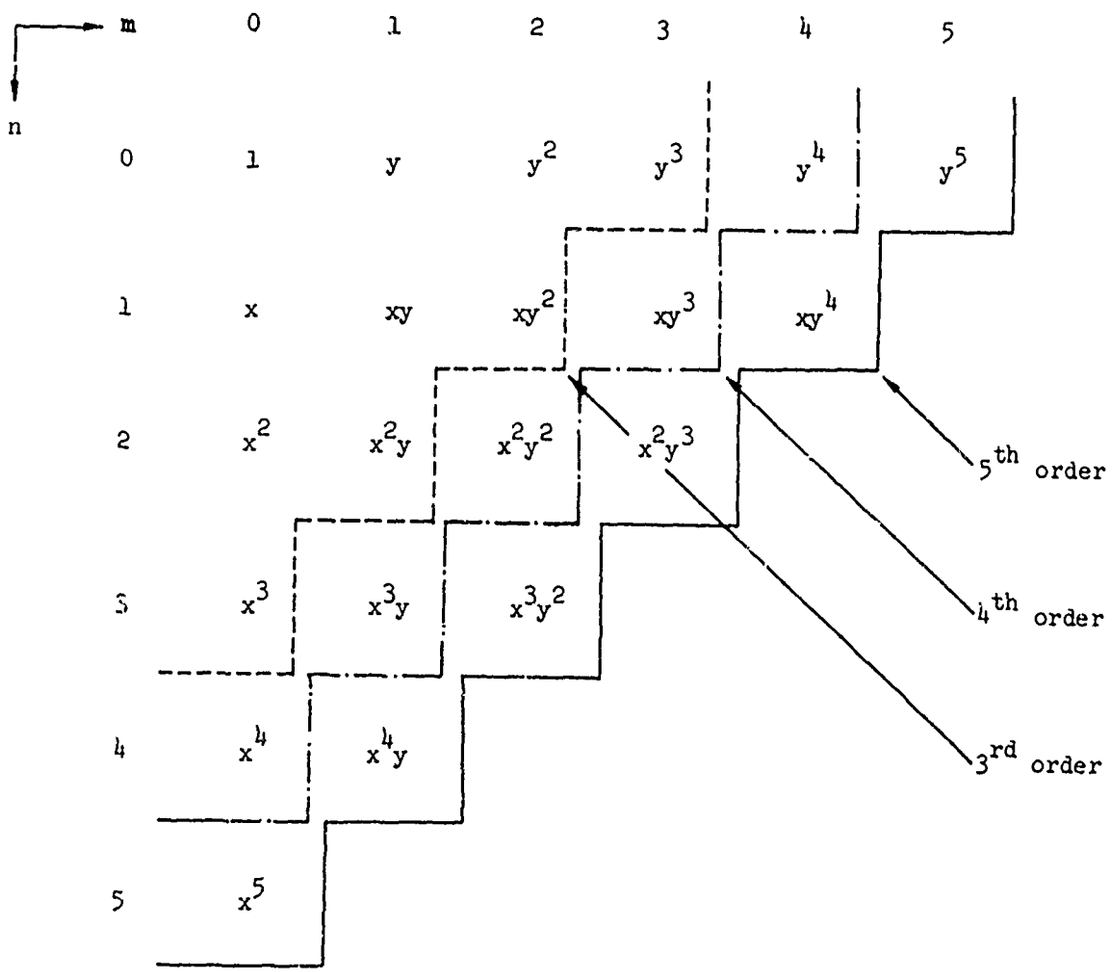

Figure 17 Summary Of Polynominal Terms

c. Thickness Corrections to the Pressure Distribution

In the realm of linearized flow solutions without interference effects, the pressure distribution due to thickness may be accounted for separately and combined by superposition. The thickness effect is more critical to flutter stability when the flow Mach number is close to one.

When interference effects are included, the thickness problems may not simply be decoupled. For simple harmonic motion, however, thickness alone would generate an oscillatory loading only when the upper and lower surface modal displacements have the opposite sign. Since this is an unlikely case, thickness has been ignored in the methods for interference calculations used in this report. However, a correction on the pressure distribution for thickness can be performed locally by applying second order piston theory (Ref. 12). This means that the local pressure is uniquely determined by the local velocity normal to the lifting surface.

The second order piston theory may be expressed

$$p - p_\infty = \rho_\infty a_\infty^2 \left[\frac{w}{a_\infty} + \frac{\gamma+1}{4} \left(\frac{w}{a_\infty} \right)^2 \right] \tag{123}$$

In this expression the velocity w is normal to the oscillating surface and p is the local static pressure.

For non-planar wings, the shape of lifting surface is expressed by

$$\begin{aligned} Z_U (x,y,t) &= \bar{Z}_M (x,y)\, e^{i\omega t} + Z_\tau (x,y) \\ Z_L (x,y,t) &= \bar{Z}_M (x,y)\, e^{i\omega t} - Z_\tau (x,y) \end{aligned} \tag{124}$$

where $Z_\tau (x,y)$ is the thickness distribution about the mean surface which is represented by the mean surface distribution, $\bar{Z}_M (x,y)$ as shown in Figure 18.

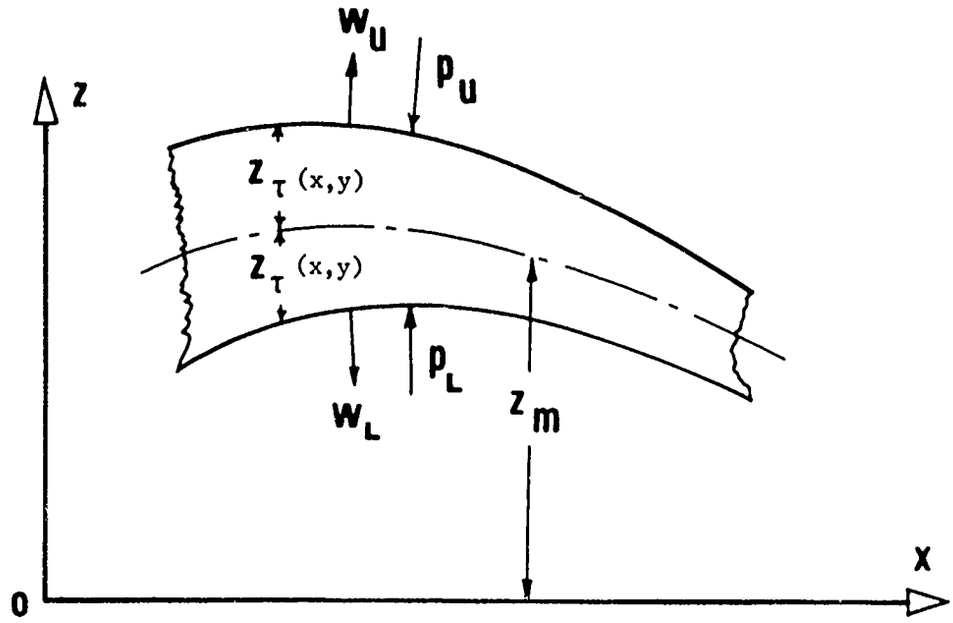

Figure 18 Thickness Distribution About Wing Mean Surface

Since surface pulsing is not allowed, $Z_\tau(x,y)$ is not time-dependent. Therefore the normal velocity at the surface Z (x,y,t) is

$$W(x,y,t) = \frac{\partial z}{\partial t} + U \frac{\partial z}{\partial x}$$

$$= \underbrace{\left[i\omega Z_M(x,y) + U \frac{\partial Z_M}{\partial x} \right] e^{i\omega t}}_{\pm W_0(x,y)\, e^{i\omega t}} \pm \frac{\partial Z_\tau}{\partial x} \qquad (125)$$

where (+) and (-) correspond to the upper and lower surface respectively and W_o (x,y) is the amplitude of the mean surface motion.

By substituting the non-time dependent term of Equation (125) into Equation (123), the pressure over the upper surface is

$$\left[p - p_\infty\right]_U = \rho_\infty a_\infty \left[W_0(x,y) + U \frac{\partial Z_\tau}{\partial x}\right] + \rho_\infty \frac{\gamma+1}{4}\left[W_0^2(x,y) + 2 W_0 U \frac{\partial Z_\tau}{\partial x} + U^2 \left(\frac{\partial Z_\tau}{\partial x}\right)^2\right] \tag{126}$$

Similarly the pressure over the lower surface is

$$\left[p - p_\infty\right]_L = -\rho_\infty a_\infty \left[W_0(x,y) - U \frac{\partial Z_\tau}{\partial x}\right] + \rho_\infty \frac{\gamma+1}{4}\left[W_0^2 - 2 W_0 U \frac{\partial Z_\tau}{\partial x} + U^2 \left(\frac{\partial Z_\tau}{\partial x}\right)^2\right] \tag{127}$$

The net pressure difference between the upper and lower surfaces is thus

$$p_U - p_L = \left[p - p_\infty\right]_U - \left[p - p_\infty\right]_L = \underbrace{2 \rho_\infty a_\infty W_0(x,y)}_{\text{1-st - order piston-theory}}\left[1 + \frac{\gamma+1}{2} M \frac{\partial Z_\tau}{\partial x}\right] \tag{128}$$

The first term in Equation (128) is equivalent to the 1st order piston theory which is computed over a planar wing. Therefore, the thickness correction, $Z_\tau(x,y)$, to be applied to the pressure difference is

$$Z_\tau(x,y) = 1 + \frac{\gamma+1}{2} M \frac{\partial Z_\tau}{\partial x} \tag{129}$$

The expression for pressure at a point is thus modified by the thickness correction factor and is

$$\Delta \bar{p}_j(x,y) = \frac{\rho U}{b_1}\left[ik_1 + b_1 \frac{\partial}{\partial x}\right] \Delta \bar{\varphi}_j(x,y)\, \bar{\bar{Z}}_\tau(x,y) \tag{130}$$

The local pressure coefficient difference becomes

$$\Delta \bar{c}_p{}^{n,m} = \frac{\Delta \bar{p}_j{}^{n,m}}{q} = \frac{2}{\alpha^{n,m} b_1} \beta \left[\left\{ \Delta \bar{\bar{\varphi}}_j(x,y) \right\} \Big|_{x_{le}}^{x_{te}} + i\alpha^{n,m} k_1 \Delta \bar{\bar{\varphi}}_j{}^{n,m} \right] \bar{\bar{Z}}_\tau{}^{n,m} \tag{131}$$

and the non-dimensionalized box lift becomes

$$\bar{\bar{L}}_j{}^{n,m} = \frac{2}{\beta}\left[\left\{ \Delta \bar{\bar{\varphi}}_j(x,y) \right\} \Big|_{x_{le}}^{x_{te}} + i\alpha^{n,m} k_1 \Delta \bar{\bar{\varphi}}_j{}^{n,m} \right] \bar{\bar{Z}}_\tau{}^{n,m} \tag{132}$$

The non-dimensionalized generalized force in the ith mode due to a unit generalized deflection of the jth mode is thus

$$\bar{\bar{Q}}_{i,j} = \frac{2}{\beta} \sum_m \sum_n \left[\bar{\bar{Z}}_\tau^{n,m} \left\{ f_i^{n,m} \Delta \bar{\bar{\varphi}}_j{}^{n,m} \right\} \Big|_{x_{le}}^{x_{te}} - b_1 \Delta \bar{\bar{\varphi}}_j{}^{n,m} \bar{\bar{Z}}_\tau{}^{n,m} \alpha^{n,m} \frac{\partial f_i{}^{n,m}}{\partial x} + i k_1 \alpha^{n,m} f_j{}^{n,m} \Delta \bar{\bar{\varphi}}_j{}^{n,m} \bar{\bar{Z}}_\tau{}^{n,m} \right] \tag{133}$$

SECTION III

COMPUTER PROGRAM USAGE

1. MACHINE AND OPERATING SYSTEM REQUIREMENTS

The program is written in FORTRAN IV for execution on the CDC 6600 under the SCOPE operating system. The FORTRAN coding is compatible with the RUN compiler and with FORTRAN Extended. Using the overlay feature of the SCOPE operating system, a field length of about 132000_8 is required to load the program, and about 124000_8 for execution. Disk space or tape drives are required for five internal binary scratch files, in addition to the standard INPUT and OUTPUT files, and further optional binary input and output files are allowed for.

2. TIMING AND OUTPUT ESTIMATES

a. TIMING

Three measures of time are available for most CDC operating systems; Central Processor (CP) time, Peripheral Processor (PP) time, and Occupancy time. Of the three, CP time is most consistent, since the program's usage of the Central Processor is not dependent upon the job mix or system configuration. The PP times for two runs of the same job may vary widely, since Peripheral Processors may be held up while waiting for other IO devices used and the operating system driving them. Occupancy (clock) time is the least consistent of the three, since it is also dependent on the priority levels of other jobs in the system. With this in mind, CP time usage is presented in this report in some detail, and rough PP and Occupancy times are given only to present an idea of order of magnitude.

CP time in seconds can be estimated from:

T = 60 to 70 for UPDATE, compilation and load

+2 to 7 for Geometry and Modal input

$$+ \sum_{i=1}^{\#\text{ of K-values}} \text{(time for AIC calculations, see following description)}$$

+ (# of modes) x (# of K-values) x (time for Velocity Potentials + time for Generalized Forces, see following descriptions)

The time necessary to do a full UPDATE, compilation and load of the program is roughly 60-70 seconds CP, 200 - 300 seconds PP, and 4 to 7 minutes occupancy. Most of this can be avoided if the program is maintained in absolute form on tape (or disk).

Geometry setup and modal input for a typical case ranges from two to seven seconds CP time.

The time involved in calculating AIC's is variable, depending upon Mach number, reduced frequency, geometry, and desired integration accuracy. In general, time increases with K-value and decreases with increased Mach number, for a constant number of rows on the box pattern. A completely flat configuration requires one AIC array if no subdivision is desired, and two with subdivision. A flat wing and flat tail with vertical separation require two sets of arrays. Dihedral angles require in addition, one set per chord of the tail for the wing/tail interaction. Thus, a typical configuration having 30 chords on the box pattern requires one AIC when completely planar, 2 AIC arrays if vertical separation is specified, and between 50 and 70 if either surface has dihedral. The timing involved is not directly proportional to the number of AIC arrays needed, since spatial AIC's are typically sparse and various sizes, so a rough rule of thumb is to multiply the time estimated for the required planar AIC by .5 for the time needed per spatial AIC set. The desired integration accuracy parameter plays an important role, since an accuracy of .01% (EXAIC = .TRUE.) takes roughly 5 1/2 times as much CP time as the default accuracy of 1.0%. Figure 19 indicates some timing results from the application phase executions.

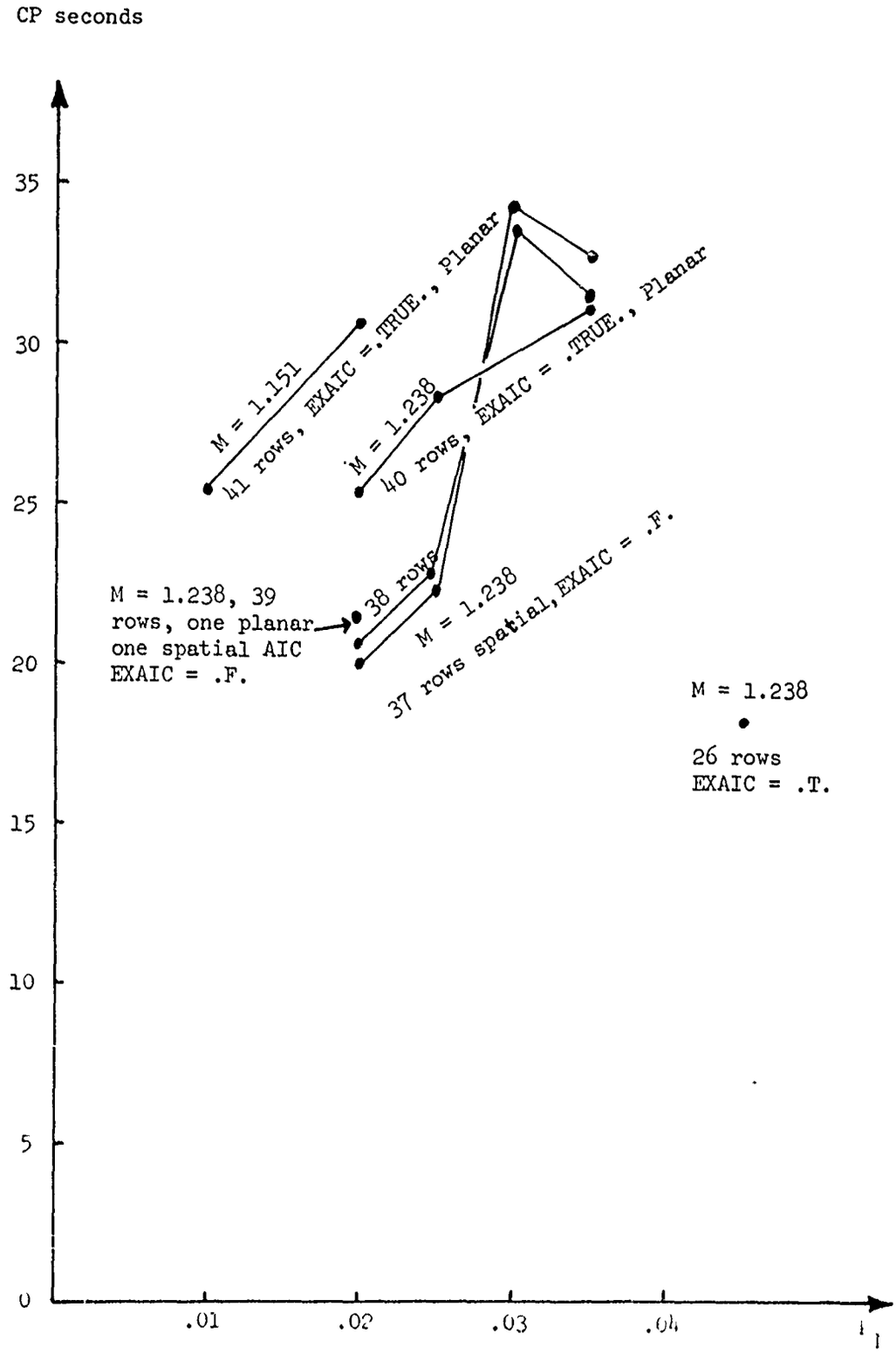

FIGURE 19 Timing of AIC Calculations

By far, the most time consuming part of the program is the section which calculates normal washes and velocity potentials. Without subdivision, CP seconds per mode can be given roughly as

$\frac{1}{15000}$ X (# of boxes)^2 , see Figure 20 . The number of boxes includes all diaphragm boxes for both wing and tail. If subdivision is specified (SUBDV = .TRUE.) the question becomes more complex. The size of the effective area controls the timing for planform box computations, and diaphragm boxes take roughly nine times as much time as planform boxes. A few examples are given in the table below:

BOX PATTERN					Effective Area, Rows	CP Seconds per Mode
# Rows	# Chords		# of Boxes			
	Planform	Total	Planform	Diaphragm		
37	10	24	242	284	8	268
36	6	21			4	39.9
37	6	22	150	300	default*	175.471
					12	0.413

* Default is 1/3 (# of rows) or 600 sub-boxes, whichever is smaller.

FIGURE 20 SAMPLE TIMING OF VELOCITY POTENTIAL CALCULATIONS WITH SUBDIVISION

The time spent calculating Generalized Forces is a function of box pattern size, number of modes, and number of reduced frequencies. The range of CP time is from 0.7 seconds to 2.1 seconds per mode for each reduced frequency.

b. Output

Output can range from a minimum of about two pages per reduced frequency, for a small case with no print options, to around 100 pages per mode for each reduced frequency, for a large case with all print options turned on.

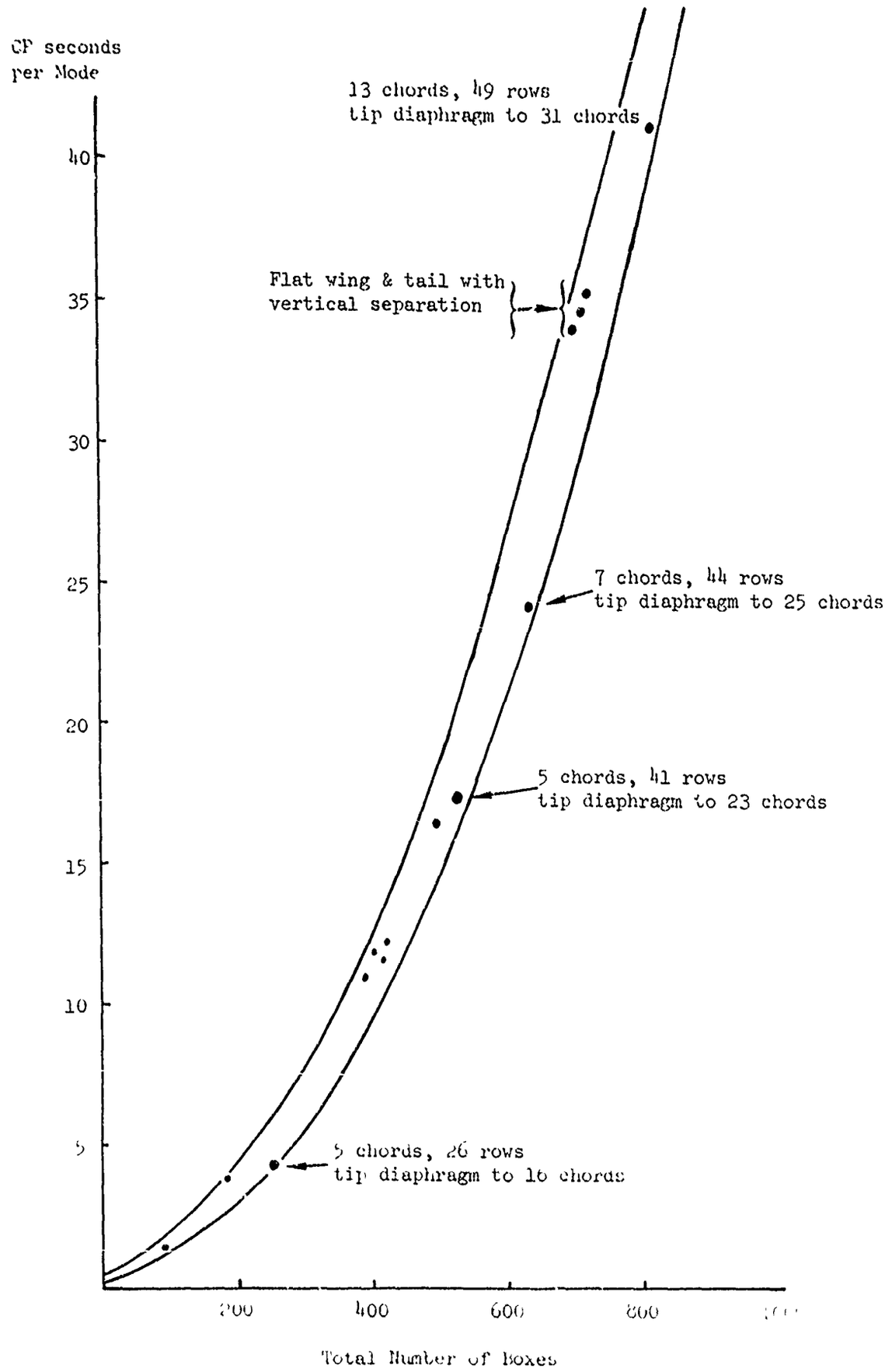

FIGURE [illegible] Velocity Potential Timing, Unsubdivided

3. PROGRAM LIMITS AND RESTRICTIONS

The primary limit on the program is the number of Mach boxes which can be handled. This is:

(1) If a single surface (or a co-planar wing-tail) without dihedral is being analyzed without subdivision, the box pattern, including tip diaphragm, may extend 50 boxes fore-to-aft and 50 boxes root-to-tip. (See Figure 22)

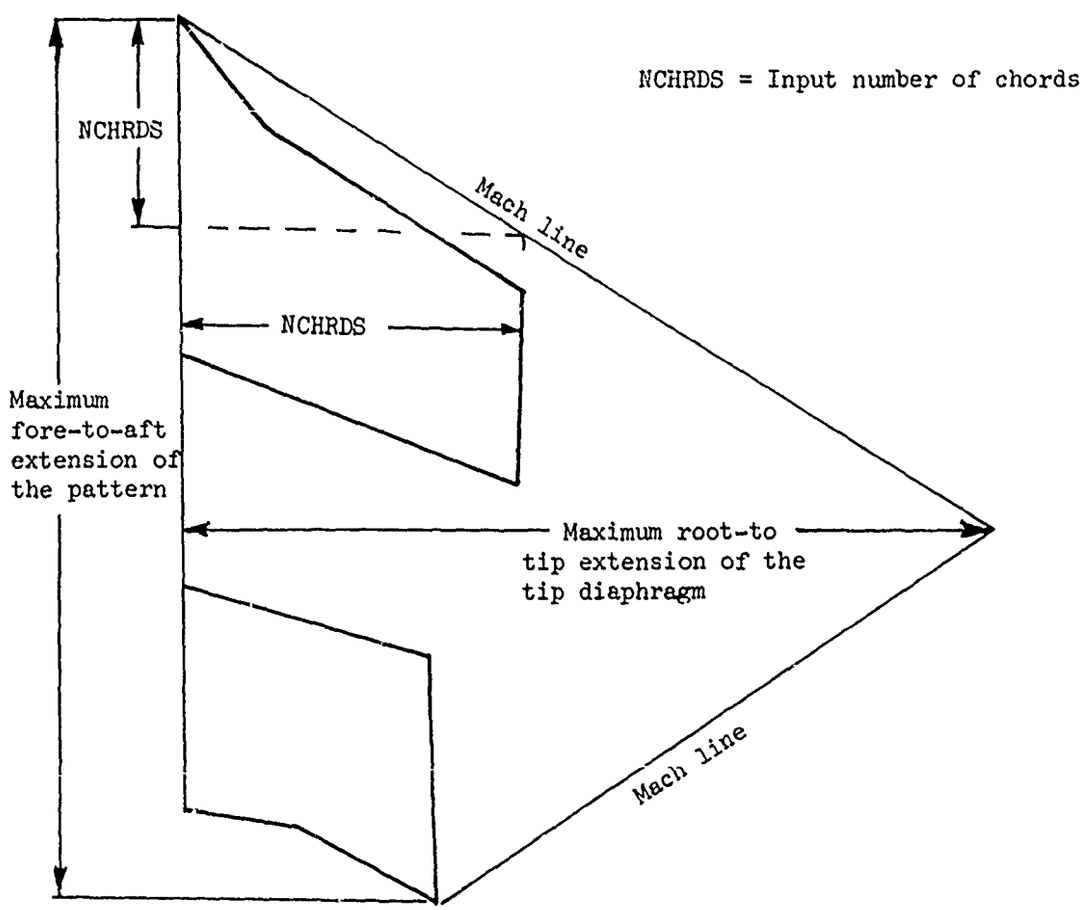

FIGURE 22 Determination of Box Pattern Limits

(All measurements are in number of boxes)

(2) For any spatial configuration or sampling case, a 40 X 40 box pattern, for wing and tail combined (with diaphragms) is the maximum.

(3) Total number of on-planform boxes (control points) $\leq$ 1000.

(4) Total number of boxes considered, planform and diaphragm, $\leq$ 1275.

Geometric configurations that fit the program analysis capabilities are shown in figures 25, 26, 27 and 29. Figures 28 and 30 illustrate some of the configurations not allowed. The planforms must be defined in terms of straight line segments and may take on various shapes as indicated in figure 25. The wing and tail may have dihedral, vertical separation and horizontal separations. Aerodynamic interaction of the tail affecting the wing may be evaluated only for the coplanar case. The tail may physically overlap the wing for the spatial case however the tail aerodynamic "Mach cone" must not intersect the wing as shown in figure 29.

Each planform edge must be defined by ≤ 10 points, located by (x, y) in the local coordinate system (fig. 25). Each edge must start with $y = 0$, and the y value for the outmost leading edge point and trailing edge point must be identical for each planform. The y-values increase outward, and x-values increase aft.

The leading edge of any planform cannot have any forward swept sections. The trailing edge may. (Figures 25, 30)

Planform edge definitions must be monotonic in y; i.e., no planform edge may "double back" in the y-direction. Segments of an edge may be parallel to the x-axis, however, other considerations may cause bad answers for planforms of this nature. (Figure 25)

The dihedral angles ψ_W and ψ_T must lie in the range $0° \leq \psi \leq 45°$ or $\psi_T = 90°$. (Figures 26, 27)

A maximum of 20 modes is allowed.

Number of reduced frequencies ≤ 20.

Mach number > 1.0
Mach number < 5.0 (recommended range from 1.2 to 3.0)

For printing purposes it is assumed that reduced frequencies based on b_1 will lie within the range $10^{-5} \leq k_1 \leq 1.0$ or $k_1 = 0.0$, and reduced frequencies based on semispan s will lie within the range

$$10^{-5} \leq k_s \leq 1000.0 \quad \text{or} \quad k_s = 0.0.$$

4. DECK SETUP

a. Deck Setup for running the program from a SCOPE 3 UPDATE tape.

Control Cards

```
Job Card    CM132000.

REQUEST TAPE.      (Tape containing OLDPL)
REWIND(TAPE)
COPYBF(TAPE,OLDPL)
UNLOAD(TAPE)

UPDATE(F)

RUN(S,,1022,COMPILE)

LGO.

End-of-Record Card
   (Optional Correction Sets)
End-of-Record Card
   (Card Data for the program)
End-of-File Card
```

b. Deck Setup for running the program as above with previously generated AIC arrays saved on tape.

Control Cards

```
Job Card     CM132000.

REQUEST TAPE.       (Tape containing OLDPL)
REWIND(TAPE)
COPYBF(TAPE,OLDPL)
UNLOAD(TAPE)
UPDATE(F)
RUN(S,,1022,COMPILE)
REQUEST PAICS.          (Tape containing planar AICs)
REQUEST SAICS.          (Tape containing spatial AICs)
REWIND(PAICS)
REWIND(SAICS)
COPYBF(PAICS,TAPE2,3)
COPYBF(SAICS,TAPE3,3)
UNLOAD(PAICS)
UNLOAD(SAICS)
LGO.

End-of-Record Card
   (Optional Correction Sets)
End-of-Record Card
   (Card Data for the program , OAIC=2, OSAIC=3)
End-of-File Card
```

5. CARD INPUT DATA

a. Namelist Format

Several of the card sets defined in this input data description are in NAMELIST format. The following few paragraphs explain this format as used here. Beginning in column 2 is the quantity $LNAME, where LNAME is a name associated with a particular card set. The LNAME for card set C is "CARDC" therefore Card Set C must begin with $CARDC in column 2.

$LNAME is followed by a blank and a string of specifications, separated by commas and terminated by a $. Each specification is one of the following forms:

(1) VNAME = VALUE

(2) VNAME(1) = VALUE1, VNAME(2) = VALUE2, VNAME(3) = VALUE3, etc.

where VNAME is one of the legal variable (or array) names for the card set, and VALUE is the value (or values) associated with VNAME.

In form (1): (a) VALUE may be of the form .TRUE., .T., .FALSE., or .F. when VNAME is a logical variable.

(b) VALUE should be an integer if VNAME is an integer variable.

(c) VALUE should be a real number if VNAME is a real variable. Examples: -1.0, 0.07, 3.5E2.

In form (2): (a) VNAME must be an array name and the values given will be stored in the specified array locations.

The field on a card consists of columns 2 through 80. The string may be continued from card to card with no restriction that a specification may not be split between cards. Embedded blanks are allowed except within $LNAME, within VNAME and within VALUE. The order of appearance on a card is not important. A variable for which a default value is desired need not be specified unless a previous pass through the program has replaced the default value.

b. Data Description Conventions

For conciseness, if two or more parameters have similar meanings, they are bracketed together in the description. Normally each bracketed parameter may be independently specified, as in $\left\{\begin{matrix}\text{PRPAIC}\\ \text{PRSAIC}\end{matrix}\right\}$. In a few cases, two methods of specifying the same information are provided. In these cases, the parameters are bracketed with the word "or", as in $\left\{\begin{matrix}\text{OAIC}\\ \text{or}\\ \text{NAIC}\end{matrix}\right\}$, and only one of the bracketed parameters should be specified.

c. Data Descriptions

Linkage Card to Execute the Program Format-(A6,4X,2I10)

```
     6                20        30
AFMBOX                 1         0
```

AFMBOX = Program Overlay File Name

1 = Primary level number

0 = Secondary level number

Card A - Title Card (Once per cycle) Format-(8A10)

```
TITLE
```

TITLE - Columns 1 to 80 are printed as page header information.

Card B - Mach Number (Once per cycle) Format-(NAMELIST)

```
$CARDB XMACH =      $
```

XMACH = Mach number for the airforces of this cycle. All calculations for a cycle are done at one Mach number.

Card Set C - Control Parameters

All of the following control parameters have default values (underlined). Any parameter not specified will take its default value. For a recycle, see parameter DEFAULT below.

Format(NAMELIST)

$CARDC . . . $

Parameter	Type	Optional Values, Default Underlined	Meaning
DEFAULT	Logical	.TRUE.	All parameters for this card set are set to default values. Any other parameter on this card set will be ignored.
		.FALSE.	All parameters listed on this card set will be used. If this is the first cycle through the program, any unspecified parameters will take their default values. If this is not the first cycle, unspecified parameters will take the values they had in the previous cycle.
PRVGEOM	Logical	.TRUE.	Use geometry defined in the previous cycle, this cycle being a change in Mach numbers and/or modes. Cards F-L are not needed. Not allowed in the first cycle of the program.
		.FALSE.	New planform geometry is to be specified for this cycle.
PRVMODE	Logical	.TRUE.	Mode shapes from the previous cycle are to be used. Not allowed in the first cycle of the program, or if geometry or Mach number has changed.
		.FALSE.	New mode shapes are to be specified for this cycle.
SYM	Real	1.0	Symmetric analysis
		-1.0	Antisymmetric analysis
		0.0	No left hand surface contributions are to be calculated.

Card Set C - continued

Parameter	Type	Optional Values, Default Underlined	Meaning
NSURF	Integer	1 or 2	Number of surfaces to be analyzed.
{MTYPEW / MTYPET}	Integer		Type of modal input for the {wing / tail}.
		1	Polynomial coefficients
		2	Arbitrary locations
		3	Box center values (Mach number dependent).
SUBDV	Logical	.TRUE.	Apply subdivision to the normal-wash calculations.
		.FALSE.	Do not apply subdivision, (Basic analysis).
NROWEA	Integer	0 to 12	If subdivision is .TRUE., this parameter allows the user to specify the maximum number of unsubdivided rows in the effective area. If 0, the program uses 1/3 the total number of rows specified. (See Figure 16)
EXAIC	Logical	.TRUE.	Calculate AIC's with an integration tolerance of 0.01%.
		.FALSE.	Calculate AIC's with an integration tolerance of 1.0%.
{DIHW / DIHT}	Logical	.TRUE.	Include dihedral in calculating the influence of the {Wing / Tail} on itself.
		.FALSE.	Use any dihedral only in the calculation of interaction between the planforms.

Card Set C - Continued

Parameter	Type	Optional Values, Default Underlines	Meaning
ISMPLW	Integer	0 to 10	Number of chords for which sampling of upwash, sidewash and/or longitudinal wash is desired off-planform. (See Card G).
{SMOOTH or CRDFIT}	Logical	.TRUE.	Smooth the velocity potential differences, $\overline{\Delta\phi}^{n,m}$, by a {surface or chordwise} least squares polynomial fit before they are used in calculation of generalized forces. Generalized forces for smoothed and unsmoothed $\overline{\Delta\phi}$ are calculated.
		.FALSE.	Do not smooth the $\overline{\Delta\phi}^{n,m}$, values; calculate generalized forces for only the unsmoothed $\overline{\Delta\phi}$ values.
NDEG	Integer	0 to 10	The maximum degree of least squares polynomial to apply for smoothing (0 causes the program to determing the degree as a function of the number of boxes on the {surface or chord}).
PLYWOOD	Logical	.TRUE.	Calculation of lifts and generalized forces is to be done using full box areas everywhere.
		.FALSE.	Calculation of lifts and generalized forces is to be done using planform defined box areas.
PRCM	Logical	.TRUE.	Print $\overline{\overline{Q}}^{m}_{ij}$, sectional generalized force for mode 1. If first mode is a pitch mode, then sectional moment coefficients may be obtained from $C^{m}_{mj} = \overline{\overline{Q}}^{m}_{ij}/c^{2}$. (See Sect. II.6, eqn. 91).
		.FALSE.	Do not print Sectional generalized forces

Card Set C - Continued

Parameter	Type	Optional Values, Default Underlines	Meaning
PRBOX	Logical	.TRUE.	Print box code pattern(s).
		.FALSE.	Do not print box pattern(s).
{PRCOEF, PRMODS}	Logical	.TRUE.	Print modal {coefficients, deflections and slopes} used, if available.
		.FALSE.	Do not print {coefficients, deflections and slopes} used.
{PRPAIC, PRSAIC}	Logical	.TRUE.	Print {planar, spatial} AIC array(s).
		.FALSE.	Do not print AIC array(s).
{PRUW, PRSW, PRLW}	Logical	.TRUE.	Print {upwashes, w/U; sidewashes, v/U; longitudinal washes, u/U} for sample chords.
		.FALSE.	Do not Print {upwashes, sidewashes, longitudinal washes}
PRNW	Logical	.TRUE.	Print normal washes(N_{RUW}, etc.) due to local source strength.
		.FALSE.	Do not print normal washes.
PRVP	Logical	.TRUE.	Print velocity potentials, $\overline{\Delta\phi}^{n,m}$.
		.FALSE.	Do not print velocity potentials.

Card Set C - Continued

Parameter	Type	Optional Value, Default Underlined	Meaning
PRBL	Logical	.TRUE.	Print box lifts, $\bar{\bar{L}}_j^{n,m}$,
		.FALSE.	Do not print box lifts.
PRDCP	Logical	.TRUE.	Print pressure difference coefficients $\Delta C_{p_j}^{-n,m}$
		.FALSE.	Do not print pressure difference coefficients.
PRSL	Logical	.TRUE.	Print section lifts, $\bar{\bar{L}}_j^m$
		.FALSE.	Do not print section lifts.
PRGNAF	Logical	.TRUE.	Print generalized air forces, $\bar{\bar{Q}}_{ij}$
		.FALSE.	Do not print generalized air forces.
PRGNAC	Logical	.TRUE.	Print generalized aerodynamic coefficients, Q'_{ij} and Q''_{ij}, if PRGNAF = .TRUE.

WARNING - To obtain generalized aerodynamic coefficients in the correct AGARD notation the planform and mode shapes must be normalized. The planform must have a semi-span of 1.0 and the mode shapes must correspond to the normalized planform.

		.FALSE.	Do not print generalized aerodynamic coefficients
WTGNAF	Logical	.TRUE.	Write generalized air forces on tape.
		.FALSE.	No generalized air forces are to be written on tape.
WTBL	Logical	.TRUE.	Write box lifts on tape.
		.FALSE.	Box lifts are not to be written on tape.

Card Set C - Continued

The following parameters may be included on Card Set C: DPPCPR, GEOCPR, MODCPR, AICCPR, NWSCPR, SMCPR, GAFCPR. They are intended for checkout only, and are described in Part II, Section II, Subsection 11, Common Block/CHECKPR/.

Card Set D - Tape Parameters, all are Integers.

Format -(NAMELIST)

$CARDD $

Variable	Default	Meaning
{OAIC or NAIC}	0	Logical tape number of {old or new} AIC tape. An "old" tape is one which was generated as a new tape by a previous execution of the program. A value of "zero" means no tape is to be used or saved.
{OSAIC or NSAIC}	0	Logical tape number of {old or new} Spatial AIC tape. An "old" tape is one which was generated as a new tape by a previous execution of the program. A value of "zero" means no tape is to be used or saved.
INTAPE	0	Logical tape number of tape containing geometry and mode shape information. If this value is 0 or 5, card input will be used, requiring cards N to Ø. Tape is always rewound before use.
NOUTP	1	Logical tape number for output requested under WT--- options. This parameter is not needed if no WT--- option is specified. Tape is rewound first cycle, used from current position in subsequent cycles.
NOTE: The above four tape numbers must be independent, if specified.		
INFSP	0	Initial file spacing on INTAPE.
IOUFSP	0	Initial file spacing on NOUTP.

Card Set E - Reduced Frequencies, Real Format - (NAMELIST)

$$\$CARDE \quad \left\{ \begin{array}{l} XKS(1) = _____,\ XKS(2) = _____,\ldots \\ \text{or} \\ XK1(1) = _____,\ XK1(2) = _____,\ldots \end{array} \right\} \ \$$$

$$\left\{ \begin{array}{l} XKS \\ \text{or} \\ XK1 \end{array} \right\} = \text{Array of reduced frequency values, based on } \left\{ \begin{array}{l} \text{semispan, } s \\ \quad \text{or} \\ \text{box length, } b_1 \end{array} \right\}$$

for which airforces will be calculated. Limit 20. If no reduced frequencies are specified, the program will determine the geometry and then terminate.

Geometry Definition

(None of these cards, F through L, are needed if PRVGEOM has been specified.)

Card F Frame of Reference Definition.

All planform description and mode definition is based on coordinate systems local to each surface. The values on this card relate the local systems to a global system. (See Figures 1 & 2)

Format - (NAMELIST)

```
$CARDF                                                    $
```

WLAX = X location of the wing local axis system origin relative to the global coordinate system. Positive aft. Real, default 0.

WLAZ = Z location of the wing local axis system origin relative to the global coordinate system. Positive upward. Real, default 0.

PSIW = Wing dihedral angle, degrees, positive upward for the right hand side. Real, default 0.

TLAX, TLAZ, PSIT } Same as above, for the tail (second surface) if needed.

Card G Box pattern size and location Format - (NAMELIST)

```
$CARDG   NCHRDS = _______, {XCENTR or XEDGE} = _____ ...   $
```

NCHRDS = Number of boxes in the spanwise direction on the wing. Integer, no default. See subsection 3 of Section III, Program Limits and Restrictions.

{XCENTR or XEDGE} = X location of a box {center / edge} in the local coordinates of the wing, from which X_c is determined. XCENTR or XEDGE may be specified anywhere on or near the wing. If XEDGE is specified, the program computes a corresponding XCENTR = XEDGE + $b_1/2$. Then the program adds or subtracts increments of b_1 until the first on-planform wing location is reached. The resulting value is X_c, the location of row 1 of the box pattern. The same grid is extended to the tail as needed. Real, no default.

Card G - Continued

ICHORD = Array of chord numbers for sample of off-planform upwash, sidewash or longitudinal wash. Integer, default is no sample. ISMPLW (Card C) gives the maximum number expected.

$\begin{Bmatrix} \text{IBOXF} \\ \text{IBOXL} \end{Bmatrix}$ Array of $\begin{Bmatrix} \text{first} \\ \text{last} \end{Bmatrix}$ box sampled on each chord. Integer, default IBOXF = IBOXL = last box of the planform. Measured along coordinate n_c. $0 < \text{IBOXF(I)} \leq \text{IBOXL(I)} \leq 40$

ZLOC = Array of Z - locations of the sample chords in the global coordinate system. Real, default 0. (The vertical separation between wing and sampling chord must be non-zero.)

NOTE: ICHORD, IBOXF, IBOXL, ZLOC will be ignored unless ISMPLW on Card C is >0, and NSURF = 1. ICHORD, IBOXF, IBOXL, ZLOC are arrays, each one requiring ISMPLW numbers.

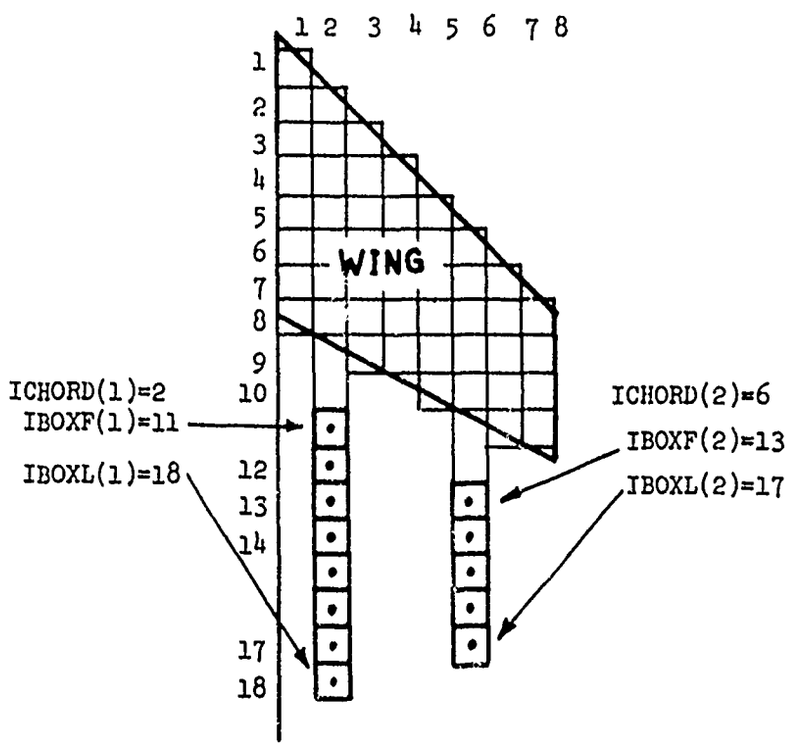

FIGURE 23 Definition of Sampling Locations
(Assuming $\Psi_w = 0$. ZLOC(I) not shown)

Modal Input

Modal input is not required if no reduced frequencies were listed on Card E or if PRVMODE was specified on Card C. Otherwise, Card M must be included, and the remainder are required if INTAPE = 0 or 5.

Card M - Number of Modes and Thickness slope distributions
This card is read once per cycle of the program.

Format - (NAMELIST)

$CARDM	NMODES = _____	...	$

NMODES = Total number of modes to be input. A "mode" as used here means the combined distortion of the wing and tail. Integer, no default.

NTSLOP = Number of thickness slope sets to be input on Card Sets P and Q. If omitted the program takes a default of 0 and generates an array of zero thickness slope everywhere. Integer.

There are three options for the form in which mode shapes may be input from cards. The form indicated by MTYPEW will be repeated NMODES times, getting all modes for the wing. Then, if NSURF = 2, cards N and O are repeated NMODES times again, this time in the form indicated by MTYPET, to obtain the corresponding mode shapes for the tail. If there is no motion of the wing (or tail) for a particular mode, the corresponding modal values must be input as zero.

Option 1: Polynomial Input - Cards N1, O1 if $\begin{Bmatrix} \text{MTYPEW} \\ \text{MTYPET} \end{Bmatrix} = 1$. Repeated NMODES times.

Card N1 Format - (I5)

5
IDEG

IDEG = Degree of polynomial, ≤ 5. This controls the number of coefficients on card Set O1.

Card Set O1 Format - (7E10.0)

a_{oo}	a_{10}	a_{01}	a_{20}	a_{11}	a_{02}	a_{30}

a_{21}	a_{12}	a_{03}	.....etc.

As many coefficients as are needed for the polynomial of degree IDEG:

$$f_j(X,Y) = a_{oo} + a_{10}X + a_{01}Y + a_{20}X^2 + a_{11}XY + a_{02}Y^2 + a_{30}X^3 + \ldots a_{o,IDEG}Y^{IDEG}$$

where point (X,Y) is in the X_W, Y_W (or X_T, Y_T) coordinate system, and

$f_j(X,Y)$ is the modal deflection.

Card L - Tail trailing edge definition points. (Omitted if NSURF = 1 on Card C).

Format - (6E10.0)

XTTE(1)	YTTE(1)	XTTE(2)	YTTE(2)	...

$\left\{\begin{matrix}\text{XTTE(i)}\\ \text{YTTE(i)}\end{matrix}\right\}$ - X and Y coordinates of the trailing edge definition points for the tail. There are NTTE pairs of coordinates, measured in the tail local coordinate system, (X_T, Y_T).

Modal Input

Modal input is not required if no reduced frequencies were listed on Card E or if PRVMODE was specified on Card C. Otherwise, Card M must be included, and the remainder are required if INTAPE = 0 or 5.

Card M - Number of Modes and Thickness slope distributions
This card is read once per cycle of the program.

Format - (NAMELIST)

$CARDM NMODES = _____ ... $

NMODES = Total number of modes to be input. A "mode" as used here means the combined distortion of the wing and tail. Integer, no default.

NTSLOP = Number of thickness slope sets to be input on Card Sets P and Q. If omitted the program takes a default of 0 and generates an array of zero thickness slope everywhere. Integer.

There are three options for the form in which mode shapes may be input from cards. The form indicated by MTYPEW will be repeated NMODES times, getting all modes for the wing. Then, if NSURF = 2, cards N and O are repeated NMODES times again, this time in the form indicated by MTYPET, to obtain the corresponding mode shapes for the tail. If there is no motion of the wing (or tail) for a particular mode, the corresponding modal values must be input as zero.

Option 1: Polynomial Input - Cards N1, O1 if $\begin{Bmatrix} \text{MTYPEW} \\ \text{MTYPET} \end{Bmatrix} = 1$. Repeated NMODES times.

Card N1 Format - (I5)

5

IDEG

IDEG = Degree of polynomial, ≤ 5. This controls the number of coefficients on card Set O1.

Card Set O1 Format - (7E10.0)

a_{oo} a_{10} a_{01} a_{20} a_{11} a_{02} a_{30}

a_{21} a_{12} a_{03} .....etc.

As many coefficients as are needed for the polynomial of degree IDEG:

$$f_j(X,Y) = a_{oo} + a_{10}X + a_{01}Y + a_{20}X^2 + a_{11}XY + a_{02}Y^2 + a_{30}X^3 + \ldots a_{o,IDEG}Y^{IDEG}$$

where point (X,Y) is in the X_W, Y_W (or X_T, Y_T) coordinate system, and

$f_j(X,Y)$ is the modal deflection.

Modal Input - Continued

Option 2: Interpolation - Cards N2, 02 if $\begin{Bmatrix} \text{MTYPEW} \\ \text{MTYPET} \end{Bmatrix} = 2$. Repeated NMODES times.

Card N2 Format - (2I5)

IDEG	NPTS

IDEG = Degree of polynomial to be least-squares fit to the surface, ≤ 5.

NPTS = Number of points at which deflections are known, ≤ 100.

Card Set 02 Locations and Deflections, NPTS/2 cards Format - (6E10.0)

XX_1	YY_1	ZZ_1	XX_2	YY_2	ZZ_2

XX_3	YY_3	ZZ_3	.....etc.

$\left.\begin{matrix} XX_i \\ YY_i \end{matrix}\right\}$ = The X and Y location of the ith point in the planform local coordinate system, X_w, Y_w (or X_T, Y_T)

ZZ_i = The deflection at point i, perpendicular to the surface.

Option 3: Deflections and Slopes at Box Centers - Card Sets N3 and 03 if $\begin{Bmatrix} \text{MTYPEW} \\ \text{MTYPET} \end{Bmatrix} = 3$. Repeated NMODES times.

Card Set N3 - Deflections array for the planform.

Format - (7E10.0)

DEFL(1)	DEFL(2)	...

DEFL(I) - Deflection values must be given for the control points of all the Mach boxes on the right half surface. These values start at the leading edge root box and proceed sequentially fore to aft on each chord, one chord at a time until the tip chord has been completed. Each chord starts on a new card.

Card Set 03 - Slopes array for the planform.

Format - (7E10.0)

SLOPE(1)	SLOPE(2)	...

SLOPE(I) - The slope array is given for the same points and in the same order as the deflections array.

Thickness Slopes

The optional thickness slope values follow all modal input. The integer variable NTSLOP on Card M determines the presence or omission of Card Sets P and Q. If NTSLOP = 0 these card sets are omitted, otherwise there will be NTSLOP sets of them. The thickness slope arrays have the same order of input as the Mode Shapes, Option 3. All the card sets for the wing (card sets P) come first, followed by all the card sets for the tail (card sets Q).

Card Set P - Thickness slopes at Box Centers for the tail.

Format - (7E10.0)

TSLFW(1)	TSLFW(2)	...

TSLFW = Array of $\frac{\delta Z_\tau}{\delta X}$ values of the wing at box centers, input in the same order as deflections on Card Set N3. See Figure 18, Section II, subsection 7.

Card Set Q - Thickness slopes at Box Centers for the tail.

Format - (7E10.0)

TSLFT(1)	TSLFT(2)

Termination Control Card:

After completion of all calculation defined by the previous data, the following card is read. If another cycle is indicated, the program will expect a new set of data, starting with Card A (Title). Otherwise the program will terminate as indicated:

Format (A6,4X,2I10)

	20	30
NAME	L1	L2

NAME File name of next overlay to be executed, if L1 > 0. Ignored if L1 ≤ 0.

L1 > 0, Primary level number of next overlay to be executed.

= 0, Call EXIT, returning to control cards.

- 1, Recycle to Card A

- 2, Return to calling overlay.

L2 = Secondary level overlay number (ignored if L1 < 0).

6. DIAGNOSTICS

The program prints warning and fatal diagnostics when error conditions are detected. A warning diagnostic is used to attract attention to a condition which is not fatal to the basic program execution, but which may be symptomatic of a data error. It will usually start with "*** WARNING---." After a warning diagnostic execution continues. A fatal diagnostic is followed by a call to the subroutine FLUSH, which may be written to interface with the error exit capability of the user's operating system. A fatal diagnostic starts with "***ERROR---."

a. General Disk Diagnostic

```
                                  GEOMETRY
                                  THICKNESS SLOPE
***ERROR - WHILE {READING}{ MODES                   }SCRATCH FILE nnnnn***
                 {WRITING}{ PLANAR AIC
                           SPATIAL AIC
                           VELOCITY POTENTIAL}

ERROR CODE nnnn WHILE {READING} THE FOLLOWING MATRIX
                      {WRITING}

MATRIX ID
PARAMETERS        n.nnnEnn     n.nnnEnn     n.nnnEnn     n.nnnEnn
   (INTEGER)         nn           nn           nn           nn
FILE SPACING = nnn                          MATRIX SPACING = nnn
MATRIX TYPE =                               DIMENSIONED (nn x nn)
```

The error code indicates the type of error encountered.

1	Matrix spacing is negative
2	File spacing is negative
4	Matrix dimensions are illegal
5	Row dimension of matrix exceeds the row dimension of BUFFER ARRAY.
1500+I	Encountered EOF after matrix I while skipping matrices.

b. Diagnostics from the Data Preprocessor

Four warning diagnostics may occur:

```
***WARNING - MACH NUMBER {LESS THAN 1.2   } IS BEING USED.
                         {GREATER THAN 3.0}
```

The Mach range for which reasonable answers can be expected is $1.2 \leq M \leq 3.0$.

WARNING - NO K1 VALUES GIVEN. PROGRAM WILL TERMINATE AFTER GEOMETRY SECTION

No values were specified on Card E, non fatal.

WARNING - ORDER FOR VELOCITY POTENTIAL SMOOTHING TOO LARGE. IT HAS BEEN REDUCED TO 10

Too large a value was read.

WARNING -- NO OUTPUT TAPE WAS REQUESTED FOR $\left\{\begin{matrix}\text{GENERALIZED FORCES}\\ \text{BOX LIFTS}\end{matrix}\right\}$

The parameters WTGNAF or WTBL were specified, but NOUTP = 0 on Card D.

One fatal diagnostic may occur:

MACH NUMBER $\left\{\begin{matrix}\text{LESS THAN 1.0}\\ \text{GREATER THAN 5.0}\end{matrix}\right\}$ CANNOT BE USED

This would normally be a data error. The theory used in the program is not valid for Mach numbers outside this range.

c. Diagnostics from the Geometry Section

WARNING - XEDGE AND XCENTR WERE BOTH SPECIFIED. XEDGE WILL BE IGNORED

The grid location may be specified at a box edge or a box center, Card G.

WARNING - SAMPLING OF UPWASHES CANNOT BE DONE IF A TAIL HAS BEEN DEFINED. ISMPLW = nn WILL BE IGNORED

Self explanatory.

WARNING - SAMPLE WASH SPECIFICATION SET nn IS IN ERROR. ONLY THE PRECEDING WILL BE CALCULATED

On card G, ICHORD(nn) $>$ NCHRDS, or ICHORD(nn) ≤ 0, or IBOXF(nn) $\leq$ IBOXL(nn), or IBOXF(nn) < 1, or IBOXL(nn) > 40.

ERROR - PARAMETER NCHRDS WAS NOT SPECIFIED. IT MUST ALWAYS BE GIVEN

Card G, required data.

ERROR - EITHER XEDGE OR XCENTR MUST BE SPECIFIED

Card G, required data.

ERROR - THE TAIL AND THE WING, OR THEIR DIAPHRAGMS, CROSS-ABOVE TO BELOW

If any portion of the tail is above the wing plane, all of it and its diaphragm must be.

ERROR - XCENTR NOT WITHIN 50 BOX LENGTHS (B1 = n.nnnnnnnnEnn) OF THE WING L.E. (n.nnnnnnnnEnn)

It is assumed that the user can place his box grid fairly accurately, and any value for XCENTR that is wildly off must be a data error. If XEDGE was specified, the program calculates XCENTR = XEDGE + B1/2.

ERROR - { PSIW, PSIT, NCHRDS, NWLE, NWTE, NTLE, NTTW } IS OUTSIDE ALLOWED RANGE

See Section III.3, Program Limits and Restrictions.

***ERROR - { WING L.E., WING T.E., TAIL L.E., TAIL T.E. } DEFINITION POINTS ERROR nn, A COMBINATION OF 1, NONMONOTONIC Y-VALUES
2, NONMONOTONIC X-VALUES
4, FIRST Y-VALUE NONZERO
8, TIP T.E. Y-VALUE DISAGREES WITH TIP L.E. VALUE

The error code nn may equal the sum of two or more conditions, if more than one error was detected. The input values being checked are from Cards I, J, K and L.

ERROR PROCESSING { WING, TAIL } GEOMETRY, { LEADING, TRAILING } EDGE

This general header may occur during calculation of box codes, and precedes one of the following 2 descriptors:

SECTION nn IS BEYOND THOSE DEFINED

Should only occur with a machine failure or coding error.

SECTION nn OF THE EDGE DOUBLES BACK TOWARD THE CENTER LINE

Nonmonotonically increasing Y-values have been encountered.

ERROR - SECTION nn OF THE TRAILING EDGE OF THE { WING, TAIL } CAUSES CHORD j TO GO TO ROW i, WHICH EXCEEDS THE LIMIT

Too many rows are being requested as a function of Mach number and number of chords.

ERROR - TOO MANY CHORDS FOR BOX CODE ARRAY

This occurs when additional tip diaphragm chords are being determined. The resulting box pattern exceeds the program limits, subsection 3.

The above three diagnostics are followed by the box code pattern currently being developed, to aid in determining the necessary data changes. The program then terminates.

d. Diagnostics from the Modes Section

WARNING - PREVIOUS MODE SHAPES HAVE BEEN SPECIFIED, BUT GEOMETRY HAS CHANGED.

The mode shapes requested were input as coefficients on the previous cycle. The planform has changed and the mode shapes must be calculated at the new box centers.

ERROR - PREVIOUS MODE SHAPES HAVE BEEN SPECIFIED, BUT THE GEOMETRY HAS CHANGED. PREVIOUS MODE SHAPES WERE AT BOX CENTERS.

The mode shapes requested were input at box centers on a previous cycle. The planform has changed and the mode shapes are no longer correct for the box centers.

e. Diagnostics from the AIC Section

ERROR - THE SIZE OF THE AIC ARRAY FOR THIS PLANFORM IS NNNN, THE MAXIMUM SIZE ALLOWED IS MMMM.

The planform for this run is such that it creates a requirement for an AIC array of size NNNN. The largest AIC array that can be used is MMMM. The planform should be checked to determine if size restrictions have been violated.

ERROR - THE ARGUMENT FOR A BESSEL FUNCTION IS OUT OF RANGE.

ARGUMENT = n.nnnnnn
LOWER LIMIT = n.nnnnnn
UPPER LIMIT = n.nnnnnn

Coding error or machine failure during integration of the AIC equations.

f. Diagnostics from the Normal Wash and Velocity Potential Section

WARNING - NO PLANFORM CONTROL POINT FOUND FOR SUBDIVIDED BOX DURING VELOCITY POTENTIAL CALCULATIONS
SUBDIVIDED BOX (i,j), CONTROL POINT (ii,jj)

A high-swept leading or trailing edge segment may yield subdivided on-planform boxes some distance from the nearest (chordwise) control point. Since the substantial derivative for any planform subdivided box is the chordwise extrapolated value of the nearest planform control point, no extrapolation beyond two box lengths will be attempted. The subdivided box in question will be ignored.

ERROR - THE TIP BOX PATTERN DOES NOT ALLOW TRAILING VELOCITY POTENTIALS TO BE COMPUTED

The tip chord must have two or more on-planform control points, or the inboard chords must have on-planform control points as indicated in Figure 24.

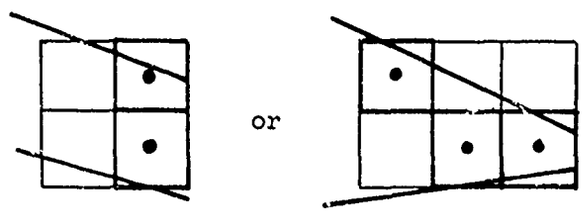

FIGURE 24 BOXES NEEDED FOR TRAILING EDGE VELOCITY POTENTIAL CALCULATIONS

ERROR - FAILURE IN STORING { SUBDIVIDED / CONTROL POINT } NORMAL-WASHES
SUBDIVIDED BOX (i,j), CONTROL POINT (ii,jj)

This is symptomatic of a machine failure or a coding error.

g. Diagnostics for the Velocity Potential Smoothing Section

ERROR - NO TIP TRAILING EDGE VELOCITY POTENTIAL CAN BE COMPUTED.

Same diagnostic as in Normal Wash and Velocity Potential section. The tip chord must have two or more on-planform control points, or the inboard chords must have on-planform control points as indicated in Figure 24.

h. Diagnostics for the Forces Section

POINTER ARRAY EXCEEDED FOR BOX (I,J)

This is symtomatic of a machine failure or a coding error.

7. OUTPUT DESCRIPTION

a. Printed Output

The first page of the printed output consists of a program title block, the user's run title, and a list of the parameters and options requested. This includes Mach number, symmetric or anti-symmetric, basic or subdivided analysis, AIC integration accuracy indicator, and all print options. All tape variables (input, output, and AIC tapes) are indicated, and the list of reduced frequencies is printed.

The geometry section prints all card data pertaining to geometric definitions. Any values not specified in the input data are printed starting with an asterisk (*), and the defaults are used. If printing of the box pattern(s) is requested (PRBOX), these follow. There is one pattern printed for the control points of each surface, and if subdivision is requested there is a subdivided box code pattern printed for each surface.

The modes section prints (optionally) the modal data. This may be polynomial coefficients (PRCOEF) and/or deflections and slopes at box centers (PRMODS).

The AIC arrays to be used are printed (optionally) as needed. For each reduced frequency, any spatial AIC arrays are printed first (PRSAIC), followed by the planar AIC array (PRPAIC), for which $W_{\bar{\nu}\bar{\mu}o}$ and $V_{\bar{\nu}\bar{\mu}o}$ are 0.0. AIC arrays needed for sampling are printed as spatial arrays.

The normal-washes may be printed under option PRNW. They are printed in the order: N_{RUW}, N_{RLW}, and if a tail is defined, N_{RUT}, N_{RLT}. If option PRVP is specified, the velocity potential differences are next printed, $\Delta\bar{\bar{\phi}}$ for the wing followed by $\Delta\bar{\bar{\phi}}$ for the tail. If sampling has been requested (ISMPLW>0), the upwash, $\frac{w}{U}$, the side wash $\frac{v}{U}$, and the longitudinal wash, $\frac{u}{U}$, may be printed for all boxes defined on each sampling chord requested, under options, PRUW, PRSW, and PRLW. All of the printing requested in this section is repeated for each mode shape.

If either of the velocity potential smoothing options was specified, a second set of $\Delta\bar{\bar{\phi}}$ arrays for all mode shapes will be printed by the smoothing routine under the control of print option PRVP.

The air forces section prints (optionally) box lifts $\bar{\bar{L}}_j^{n,m}$, pressure difference coefficients $\Delta C_{pj}^{n,m}$, section lifts $\bar{L}_j^m$, generalized air forces $\bar{\bar{Q}}_{ij}$, and generalized aerodynamic coefficients Q' and Q". The options controlling this are PRBL, PRDCP, PRSL, PRGNAF, and PRGNAC. If a velocity potential smoothing option was specified, two sets of box lifts, pressures, etc., are computed and printed. The first set corresponds to the smoothed $\Delta\bar{\bar{\phi}}$ arrays, and the second set corresponds to the unsmoothed $\Delta\bar{\bar{\phi}}$'s. This section terminates the printing for each reduced frequency. Printing for subsequent reduced frequencies starts again at the optional printing of AIC arrays.

b. Tape Output

Tape Output is optionally available for box lifts $\bar{\bar{L}}_j^{n,m}$ and generalized air forces $\bar{\bar{Q}}_{ij}$. The planar AIC arrays, $C_{\bar{\nu},\bar{\mu},o}$, and the spatial AIC arrays, $C_{\bar{\nu}\bar{\mu}\bar{\lambda}}$, $W_{\bar{\nu}\bar{\mu}\bar{\lambda}}$, and $V_{\bar{\nu}\bar{\mu}\bar{\lambda}}$, may be saved for reuse by the program during subsequent execution. Tape maps for all three are in Part II.

TABLE 1 ORDER OF ALL OPTIONAL OUTPUT

Option List			
Reduced Frequency List			
Geometry and Box Patterns			
Mode Shapes			
Spatial AICS			Repeated for Each Reduced Frequency
Planar AIC			
Subdivided AIC			
Wing Upper Normal Wash	Repeated for each mode shape		
Wing Lower Normal Wash			
Tail Upper Normal Wash			
Tail Lower Normal Wash			
Wing Velocity Potential Difference			
Tail Velocity Potential Difference			
Smoothed Wing Velocity Potential Differences	Repeated for each mode shape		
Smoothed Tail Velocity Potential Differences			
Wing Box Lifts	Repeated for each mode shape	Smoothed	
Tail Box Lifts			
Wing Pressure Differences			
Tail Pressure Differences			
Section Lifts			
Total Lift			
Sectional Generalized Forces (c^2C_m)			
Generalized Air Forces			
Generalized Aerodynamic Coefficients			
Wing Box Lifts	Repeated for each mode shape	Unsmoothed	
Tail Box Lifts			
Wing Pressure Differences			
Tail Pressure Differences			
Section Lifts			
Total Lift			
Sectional Generalized Forces (c^2C_m)			
Generalized Air Forces			
Generalized Aerodynamic Coefficients			

SECTION IV

APPLICATIONS

1. INTRODUCTION

The computer program described in the previous sections has been developed to evaluate the unsteady airforces existing on wing-tail lifting surfaces in supersonic flow. This portion of the report describes some of the operational aspects of the program and presents an application of the numerical procedures used in a flutter analysis of wing-tail models previously tested at Cornell Aeronautical Laboratory.

Pressure distributions, perturbation velocities, and generalized forces are presented for various planform configurations identified as AGARD configurations.

2. PROGRAM LIMITATIONS

Configurations that fit the program analysis capabilities are shown in figure 25, figure 26, and figure 27. The planforms must be defined in terms of straight line segments and may take on various shapes as indicated in figure 25. The wing and tail may have dihedral, vertical separation and horizontal separations. Aerodynamic interaction of the tail affecting the wing may be evaluated only for the coplanar case. The tail may physically overlap the wing for the spatial cases however the tail aerodynamic "Mach cone" must not intersect the wing as shown in figures 28 and 29. A complete set of other program limitations are presented in section III, Computer Program Usage.

3. PRELIMINARY COMMENTS ON PROGRAM CHARACTERISTICS

In applying the numerical technique known as the "Mach Box" method to the solution of supersonic flow problems one is bound by the restrictions of the method and must accept the errors incurred by the built-in approximations. Probably the most critical approximation made within the present method is the assumption that the normal washes are of constant value over the individual box areas. This approximation may apply without too much error within regions on the lifting surface where small normal wash variations exist and also provided that the box sizes are relatively small. However, relatively large errors may result in predicting the normal wash distribution over the "off-wing" diaphragm region where large variations in the normal wash exist that are inversely proportional to the square root of the distance from the planform edge.

In order to allow a variation in the basic box size to reduce the errors in the downwash calculation, the program has been devised such that two basic sizes of boxes may be used within the solution process. The basic program uses a uniform size box over the entire wing and "off-wing" diaphragm regions. The application of the optional data item SUBDV = .TRUE. allows a three to one subdivision of the basic box lengths over an "effective area" of the wing and "off-wing" diaphragm region. Figure 31 shows the distribution of uniform size boxes over the wing and the "off-wing" diaphragm used in the basic analysis case. Figure 32 displays the "effective area" concept used in the subdivision case. The streamwise width of the "effective-area" may be maintained at a constant value or may be variable upon the users request. The "effective area" slides from row-to-row in a streamwise direction and is used to obtain a more accurate definition of the velocity potentials at the box centers of the basic case.

It should be noted that once the box pattern has been selected to approximate the original planform shape then the original shape no longer may be used in the analysis. There is one modification of this condition in that in using the subdivision option the subdivided boxes are used to refine the velocity potentials at the box center of the basic box pattern and do not enter into the box load or generalized force calculations. However, the leading edge and trailing edge box loads may include the effect of the additional subdivided boxes located at the leading and trailing edges provided that the program option PLYWOOD is not used. The option, PLYWOOD = .TRUE., forces all boxes to have the same area as given in the basic analysis case by setting the area ratio factor $\alpha^{n,m} = 1.0$ for all box areas. If the program option PLYWOOD is not used, then the program will calculate the $\alpha^{n,m}$ values used to modify the box areas contained within the leading and trailing edge regions for use within the loads and generalized force calculations. Figure 33 displays the method used to evaluate the $\alpha^{n,m}$ factors used in the subdivision case. It should be noted that the option PLYWOOD = .TRUE. ($\alpha^{n,m} = 1.0$) is to be applied for all cases except when subdivision is being used, otherwise the original mathematical definition of the analysis planform will be violated and will produce inconsistent results.

The purpose of subdividing the box sizes into smaller boxes is to smooth out the streamwise variations in the velocity potentials since it is established that the chordwise loadings are a function of the velocity potentials and the first derivatives of the velocity potentials. Small variations in the velocity potentials will cause large variations in the chordwise loadings and may appear to be unrealistic from a physical standpoint. The variations in the chordwise definition of the velocity potentials are caused by the irregularities of the planform defined by the Mach box pattern and also is affected by the amount of diaphragm existing between the foremost Mach line and the leading edge of the planform. An example of how well the chordwise loading irregularities are reduced through use of the subdivision

process is shown in figure 34 (reproduced from reference 10). The reduction in the chordwise load variation is due to reducing the irregularities of the velocity potentials shown in figure 35 (reproduced from reference 10). It can be shown that subdividing the boxes even further will produce a smooth converged velocity potential definition providing smooth chordwise loadings that more readily simulate the physical flows. However, further subdivision would result in an exorbitant amount of computer time required to achieve the smooth loading results. Consequently velocity potential smoothing techniques were investigated in the hope that a single smoothing process could be developed and applied to the basic box pattern velocity potentials that would produce results similar to the highly subdivided case.

One of the smoothing techniques investigated and available within the program is the least-squares-error surface fitting function used in the modal interpolation portion of the program. The program data option SMOOTH = .TRUE. will apply this surface fitting technique to the velocity potentials. An accuracy evaluation was made on this smoothing technique and it was found that it produced reasonable results for those planforms that did not have many irregularities in the box pattern that approximates the planform leading and trailing edges as well as meeting the condition of having a small angle between the foremost Mach line and the planform leading edge. However, questionable results were achieved whenever the above conditions were not met. It was also determined that a least-squares-error smoothing process applied directly to the velocity potentials produced unreliable loading results at the ends of the intervals where there may be appreciable variations in the original velocity potential data. Although the least-squares-error does fit the potentials reasonably well over the interval, the first derivative of the resulting fitting function (which defines the major portion of the box loadings) is not well defined at the ends of the intervals. Consequently, it is advisable to exercise caution when using this smoothing option. An alternate smoothing option is available to the user by specifying CRDFIT = .TRUE. within the input data. This smoothing technique was devised to eliminate the need of taking a derivative of a least-squares-error polynomial and is obtained by an integration process that provides smoothing on the average over the interval.

This process, as shown in figure 36, smooths the velocity potentials of individual chordwise strips by (1) formulating a finite difference derivative distribution from the basic velocity potential data, (2) performs a least-squares-error fit of the derivatives, (3) integrates the least-squares-error polynomial to obtain the smoothed chordwise velocity potential distribution.

It should be noted that the only basis for applying a smoothing operation to the velocity potentials lies in the fact that the velocity potentials do indeed become very smooth as the basic box size is increasingly subdivided into many small sub-areas.

Comparisons of chordwise loadings obtained using smoothed and non-smoothed velocity potentials are presented in the flutter model correlation studies and these comparisons indicate that reasonable load distributions may be obtained using the program option CRDFIT = .TRUE.

4. PRELIMINARY CHECKOUT OF THE PROGRAM

A preliminary checkout of the program has been accomplished to evaluate the validity of the program output. Since there are no unsteady pressure data available for the supersonic cases then only a qualitative evaluation can be made.

a. Interaction Loadings

A comparison of how the chordwise loadings on mutual interacting lifting surfaces are affected by horizontal separation spacings is presented by White and Landahl in reference 14. Figure 37 reproduced from reference 14 displays the variation on chordwise loadings for various separation spacings in subsonic flow. For a zero gap spacing the loadings produced at the wing-tail junction exhibits the typical logarithmic singularity identified for a discontinuous downwash distribution encountered on a wing-control surface configuration in subsonic flow. As separation begins, the loadings on the wing near the wing trailing edge change from a singularity characteristic to a loading that becomes equal to zero. As the gap spacing becomes large the loadings at the wing trailing edge fall off as the square root of the distance from the trailing edge, meeting the Kutta condition. However, the loadings near the leading edge of the tail change from a logarithmic character to that of having an inverse square root singularity that is more highly loaded for the large gap than it is for the zero gap condition. Although the analysis of reference 14 is applicable to subsonic flows, the trends should exhibit the same behavior in three dimensional supersonic flow provided that the span station being examined lies well within the subsonic communication region where the lower and upper surfaces may mutually affect each other.

Numerical results were obtained to evaluate the effect of gap spacing in supersonic flow for the 45° swept wing-tail planform used in the Cornell flutter model tests shown in figure 38. The gap spacing between the surfaces was obtained for integer numbers of boxes within wing wake diaphram. The fourth coupled mode shape of the flutter analysis which contains a large amount of wing-tail angle of attack in a streamwise direction was selected for the data comparison of White and Landahl of reference 14.

Figure 39 shows the chordwise loadings obtained for various gap sizes on the span station $\eta = 0.85$ at $M = 1.238$. The analysis

chord lies well within the subsonic communication region and the results obtained exhibit the same trends as predicted by reference 14. The loading in the trailing edge of the wing change from a singular characteristic to one of tending to zero. Also the loadings on the tail near the tail leading edge increase in magnitude with an increase in gap spacing as is predicted by reference 14.

Figure 40 is a plot of the chordwise loadings for the same mode shape but at the inboard station $\eta = 0.35$. The loadings on the wing near the wing trailing edge do not change appreciably with an increase in gap spacing. This is to be expected since there is only a very small region where subsonic communication can exist between the lower and upper wing surfaces. However the tail leading edge loads do increase with gap spacing as more of the wing-wake region becomes available for upper and lower surface communication.

b. Velocity Potential Smoothing

The velocity potential smoothing option CRDFIT = .TRUE. was applied to various configurations to evaluate its accuracy and behavior characteristics. For velocity potential distributions that were initially quite smooth the smoothing operation provided a slight increase in smoothness and consequently provided a chordwise loadings that were more smooth on the average than was obtained without the smoothing process. No large variations in box loads were observed at the ends of the intervals as had been the case for some of the configurations when the original smoothing option SMOOTH = .TRUE. was used. The largest deviations were observed to occur for those chordwise strips where large gradients exist in the original velocity potential data.

Figure 41 shows the results of applying smoothing to the velocity potentials on a highly loaded section of the 45° wing-tail analysis configuration of the Cornell flutter model test. The velocity potentials and resulting loadings are shown for a chord that is located at the $\eta = 0.85$ span station. The fourth coupled mode shape of the Cornell modal data is used in the analysis. The fourth mode contains a large amount of wing and tail angle of attack that generates the large variation in chordwise distribution of the velocity potentials.

Also, the second mode shape (primarily a differential bending mode between wing and tail) was used to evaluate the smoothing process at the same span station and the results for this condition are shown in figure 42. It is apparent that no large deviations result (even for a highly load chord) in applying the smoothing option and also provides more realistic load distribution while retaining the original overall loading characteristics.

c. Normalwash Examination

Normalwash distributions in the wake of the wing were examined for smoothness and reasonableness as a preliminary exercise prior to performing a flutter analysis of the wing-tail configurations for various horizontal separation spacings. The wing of the 45° sweep Cornell Configuration 15 was used in the evaluation. The third and fourth coupled mode shapes of the Cornell modes data were used and the deflection shapes are shown in figure 43 and figure 44. The normalwash distributions within the wing wake are shown in figure 45 and figure 46.

There are variations within the wing-wake normalwash distributions as would be expected, however there are no large excursions and the trends are reasonably consistent with the mode shapes causing these distributions.

Vertical wash distributions were obtained for various vertical separation values and are displayed in figure 47. Again there are no large excursions in the distributions and the expected trends of having a diminishing normalwash with an increase in vertical separation is well defined.

5. FLUTTER MODEL CORRELATION

Flutter model test data used in this correlation study were obtained from reference 2. The tests were conducted in the Cornell Aeronautical Laboratory 8' x 8' variable density Transonic Wind Tunnel. The test Mach number range was $0.40 \leq M \leq 1.24$. Of the many test points obtained there are only five points that lie well enough within the supersonic range to allow a theoretical analysis to be performed. The models were constructed such that the planform shapes were identical for both wing and tail configurations. The supersonic tests were conducted having both models contained in the same plane with a very small horizontal clearance gap between the models. The models were elastically coupled by means of an inter-connecting torsion spring simulating a fuselage torsion degree of freedom.

Test flutter modes consisted primarily of the bending modes of the wing-tail surfaces coupled with fuselage torsion degree of freedom. The construction details of the models are well discussed within reference 2 and will not be repeated here. The overall dimensions of the 45° sweep configuration are presented in figure 48 and figure 49 displays the geometry of the 60° sweep configuration used in the flutter model test.

a. Vibration Analysis and Flutter Solution

The vibration analysis, based on the elastic axis and lumped mass idealization, was carried out for each configuration using the

following data supplied by AFFDL:

1) the weight, static unbalance, and moment of inertia of the stations along the model elastic axis, 40 percent chord. (Tables 3,4 and 5)

2) the first two uncoupled cantilever bending and the first uncoupled cantilever torsion mode of the wing and tail (Tables 6 and 7)

3) the uncoupled rigid body roll mode and the uncoupled fuselage torsion mode (Table 8)

4) the generalized coordinate transformation matrix between the eight uncoupled modes and the five coupled modes,(Tables 9,10 & 11)

The five coupled modes used for flutter analysis were calculated by taking matrix product of the uncoupled modes and the generalized coordinate transformation. These coupled mode shapes are expressed as bending and torsion displacements at the model elastic axis stations and as the angular displacement about the roll axis at the fuselage wing and tail stations. The generalized mass matrix associated with these coupled modes are calculated as described in reference 15. As the program input for calculating generalized forces, the coupled mode shapes were evaluated at the arbitrary points along the chords normal to the model elastic axis.

The generalized forces matrices were calculated each time for a Mach number and a few reduced frequencies. A chain of cubic interpolation was then used to find the elements of the generalized forces matrices at many intermediate reduced frequencies. This substantially reduces the cost of performing a flutter analysis without marked loss in accuracy, since the generalized forces vary smoothly with reduced frequencies. The interpolation routine also scales the generalized forces matrix by $-\frac{1}{k_1^2}$.

The flutter speeds and frequencies were obtained from the following complex eigenvalue equation, using the conventional V-g solution technique with complex QR algorithm:

$$\left([M] - \frac{1}{\Gamma}[C] \right)\{\bar{q}\} = \lambda [K]\{\bar{q}\}$$

$$g = \frac{\lambda_I}{\lambda_R}$$

$$\omega = \frac{1}{\sqrt{\lambda_R}} \quad , \quad V = \frac{b_1 \omega}{k_1}$$

where

[M] is the generalized mass matrix

[K] is the generalized stiffness matrix; the elements are given by

$$K_{ii} = \omega_i^2 M_{ii}$$

ω_i is the circular frequency of the ith coupled mode

[c] is the interpolated generalized forces matrix

$$[c] = -\frac{1}{k_1^2}[\bar{Q}], \quad k_1 = \frac{b_1 \omega}{V}$$

$\frac{1}{\Gamma}$ is the airforce coefficient equal to $\frac{\rho b_1^3}{2\beta}$

$\left.\begin{matrix}\lambda_R \\ \lambda_I\end{matrix}\right\}$ is the $\left\{\begin{matrix}\text{real} \\ \text{imaginary}\end{matrix}\right.$ part of the complex eigenvalue

g is the artificially added structural damping

ω is the flutter circular frequencies when g = 0

V is the flutter speed when g = 0

b. Node Line Correlation

The procedures described in the previous section to obtain the coupled mode surface deflections were applied and the resulting node line comparisons are given in figure 50, figure 51, and figure 52 for the three test-analysis correlation configurations.

Only the node lines of coupled modes number three (3) and four (4) are displayed for comparison purposes. Although the data of the test report (reference 2) showed good correlation between the theoretical and experimental natural mode frequencies, the node line correlation displayed large discrepancies in the location of the modal node lines. The general shape of the theoretical node lines obtained within reference 2 compare favorably with the experimental node lines however they are displaced aft toward the trailing edge of both the wing and tail planforms. Also, the theoretical node lines obtained at Boeing using the Cornell data are displaced even further aft of the Cornell theoretical node line positions even though the same modal data were used in the calculations. It should be noted that the largest discrepancies

occur on the tail for each of the configurations evaluated. It was determined, through a cross plotting process, that the Boeing node line definitions could be made to coincide with experimental node lines simply by adding a constant value to each of the mode shapes. The values to be added to the wing modes have different values than those to be added to the tail mode shapes. As a consequence of the mismatch in the mode shape definition the flutter correlation study was accomplished in two parts. The initial evaluation of flutter speeds was accomplished using the original theoretical mode shapes as obtained from the Cornell data, and the second correlation study was accomplished using modified mode shapes that provided a match of the test node line locations.

c. Flutter Results Using Original Modal Data

The results of the flutter analysis using the original modal values are presented in Table 12 for configuration 15 and Table 13 and 1 presents the results for configurations 22 and 23. Although no test data are available to correlate the effects of horizontal and vertical separations in supersonic flow theoretical investigations were performed to determine the flutter trends for these spacings. The separation studies were conducted only on the 45° sweep planform of configuration 15.

d. Effects of Horizontal Spacing

The effect of horizontal separation on flutter speed is shown in figure 53 indicating that only a very small reduction in flutter velocity is obtained for relatively large values of horizontal separation. No test data are available for the supersonic separation studies, however the subsonic test results of configurations 5 and 10 supports this trend by indicating that the flutter speeds are only slightly affected by horizontal separation. It should be noted that the lowest flutter speed shown within the horizontal separation studies was obtained for the case of $\frac{x}{b} = 0$.

This condition is one that simulates the existence of an aerodynamic seal or a no flow through boundary between the wing and tail surfaces. Figure 39 shows that although the loadings on the tail leading edge are reduced by this no flow thru condition, there is a large overturning moment developed on the wing causing the wing to respond more readily than it does for the open gap condition.

e. Effects of Vertical Separation

The effects of vertical separation on flutter speed and frequency ratio are shown in figure 54 for a constant Mach number, tunnel density and fuselage torsional frequency. It should be noted that the flutter mode shape is changing with an increase in vertical separation as indicated by the increase in the flutter frequency

ratio and the analysis configuration is taking on the characteristics of single surface bending-torsion flutter mode.

f. Thickness Effects

The inclusion of airfoil thickness effects within the flutter studies resulted in only a very small reduction in flutter speeds for all three study configurations as indicated by analysis no. 9, 14, and 19. The chordwise loadings on both the wing and tail surfaces increased in the region of the leading edges and decreased in value over the aft portion of the surfaces. No large changes in flutter frequency or mode shape resulted from including thickness effects within the analysis. This was anticipated since the streamwise thickness ratios are quite small and cannot appreciably change the loadings or center of pressure locations.

g. Mach Number Effects

Non-dimensional values of flutter frequency and flutter velocity are presented as a function of Mach number in figure 55, figure 56 and figure 57 for the three study configurations. The analytical results obtained for M=1.35 of configuration 15 and for M=1.414 for configurations 22 and 23 were obtained by using extrapolated density data and may be somewhat in error. The overall trends as shown in Figures 84 and 85 indicate that the flutter speed ratios do not change by any large amount over the Mach number range investigated. The resulting flutter modes consisted of a strong coupling between the wing-tail bending modes with the body torsion mode for most of the analysis cases with the exception of configuration 23 for M = 1.232. Configuration 23 at M = 1.232 had a flutter mode that contained an unusual amount of the fourth coupled mode. Various parameters such as stiffnesses and densities were changed to try to identify what was the cause for this behavior however, the flutter mode remained essentially the same throughout the parameter variation study.

The error between theoretical and experimental flutter frequencies is quite small for all of the analysis cases with the exception of configuration 23 at M = 1.232. However, the errors between theoretical and experimental flutter velocities are larger than desired and this error could not be greatly reduced with normal changes in various parameters. The errors in flutter velocities are of the same magnitude for the subsonic correlation studies of reference 15, at least for configurations 16 and 22, as reported by Albano, Perkinson and Rodden.

Results of the subsonic studies are shown in figure 58 and figure 59 that have been reproduced from reference 15. Since rather large errors are incurred for both the subsonic and supersonic studies using the original modal data, an attempt was made to modify the mode

shapes such that the theoretical node lines would coincide with the experimental node lines and thus evaluate the sensitivity of mode shape variations on flutter velocity.

h. Effect of Mode Shape Variations

Modifications to the mode shapes were accomplished by allowing a rigid body rotation about an axis parallel to the node lines. The rotation axis was located at the attachment fittings at wing and tail root sections. The directions of the axes were essentially perpendicular to the air stream and could be thought of as allowing a pitching flexibility of the support system to take place. The amount of rotation allowed in each of the modes was just enough to shift the theoretical node line position to coincide with the experimental node line. A typical value of rigid body rotation that was applied within the mode modification amounted to a rotation value of 0.0024 radians which would change the deflection at the theoretical node line position by 0.05 inches. It should be noted that all mode shapes were normalized to a maximum value of 1.0. Consequently the mode shape changes that were applied amounted to values that were approximately equal to 5% of the maximum deflection. A new set of coupled modes, generalized masses, generalized stiffness, and airforces were produced for use within the flutter solution program. Table 15 presents the results obtained for configuration 15, configuration 22 and configuration 23. Use of the modified mode shapes produce results that are closer to the experimental results and may indicate that the original modal data and encompassing assumptions may not be completely correct. There are no means available, within the modal data, to verify how much the support system flexibility could have contributed to the coupled modes, however, the analysis indicates that the prediction of flutter velocities are highly influenced by small changes in the mode shape distribution.

i. Discussion of Results

The theoretical trends obtained in the flutter analysis are similar to those obtained during the experimental flutter tests. Horizontal separation has very little effect on flutter speeds for the coplanar cases and there is an increase in flutter speed with vertical separation. The flutter modes were found to be composed of wing bending coupled with fuselage torsion for all of the analysis cases with the exception of configuration 23 at M = 1.232 where the flutter mode contained a high frequency torsion mode. Although the theoretical-experimental trends are similar, it appears that the theory is conservative and may be due to unknown effects such as shocks attached on the wing and tail leading-trailing edges, or may be due to flow blockage over the tail due to the wings presence.

There are other possible sources of error that may contribute to the conservatism, one of which is due to the numerical solution technique itself. Probably the most critical approximation made within the "Mach Box" (or any other Box pattern program) is the assumption that normal washes are of constant value over the invididual box areas. This approximation may apply very well over the lifting surface planform where the normal wash distributions are relatively small and are only functions of the modal deflections. However, relatively large errors may result in predicting the normal wash distributions over the "off-wing" diaphram region near the side edges of the planform where the normal wash varies in proportion to the square root of the distance from the planform edge.

The resulting predicted normal washes will invariably be larger than exist in reality and will result in predicting velocity potentials (or loadings) over the lifting surface that are larger than those existing in the true flow field.

There are possible sources of error in the basic mathematical model of the coupled modes used in the flutter analysis that may contribute to the conservative velocities. Five coupled mode shapes were obtained for flutter analysis using only eight primative "uncoupled" modes as a basic set of modes to establish the final coupled mode definition.

The eight primitive modes consisted of two cantilevered "uncoupled" bending modes and one "uncoupled" torsion for each surface plus one rigid body roll mode and one fuselage differential torsion mode. No allowance was made for pitch flexibility of the support system. The cantilever analysis considered each lifting surface as a straight beam of variable stiffness and inertia distribution that were allowed to deform in bending and torsion. This "elastic axis" assumption requires all sections perpendicular to the elastic axis to deform as a rigid body which may be questionable when applied to the lifting surfaces used in the present analysis that do not have a well defined structural axis nor have rigid ribs to enforce the rigid deformation requirements of the cantilever analysis.

There is no method available to determine if any errors (or even less, the modal distribution of errors) exist within the original modal data, however, the flutter analysis does indicate that the accuracy of predicting flutter velocities is quite sensitive to small changes in mode shapes of highly swept low aspect ratio configurations.

TABLE 2 MEASURED CANTILEVER COUPLED-MODE FREQUENCIES

CONFIGURATION NUMBER	MODEL	1st COUPLED MODE (CPS)	2nd COUPLED MODE (CPS)	3rd COUPLED MODE (CPS)	$\frac{\omega_1}{\omega_2}$	$\frac{\omega_3}{\omega_2}$
15	45P3 (WING)	17.6	67.3	87.5	.262	1.300
	45P6 (TAIL)	21.7	83.5	106.8	.260	1.279
22 & 23	60P4 (WING)	16.1	60.7	94.7	.265	1.560
	60P8 (TAIL)	19.0	69.4	116.0	.274	1.671

TABLE 3 MASS PROPERTIES OF CONFIGURATION 15

(45° SWEPT MODEL)

ELASTIC AXIS STATION NO.	η =LENGTH INCHES FROM ROLL AXIS	WEIGHT (LBS)		STATIC UNBALANCE (LB-IN)		MOMENT OF INERTIA (LB-IN^2)	
		WING (45P3)	TAIL (45P6)	WING (45P3)	TAIL (45P6)	WING (45P3)	TAIL (45P6)
1*	0.	.01	.01	0.	0.	0.	0.
2*	2.83	.01	.01	0.	0.	0.	0.
3	5.09	4.31	4.33	-4.11	-4.18	12.84	13.06
4	7.26	3.370	3.39	- .164	- .158	9.86	9.06
5	12.25	1.003	.994	.68	.799	13.98	14.79
6	17.44	.436	.498	.560	.680	9.79	11.68
7	21.72	.304	.325	.335	.367	6.14	6.66
8	25.77	.304	.325	.335	.367	6.14	6.66
9	29.82	.304	.325	.335	.367	6.14	6.66
10	33.87	.304	.325	.335	.367	6.14	6.66
11	38.19	.313	.334	.601	.655	5.85	6.37
12	42.69	.186	.201	.782	.847	4.84	5.27
13	47.56	.110	.118	.718	.785	5.36	5.89

* STATIONS ADDED IN THIS STUDY

TABLE 4 MASS PROPERTIES OF CONFIGURATION 22 & 23

(60° SWEPT MODEL)

ELASTIC AXIS STATION NO.	η = LENGTH INCHES FROM ROLL AXIS	WEIGHT (LBS)		STATIC UNBALANCE (LB-IN)		MOMENT OF INERTIA (LB-IN^2)	
		WING (60P4)	TAIL (60P8)	WING (60P4)	TAIL (60P8)	WING (60P4)	TAIL (60P8)
1*	0.	.01	.01	0.	0.	0.	0.
2	5.0	1.43	1.5	-2.35	-2.70	18.3	20.0
3	8.34	2.72	2.77	-2.43	-2.67	8.74	10.06
4	13.45	2.32	2.26	0.254	.211	8.21	8.82
5	18.55	.871	.916	.616	.686	11.73	13.55
6	23.75	.384	.421	.538	.597	8.19	10.00
7	28.98	.393	.426	.396	.467	7.35	8.29
8	34.93	.393	.426	.396	.467	7.35	8.29
9	40.45	.312	.336	.481	.558	5.55	6.28
10	45.5	.241	.261	.693	.784	4.50	5.14
11	50.5	.170	.185	.725	.820	4.27	4.93
12	54.9	.0746	.0843	.447	.513	2.94	3.43
13	59.74	.0559	.0665	.426	.509	3.41	4.10

* ADDED STATION IN THIS STUDY

TABLE 5 ROLL INERTIA OF FUSELAGE OF CORNELL WING-HORIZONTAL TAIL FLUTTER MODELS

CONFIGURATION NUMBER	ROLL INERTIA OF FUSELAGE AT WING LOCATION (lb-in^2)	ROLL INERTIA OF FUSELAGE AT TAIL LOCATION (lb-in^2)
15	1180	985
22, 23	845	700

TABLE 8 UNCOUPLED RIGID BODY ROLL AND FUSELAGE TORSION MODE SHAPES OF THE CORNELL WING-HORIZONTAL TAIL FLUTTER MODELS

CONFIGURATION NUMBER	RIGID BODY ROLL			FUSELAGE TORSION		
	WING	TAIL	FREQ. (CPS)	WING	TAIL	FREQ. (CPS)
15	1.0	1.0	4.0	-.972	1.0	33.0
22	1.0	1.0	4.7	-.954	1.0	24.7
23	1.0	1.0	4.7	-.954	1.0	30.7

TABLE 7 UNCOUPLED CANTILEVER MODE SHAPES OF CONFIGURATIONS 22 and 23 (60° SWEPT MODELS)

ELASTIC AXIS STATION NUMBER	η-LENGTH (INCHES FROM ROLL AXIS)	WING AND TAIL					
		1st CANTILEVER BENDING		2nd CANTILEVER BENDING		1st CANTILEVER TORSION	
		FREQ.(Hz)		FREQ.(Hz)		FREQ.(Hz)	
		WING	TAIL	WING	TAIL	WING	TAIL
		17.5	20.4	70.0	80.4	58.7	71.8
1	0.	0.		0.		0.	
2	5.0	0.		0.		0.	
3	8.34	0.001		-0.006		0.002	
4	13.45	0.004		-0.024		0.004	
5	18.55	0.011		-0.055		0.007	
6	23.75	0.024		-0.108		0.022	
7	28.98	0.069		-0.209		0.103	
8	34.93	0.178		-0.325		0.215	
9	40.45	0.323		-0.330		0.304	
10	45.49	0.480		-0.207		0.383	
11	50.5	0.650		0.054		0.484	
12	54.9	0.811		0.420		0.630	
13	59.74	1.00		1.00		1.00	

TABLE 8 UNCOUPLED RIGID BODY ROLL AND FUSELAGE TORSION MODE SHAPES OF THE CORNELL WING-HORIZONTAL TAIL FLUTTER MODELS

CONFIGURATION NUMBER	RIGID BODY ROLL			FUSELAGE TORSION		
	WING	TAIL	FREQ. (CPS)	WING	TAIL	FREQ. (CPS)
15	1.0	1.0	4.0	-.972	1.0	33.0
22	1.0	1.0	4.7	-.954	1.0	24.7
23	1.0	1.0	4.7	-.954	1.0	30.7

TABLE 9 GENERALIZED COORDINATE TRANSFORMATION MATRIX FOR CONFIGURATION 15

GENERALIZED COORDINATES									
COUPLED MODES	RIGID BODY ROLL	FUSELAGE TORSION	Wing Cantilever			Tail Cantilever			FREQ. CPS
			FIRST* BENDING	SECOND* BENDING	FIRST TORSION	FIRST* BENDING	SECOND BENDING	FIRST TORSION	
1	6.39	0	1.598	-0.04	0.0800	1.0	-0.023	0.043	3.9
2	0.0571	0.0571	-2.671	0.002	-0.1962	1.0	-0.009	0.0562	17.6
3	-0.0685	0.0186	0.810	0.025	0.0852	1.0	0.007	0.0721	25.3
4	-0.0165	-0.1407	-0.637	-0.136	-0.2034	1.0	0.085	0.1511	42.8
5	0.765	-1.045	-29.86	15.56	44.92	1.0	0.886	1.219	72.2

* Denotes the Coordinate has been Scaled to $\frac{1}{b_r}$, b_r = 8.5 in.

TABLE 10 GENERALIZED COORDINATE TRANSFORMATION MATRIX FOR CONFIGURATION 22

GENERALIZED COORDINATES									
COUPLED MODES	RIGID BODY ROLL	FUSELAGE TORSION	Wing Cantilever			Tail Cantilever			FREQ. CPS
			FIRST* BENDING	SECOND* BENDING	FIRST TORSION	FIRST* BENDING	SECOND* BENDING	FIRST TORSION	
1	3.731	0	1.446	-0.0605	0.106	1.0	-0.0424	0.0676	4.7
2	0.0348	0.0718	-2.277	0.00308	-0.24	1.0	-0.0143	0.0874	16.3
3	-0.0564	0.0225	0.901	0.0339	0.123	1.0	0.0115	0.106	21.6
4	-0.0128	-0.122	-0.634	-0.108	-0.156	1.0	0.0921	0.164	31.4
5	-4.238	4.705	128.401	-171.801	-159.55	1.0	-8.234	-6.33	67.2

* Denotes the Coordinate Has Been Scaled to $\frac{1}{b_r}$, $b_r = 8.0$ in.

TABLE 11 GENERALIZED COORDINATE TRANSFORMATION MATRIX FOR CONFIGURATION 23

GENERALIZED COORDINATES									
COUPLED MODES	RIGID BODY ROLL	FUSELAGE TORSION	Wing Cantilever			Tail Cantilever			FREQ. CPS.
			FIRST* BENDING	SECOND* BENDING	FIRST TORSION	FIRST* BENDING	SECOND* BENDING	FIRST TORSION	
1	3.7306	0.0	1.4456	-0.0606	0.1062	1.0	-0.0424	0.0676	4.7
2	0.0422	0.0432	-2.5358	-0.0051	-0.2741	1.0	-0.0121	0.0890	16.9
3	-0.0507	0.0126	0.7009	0.0280	0.0971	1.0	0.013	0.1067	21.9
4	-0.0110	-0.1544	-0.7032	-0.2223	-0.261	1.0	0.1682	0.2191	37.0
5	-2.1008	2.4649	63.0240	-82.4125	-76.6715	1.0	-6.9564	-5.3417	67.6

* Denotes the Coordinate Has Been Scaled to $\frac{1}{b_r}$, $b_r = 8.0$ in.

TABLE 12 ANALYTICAL FLUTTER RESULTS ON CONFIGURATION 15
(ORIGINAL MODES, 45° SWEPT MODELS, $\omega_\theta/\omega_h = 1.765$)

ANALYSIS NUMBER	M	$\frac{x}{b_s}$	$\frac{z}{b_s}$	μ	ρ slug/ft^3 ($\times 10^4$)	THEORETICAL RESULTS					TEST RESULTS			
						THICKNESS CORRECTION	V_f ft/sec	η_f cps	$\frac{V_f}{b_s\omega_\theta\sqrt{\mu}}$	$\frac{\omega}{\omega_\theta}$	V_f ft/sec	η_f cps	$\frac{V_f}{b_s\omega_\theta\sqrt{\mu}}$	$\frac{\omega}{\omega_\theta}$
	1.121	.021	0.0	44.5	4.0						1150.	22.7	.830	.688
1	1.121	.166	0.0			NO	*858.2 873.3	24.6 24.08	.6190 .6043	.7455 .7297				
	1.238	.021	0.0	50.9	3.5						1254.	26.	.846	.788
2		0.0	0.0			NO	976. 974.9	25.70 25.49	.6592 .6584	.7789 .7724				
3		.167	0.0			NO	1006.8 1001.1	26.5 26.27	.6799 .6760	.8035 .7959				
4		.505	0.0			NO	1001.2 1001.9	26.08 25.91	.6762 .6766	.7903 .7851				
5		1.0	0.0			NO	991. 990.	25.58 25.37	.6693 .6686	.7752 .7688				
4	1.238	.505	0.0	50.9	3.5	NO	1001.2 1001.9	26.08 25.91	.6762 .6766	.7903 .7851				
6		.505	0.0835			NO	1061.4 1057.5	26.5 26.34	.7168 .7142	.8042 .7982				
7		.505	.167			NO	1128.6 1123.2	27.5 27.23	.7623 .7585	.8325 .8252				
8		.505	.505			NO	1430.8 1436.7	35.09 34.69	.9662 .9702	1.0635 1.0512				
3	1.238	.167	0.0	50.9	3.5	NO	1006.8 1001.1	26.5 26.27	.6799 .6760	.8035 .7959				
9		.167	0.0			YES	964.1 959.5	26.1 25.91	.6511 .6480	.7916 .7851				
10	1.35	.167	0.0	**59.3	**3.0	NO	1021.3 1023.7	26.4 26.32	.6389 .6403	.8013 .7975	NO TEST RESULTS AVAILABLE			

* THE FIRST LINE OF THE THEORETICAL RESULTS FOR EACH CASE DENOTES THE RESULTS IN WHICH THE SMOOTHING TECHNIQUE (REFINEMENT) IS APPLIED

** ESTIMATED VALUE

TABLE 13 ANALYTICAL & TEST FLUTTER RESULTS ON CONFIGURATION 22

(ORIGINAL MODES, 60° SWEPT MODELS, ω_θ/ω_h=1.428)

ANALYSIS NUMBER	M	$\frac{x}{b_s}$	$\frac{z}{b_s}$	μ	ρ slug/ft^3 (x10^4)	THEORETICAL RESULTS					TEST RESULTS			
						THICKNESS CORRECTION	V_f ft/sec	η_f cps	$\frac{V_f}{b_s\omega_\theta\sqrt{\mu}}$	$\frac{\omega}{\omega_\theta}$	V_f ft/sec	η_f cps	$\frac{V_f}{b_s\omega_\theta\sqrt{\mu}}$	$\frac{\omega}{\omega_\theta}$
11	1.151	.19	0.0	**53.9	**3.3	NO	916.6	21.67	.6022	.8773	NO TEST RESULTS AVAILABLE			
							882.7	21.14	.5806	.8558				
	1.24	.0257	0.0	65.3	2.7						1317	20.8	.788	.842
12		0.0	0.0			NO	1089.0	22.19	.6513	.8984				
							1073.7	21.96	.6422	.8892				
13		.19	0.0			NO	1139.8	23.70	.6817	.9594				
							1058.7	22.46	.6332	.9091				
13	1.24	.19	0.0	65.3	2.7	NO	1139.8	23.70	.6817	.9594				
							1058.7	22.46	.6332	.9091				
14		.19	0.0			YES	1101.9	23.23	.6591	.9406				
							1035.2	22.22	.6191	.8994				
15	1.414	.197	0.0	**116.	**1.52	NO	1282.6	22.02	.5755	.8916	NO TEST RESULTS AVAILABLE			
							1238.0	21.61	.5555	.8764				

* THE FIRST LINE OF THE THEORETICAL RESULTS FOR EACH CASE DENOTES THE RESULTS IN WHICH THE SMOOTHING TECHNIQUE (REFINEMENT) IS APPLIED

** ESTIMATED VALUE

TABLE 14 ANALYTICAL & TEST FLUTTER RESULTS ON CONFIGURATION 23

(ORIGINAL MODES, 60° SWEPT MODELS, ω_θ/ω_h = 1.775)

ANALYSIS NUMBER	M	$\frac{x}{b_s}$	$\frac{z}{b_s}$	μ	ρ slug/ft^3 ($\times 10^4$)	THEORETICAL RESULTS					TEST RESULTS			
						THICKNESS CORRECTION	V_f ft/sec	η_f cps	$\frac{V_f}{b_s\omega_\theta\sqrt{\mu}}$	$\frac{\omega}{\omega_\theta}$	V_f ft/sec	η_f cps	$\frac{V_f}{b_s\omega_\theta\sqrt{\mu}}$	$\frac{\omega}{\omega_\theta}$
16	1.151	.0257	0.0	32.7	5.4	NO	*1012.1	28.82	.6879	.9388	1214.	23.5	.826	.765
		.19	0.0				909.0	24.43	.6179	.7956				
17	1.232	.0257	0.0	36.7	4.8	NO	1009.3	25.63	.6476	.8283	1292.	24.2	.829	.788
		0.0	0.0				950.2	24.26	.6096	.7903				
18		.19	0.0			NO	1063.2	30.95	.6821	1.008				
							1094.8	31.03	.7024	1.011				
18	1.232	.19	0.0	36.7	4.8	NO	1063.2	30.95	.6821	1.008				
							1094.8	31.03	.7024	1.011				
19		.19	0.0			YES	1053.9	30.86	.6763	1.005				
							1086.9	30.80	.6970	1.003				
20	1.414	.19	0.0	**50.3	**3.5	NO	1094.8	20.77	.5703	.8068	NO TEST RESULTS AVAILABLE			
							1014.4	23.50	.5138	.7654				

* THE FIRST LINE OF THE THEORETICAL RESULTS FOR EACH CASE DENOTES THE RESULTS IN WHICH THE SMOOTHING TECHNIQUE (REFINEMENT) IS APPLIED

** ESTIMATED VALUE

TABLE 15 ANALYTICAL & TEST FLUTTER RESULTS ON CONFIGURATIONS 15,22,23

(MODIFIED MODES, 45° and 60° SWEPT MODELS)

ANA. NO.	CONFIG NO.	M	$\frac{\omega_\theta}{\omega_h}$	$\frac{x}{b_s}$	$\frac{z}{b_s}$	μ	ρ slug/ft^3 (x10^4)	THEORETICAL RESULTS					TEST RESULTS			
								MODES MODIFIED	V_f ft/sec	η_f cps	$\frac{V_f}{b_s\omega_\theta\sqrt{\mu}}$	$\frac{\omega}{\omega_\theta}$	V_f ft/sec	η_f cps	$\frac{V_f}{b_s\omega_\theta\sqrt{\mu}}$	$\frac{\omega}{\omega_\theta}$
	15	1.238	1.765	.021	0.0	50.9	3.5						1254.	26.0	.846	.788
3				.167	0.0			NO	*1006.8	26.5	.6799	.8035				
									1001.1	26.27	.6760	.7959				
21				.167	0.0			YES	1103.6	27.6	.7454	.8363				
									1094.3	27.26	.7389	.8260				
	22	1.24	1.428	.0257	0.0	65.3	2.7						1317.	20.8	.788	.842
13				.19	0.0			NO	1139.8	23.70	.6817	.9594				
									1058.7	22.46	.6332	.9091				
22				.19	0.0			YES	1205.4	24.259	.7210	.9821				
									1138.0	23.284	.6806	.9427				
	23	1.232	1.775	.0257	0.0	36.7	4.8						1292.	24.2	.829	.788
18				.19	0.0			NO	1063.2	30.95	.6821	1.008				
									1094.8	31.03	.7024	1.011				
23				.19	0.0			YES	1083.5	31.17	.6951	1.015				
									1123.5	30.98	.7209	1.009				

* THE FIRST LINE OF THE THEORETICAL RESULTS FOR EACH CASE DENOTES THE RESULTS IN WHICH THE SMOOTHING TECHNIQUE (REFINEMENT) IS APPLIED

6 UNSTEADY AERODYNAMIC APPLICATIONS

A typical wing-tail configuration has been specified by the Advisory Group for Aeronautical Research and Development (AGARD) of NATO for use in comparison of various aerodynamic theories and experimental results. The basic configuration is shown in Figure 60.

As shown in the figure, all dimensions have been normalized on the basis of semi-span. In order to test and demonstrate the various capabilities of the computer program, three variations of the basic configuration have been used. These may be summarized as follows:

Configuration Number	Characteristics
1	Wing alone (with flow field sampling)
2	Wing and tail with very small longitudinal separation $(x_{WTE} - x_{TLE})_{Root} = 0.25$
3	Wing and tail with moderate longitudinal and vertical separation, $(x_{TLE} - x_{WTE})_{Root} = 0.45$ and $(z_T - z_W)_{Root} = 0.5$, and tail dihedral, $\psi_T = 30°$.

For the case of a wing alone, the perturbation velocity components (longitudinal wash, sidewash and upwash) have been sampled in the flow field for some local-chord lengths behind the wing. The first sampling chord is located at a spanwise distance of 0.056s from the centerline and a vertical distance above the wing plane of 0.5s. The second is located at a spanwise distance of 0.72s and a vertical distance of 0.1s.

In addition to the perturbation velocities, the chordwise pressure distributions, generalized forces, and generalized aerodynamic coefficients have been determined for various reduced frequency-Mach number combinations. Table 16 summarizes the cases analyzed.

Figures 61 through 66 give the values of longitudinal wash, sidewash and upwash plotted along the sample chord for some local-chord lengths behind the wing. These values are computed by applying the smoothing technique for two reduced frequencies, k_s, equal to 0.75 and 1.5 based on the wing semi-span for antisymmetric wing bending and torsion modes. These mode shapes are also given in Table 16.

Sample plots of the pressure distributions obtained on the wing for M = 1.56 are given in Figures 67 through 74. The pressures are plotted at Chord 1, y/s = 0.056 and Chord 7, y/s = 0.75. Values are given for reduced frequencies k_s = 0.75 and 1.5 based on a wing semi-span, s, and are computed by applying the smoothing technique.

TABLE 16 SUMMARY OF AGARD CONFIGURATION CASES

Case	Config.	M	k_s	Surface	Mode 1	Mode 2	Sym. or Anti.
1-1	1	1.56	0.75 1.5	Wing	$z = y^2$	$z = xy$	Symmetric
1-2	1	1.56	0.75 1.5	Wing	$z = y^2$	$z = xy$	Antisym.
2-1	2	1.414	0.75 1.5	Wing & Tail	Wing $z = y^2$ Tail $z = y^2$	Wing $z = xy$ Tail * $z = x'y$	Symmetric Antisym.
2-2	2	3.162	0.75 1.5	Wing & Tail			
2-3	3	1.56	0.75 1.5	Wing & Tail			

* The x'- reference location for the tail torsion mode is taken to be the root of the tail leading edge.

The generalized unsteady aerodynamic coefficients at k_s = 0.75 and 1.5 for these antisymmetiric wing bending and torsion modes are given in Table 17. The lower values which are superscripted by * show the quantities in which the smoothing technique is applied.

The pressure distributions obtained for the wing-horizontal tail configuration with very small longitudinal separation which is specified by Configuration Number 2 are given in Figures 75 through 78 for M = 1.414 (Subsonic edge) and M = 3.162 (Supersonic edge) at two reduced frequencies equal to 0.75 and 1.5 based on wing semi-span for wing bending, wing torsion, tail bending and tail torsion modes (symmetric). The generalized unsteady aerodynamic coefficients at k_s = 0.75 and 1.5 for these modes are given in Table 18 for M = 1.414 and in Table 19 for M = 3.162.

The pressure distributions obtained for the wing-horizontal tail configuration with a combined moderate longitudinal separation, moderate vertical separation and tail dihedral which is specified by Configuration 3 are given in Figures 79 and 80 for M = 1.56. The modes associated with this case are symmetric wing bending and torsion and symmetric tail bending and torsion modes as listed in Table 16 for two reduced frequencies equal to 0.75 and 1.5 based on wing semi-span. The generalized unsteady aerodynamic coefficients in this case are given in Table 20.

TABLE 17 GENERALIZED UNSTEADY AERODYNAMIC COEFFICIENTS FOR AGARD CASE 1-1 (M = 1.56)

REDUCED FREQUENCY k_s = 0.75				
	MODE 1		MODE 2	
	REAL	IMAGINARY	REAL	IMAGINARY
MODE 1	-0.0641312 -0.0546578*	0.2485696 0.2543928*	0.1388799 0.1457878*	1.2561458 1.2726424*
MODE 2	-.2506159 -.2497786*	0.8428621 0.8613414*	0.3216954 0.3512486*	4.5499897 4.59171278*

REDUCED FREQUENCY k_s = 1.5				
	MODE 1		MODE 2	
	REAL	IMAGINARY	REAL	IMAGINARY
MODE 1	-0.24607075 -0.24976521*	0.2999881 0.3056733*	-0.33238136 -0.33591923*	1.4369894 1.4541712*
MODE 2	-0.96633197 -0.97639619*	1.0472075 1.0614159*	-1.6243165 -1.6391248*	5.3033931 5.3425156*

Note * denotes a value in which the smoothing technique is applied.

TABLE 18 GENERALIZED UNSTEADY AERODYNAMIC COEFFICIENTS FOR AGARD CASE 2-1 (M = 1.414)

REDUCED FREQUENCY k_s = 0.75

		WING				TAIL			
		BENDING		TORSION		BENDING		TORSION	
		REAL	IMAG.	REAL	IMAG	REAL	IMAG.	REAL	IMAG.
WING	BEND	-.061454	.251265	.206619	1.25459	.000342	.000448	.001930	-.001304
		-.060726	.252038	.210765	1.25701	.000286	.000388	.001622	-.001217
	TORS.	-.242002	.861716	.604679	4.62587	.001303	.001715	.007390	-.004928
		-.238927	.866631	.625681	4.64090	.001078	.001471	.006149	-.004558
TAIL	BEND	-.067101	-.169840	-.547404	-.52169	.004768	.226054	.360195	.369973
		-.067969	-.169749	-.551913	-.51881	.005781	.225533	.360229	.366786
	TORS.	-.110388	-.234990	-.842003	-.65508	.007463	.345316	.565537	.615344
		-.112006	-.236638	-.852978	-.65769	.009059	.346430	.568114	.611553

REDUCED FREQUENCY k_s = 1.5

		WING				TAIL			
		BENDING		TORSION		BENDING		TORSION	
		REAL	IMAG.	REAL	IMAG.	REAL	IMAG.	REAL	IMAG.
WING	BEND	-.249145	.289408	-.318119	1.38183	.000905	.000002	.001277	-.001442
		-.245253	.289800	-.304208	1.38083	.000768	.000021	.000995	-.001168
	TORS.	-.961342	1.019511	-1.45263	5.15058	.003461	.000020	.004947	-.005501
		-.946629	1.022599	-1.39449	5.15137	.002908	.000088	.003818	-.004410
TAIL	BEND	-.211750	-.102803	-1.03469	-.27909	-.012036	.214599	.342121	.371472
		-.214975	-.101748	-1.04998	-.27055	-.008297	.213108	.343239	.367647
	TORS.	-.319626	-.116276	-1.49341	-.25048	-.029008	.325291	.524819	.620377
		-.325863	-.115784	-1.52411	-.24191	-.022935	.324948	.529459	.615706

* The lower values are ones in which the smoothing technique is applied.

TABLE 19 GENERALIZED UNSTEADY AERODYNAMIC COEFFICIENTS
FOR AGARD CASE 2-2 (M = 3.162)

REDUCED FREQUENCY k_s = 0.75

		WING				TAIL			
		BENDING		TORSION		BENDING		TORSION	
		REAL	IMAG.	REAL	IMAG.	REAL	IMAG.	REAL	IMAG.
WING	BEND.	-.018634	.212557	.278447	.841141	0.00	0.00	0.00	0.00
		-.017578	.211982	.279757	.837123	0.00	0.00	0.00	0.00*
	TORS.	-.082534	.728195	.924261	3.082659	0.00	0.00	0.00	0.00
		-.078735	.728178	.931307	3.072145	0.00	0.00	0.00	0.00
TAIL	BEND.	-.041406	-.070962	-.233794	-.162768	.001027	.125955	.176227	.197210
		-.041299	-.071173	-.233216	-.164091	.000954	.126363	.176380	.197609
	TORS.	-.061729	-.098218	-.349047	-.214711	.001443	.197056	.288144	.327728
		-.061322	-.098806	-.347626	-.218341	.001168	.197903	.288335	.328579

REDUCED FREQUENCY k_s = 1.5

		WING				TAIL			
		BENDING		TROSION		BENDING		TORSION	
		REAL	IMAG.	REAL	IMAG.	REAL	IMAG.	REAL	IMAG.
WING	BEND.	-.062751	.228501	.175233	.866024	0.00	0.00	0.00	0.00
		-.059223	.227037	.181251	.861009	0.00	0.00	0.00]	0.00*
	TORS.	-.271330	.803960	.490654	3.212103	0.00	0.00	0.00	0.00
		-.258011	.800790	.515263	3.198675	0.00	0.00	0.00	0.00
TAIL	BEND.	-.106197	-.020038	-.404513	-.030997	.003007	.124253	.176189	.195748
		-.106506	-.020820	-.405956	-.034804	.003091	.125091	.176565	.196603
	TORS.	-.154867	-.019555	-.592626	-.005787	.003838	.194329	.286812	.325569
		-.154701	-.021477	-.593312	-.014707	.003516	.196067	.287027	.327366

* The lower values are ones in which the smoothing technique is applied.

TABLE 20 GENERALIZED UNSTEADY AERODYNAMIC COEFFICIENTS
FOR AGARD CASE 2-3 (M=1.56)

REDUCED FREQUENCY k_s = 0.75

		WING				TAIL			
		BENDING		TORSION		BENDING		TORSION	
		REAL	IMAG.	REAL	IMAG.	REAL	IMAG.	REAL	IMAG.
WING	BEND.	-.056069	.244731	.225831	1.194187	0.00	0.00	0.00	0.00
		-.054522	.243512	.229380	1.187548	0.00	0.00	0.00	0.00*
	TORS.	-.218139	.837243	.697713	4.392965	0.00	0.00	0.00	0.00
		-.212479	.836331	.716314	4.378940	0.00	0.00	0.00	0.00
TAIL	BEND.	-.005720	-.026525	-.082956	-.078585	0.004701	.218944	.344831	.359459
		-.006964	-.026167	-.089933	-.068292	0.007039	.226998	.353614	.350774
	TORS.	-.000592	-.045929	-.091397	-.169644	.004576	.331840	.529935	.602395
		-.003525	-.045710	-.108395	-.150593	.008575	.348615	.549506	.594668

REDUCED FREQUENCY k_s = 1.5

		WING				TAIL			
		BENDING		TORSION		BENDING		TROSION	
		REAL	IMAG.	REAL	IMAG.	REAL	IMAG.	REAL	IMAG.
WING	BEND.	-.233814	.284202	-.24294	1.31985	0.00	0.00	0.00	0.00
		-.228539	.281925	-.23006	1.30945	0.00	0.00	0.00	0.00
	TORS.	-.902674	.996337	-1.1513	4.90717	0.00	0.00	0.00	0.00
		-.882784	.991482	-1.0965	4.87823	0.00	0.00	0.00	0.00
TAIL	BEND.	-.057175	-.00831	-.24617	.02726	.000874	.20908	.342106	.353397
		-.054135	-.00592	-.22307	.03691	.009689	.21507	.352259	.347620
	TORS.	-.096174	-.02787	-.43834	-.02555	-.012916	.31745	.514428	.594510
		-.091677	-.02285	-.39995	-.00283	.002798	.33083	.539510	.586211

* The lower values are ones in which the smoothing technique is applied.

SECTION V

CONCLUSIONS AND RECOMMENDATIONS

1. RECOMMENDATIONS FOR FUTURE PROGRAM DEVELOPMENTS

The computer program developed for evaluating the unsteady loadings on wing-tail combinations in supersonic flow appears to provide reasonable results when applied to analysis configurations that meet the restrictions of the "Mach-Box" method.

Analysis configurations that lie within the program limitations are shown in figure 25 through figure 27. The analysis configurations that do not meet the program limitations are shown in figure 28 and figure 30.

Aerodynamic influence effects of the tail on the wing is allowed only for coplanar configurations and is not allowed for vertical separation cases. It is recommended that the program be extended to include this capability which would involve a reorganization of the procedures used to evaluate the normal washes and velocity potentials of the individual surfaces. Modification of the program would allow analysis of a wide variety of configurations such as "T" tails, horizontal-vertical tails, and bi-plane configurations that would be applicable to the space shuttle configurations now under study.

Unreasonable load distributions may result within an analysis on extremely low Mach number for those configurations that have large leading edge sweep angles such as shown in figure 81. The chordwise loadings may have large fluctuations that are caused by the basic box pattern that defines the leading edge and is also affected by the large normalwash values defined in the "off-wing" diaphragm region. Mach lines proceeding from the "outside" corners of the planform box pattern will cause box loads to be overestimated and the loadings on those boxes affected by "inside" corners will be underestimated. The fluctuations in the loadings may be reduced by using the subdivision options within the present program. However, the computer time requirements are severely affected by the present subdivision process, especially when the program limits are being used. The present program subdivides all boxes within a specified streamwise band width from the left hand Mach line to the right hand Mach line. This procedure does improve the chordwise load distributions, however it is costly to use on highly swept configurations at very low Mach numbers. It is therefore recommended that the subdivision procedure be reorganized such that the boxes to be subdivided are only those boxes in the diaphragm that are cut by the planform leading-trailing edges shown in figure 82.

One further item that needs attention is the basic solution method itself. The present solution is modal dependent in that the normalwashes in the diaphragm and the velocity potentials on the planform are evaluated for a given mode shape, reduced frequency, and Mach number. The process is

repeated over again for every mode shape to be included in the analyses. Recent advances in computer technology now make it practical to remove this modal dependency by performing a matrix manipulation on the known aerodynamic influence coefficients and known diaphragm velocity potentials as shown in figure 83. Application of this procedure will remove the modal dependency from the solution and will provide a program that will be an order of magnitude more economical than presently available in evaluating interaction loadings in supersonic flow.

2. RECOMMENDATIONS FOR FUTURE FLUTTER MODEL TESTS

Flutter analyses of Cornell configuration 15 and configuration 22 were extended to evaluate the flutter speed variations at Mach numbers higher than those tested within the Cornell flutter model tests of reference 2. Although no tables of density versus Mach number are available for the analysis, an extrapolated density-Mach number variation was devised for use in the analysis to represent the possible upper and lower limits of density as a function of Mach number. The assumed density variations are shown in figure 84 and figure 85 where the results of the flutter analysis given in terms of $\frac{V}{b_s \omega_\theta \sqrt{\mu}}$. Numerical results are presented in table 21.

It should be noted that there is no large change in the velocity parameter or in the frequency ratio $\frac{\omega}{\omega_\beta}$ for configuration 15, indicating that adverse coupling persists throughout the Mach range for the particular value of wing bending to fuselage torsion ratio used in the test. There is a small change in the velocity parameter with Mach number for configuration 22, however, adverse coupling still remains for most of the Mach range investigated. The change in $V/b_s \omega_\theta \sqrt{\mu}$ is only slight when compared with the results of a single surface analysis which displays a dramatic increase in $\frac{V}{b_s \omega_\theta \sqrt{\mu}}$ with Mach number.

The increased values for single surface tests are usually observed to start within the transonic range and are attributed to an aft shift in chordwise center of pressure that are accompanied by a reduction in C_{L_α} values with increasing Mach number. The source of the adverse coupling problem associated with wing-tail configurations in close proximity appears to be identified with the fuselage flexibility that allows differential bending (or flapping) to take place that causes aerodynamic driving force to exist on the tail that is out of phase with the wing motion. Within the differential flapping mode, the tail will be aerodynamically driven in the opposite direction to the wing motion (caused by the normalwash of the wing wake). The highly loaded tail will then tend to mechanically drive the wing to larger amplitudes (than would be experienced by a single surface alone) by means of the fuselage torsion spring. The amount of circular coupling that is present in wing-tail configurations appears to be a direct function of relative stiffnesses of the two surfaces, the span length ratios of the surfaces, and the fuselage torsional stiffness parameter. Mach number effects appear to have a negligible influence in changing the velocity parameter $\frac{V}{b_s \omega_\theta \sqrt{\mu}}$.

It appears that the most critically coupled wing-tail combination is one that has (1) the wing and tail in the same plane (coplanar), (2) leading surface more flexible than the trailing surface, (3) planform taper ratios of 1.0 or larger, (4) span lengths are equal, (5) and fuselage torsion flexibility is allowed.

The maximum aerodynamic loading induced on the tail (tending to aerodynamically drive the tail) is obtained when the tail is fully exposed to the wing wake. It is expected that tail induced loadings will be smaller for tail spans that are less than or greater than the span of the leading surface and this in turn will proportionally reduce the coupling effects of the system.

Therefore, it is recommended that series of supersonic flutter model tests be conducted on variable sweep wing-tail models to evaluate the effects on flutter speed due to the critical parameters of (1) wing-tail flexibility ratio, (2) ratio of wing-tail span lengths, (3) fuselage torsional flexibility, (4) and Mach number.

It is suggested that the variable sweep capabilities be incorporated only on the wing (or leading surface). Planforms of the wing and tail should be representative of a typical aircraft configuration (such as the F-111) to provide a realistic evaluation of the tail induced load coupling effects of modern aircraft. Inexpensive model construction techniques may be applied to the model design, however, a very accurate description of the modal data, inertia and mass data, and structural influence coefficients are required and must be carefully defined and documented. Vibration tests and theoretical vibration analyses must be conducted to correlate the quality of the mode shape definition prior to tunnel testing and flutter analyses.

The wing models to be constructed should provide a large variation in wing flexibility to evaluate the effect of wing-tail flexibility ratios on flutter speed.

The model support system should allow flutter testing of wing-tail combinations having horizontal and vertical separations as well as being able to test coplanar configurations. The support system should be designed to allow testing over a wide range of fuselage torsion spring rates to determine spring rates that may preclude any adverse coupling effects.

Finally, the Mach number range to be covered within the tests should extend from very low supersonic Mach numbers to Mach numbers that are slightly higher than the sonic edge Mach number of the planform having the largest sweep angle.

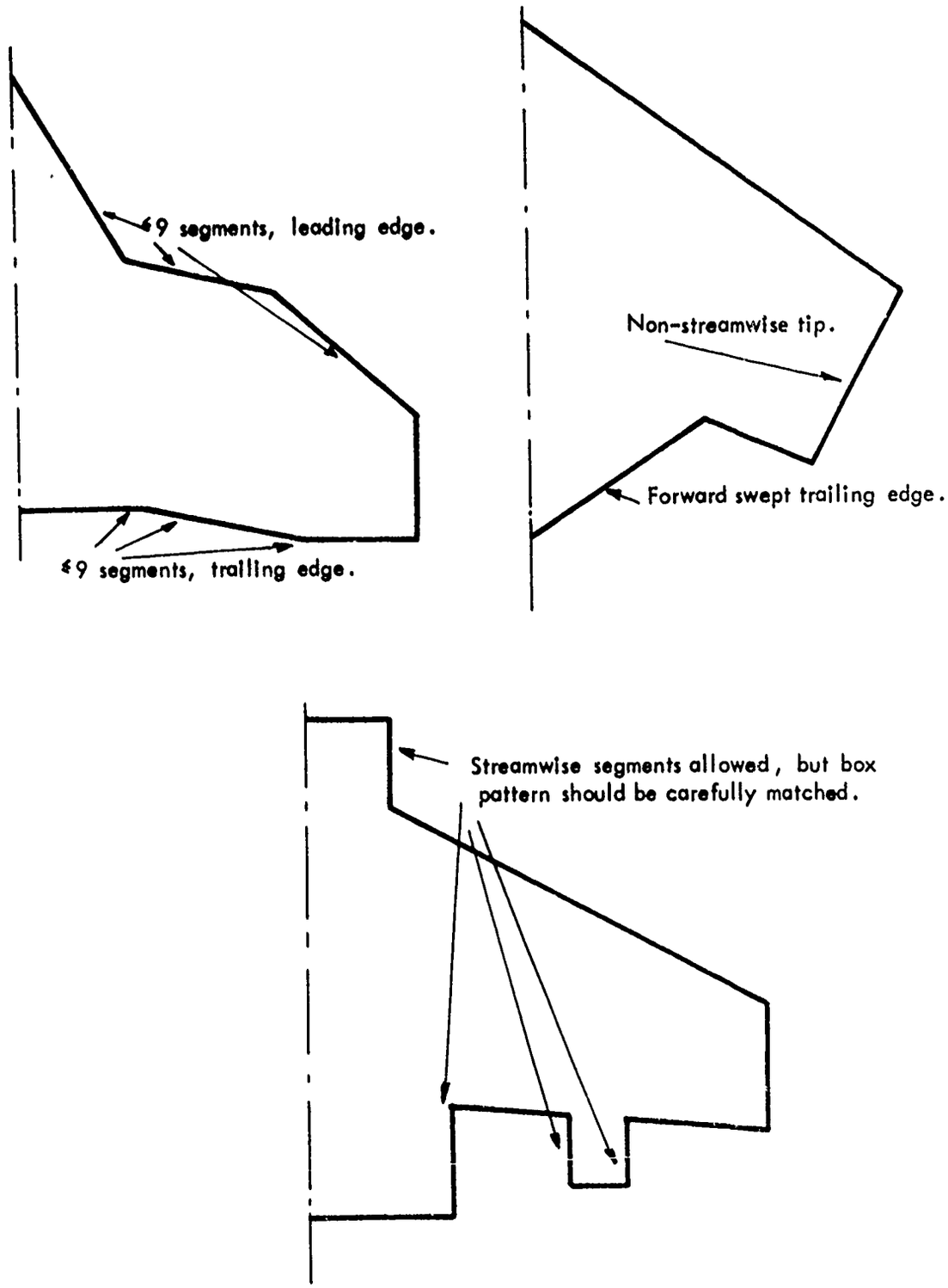

FIGURE 25 PLANFORM EDGE DEFINITION, WING OR TAIL

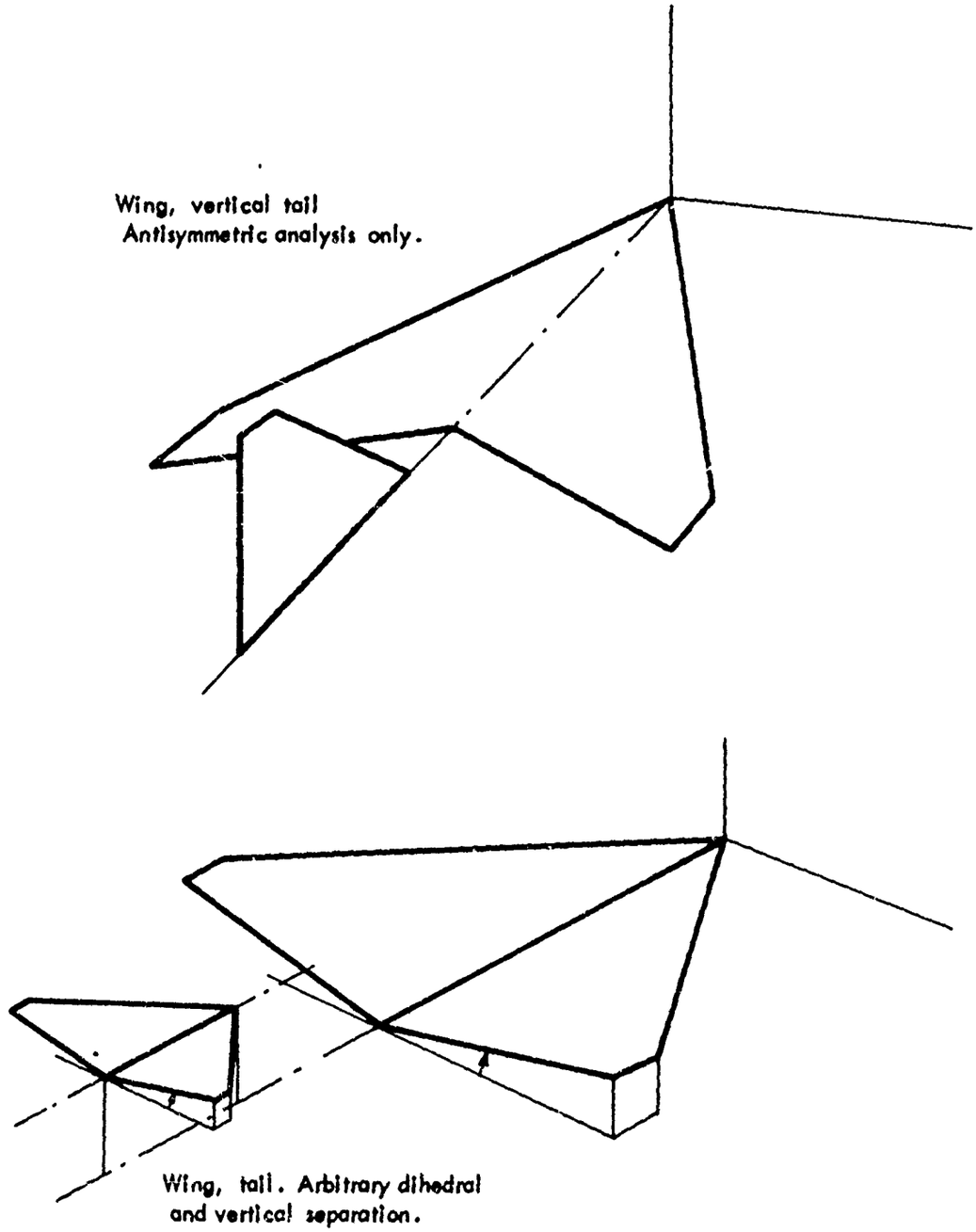

FIGURE 26 ALLOWABLE WING/TAIL CONFIGURATIONS

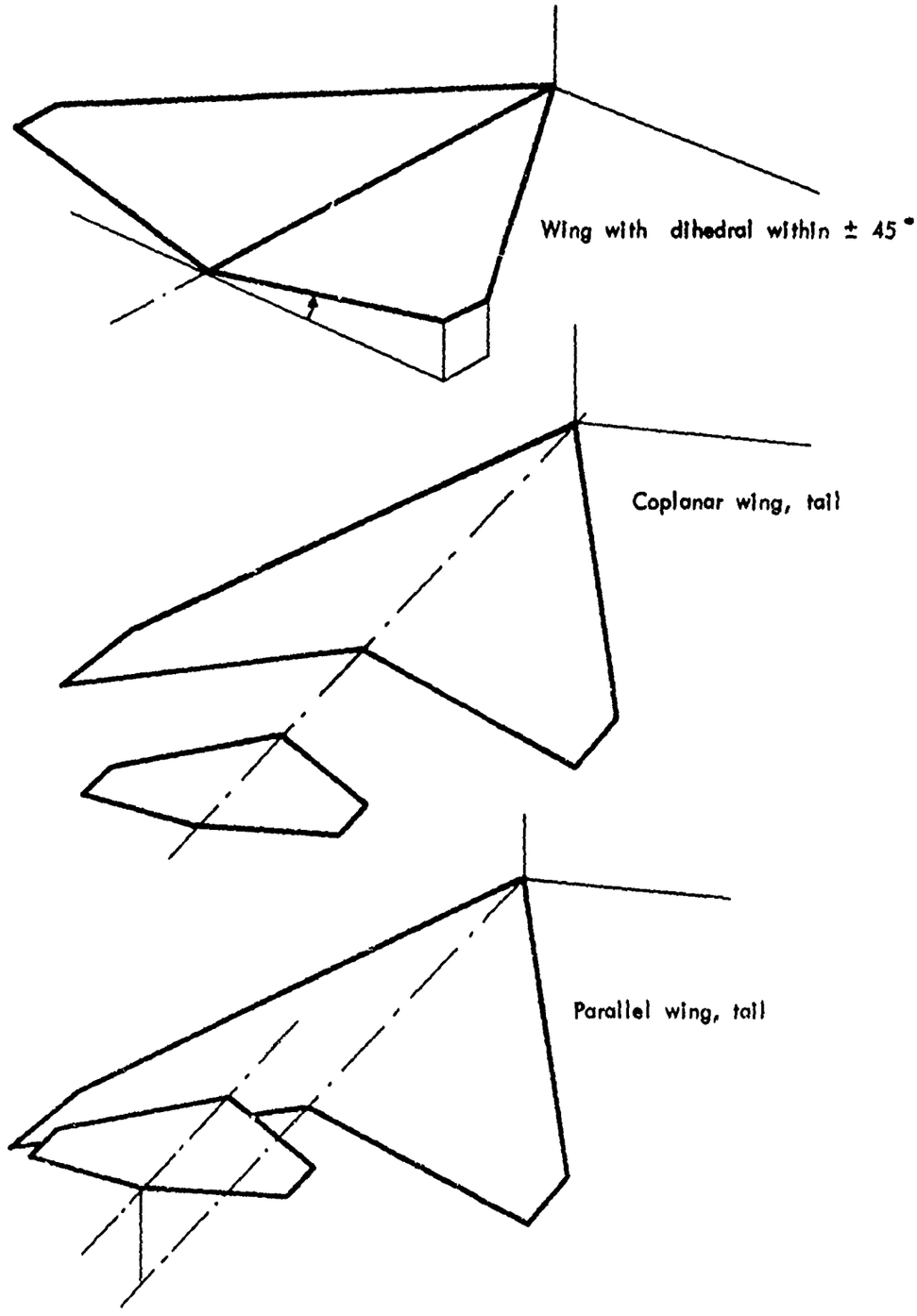

FIGURE 27 ADDITIONAL ALLOWABLE WING/TAIL CONFIGURATIONS

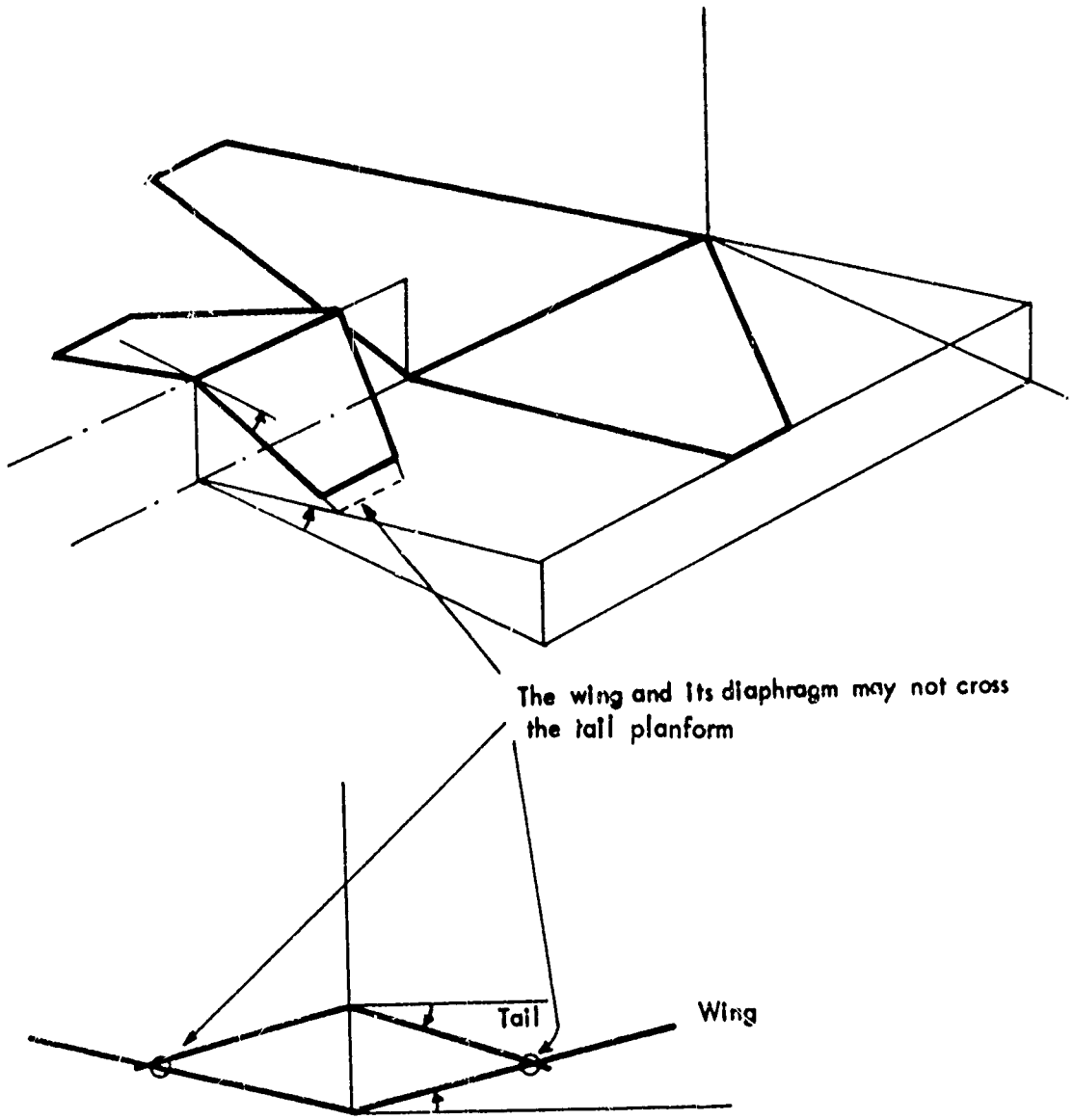

FIGURE 28 DIHEDRAL COMBINATION NOT ALLOWED

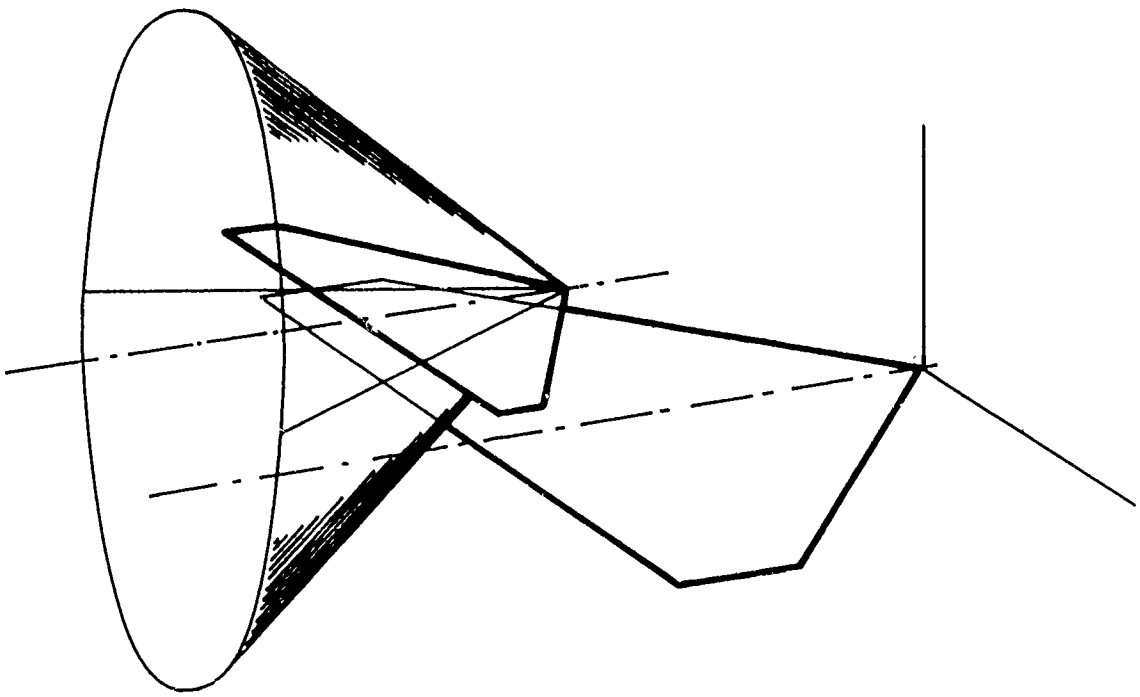

Overlapped wing and tail allowed if mutual interaction does not occur. (Tail Mach cone does not intersect wing).

FIGURE 29 TAIL OVERLAP RESTRICTION

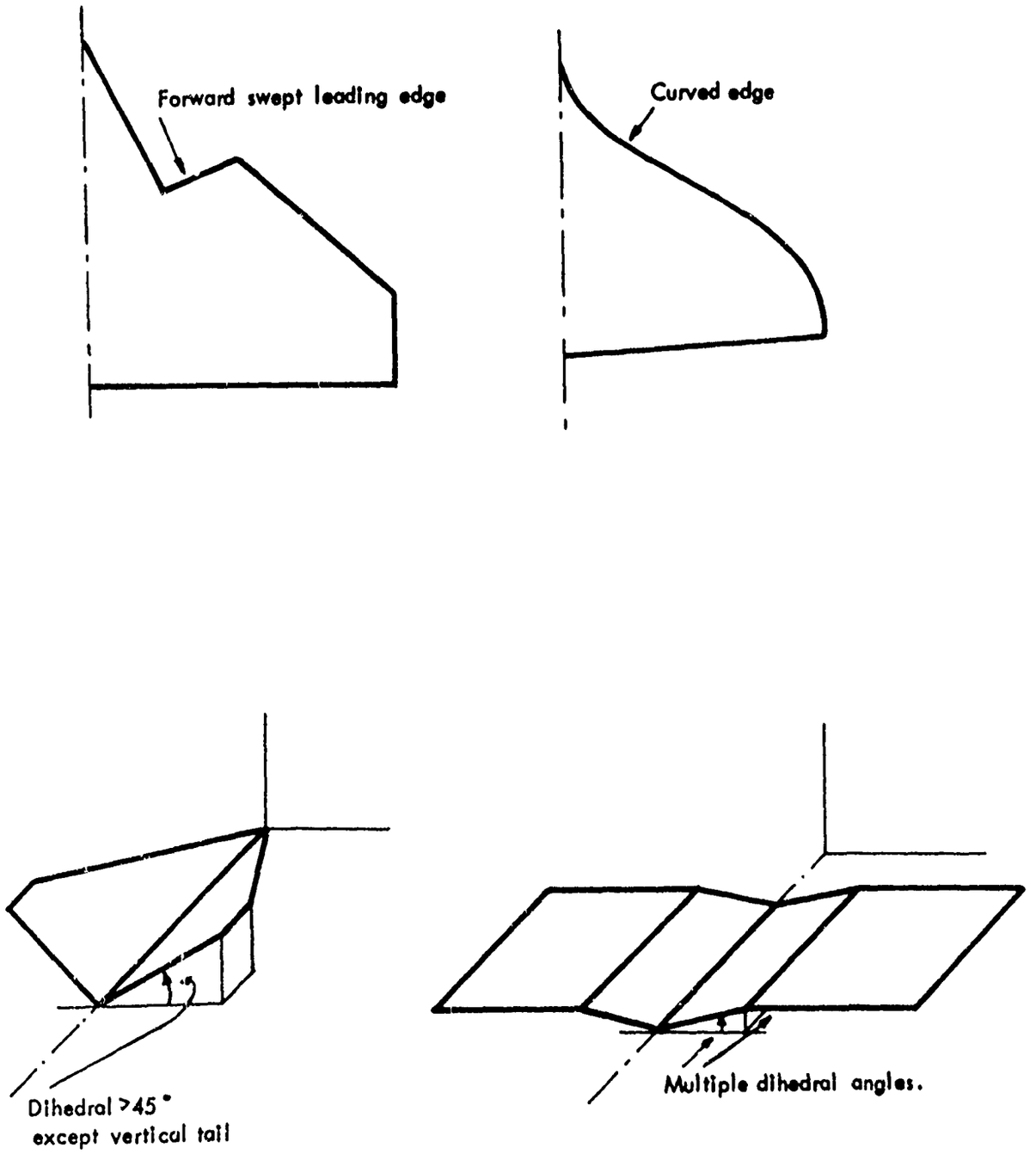

FIGURE 30 OTHER CONFIGURATIONS NOT ALLOWED

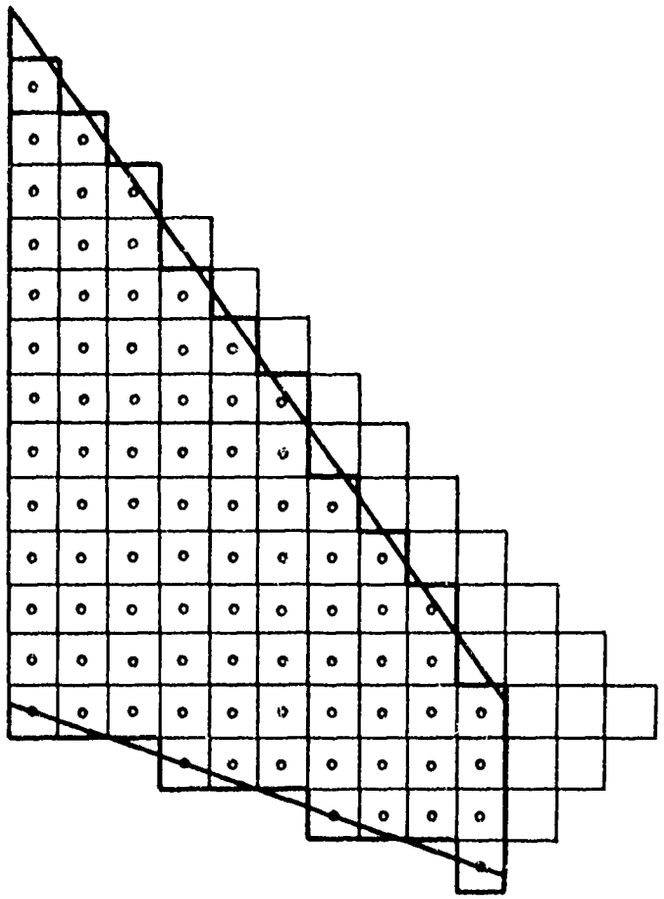

FIGURE 31 MACH BOX GRID SYSTEM WITHOUT SUBDIVISION

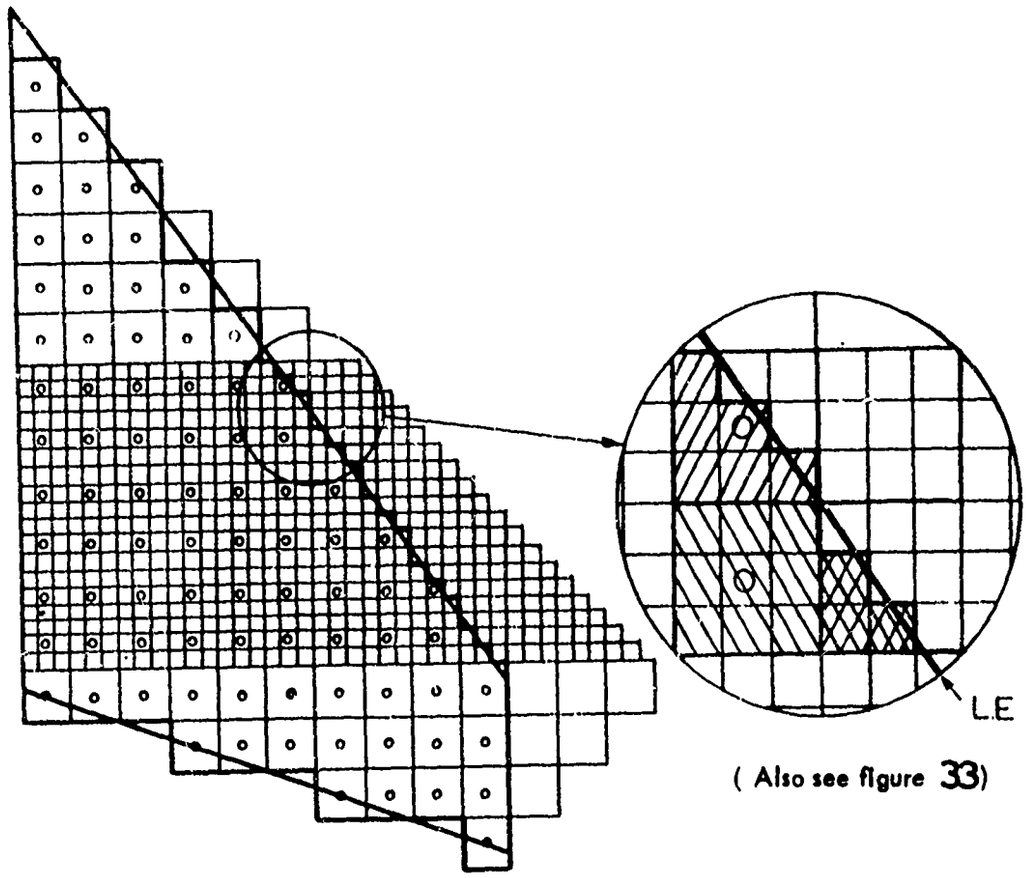

FIGURE 32 MACH BOX GRID SYSTEM WITH SUBDIVISION

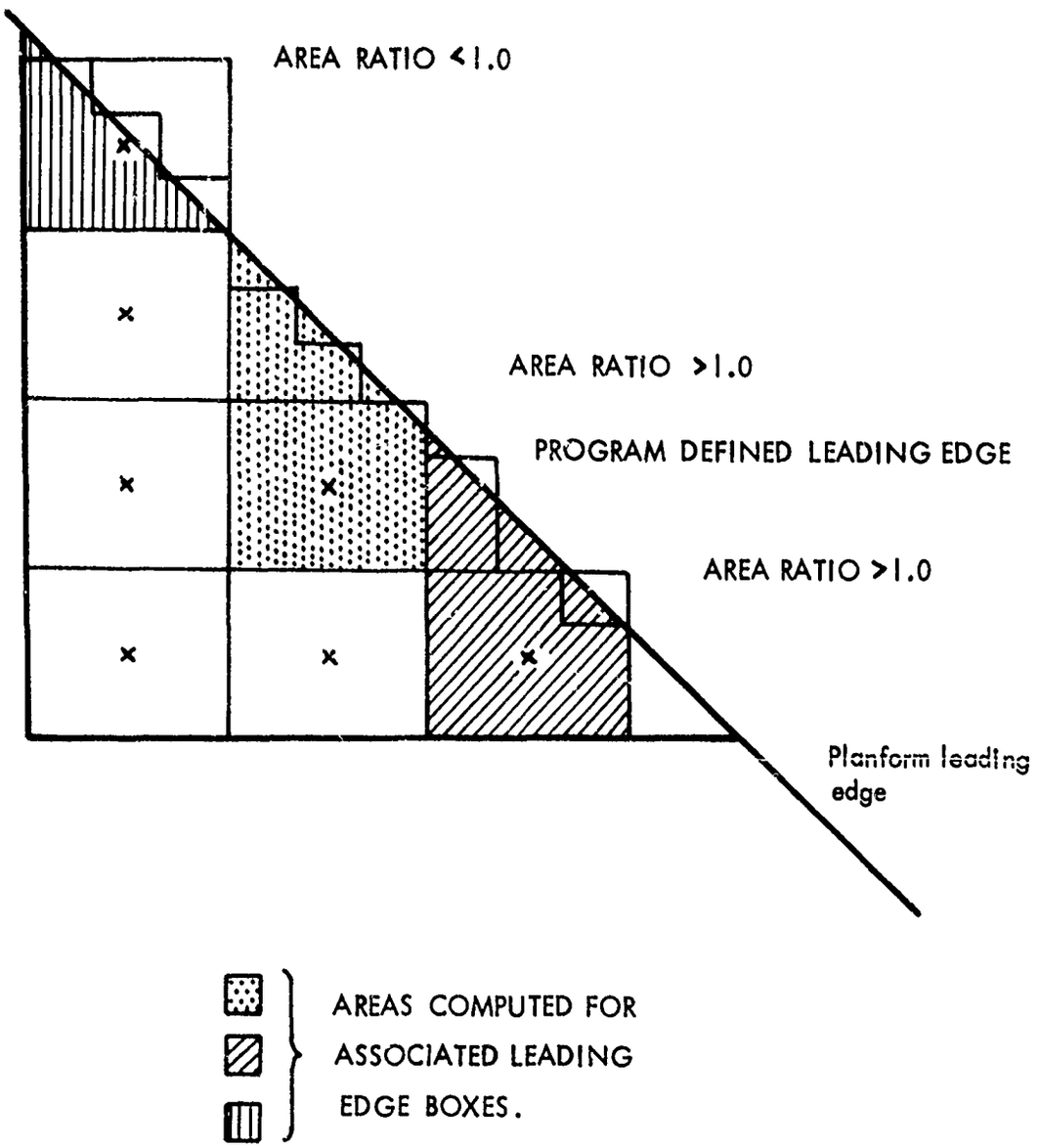

FIGURE 33 METHOD OF EVALUATING $\alpha^{n,m}$ USED IN SUBDIVISION

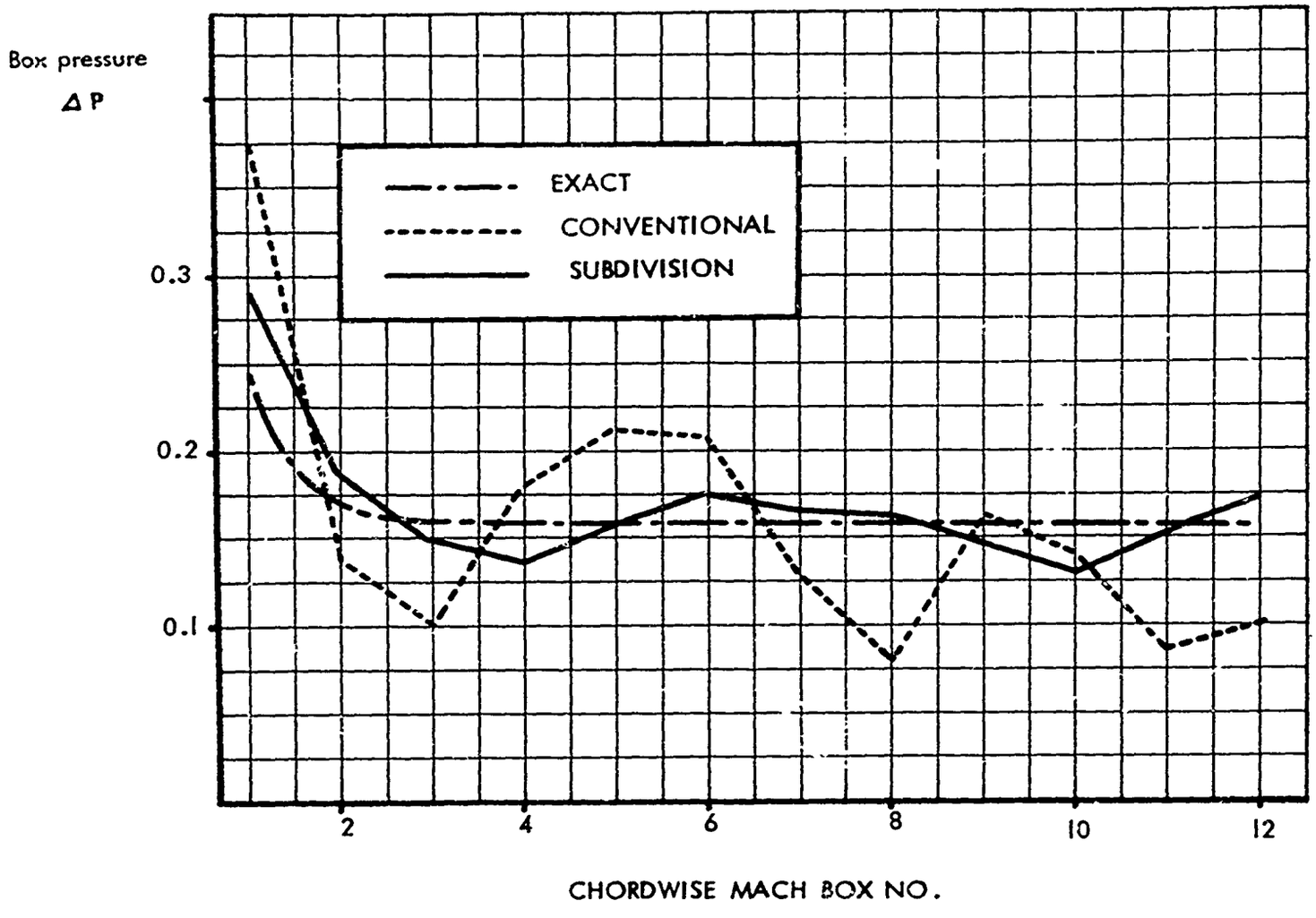

FIGURE 34. EFFECT OF SUBDIVISION ON CHORDWISE LOADING.

(Reproduced from reference 10)

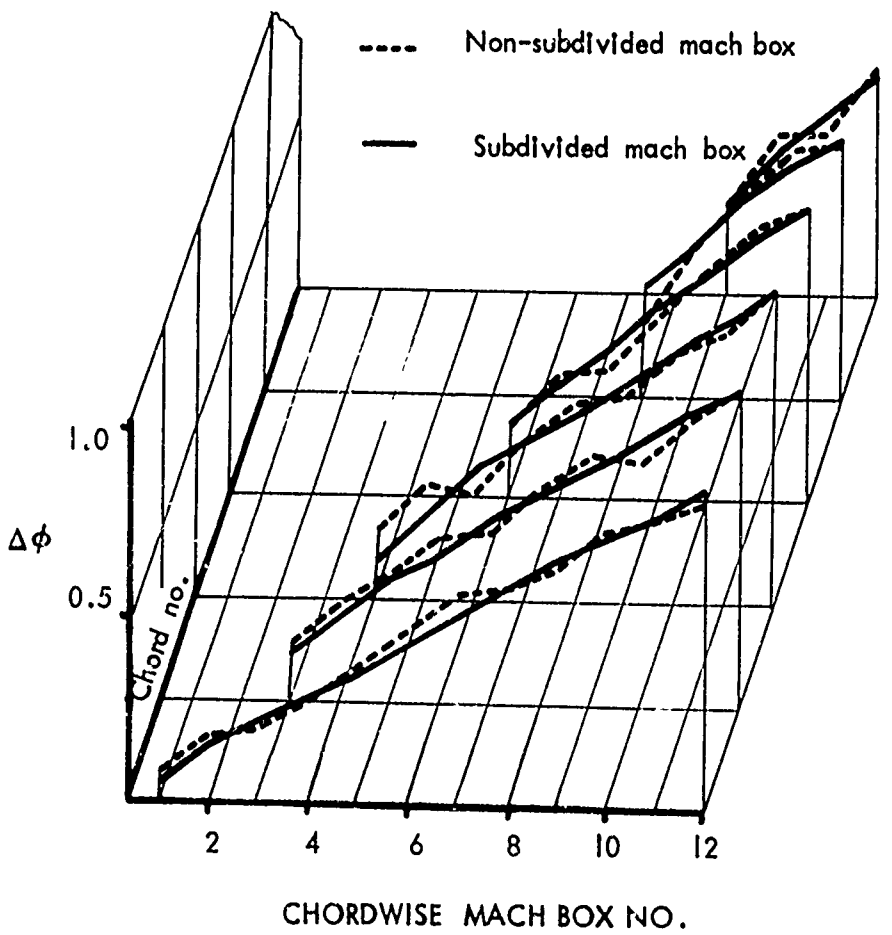

FIGURE 35 EFFECT OF SUBDIVISION ON VELOCITY POTENTIALS.

(Reproduced from reference 10)

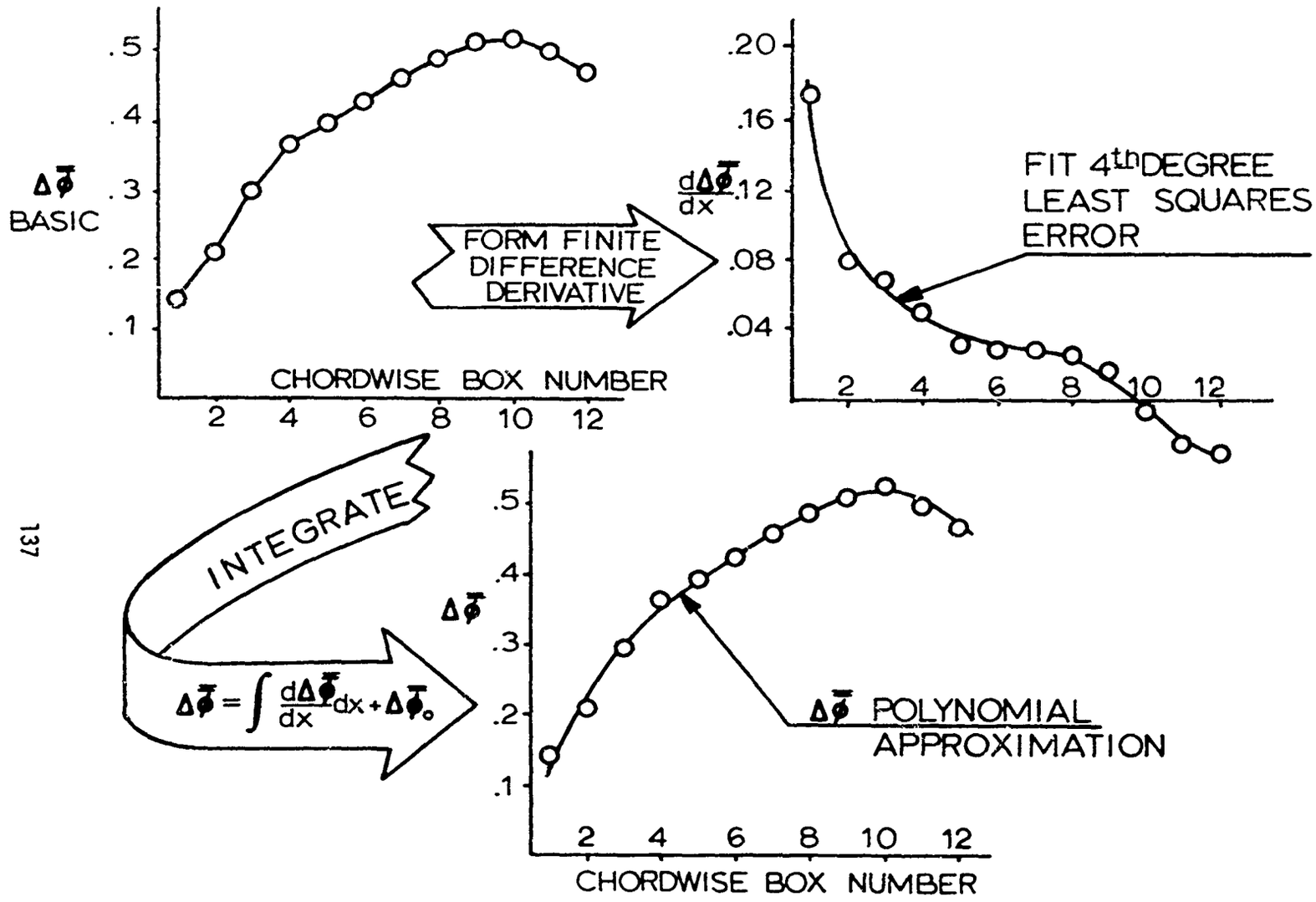

Figure 36 VELOCITY POTENTIAL SMOOTHING PROCESS

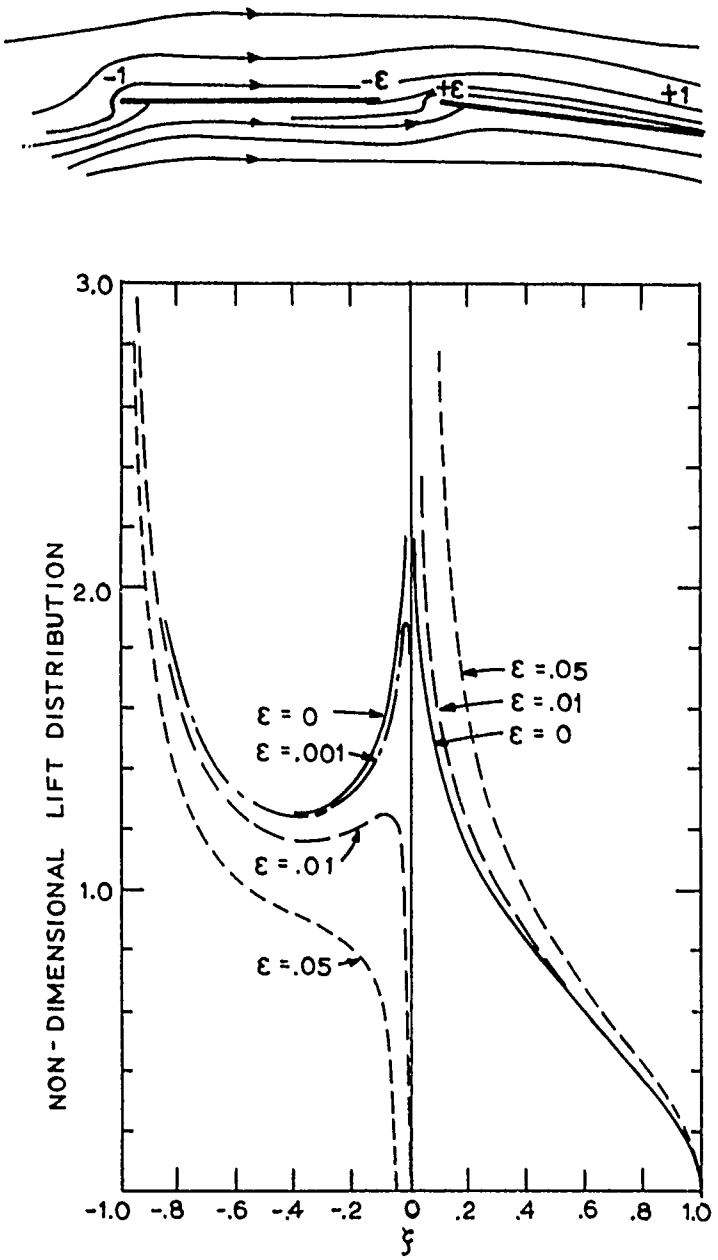

FIGURE 37 NON - DIMENSIONAL LIFT DISTRIBUTION

(Reproduced from reference 14)

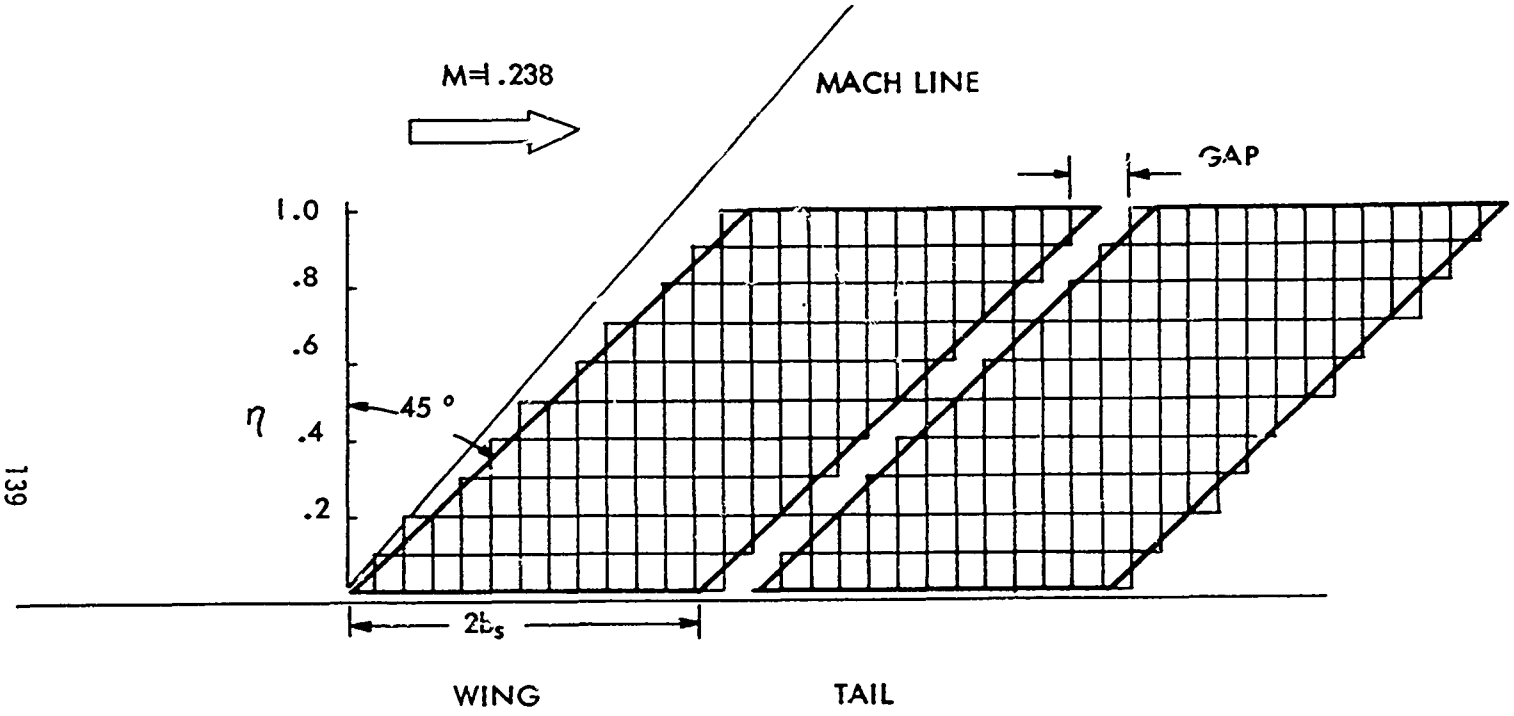

FIGURE 38 ANALYSIS PLANFORM OF CHORDWISE LOADINGS - GAP STUDY

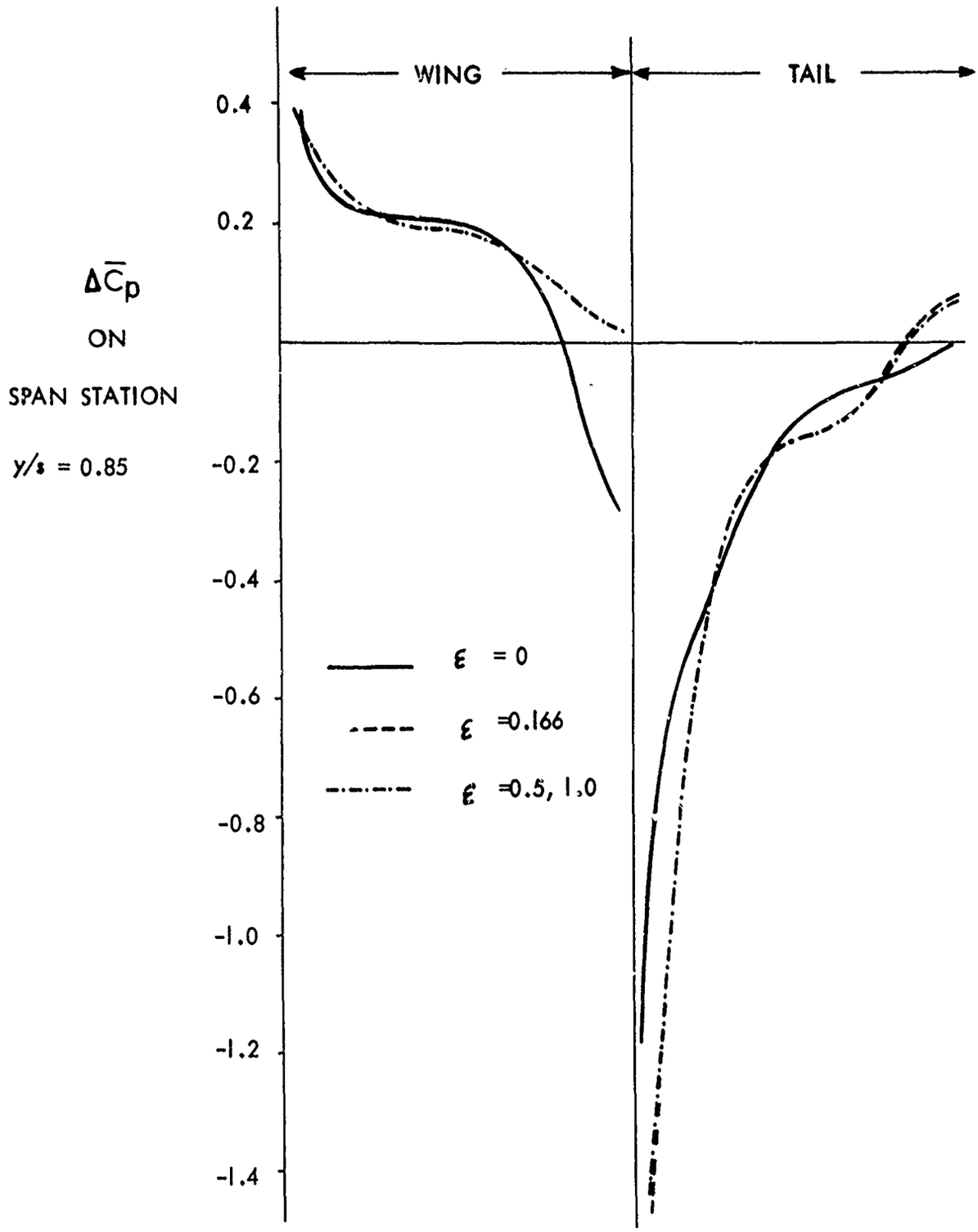

FIGURE 39 CHORDWISE LOADINGS FOR VARIOUS WING - TAIL SEPARATIONS IN WING TIP REGION.

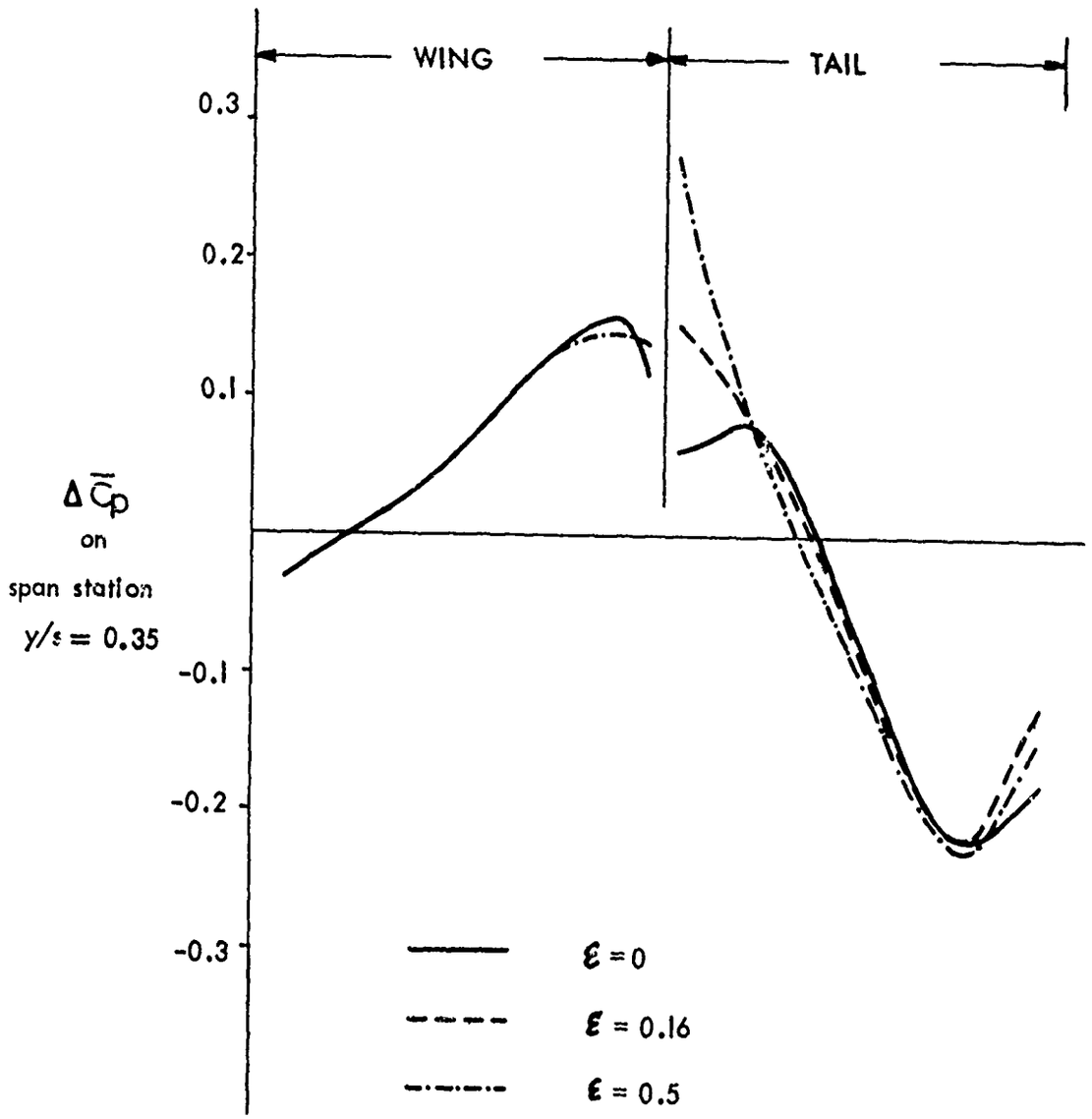

FIGURE 40 CHORDWISE LOADINGS NEAR ROOT REGION

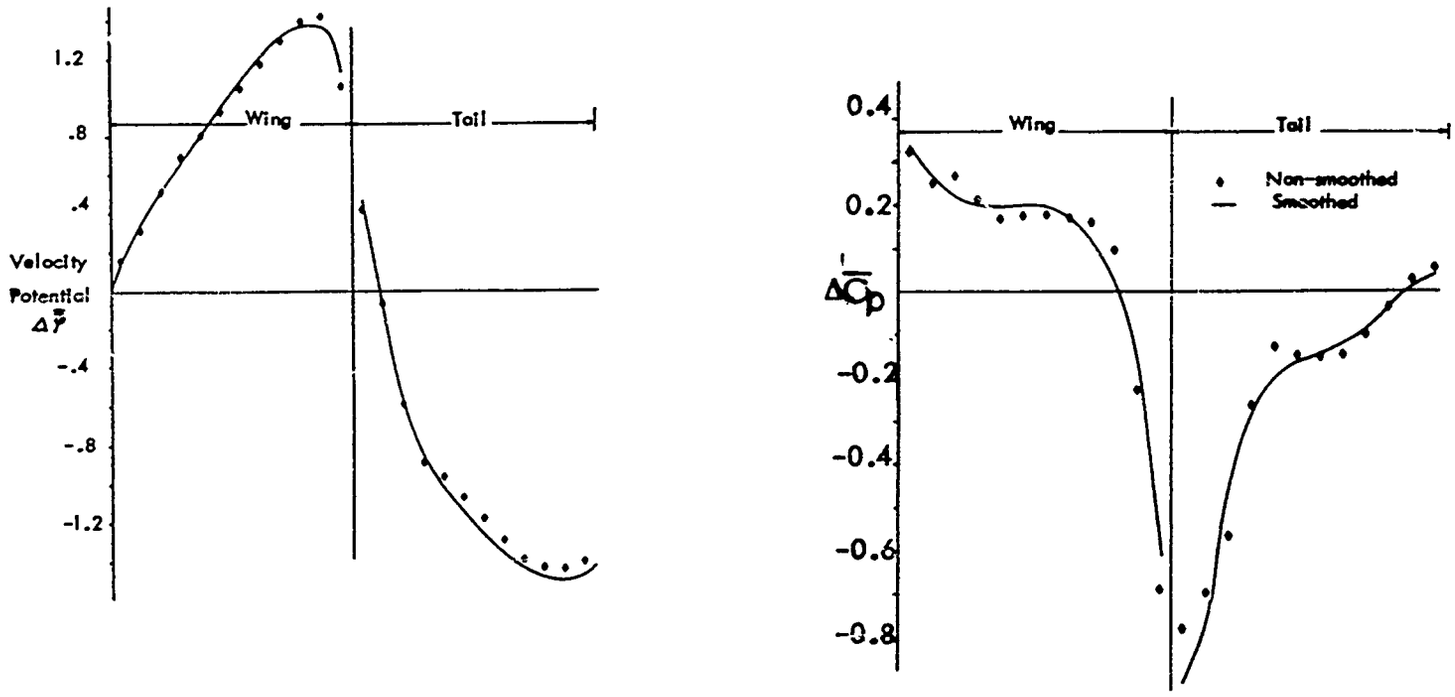

FIGURE 41 VELOCITY POTENTIAL SMOOTHING AND RESULTING CHORDWISE LOADINGS FOR CONFIGURATION 15, M = 1.238, k_s = 0.338, y/s = 0.85

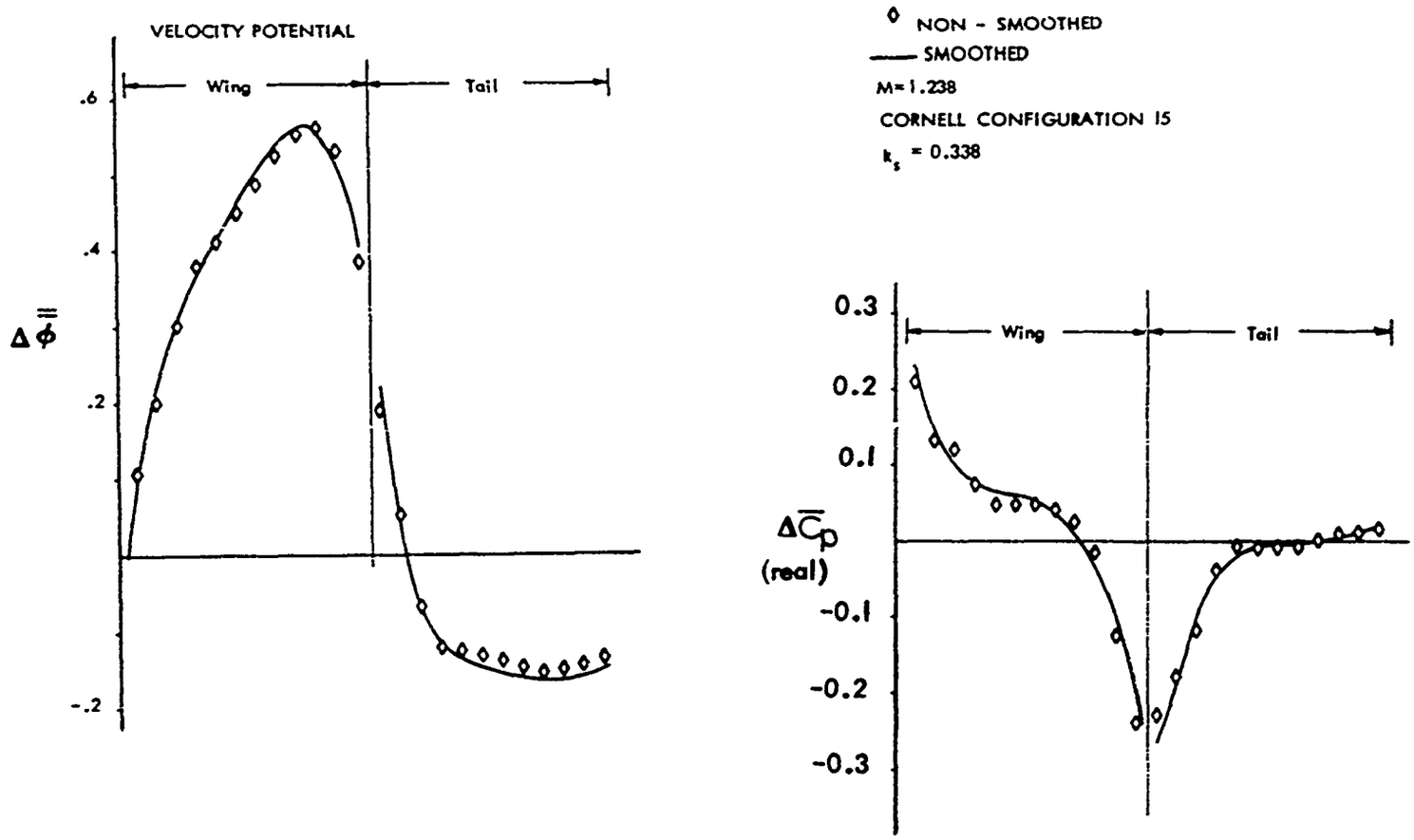

FIGURE 42 APPLICATION OF CRDFT*. TRUE. AND RESULTING CHORDWISE LOADINGS./AT = 0.85

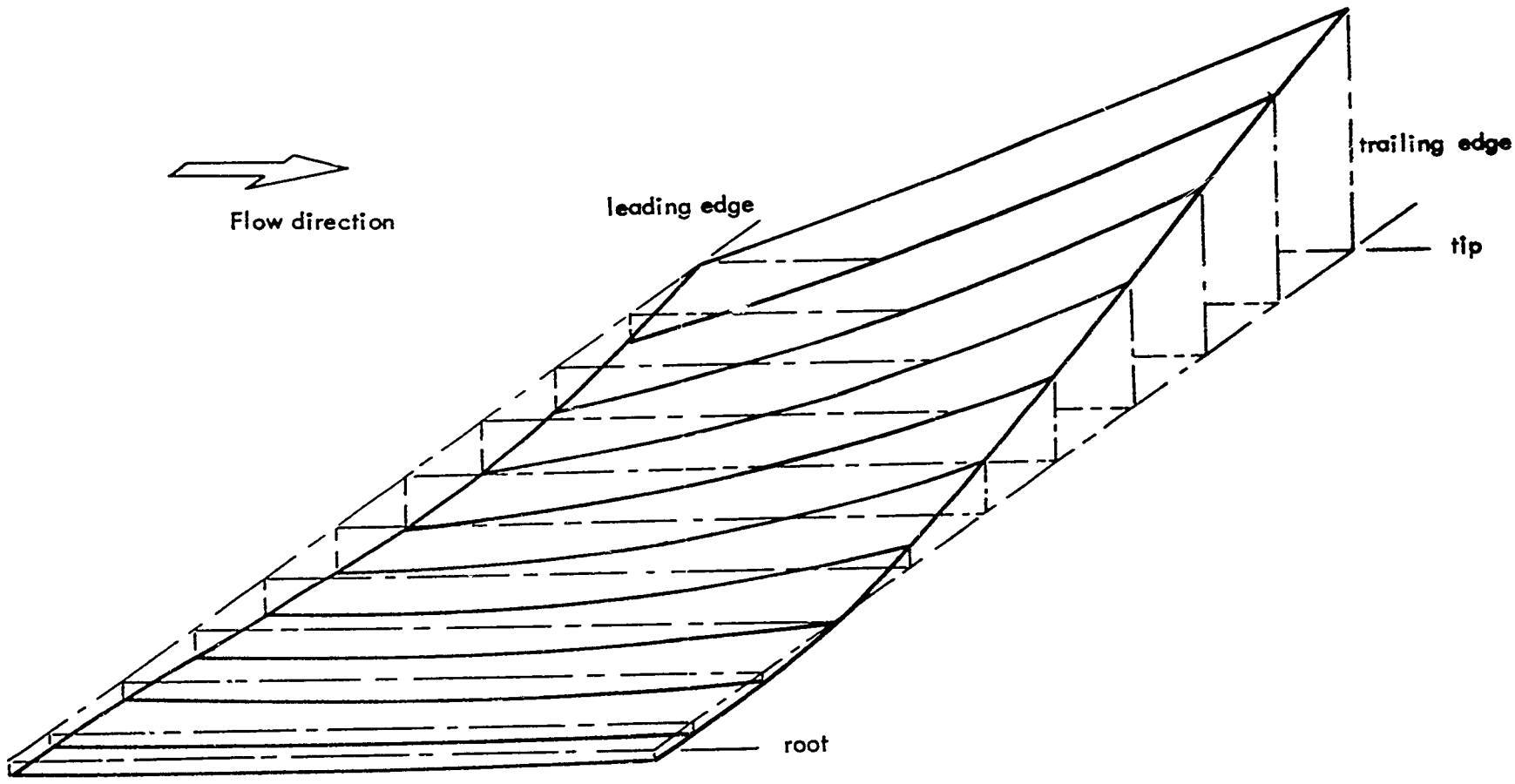

FIGURE 43 WING DEFLECTION SHAPE, MODE NO. 3, CORNELL CONFIGURATION 15

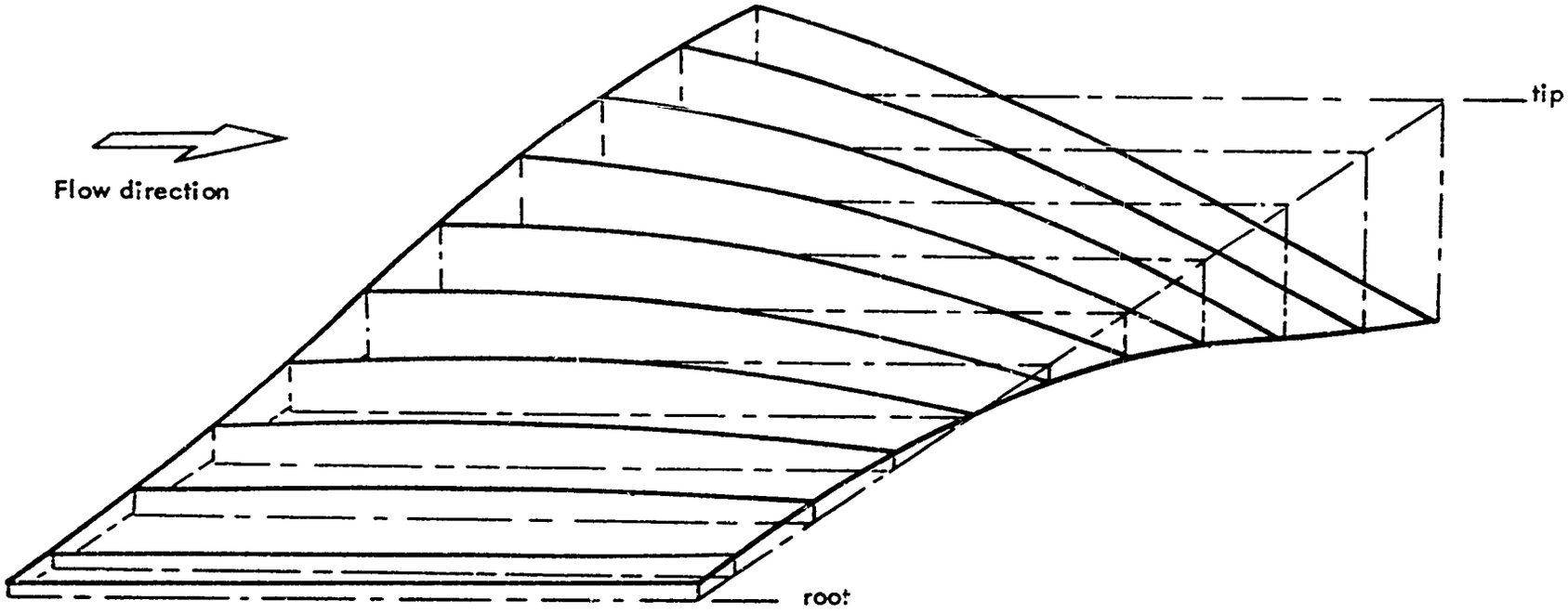

FIGURE 44 WING DEFLECTION SHAPE, MODE NO. 4, CORNELL CONFIGURATION 15

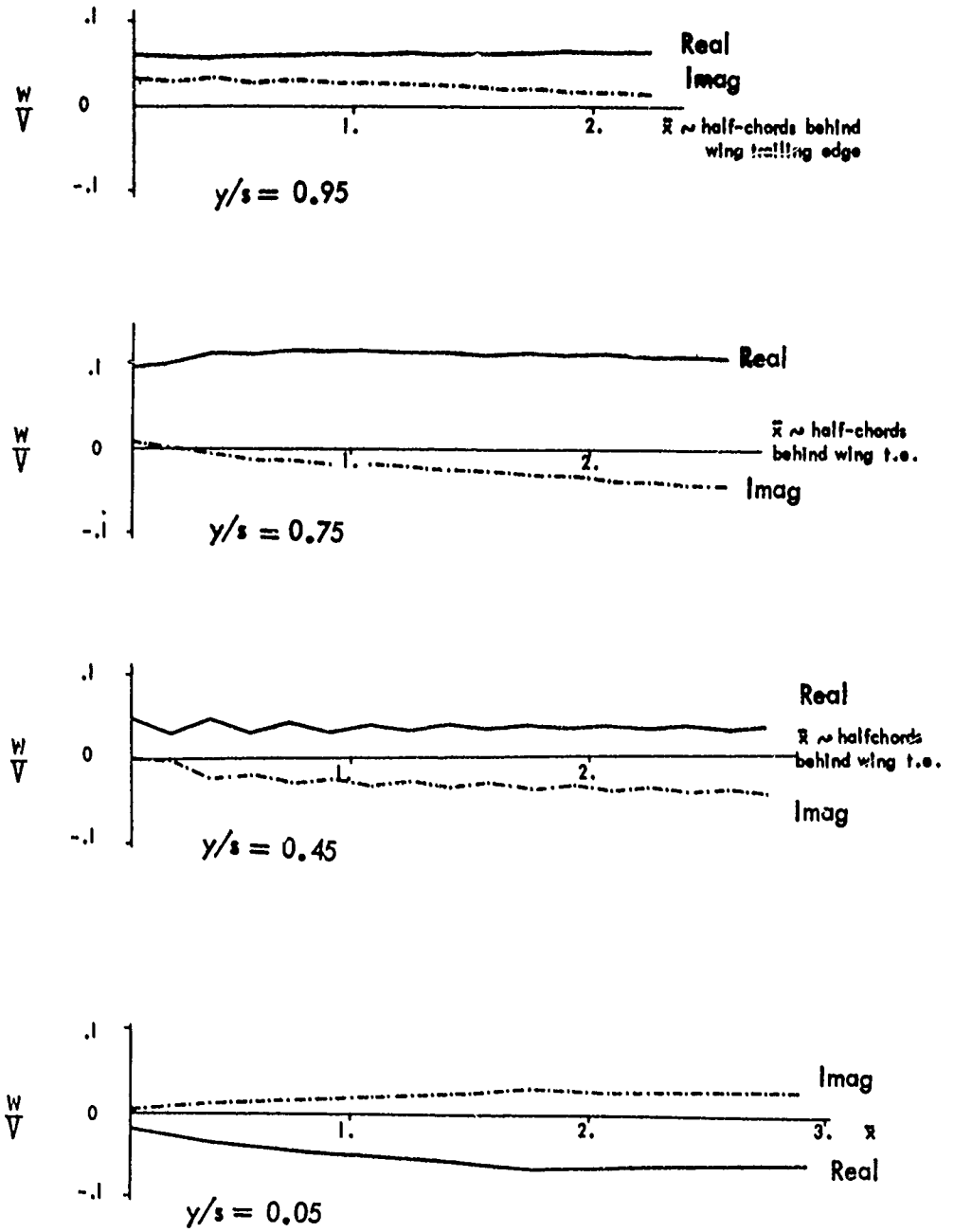

FIGURE 45 DOWNWASH DISTRIBUTION IN WING WAKE, MODE NO. 3, M = 1.238, k_s = .3425

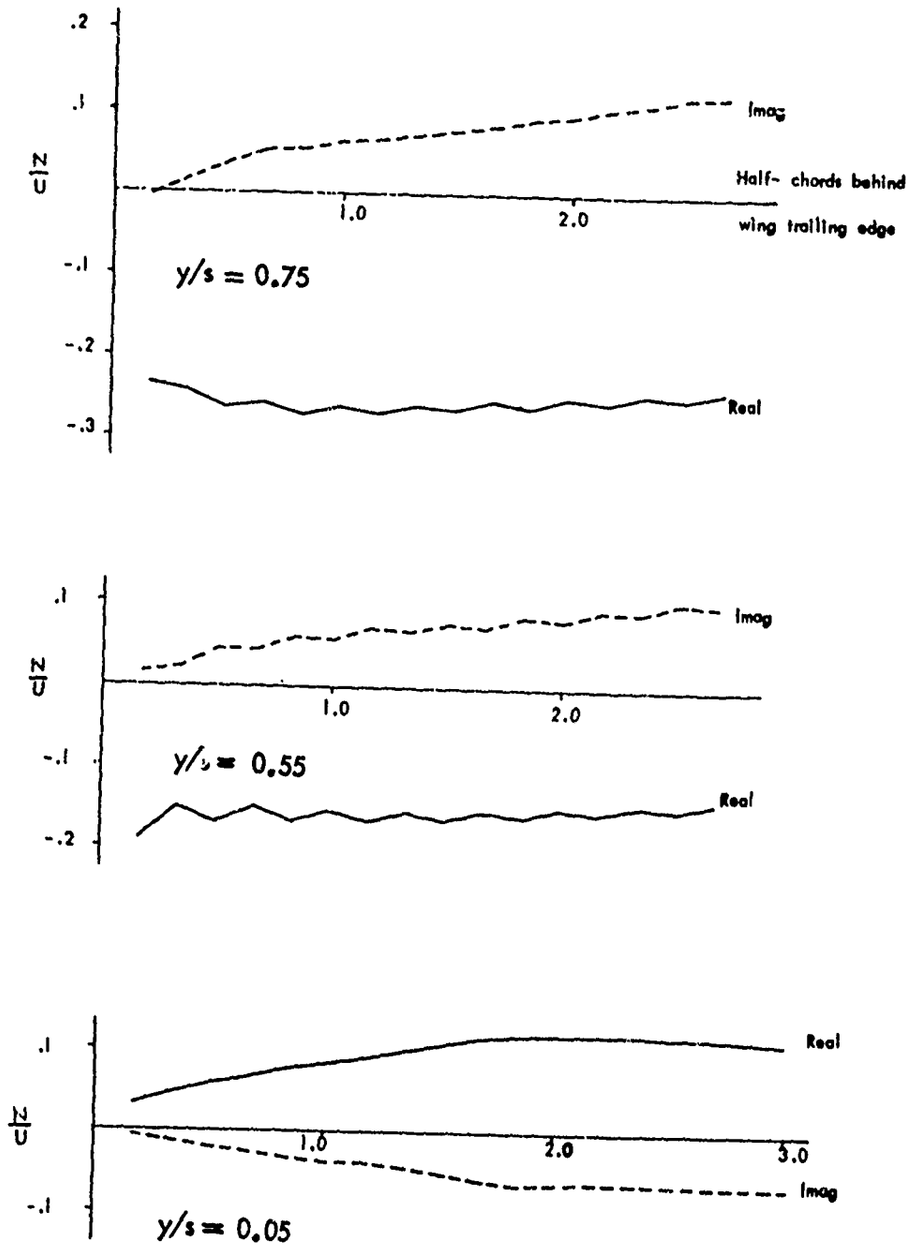

FIGURE 46 NORMAL WASH DISTRIBUTION IN WING WAKE, MODE NO. 4, $M = 1.238$, $k_s = 0.3425$

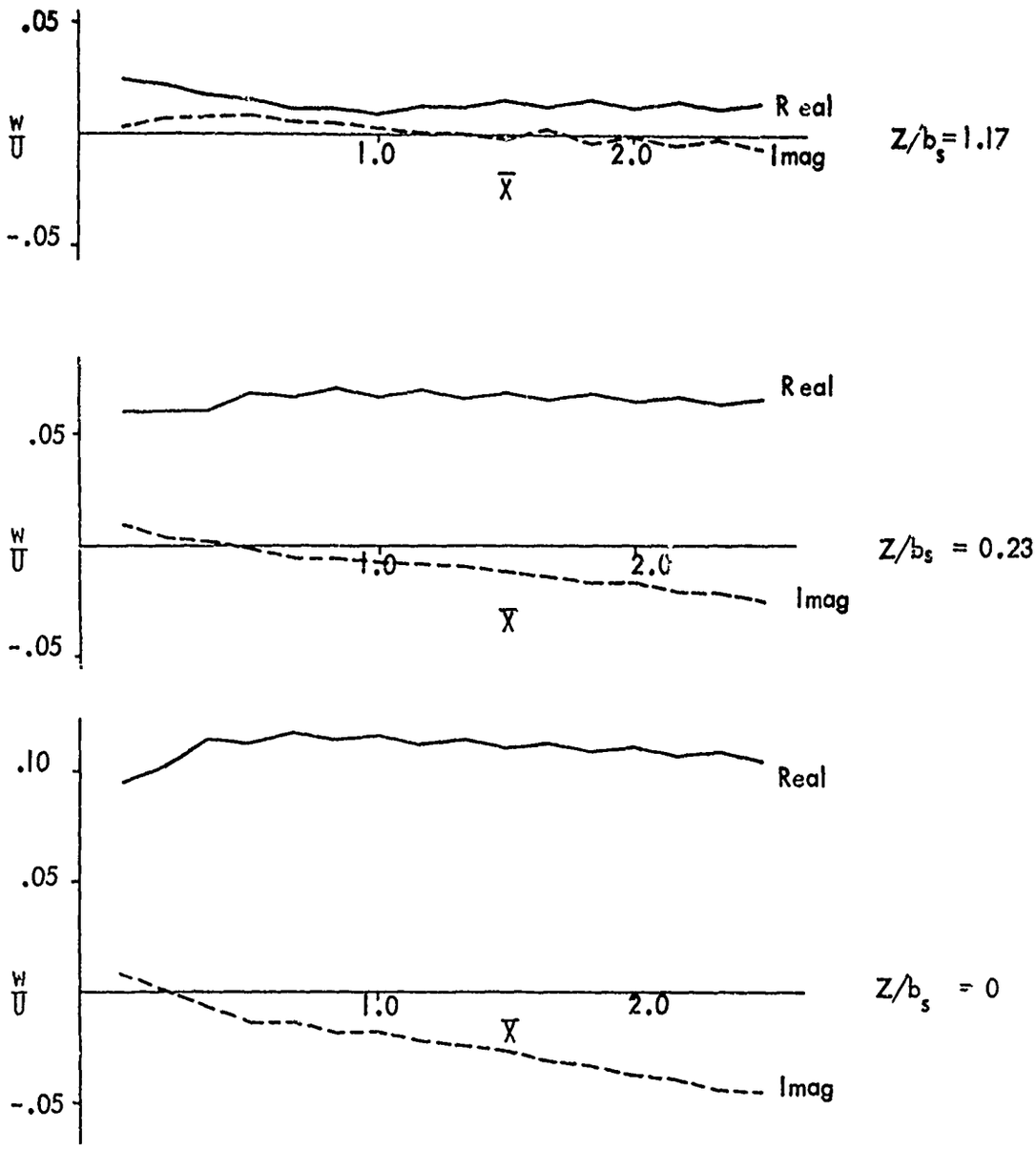

FIGURE 47 SPATIAL VARIATION IN VERTICAL WASH, CONFIGURATION 15

$M = 1.238$, $k_s = 0.338$, $\eta = 0.85$

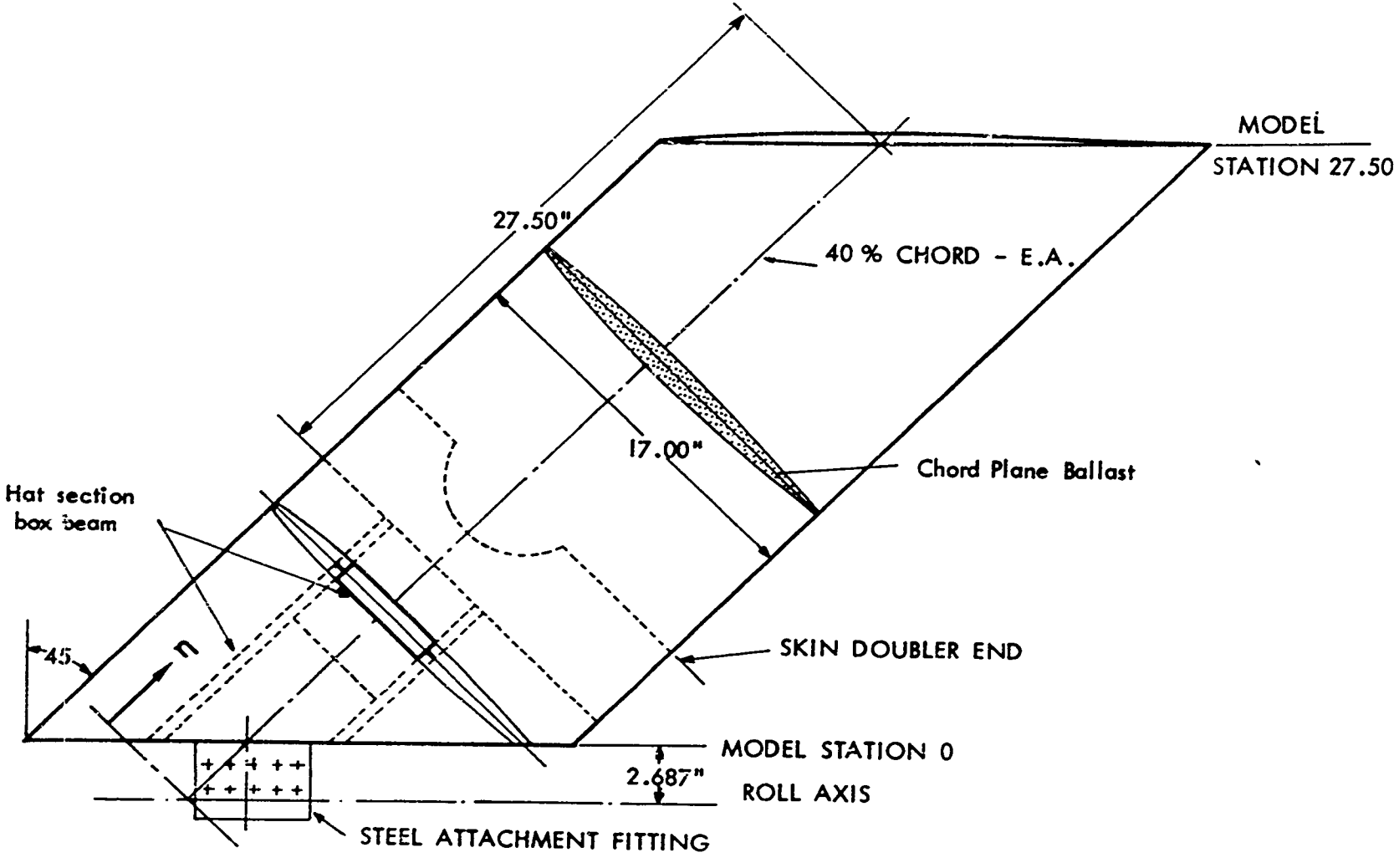

FIGURE 48 45° SWEPT MODEL ASSEMBLY. (Reproduced from reference 2)

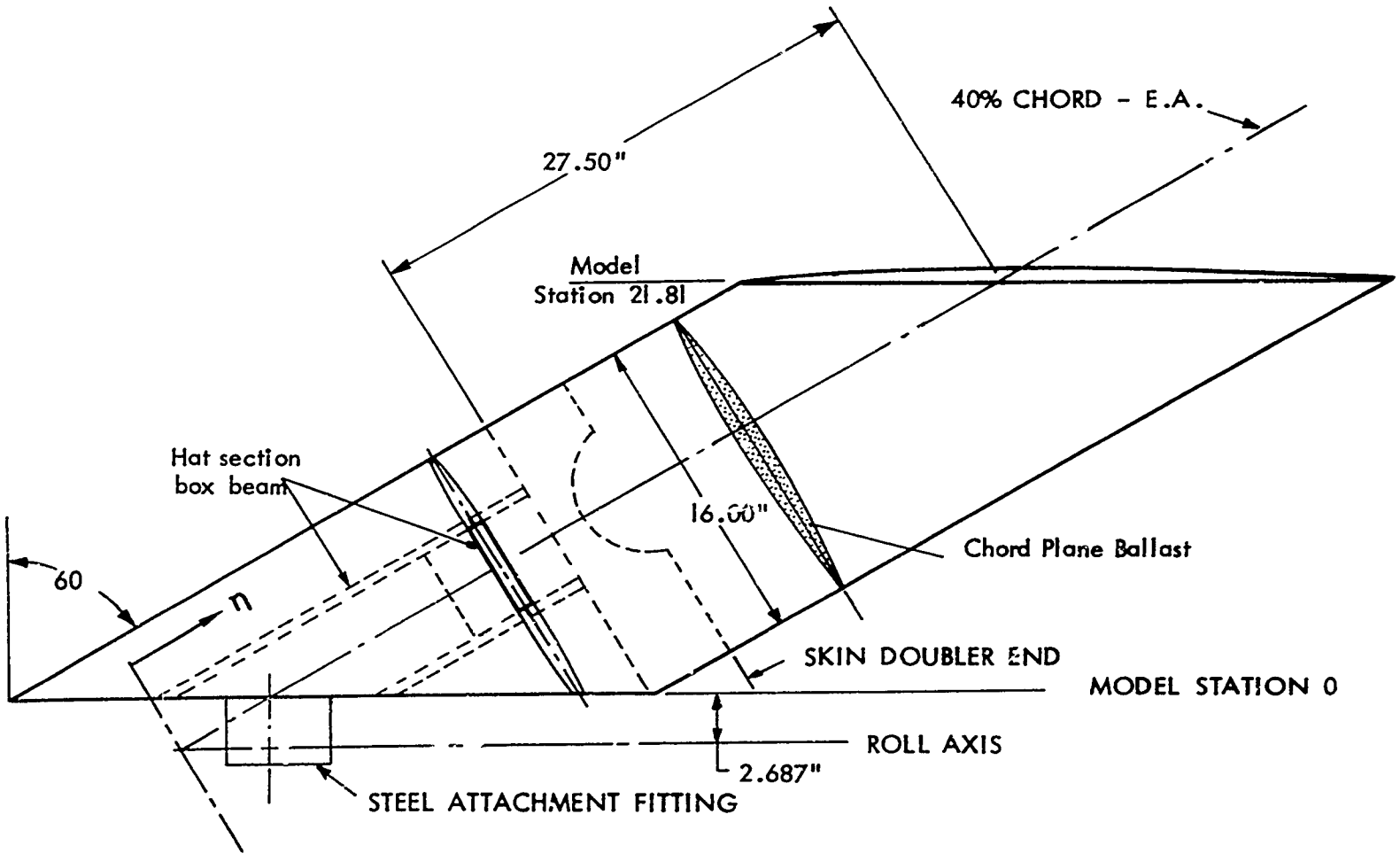

FIGURE 49 60° SWEPT MODEL ASSEMBLY. (Reproduced from reference 2)

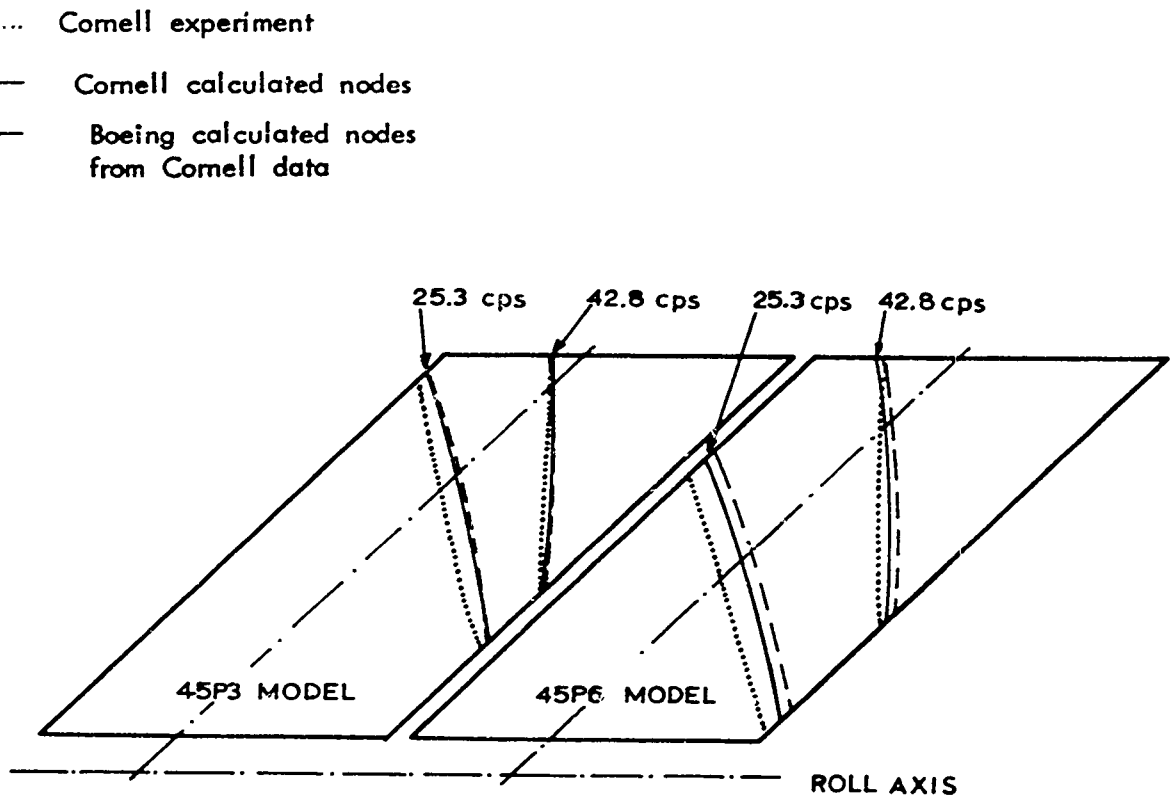

FIGURE 50 COMPARISON OF CALCULATED AND EXPERIMENTAL NODE LINES, TEST CONFIGURATION 15

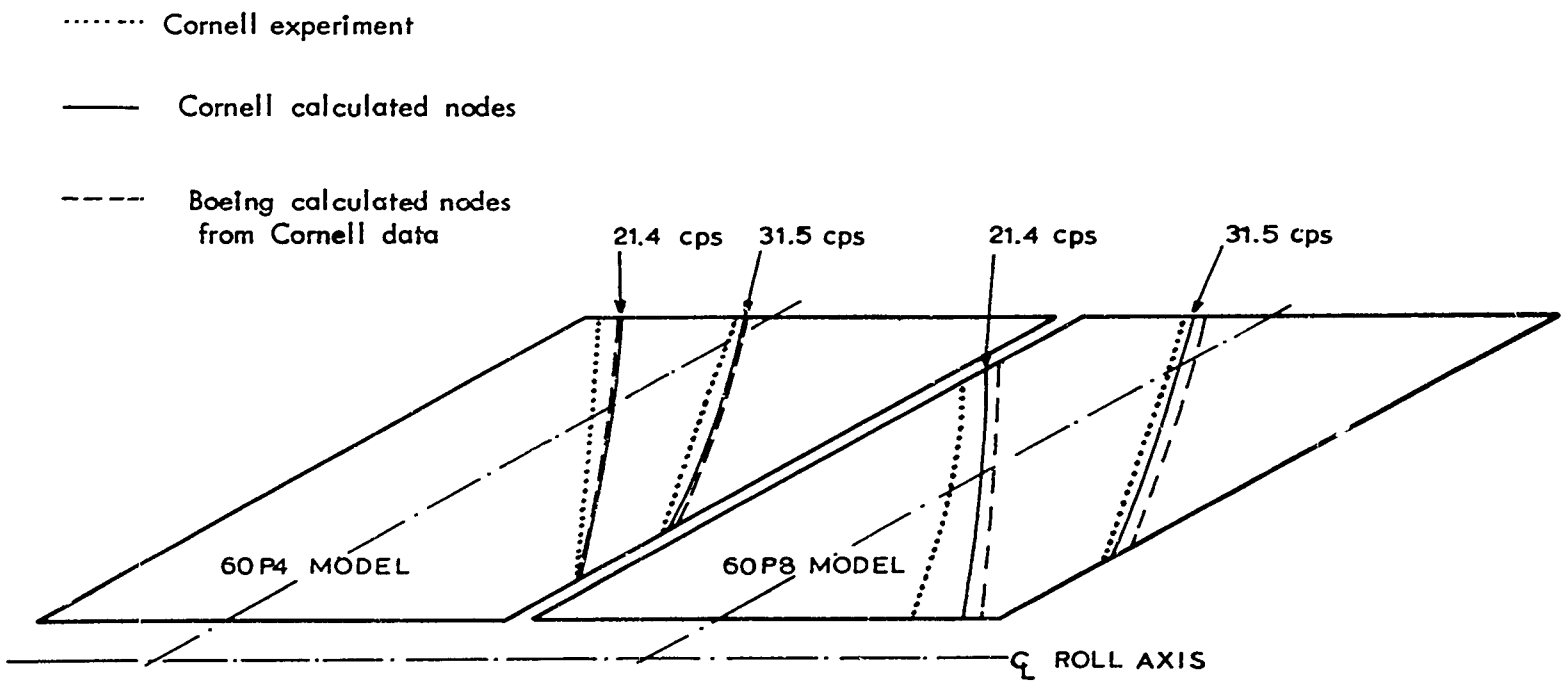

FIGURE 51 COMPARISON OF CALCULATED AND EXPERIMENTAL NODE LINES, TEST CONFIGURATION 22

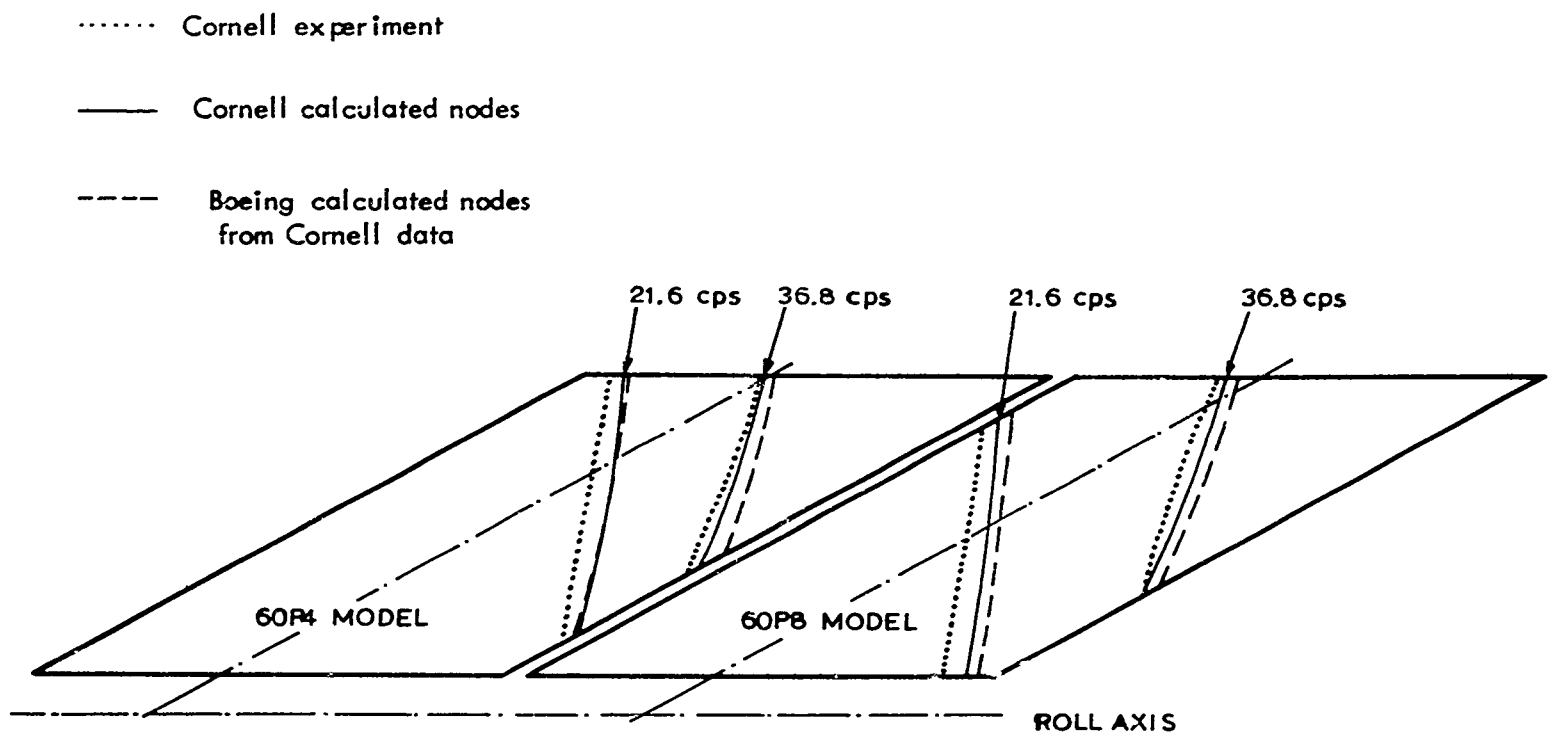

FIGURE 52 COMPARISON OF CALCULATED AND EXPERIMENTAL NODE LINES, TEST CONFIGURATION 23

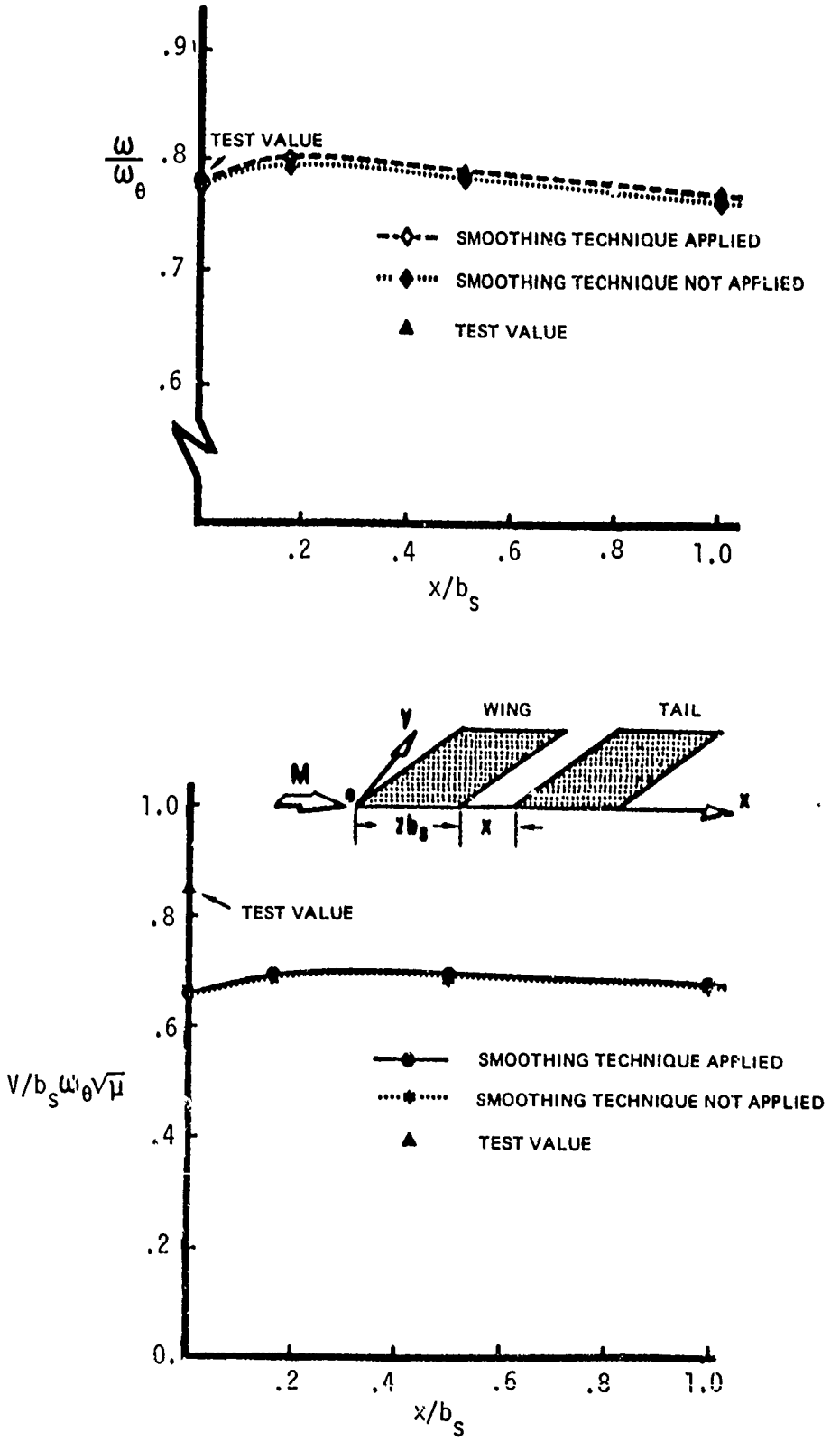

Figure 53. Flutter Speed and Frequency vs Horizontal Separation
For Configuration 15, 45° Swept Model, Mach Number = 1.238, $z/b_s = 0$

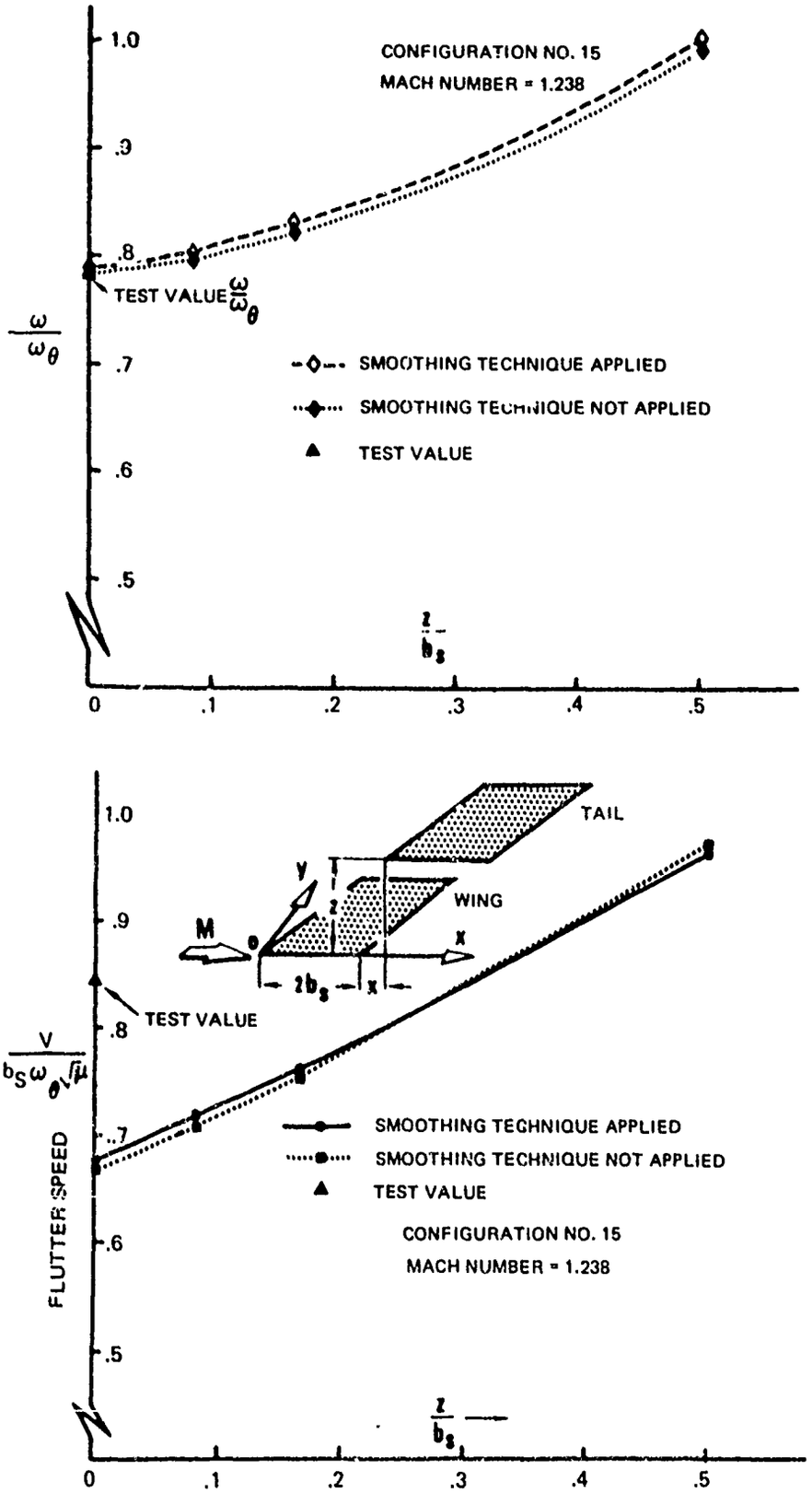

Figure 54. Flutter Speed and Frequency vs Vertical Separation for Configuration 15, 45° Swept Model, Mach Number = 1.238, $x/b_s = 0.505$

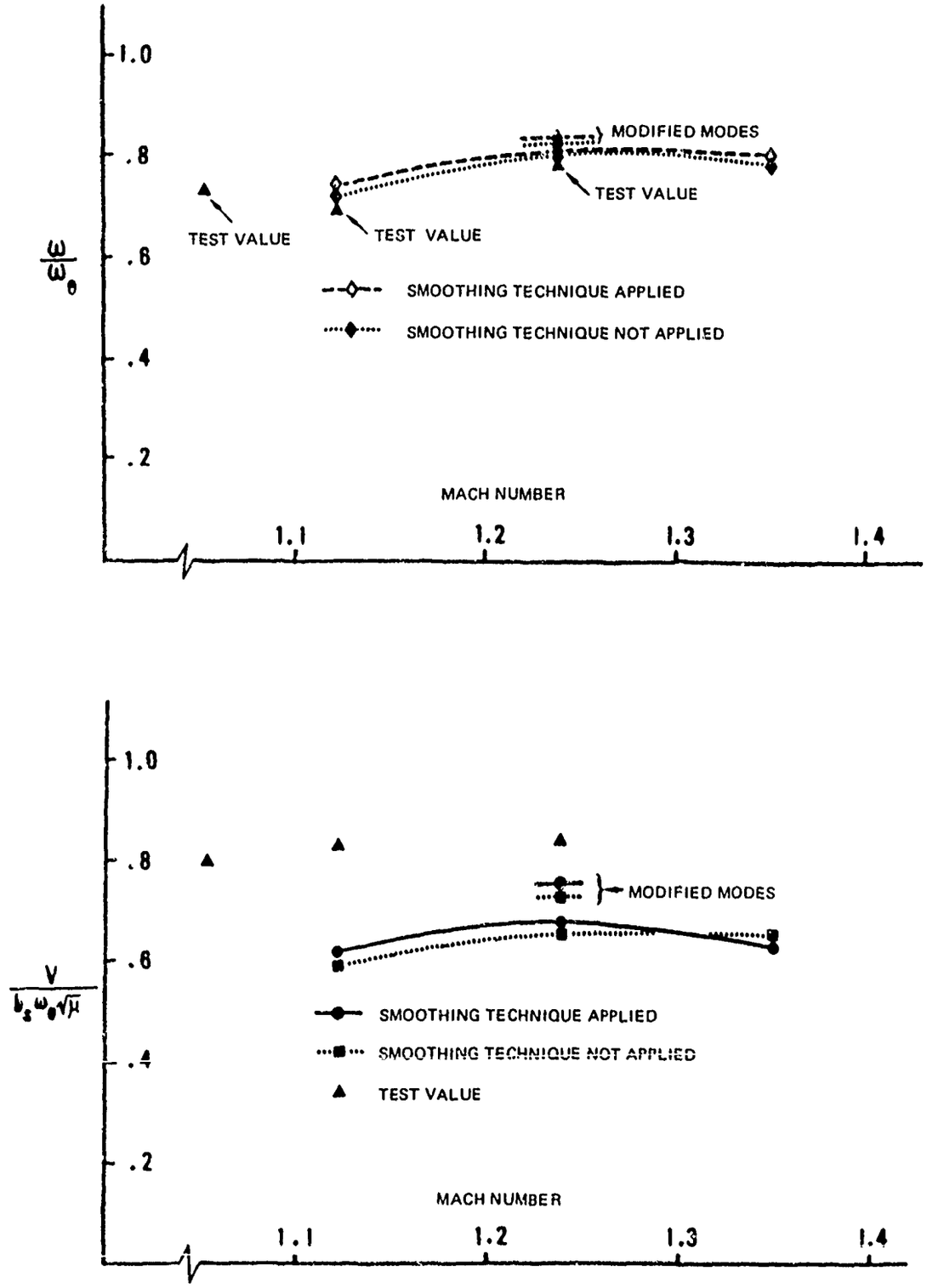

Figure 55. Flutter Speed and Frequency vs Mach Number for Configuration 15, 45° Swept Model, $z/b_s = 0$, $x/b_s = 0.166$

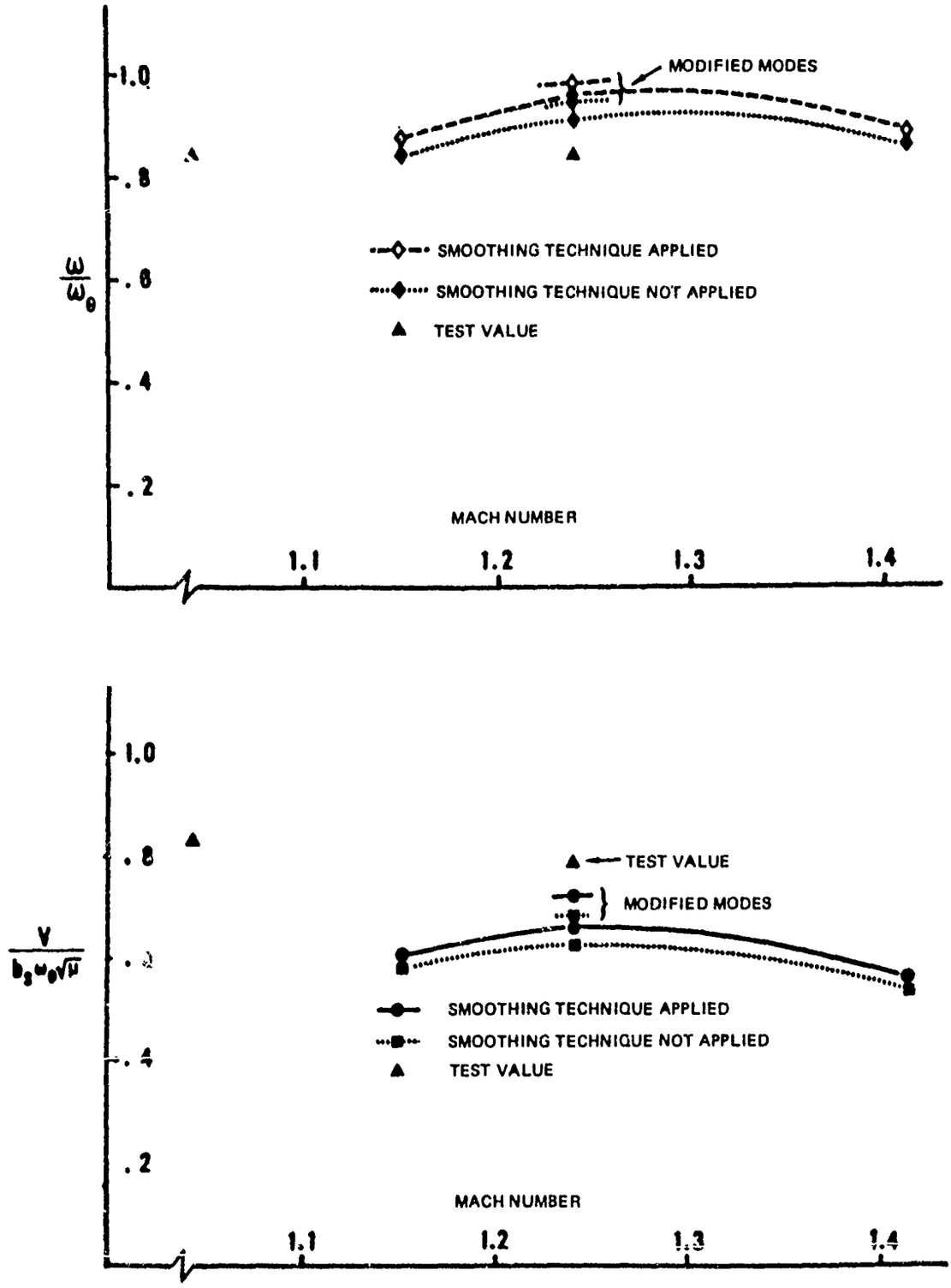

Figure 56. Flutter Speed and Frequency vs Mach Number for Configuration 22, 60° Swept Model, $z/b_s = 0$, $x/b_s = 0.19$

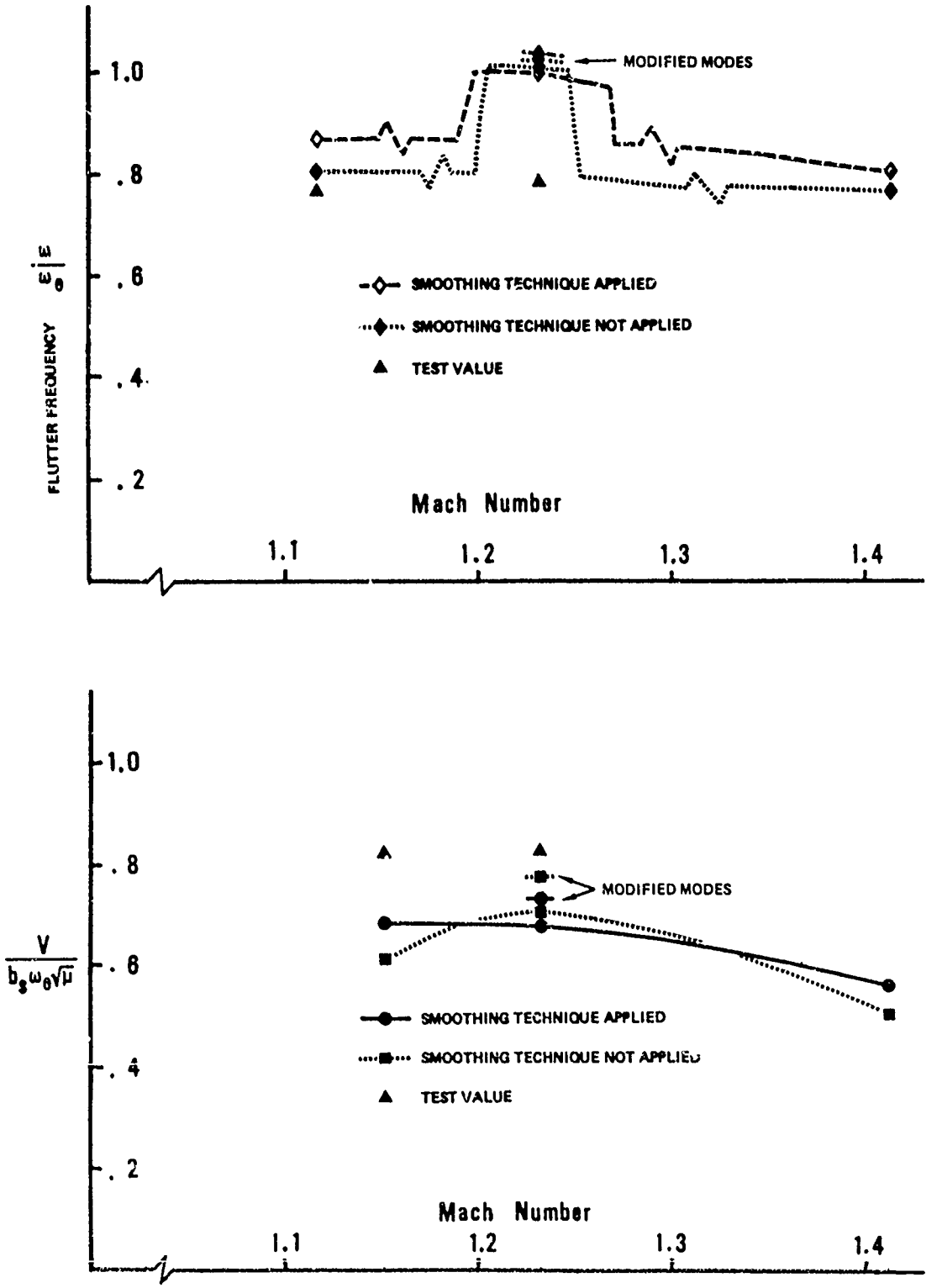

Figure 57 Flutter Speed and Frequency vs Mach Number for Configuration 23, 60° Swept Model, $z/b_s = 0$, $x/b_s = 0.19$

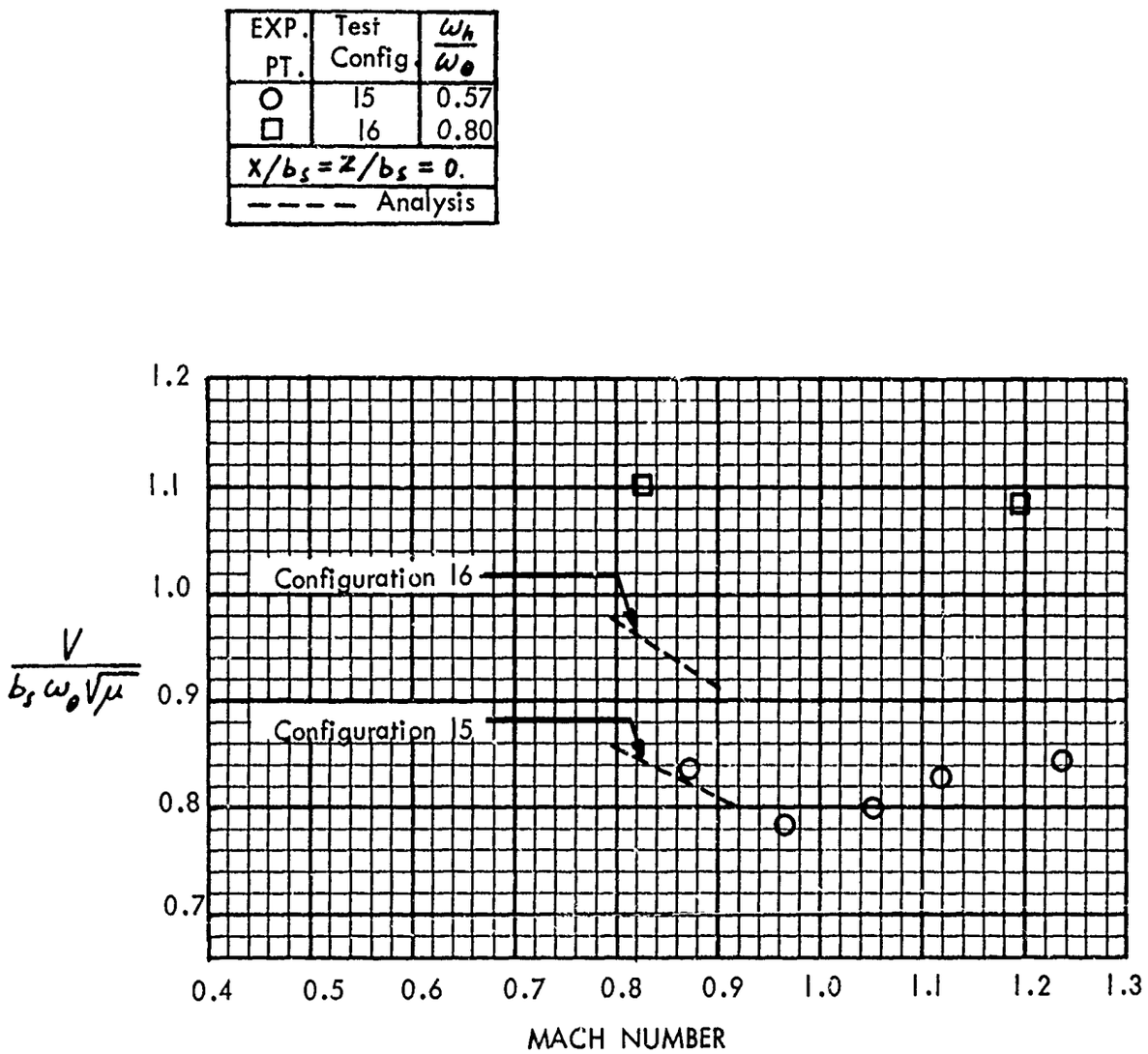

FIGURE 58 FLUTTER SPEED VS MACH NUMBER, 45° MODELS

(Reproduced from reference 15)

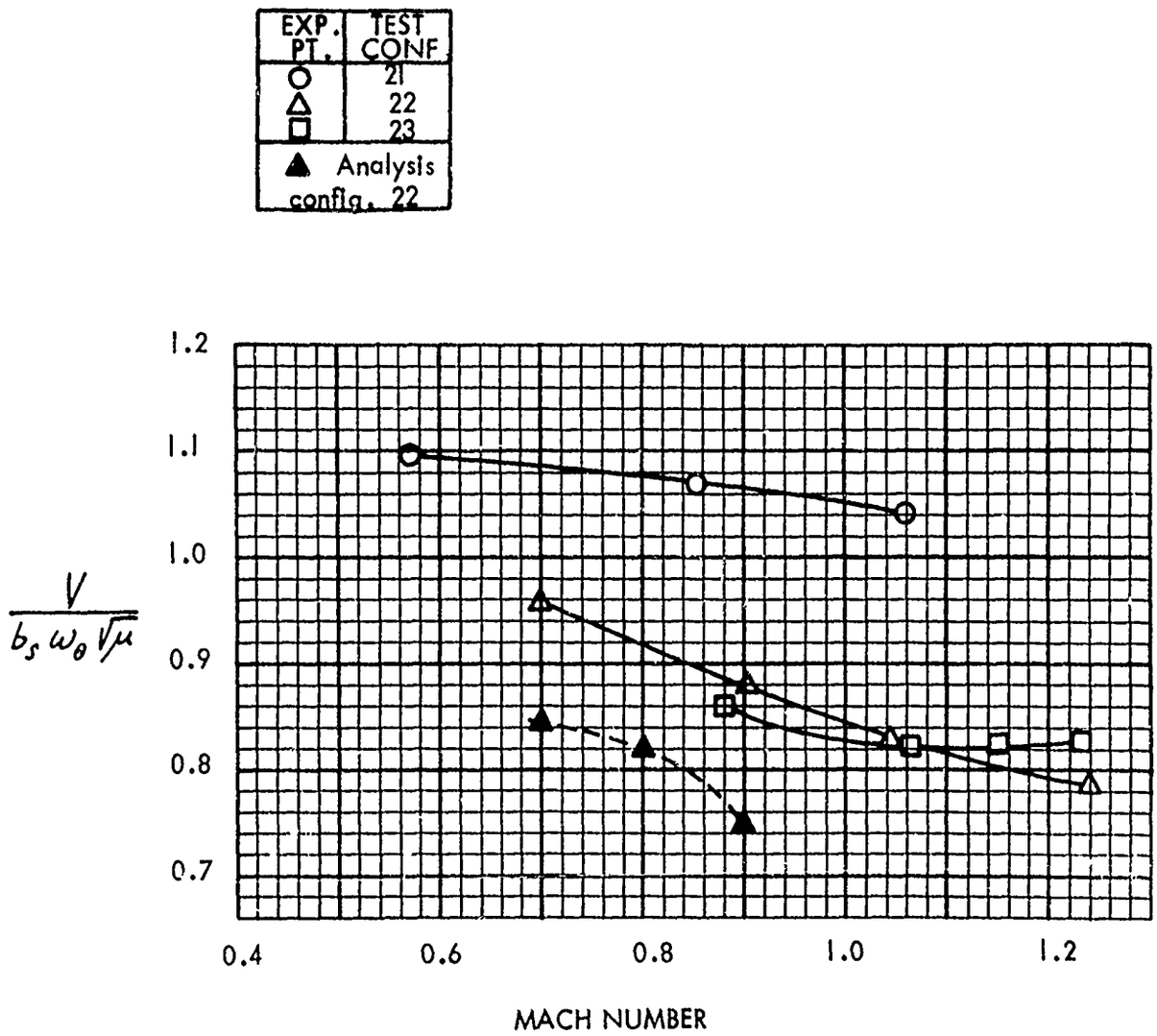

FIGURE 59 FLUTTER SPEED VS MACH NUMBER, 60° SWEPT MODELS

(Reproduced from reference 15)

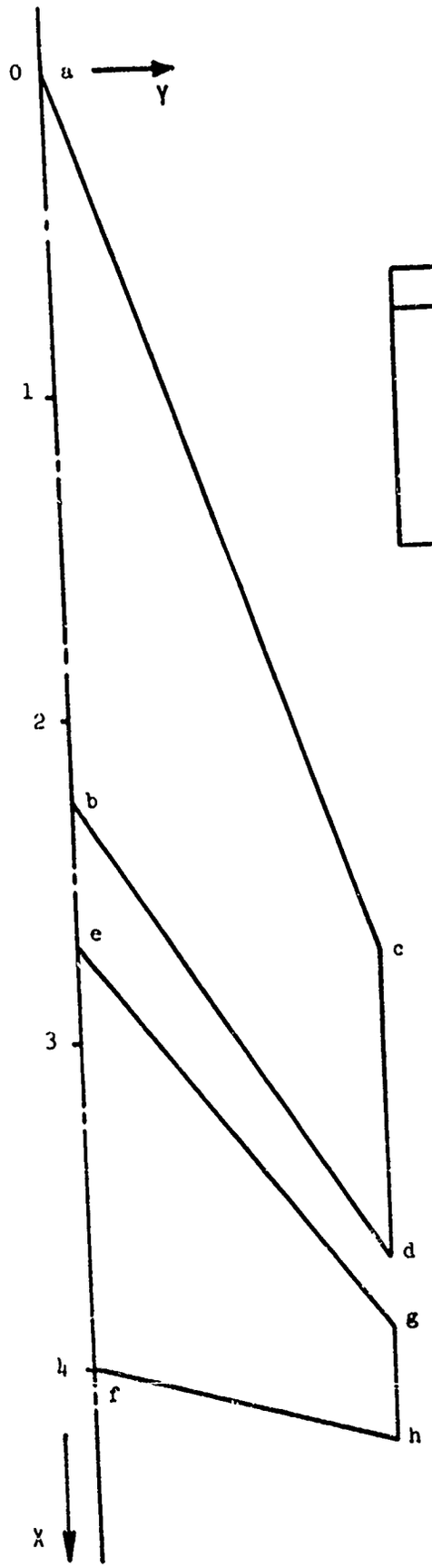

	x	y
a	0	0
b	2.25	0
c	2.75	1.00
d	3.70	1.00
e	2.70	0
f	4.00	0
g	3.90	1.00
h	4.25	1.00

FIGURE 60 AGARD WING-TAIL CONFIGURATION

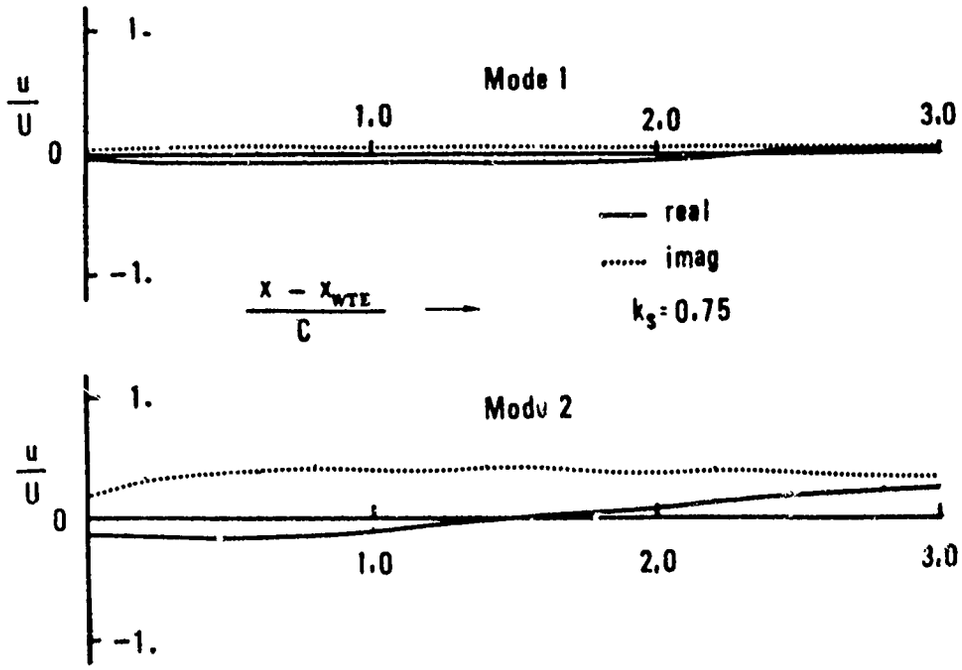

Figure 61 . Longitudinal Wash on A Sampling Chord, y/s = 0.72, z/s = 0.2

For k_s = 0.75 and M = 1.56 (Antisymmetric)

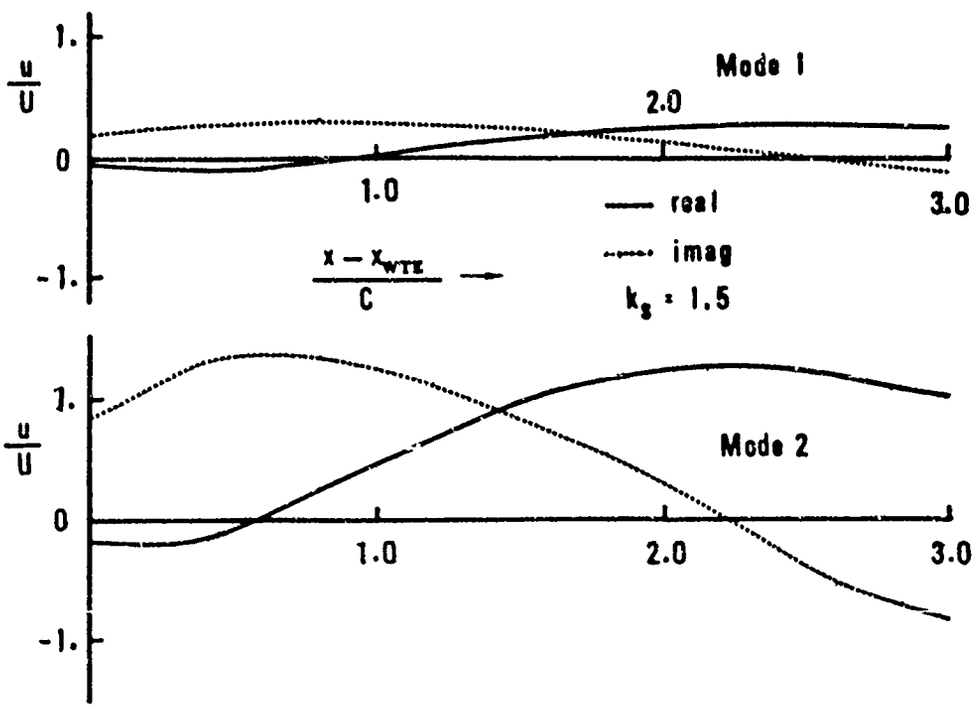

Figure 62. Longitudinal Wash on A Sampling Chord, y/s = 0.72, z/s = 0.2

For k_s = 1.5 and M = 1.56 (Antisymmetric)

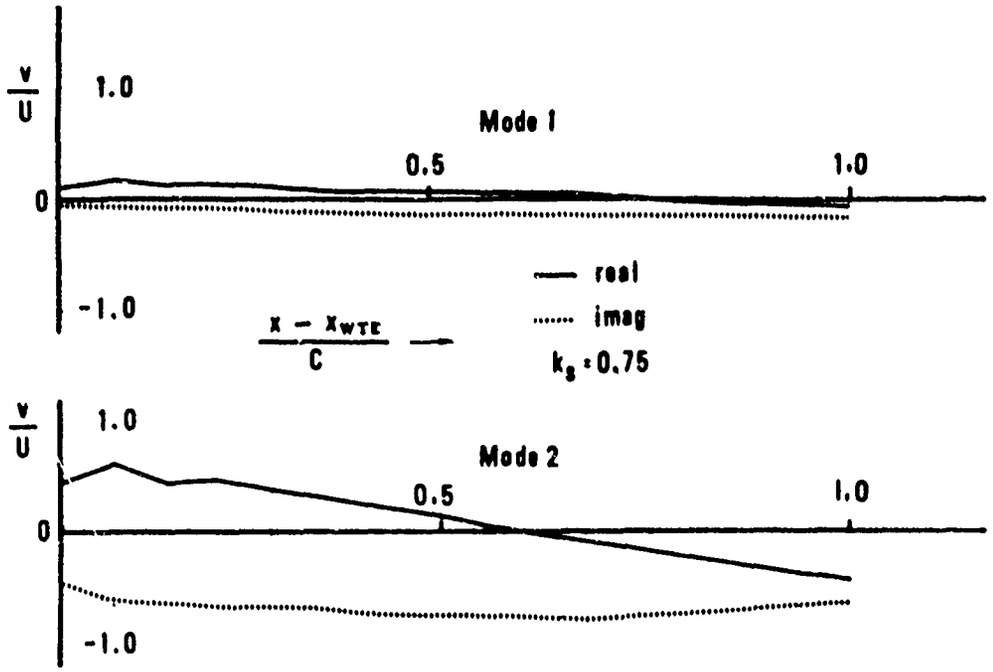

Figure 63 . Sidewash on A Sampling Chord, y/s = 0.72, z/s = 0.1
For k_s = 0.75 and M = 1.56 (Antisymmetric)

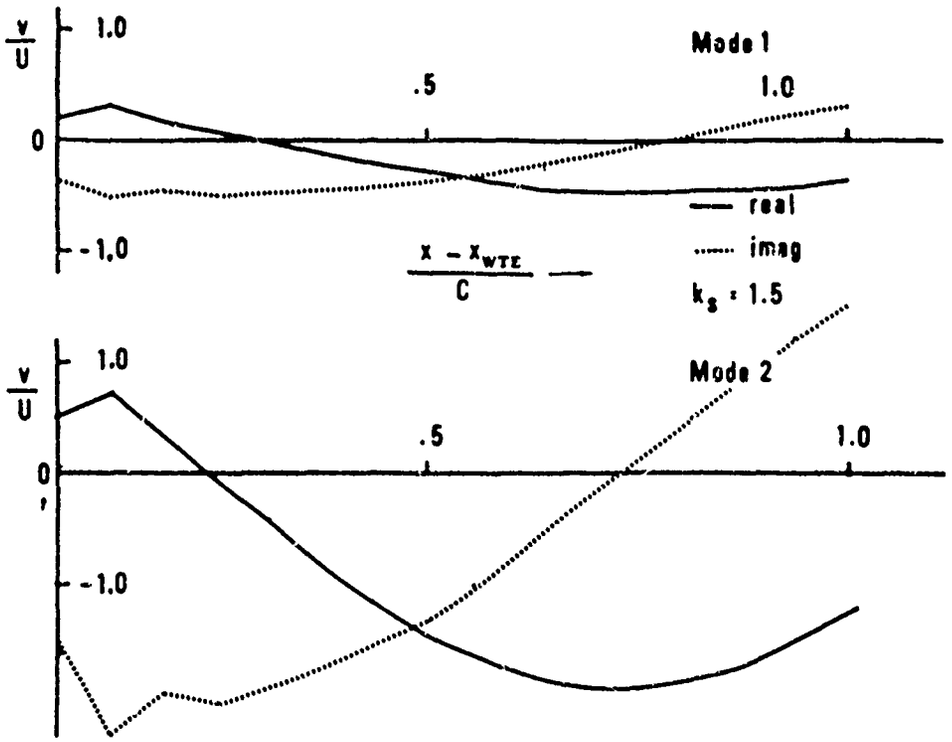

Figure 64 . Sidewash on A Sampling Chord, y/s = 0.72, z/s = 0.1
For k_s = 1.5 and M = 1.56(Antisymmetric)

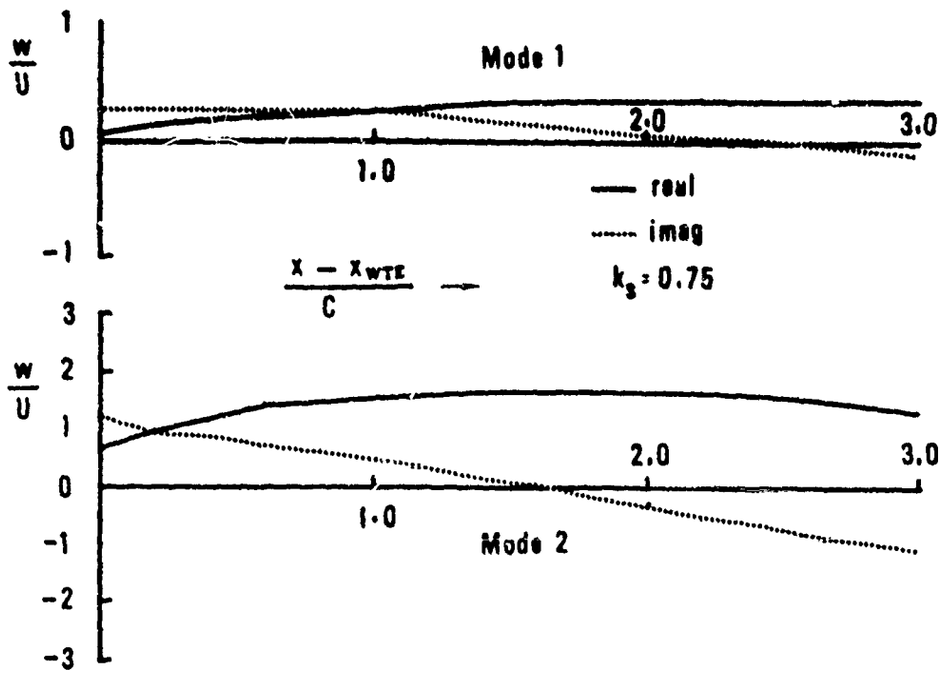

Figure 65 . Upwash on A Sampling Chord, y/s = 0.056, z/s = 0.5
For k_s = 0.75 and M = 1.56 (Antisymmetric)

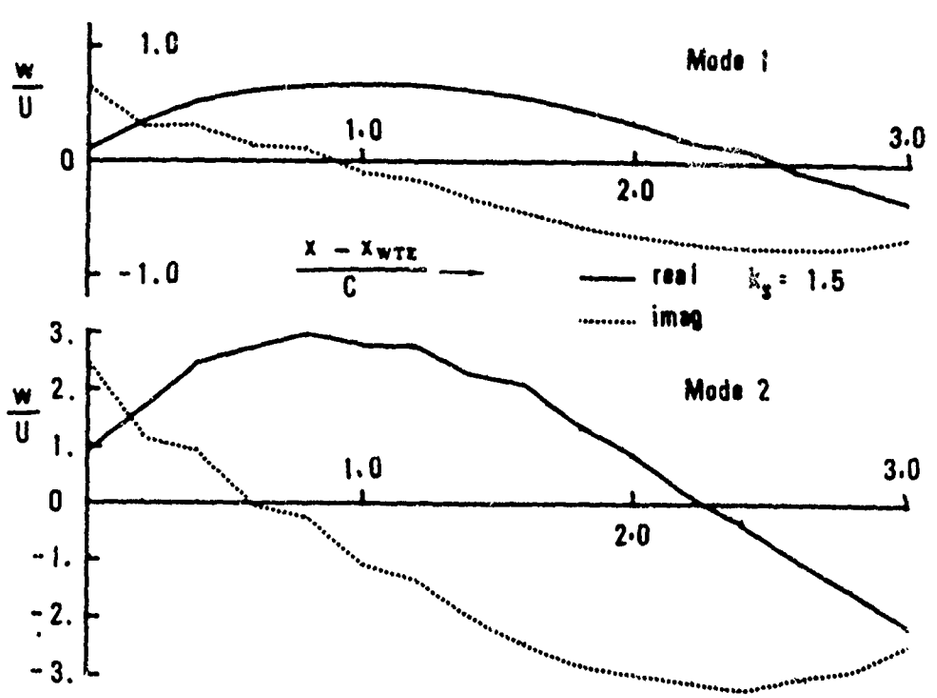

Figure 66 . Upwash on A Sampling Chord, y/s = 0.056, z/s = 0.5
For k_s = 1.5 and M = 1.56 (Antisymmetric)

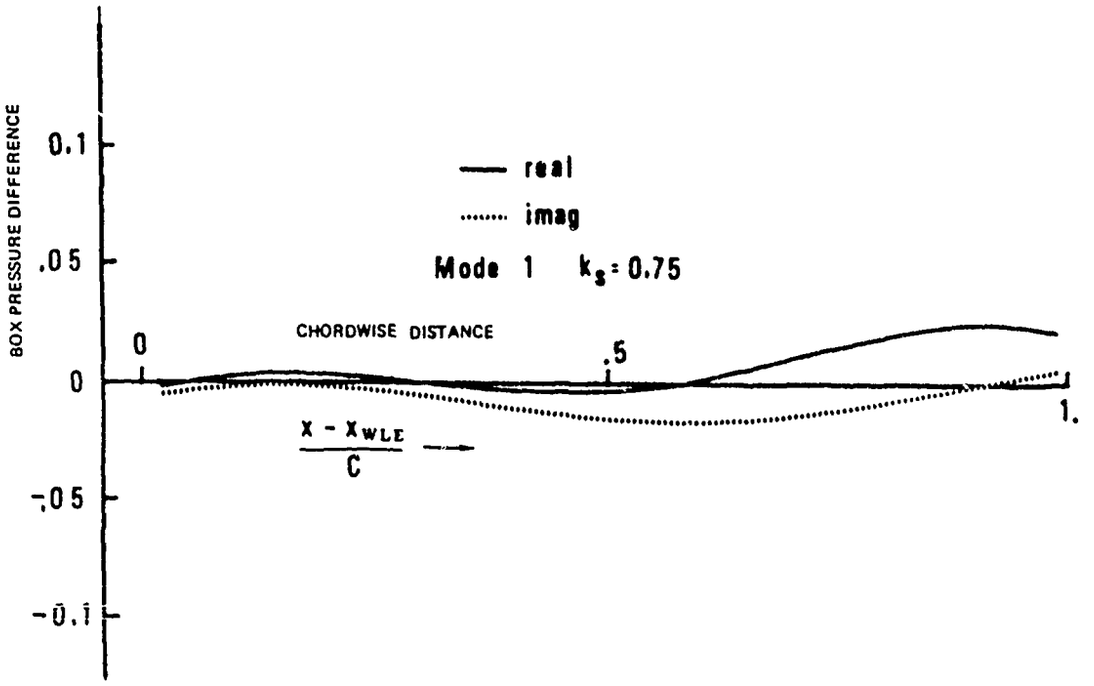

Figure 67. Pressure Distribution Along Chord No. 1, y/s = 0.056 For k_s = 0.75, M = 1.56 and Mode 1 (Antisymmetric Bending Mode)

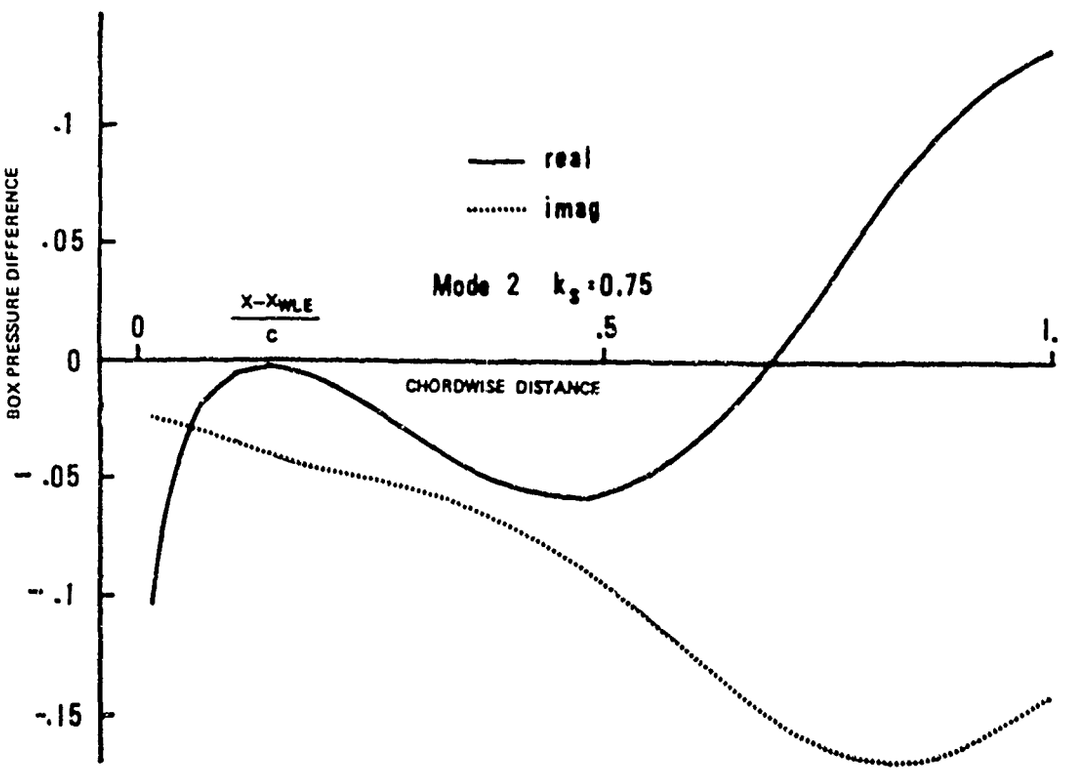

Figure 68. Pressure Distribution Aong Chord No. 1, y/s = 0.056 For k_s = 0.75, M = 1.56 and Mode 2 (Antisymmetric Torsion Mode)

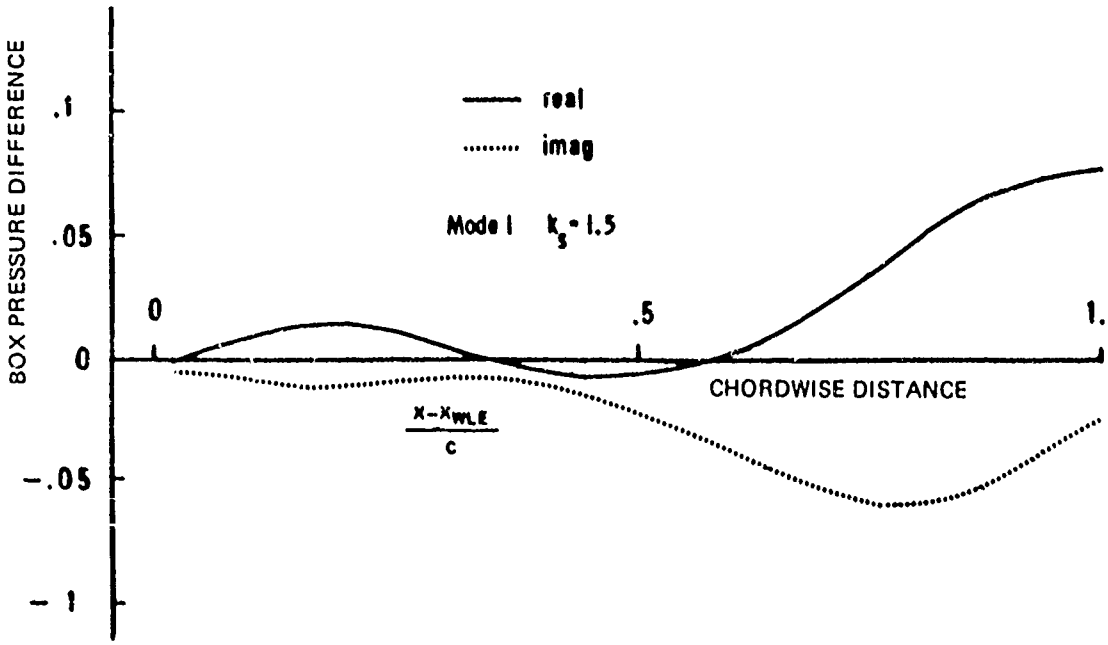

Figure 69. Pressure Distribution Along Chord No. 1, y/s = 0.056
For k_s = 1.5, M = 1.56 and Mode 1 (Antisymmetric Bending Mode)

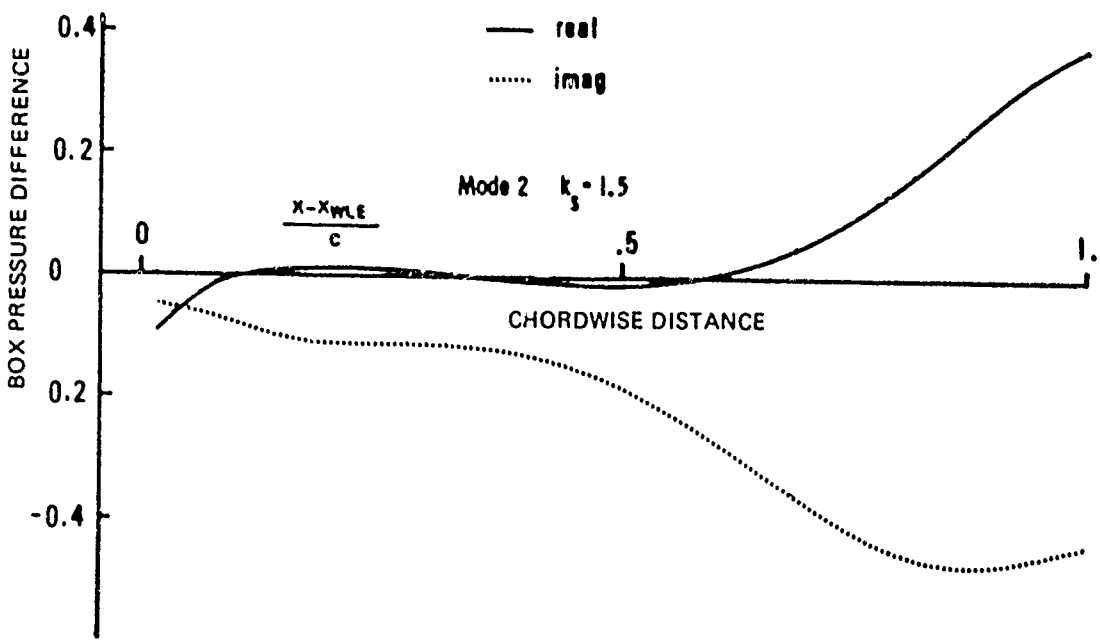

Figure 70. Pressure Distribution Along Chord No. 1, y/s = 0.056 For k_s = 1.5,
M = 1.56 and Mode 2 (Antisymmetric Torsion Mode)

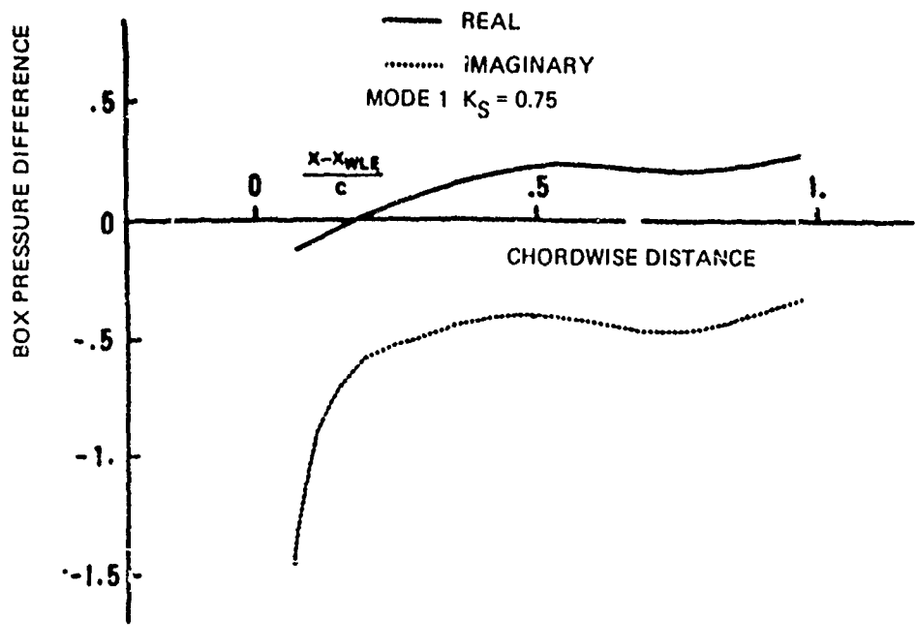

Figure 71. Pressure Distribution Along Chord No. 7, y/s = 0.72 For k_s = 0.75 M = 1.56 and Mode 1 (Antisymmetric Bending Mode)

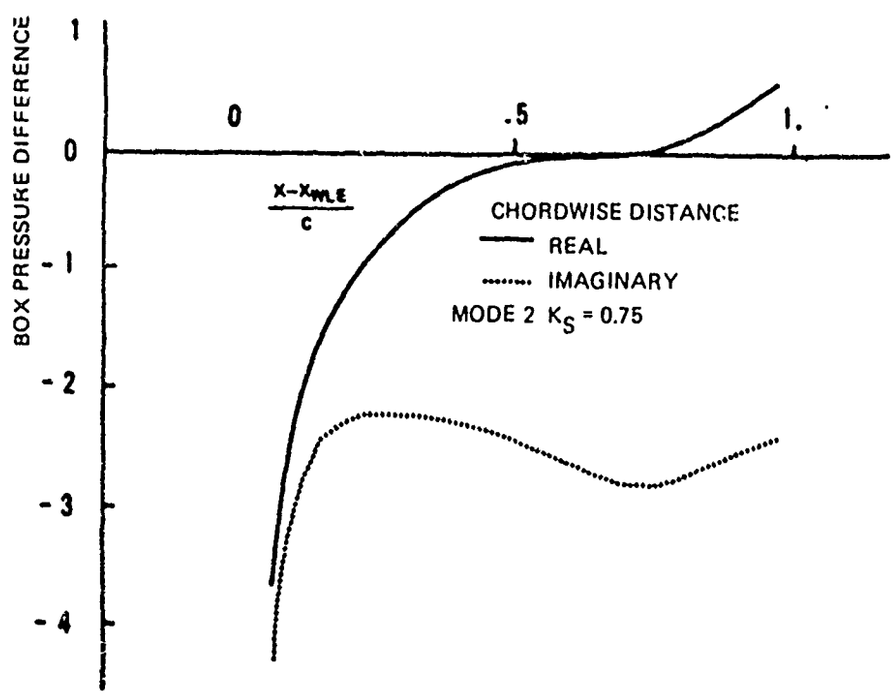

Figure 72. Pressure Distribution Along Chord No. 7, y/s = 0.72 For k_s = 0.75 M = 1.56 and Mode 2 (Antisymmetric Torsion Mode)

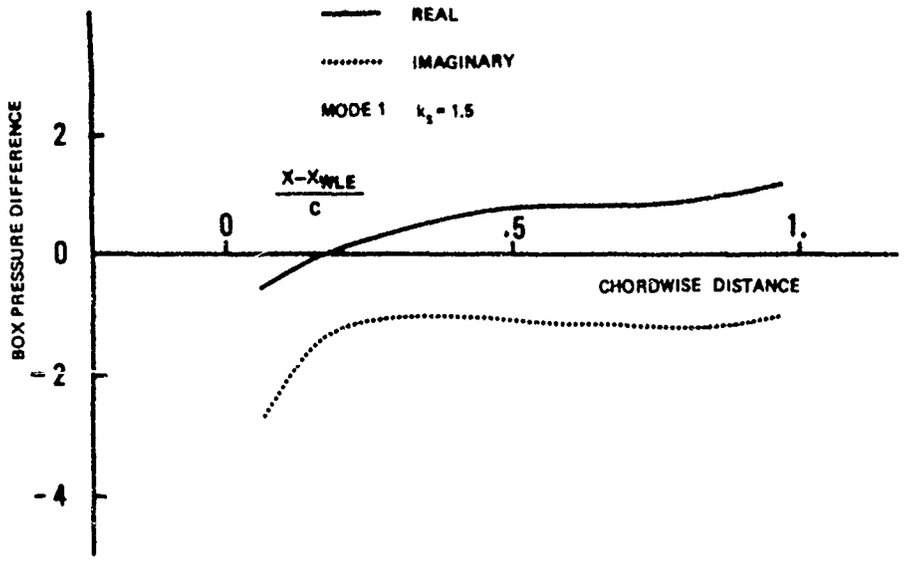

Figure 73. Pressure Distribution Along Chord No. 7, y/s = 0.72 For k_s = 1.5 M = 1.56 and Mode 1 (Antisymmetric Bending Mode)

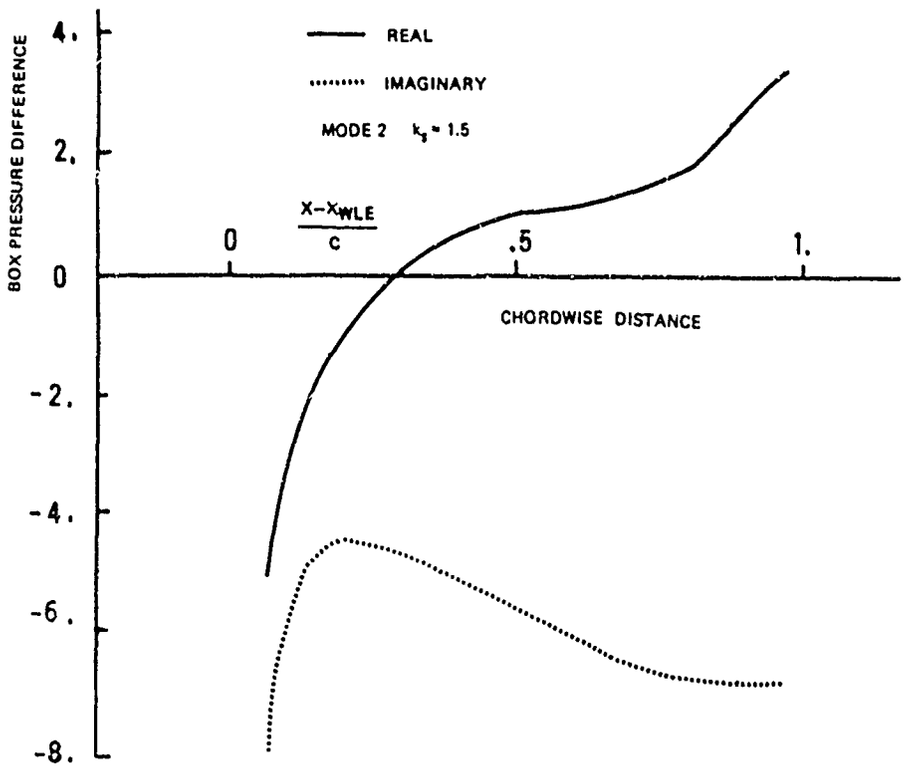

Figure 74. Pressure Distribution Along Chord No. 7, y/s = 0.72 For k_s = 1.5 M = 1.56 and Mode 2 (Antisymmetric Torsion Mode)

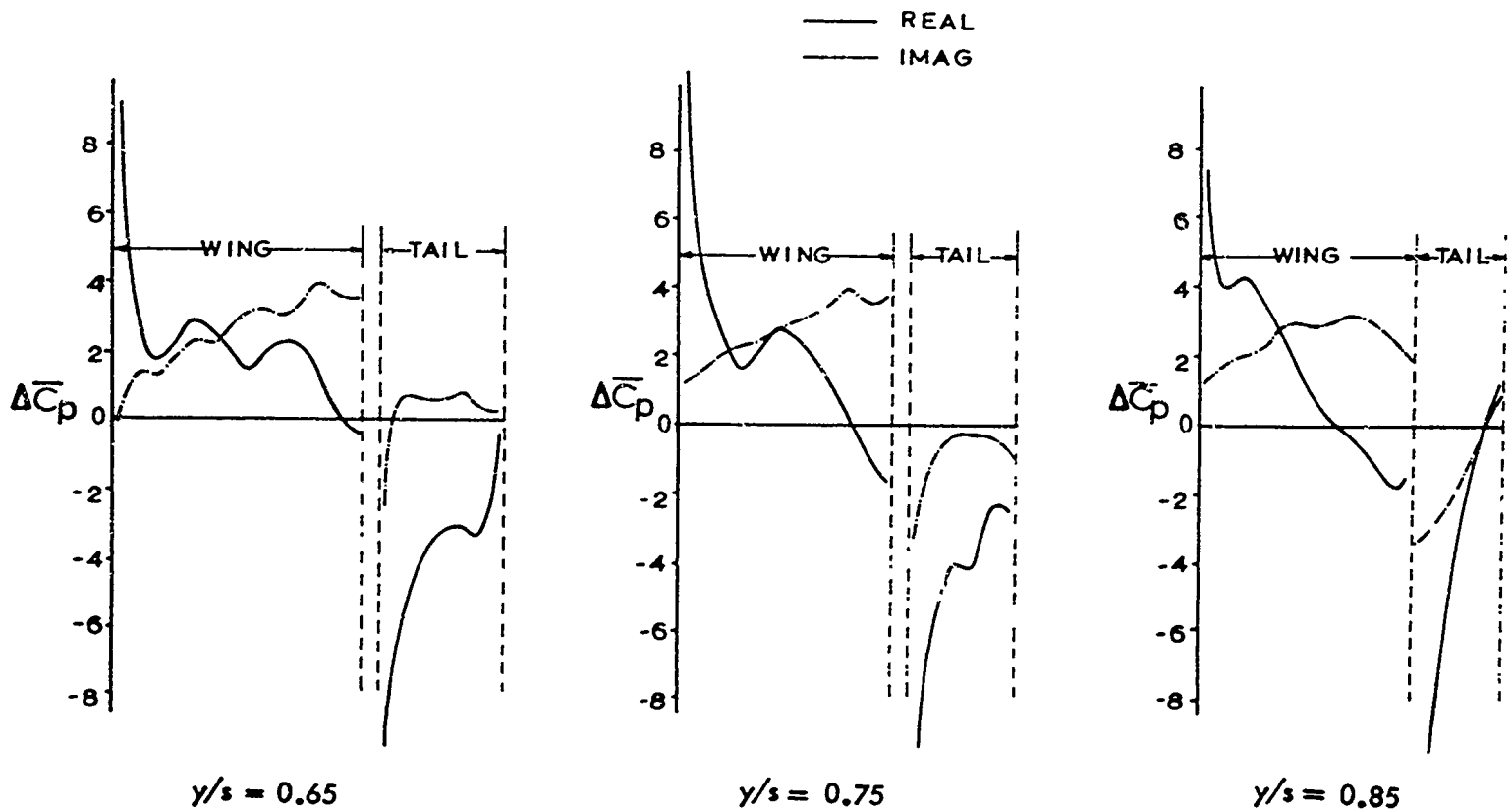

FIGURE 75 CHORDWISE PRESSURE DISTRIBUTION, AGARD PLANFORM, SMALL SEPARATION, WING PITCH MODE, M = 1.414, k_s = 0.75

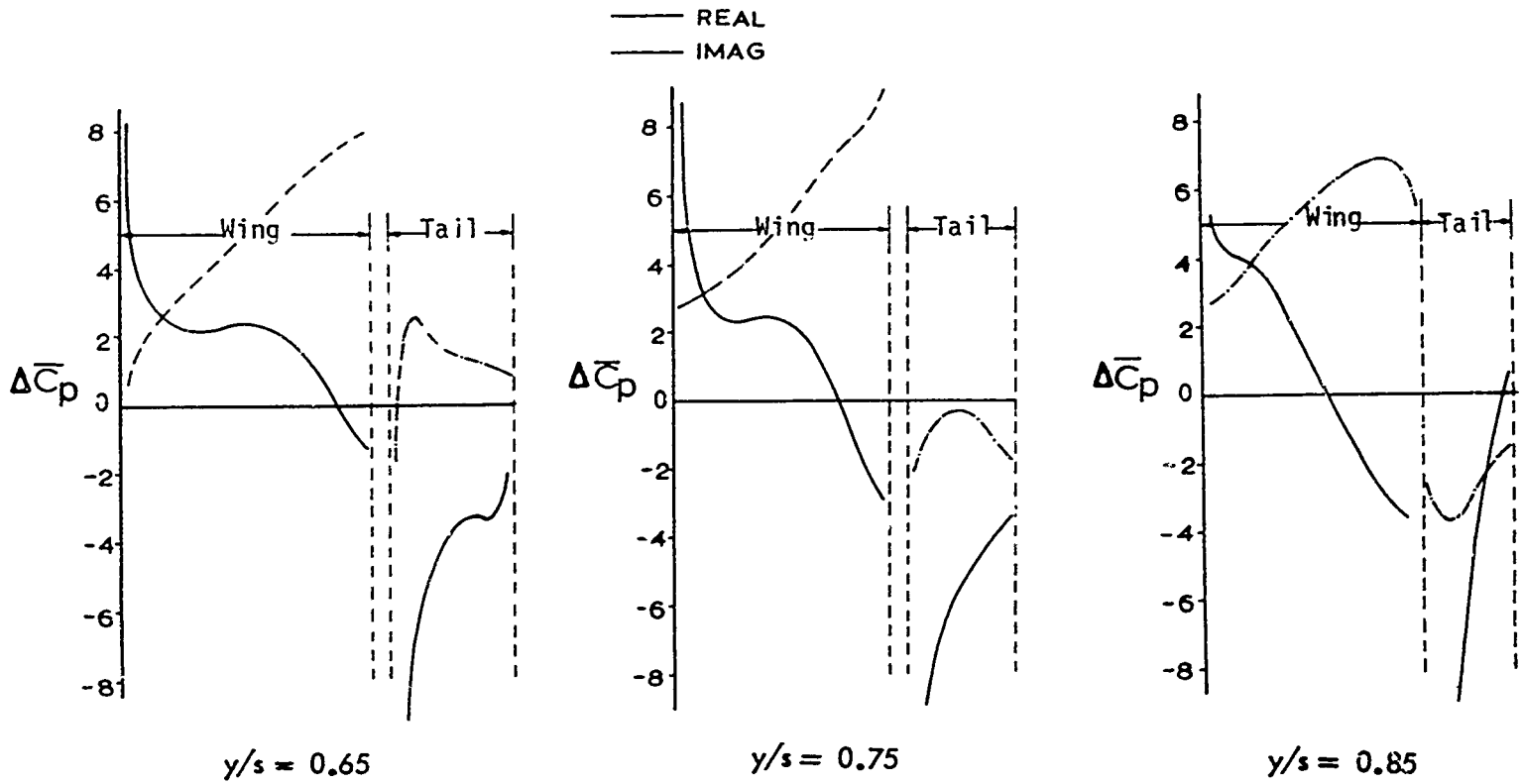

FIGURE 76 CHORDWISE PRESSURE DISTRIBUTION, AGARD PLANFORM, SMALL SEPARATION, WING PITCH MODE, M = 1.414, k_s = 1.5

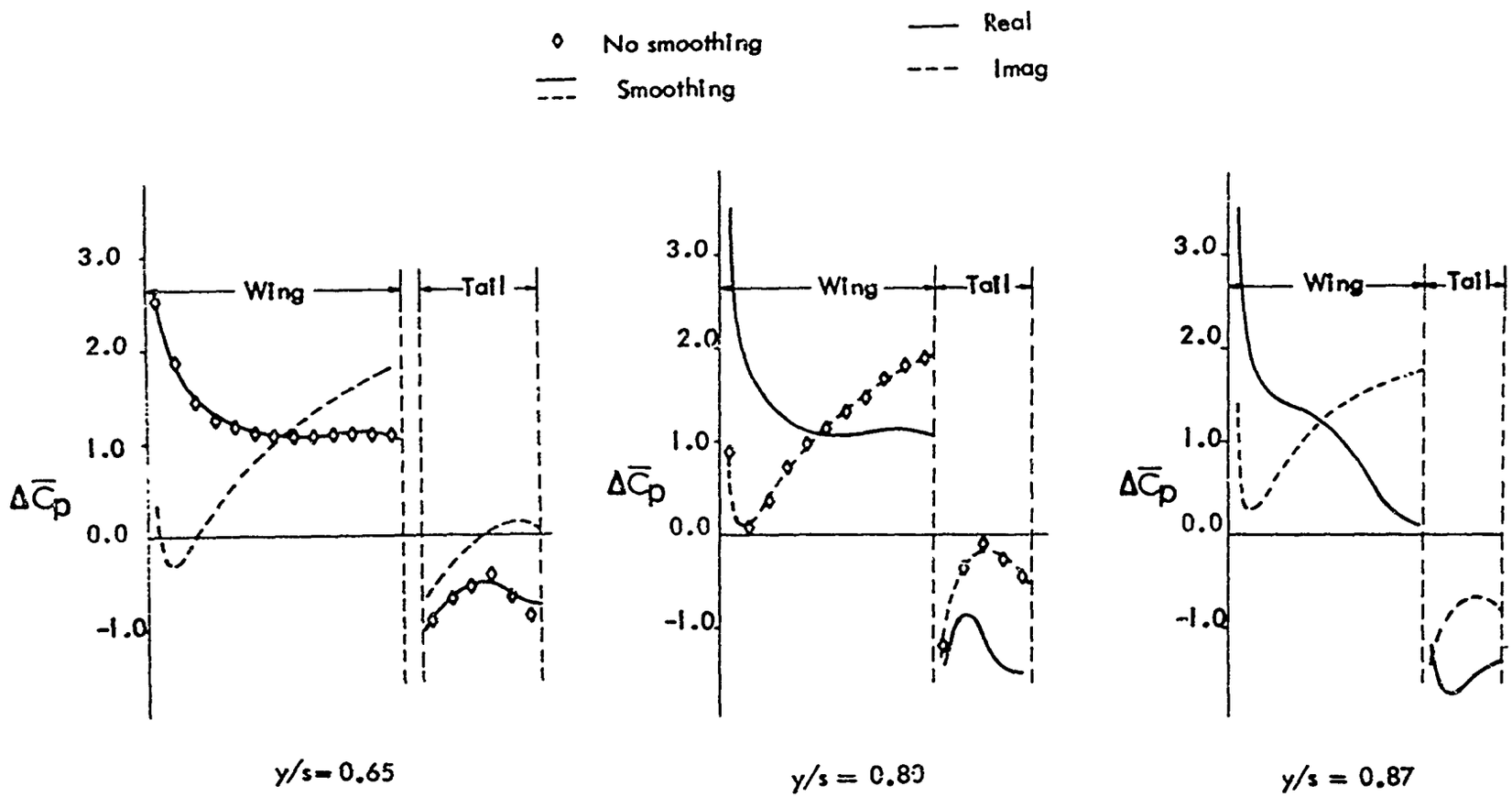

FIGURE 77 CHORDWISE PRESSURE DISTRIBUTION, AGARD PLANFORM, SMALL SEPARATION, WING PITCH MODE, M = 3.162, k_s = 0.75

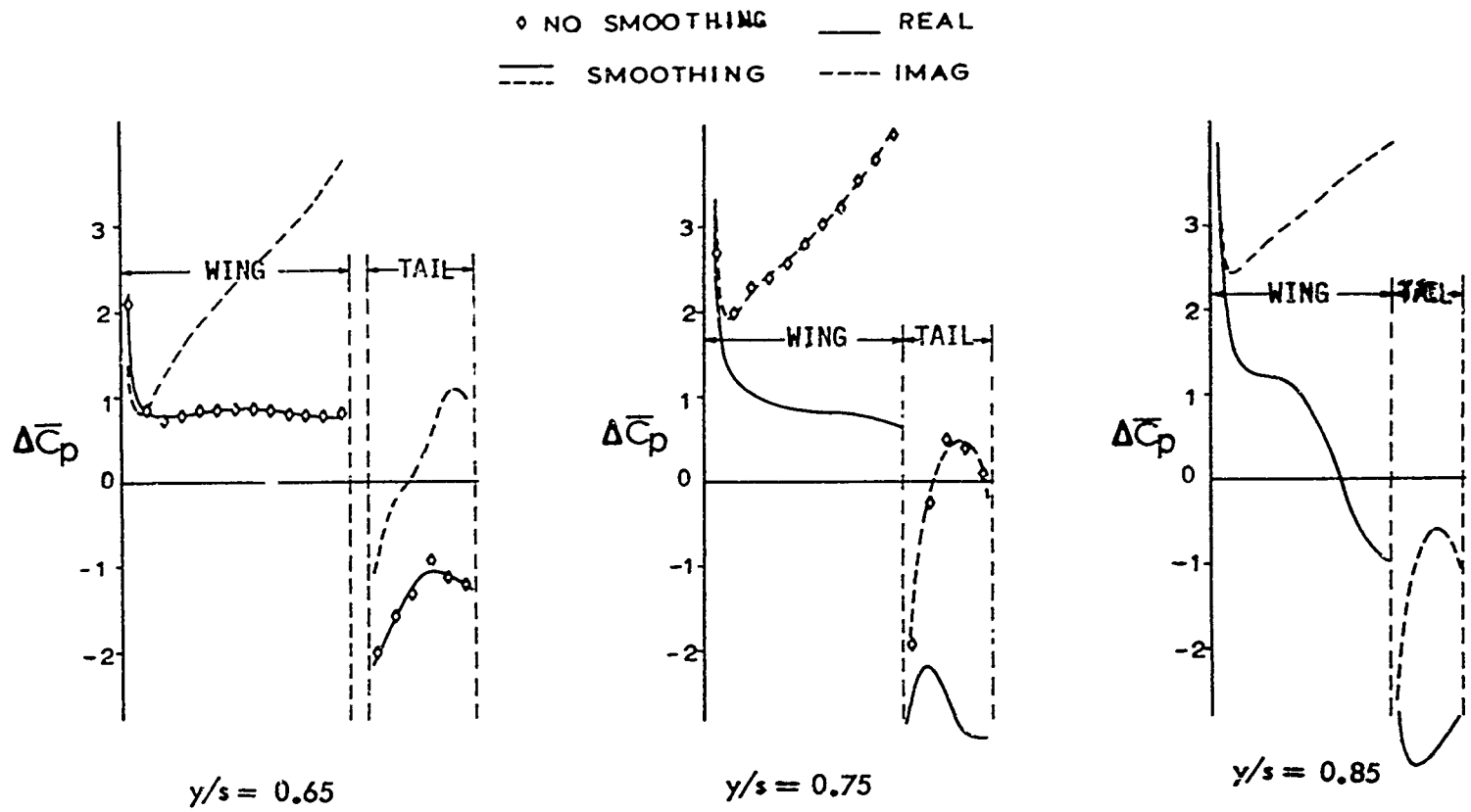

FIGURE 78 CHORDWISE PRESSURE DISTRIBUTION, AGARD PLANFORM, SMALL SEPARATION, WING PITCH MODE, M = 3.162, k_s = 1.50

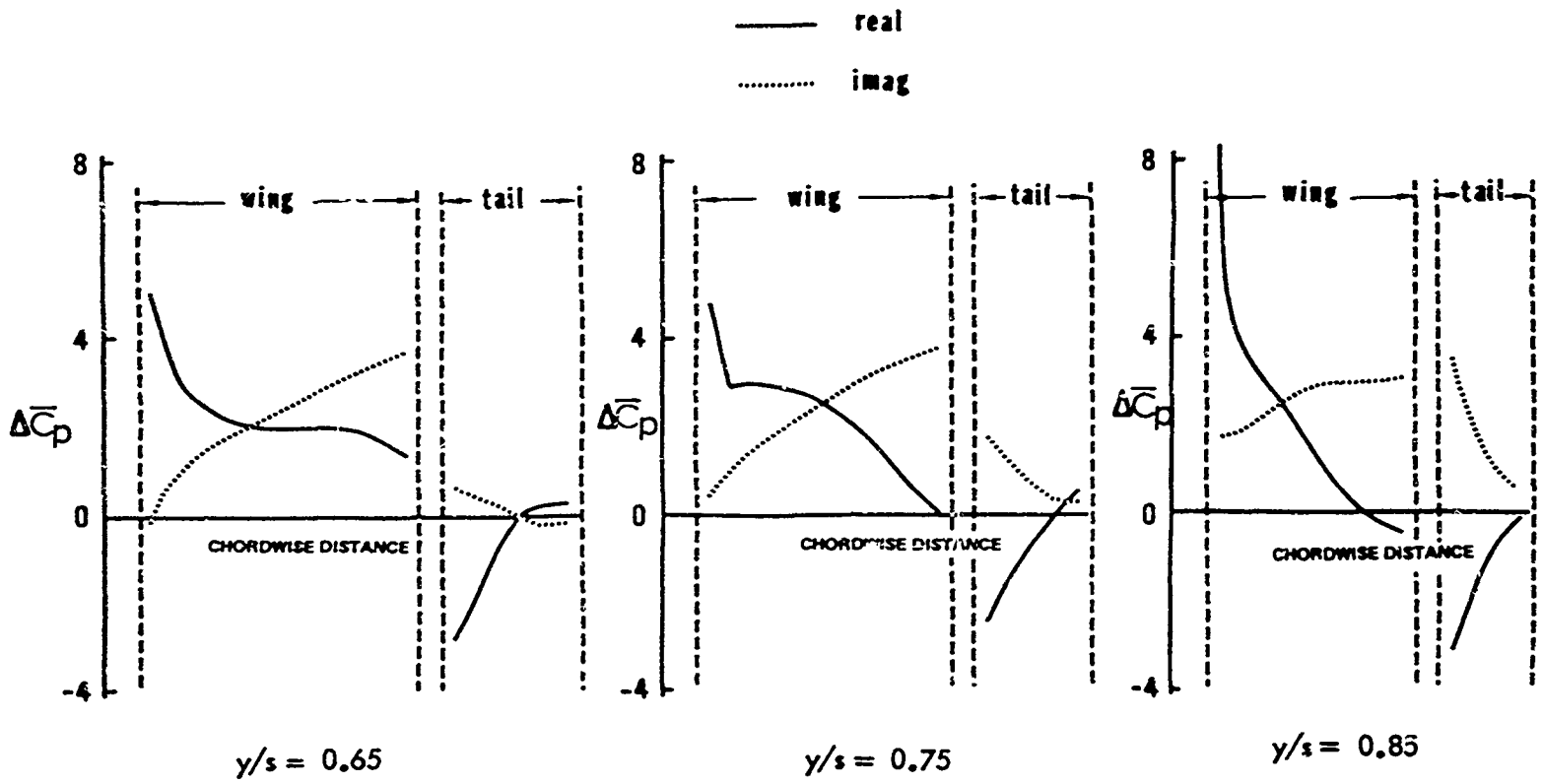

FIGURE 79 CHORDWISE PRESSURE DISTRIBUTION, AGARD PLANFORM, MODERATE SEPARATION, WING PITCH MODE, M = 1.56, k_s = 0.75

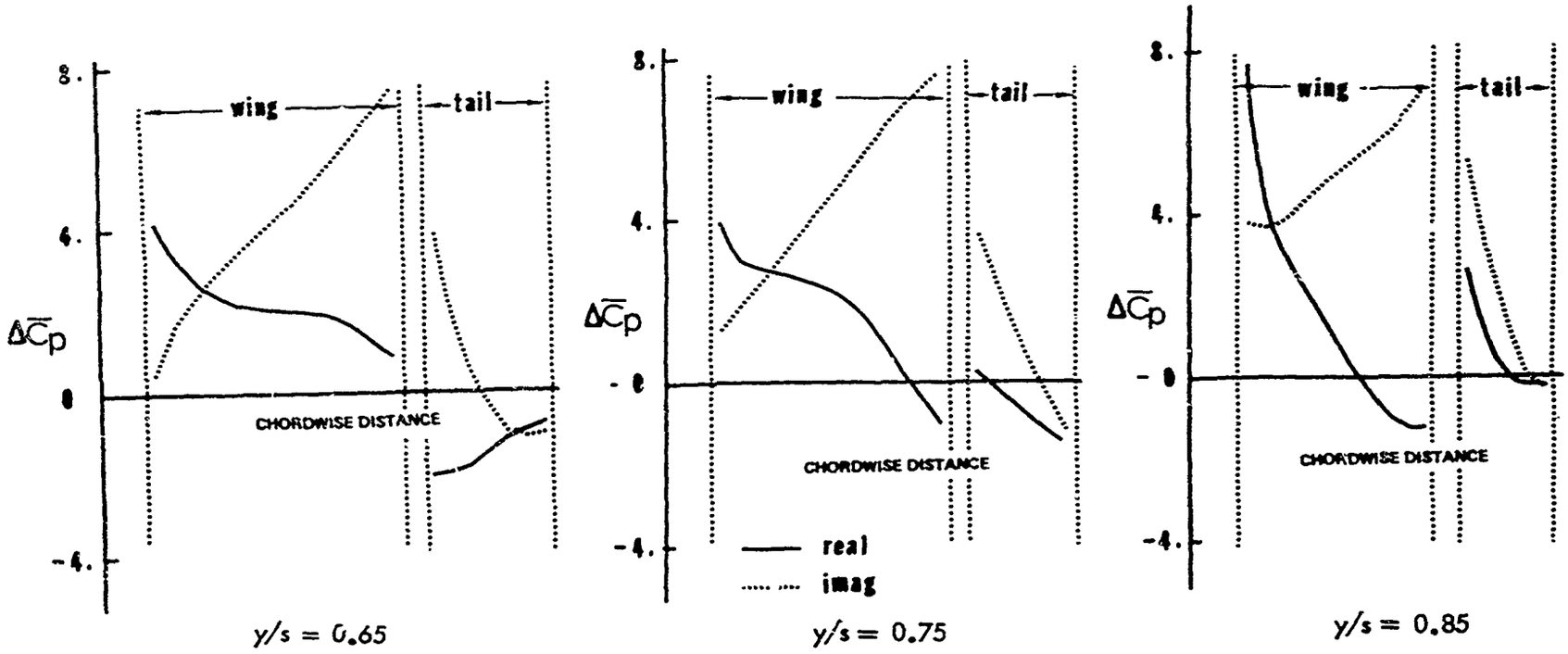

FIGURE 80 CHORDWISE PRESSURE DISTRIBUTION, AGARD PLANFORM, MODERATE SEPARATION, WING PITCH MODE, M = 1.56, k_s = 1.5

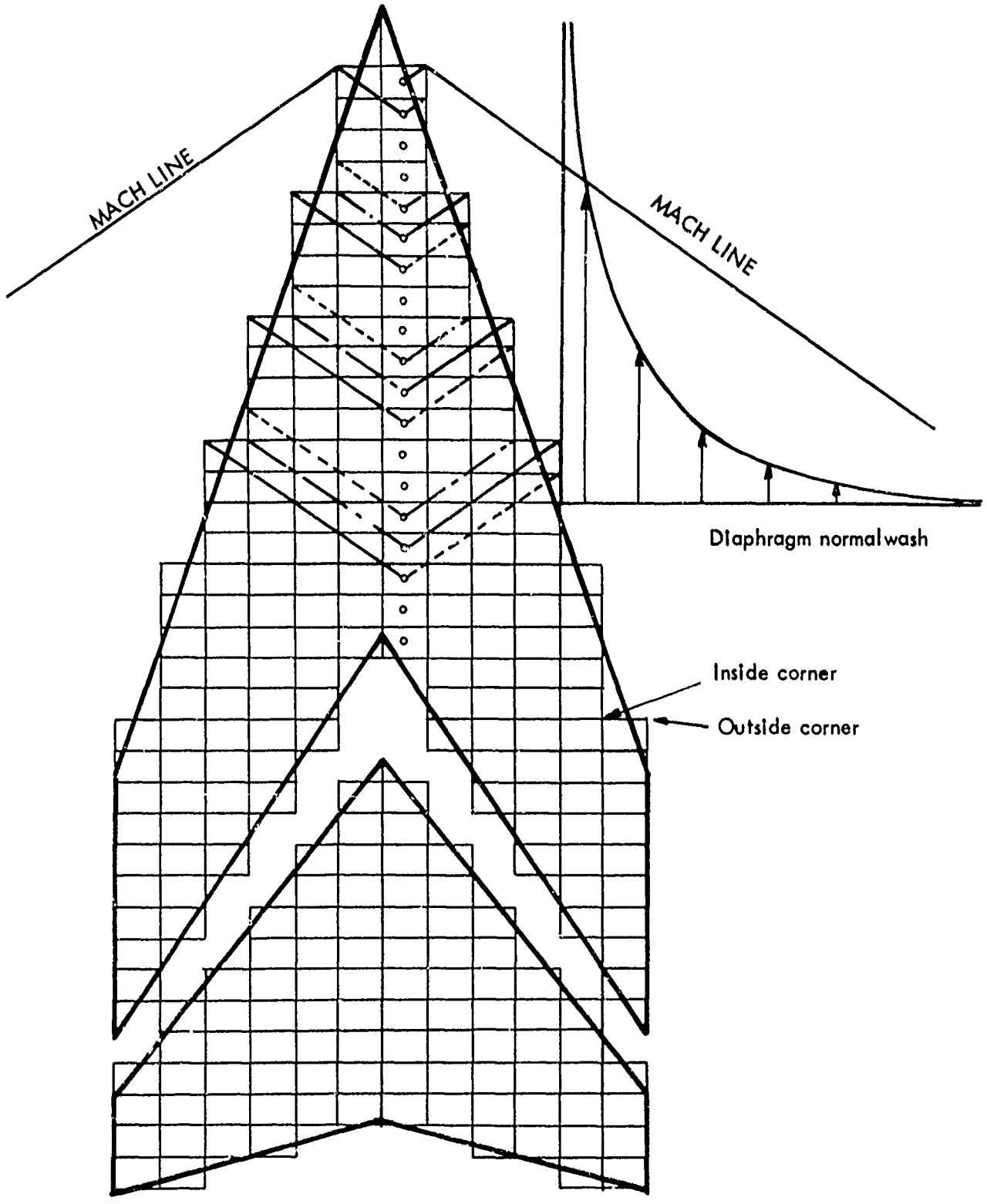

FIGURE 81 SOURCE OF LOAD IRREGULARITIES DUE TO L.E. DEFINITION.

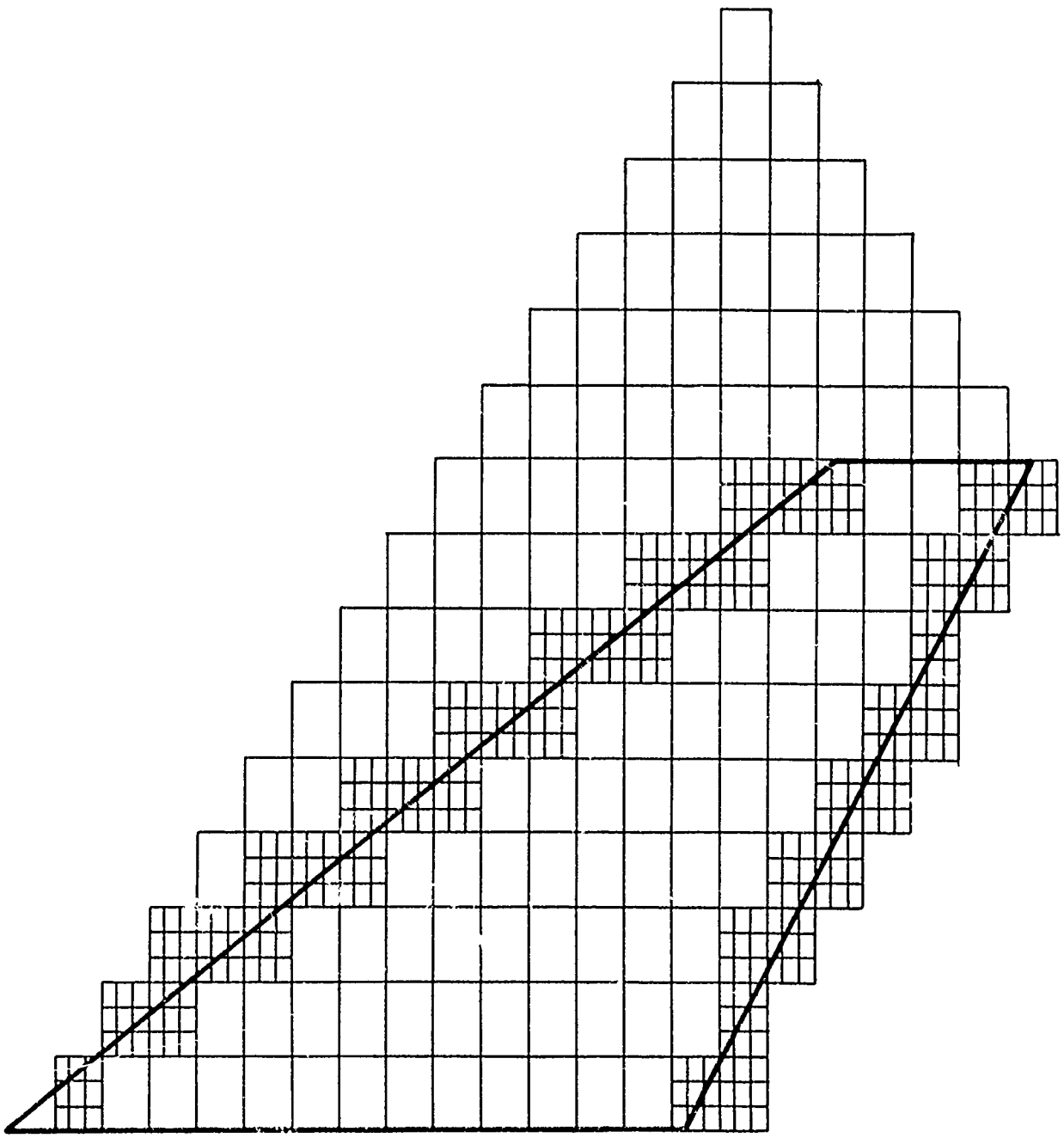

FIGURE 82 RECOMMENDED REVISED SUBDIVISION PATTERN.

$$\{\Delta\Phi\} = [C]\{W\}$$

where $\{\Delta\Phi\}$ = Velocity potential vector

$[C]$ = Aerodynamic Influence Coefficient matrix

$[W]$ = Normal-wash vector

$$\begin{Bmatrix} \Delta\Phi_w \\ \Delta\Phi_d \end{Bmatrix} = \begin{bmatrix} C_{ww} & C_{wd} \\ C_{dw} & C_{dd} \end{bmatrix} \begin{Bmatrix} W_w \\ W_d \end{Bmatrix}$$

w : Wing surface

d : Diaphragm area

Known: $\Delta\Phi_d$, W_w, C

Unknown: $\Delta\Phi_w$, W_d

$$\{\Delta\Phi_d\} = \{0\} \quad \Rightarrow \quad \{W_d\} = -[C_{dd}]^{-1}[C_{dw}]\{W_w\}$$

$$\{\Delta\Phi_w\} = \left([C_{ww}] - [C_{wd}][C_{dd}]^{-1}[C_{dw}]\right)\{W_w\}$$

C_{ww}, C_{dd} : Lower triangular

C_{dw}, C_{wd} : Lower triangular properties

FIGURE 83 SOLUTION EXTENSION TO REMOVE MODAL DEPENDENCY

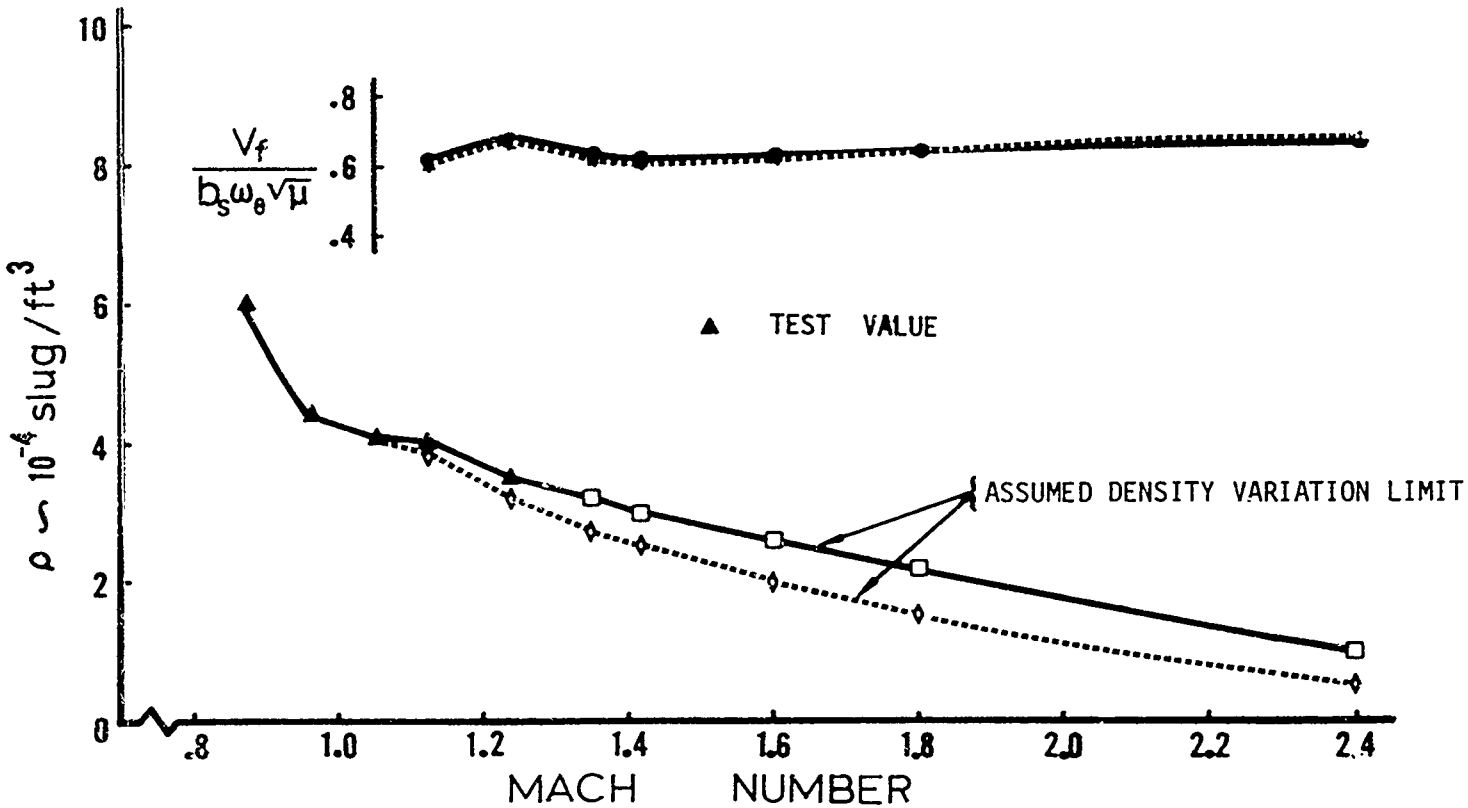

FIGURE 84 FLUTTER SPEED AND AIR DENSITY v.s. FLOW MACH NUMBER FOR CORNELL CONFIGURATION NO. 15

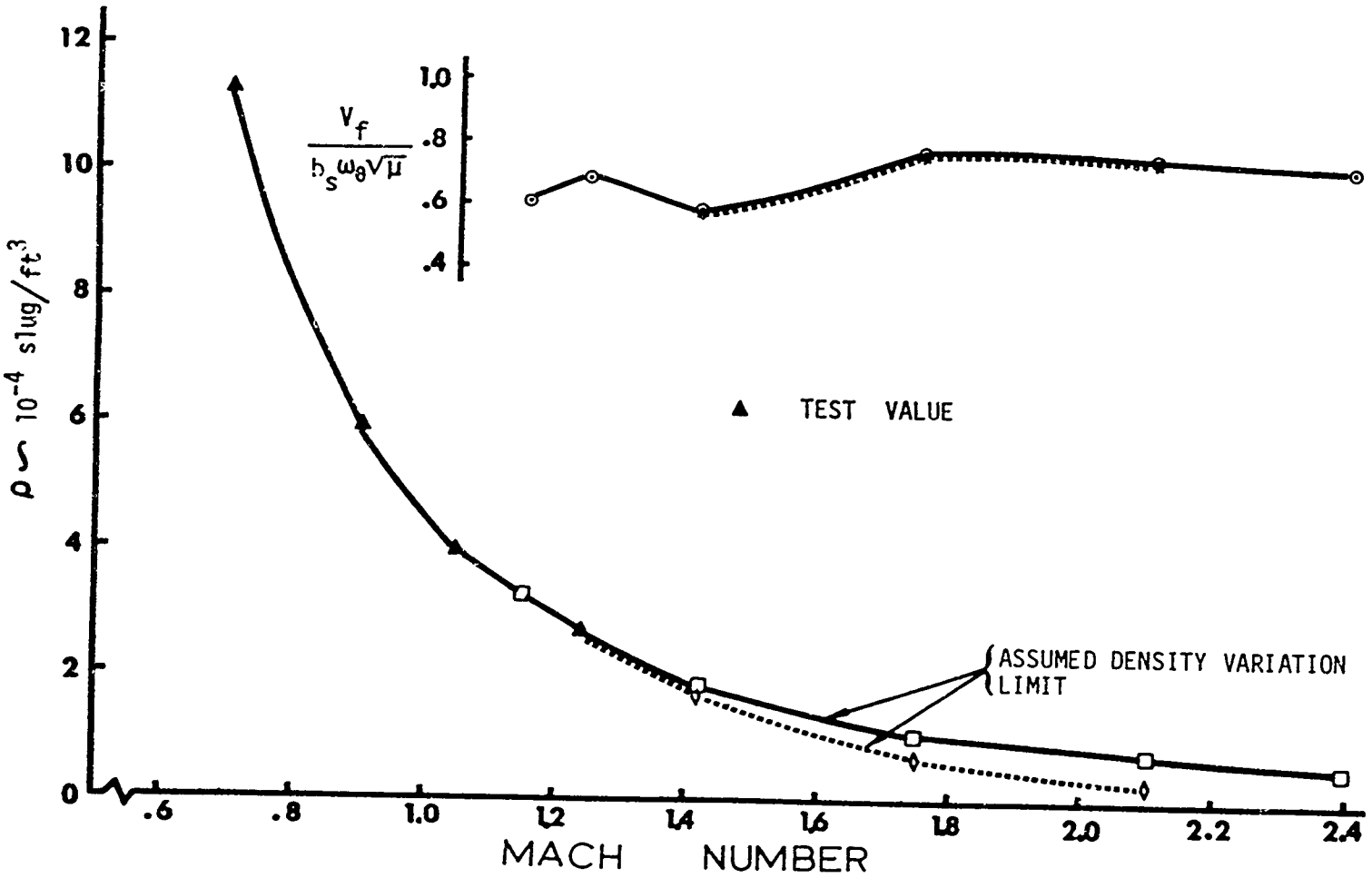

FIGURE 85 FLUTTER SPEED AND AIR DENSITY v.s. FLOW MACH NUMBER FOR CORNELL CONFIGURATION NO. 22

TABLE 21 ANALYTICAL FLUTTER RESULTS v.s. FLOW MACH NUMBER

CONF. NO.	M	ρ slug/ft^3 ($\times 10^4$)	μ	V_f (ft/sec)	η_f	$\frac{V_f}{b_s \omega_\theta \sqrt{\mu}}$	$\frac{\omega}{\omega_\theta}$
15	1.121	4.0*	44.5	858.15	24.6	.6192	.7455
		3.8	46.84	869.81	24.4	.6119	.7394
	1.238	3.5*	50.9	1006.78	26.51	.6794	.8035
		3.2	55.63	1039.55	26.39	.6710	.7997
	1.350	3.2	55.63	993.77	26.46	.6417	.8018
		2.7	65.93	1069.95	26.43	.6348	.8008
	1.414	3.0	59.33	1000.87	26.17	.6255	.7929
		2.5	71.20	1083.46	26.16	.6180	.7928
	1.60	2.6	68.44	1093.25	25.60	.6363	.7758
		2.0	89.00	1237.66	25.58	.6318	.7751
	1.80	2.15	82.79	1217.05	25.05	.6443	.7592
		1.50	118.67	1460.09	25.42	.6456	.7702
	2.40	1.0	178.00	1889.93	24.28	.6819	.7358
		0.5	356.00	2702.31	24.50	.6896	.7424
22	1.151	3.3	53.43	916.59	21.67	.6060	.8773
	1.240	2.7*	65.30	1139.70	23.70	.6815	.9594
	1.414	1.85	95.27	1180.40	22.13	.5844	.8959
		1.70	103.70	1224.82	22.09	.5813	.8944
	1.750	1.1	160.31	2004.95	25.06	.7653	1.0147
		0.7	251.86	2465.35	24.87	.7506	1.007
	2.100	0.72	244.88	2431.23	24.38	..7508	.9870
		0.30	587.70	3742.02	24.28	.7460	.9829
	2.400	0.50	351.62	2786.76	23.22	.7173	.9401

* denotes the test values.

REFERENCES

1. Zartarian, G., and Hsu, P.T., Theoretical Studies on the Prediction of Unsteady Supersonic Airloads on Elastic Wings, Part I Investigations on the Use of Oscillatory Supersonic Aerodynamic Influence Coefficients, WADC TR 56-97, December 1955.
   Zartarian, G., Part II Rules for Application of Oscillatory Supersonic Aerodynamic Influence Coefficients, WADC TR 56-97, February 1956.

2. Balcerak, J., Flutter Tests of Variable Sweep Configurations, AFFDL-TR-68-101, Air Force Flight Dynamics Laboratory, September 1968.

3. Sears, W.R., General Theory of High Speed Aerodynamics, Princeton High Speed Series Vol. VI, Section D. Princeton University Press, 1954.

4. Garrick, I.E., and Rubinow, S.I., Theoretical Study of Airforces on an Oscillating or Steady Thin Wing in a Supersonic Main Stream, NACA Report No. 872, June 1947.

5. Goldstein, H., "Classical Mechanics", Addison-Wesley Publishing Co., Inc., 6th Printing, June, 1959.

6. Donovan, A.F., and Lawrence, H.R., Aerodynamic Components of Aircraft at High Speeds, Princeton University Press, 1957.

7. Evvard, J.C., Distribution of Wave Drag and Lift in the Vicinity of Wing Tips at Supersonic Speeds, NACA TN 1382, July, 1947.

8. Sensburg, O., and Lashka, B., Flutter Induced by Aerodynamic Interference Between Wing and Tail, Presented at AIAA/ASME Structural Dynamics and Aeroelasticity Specialist Conference, New Orleans, April 16-17, 1969.

9. Weatherill, W.H., and Mimmack, J.J., An IBM 7090 Program for Calculating Unsteady Airloads on Arbitrary Lifting Planforms in Supersonic Three-Dimensional Flow, The Boeing Document D2-12281, November 1961.

10. Ii, J.M., Refinement to the Aerodynamics for Use in Supersonic Airloads and Flutter Prediction, Boeing Document D6-23679TN, October 1970.

11. Ii, J.M., Theoretical Studies to Refine the Prediction of Unsteady Aerodynamics of Supersonic Elastic Aircraft, AIAA Paper No. 70-944, Proceeding of the AIAA Guidance, Control and Flight Mechanics Conference, August, 1970.

12. Ashley, H., and Zartarian, G., Piston Theory - A New Tool for the Aeroelastician, Journal of the Aeronautical Sciences, Vol. 23, No. 12, December 1956.

13. Ashley, H., Supersonic Airloads on Interfering Lifting Surfaces by Aerodynamic Influence Coefficient Theory, Boeing Document D2-22067TN, 1962.

14. White, R.B.,and Landahl, M.T., Effect of Gaps on the Loading Distribution of Planar Lifting Surfaces,AIAA Journal, April 1968.

15. Albano,E.,Perkinson, F.,and Rodden,W.P., Subsonic Lifting-Surface Theory Aerodyanmics and Flutter Analysis of Interfering Wing/Horizontal-Tail Configurations, Part II. Wing/Tail Flutter Correlation Study, AFFDL-TR-70-59, September 1970.

10 entry
J. [illegible] II,
etc.

UNCLASSIFIED
Security Classification

DOCUMENT CONTROL DATA - R & D

(Security classification of title, body of abstract and indexing annotation must be entered when the overall report is classified)

1. ORIGINATING ACTIVITY *(Corporate author)*
The Boeing Company
Commercial Airplane Group

2a. REPORT SECURITY CLASSIFICATION
UNCLASSIFIED

2b. GROUP

3. REPORT TITLE
(6) PREDICTION OF UNSTEADY AERODYNAMIC LOADINGS ON NON-PLANAR WINGS AND WING-TAIL CONFIGURATIONS IN SUPERSONIC FLOW. Part I. Theoretical Development, Program Usage, and Application.

4. DESCRIPTIVE NOTES *(Type of report and inclusive dates)*
(9) Final Technical Report. Dec[redacted]69 [redacted]-Apr[redacted]71,

5. AUTHOR(S) *(First name, middle initial, last name)*
(10) Jack [redacted] II, (Morito)
Christopher J. Borland
John R. Hogley

6. REPORT DATE
(11) Mar[redacted]72 (12) 213p.

7a. TOTAL NO. OF PAGES
~~210~~

7b. NO. OF REFS
15

8a. CONTRACT OR GRANT NO.
(15) F33615-70-C-1126

b. PROJECT NO.
(16) AF-1370

c.
Task No. (17) 137003

d.

9a. ORIGINATOR'S REPORT NUMBER(S)
(14) D6-24860 Pt-1

9b. OTHER REPORT NO(S) *(Any other numbers that may be assigned this report)*
(18) AFFDL-TR-71-108, Part I

10. DISTRIBUTION STATEMENT
(19) Distribution limited to U.S. Government agencies only; test and evaluation; statement applied August 1971. Other requests for this document must be referred to AF Flight Dynamics Laboratory (FY).

11. SUPPLEMENTARY NOTES

12. SPONSORING MILITARY ACTIVITY
Air Force Flight Dynamics Laboratory
Wright-Patterson AFB, OH 45433

13. ABSTRACT

A three-dimensional extension of the Mach Box technique was ~~has been~~ developed for the unsteady aerodynamic analysis of non-planar wings and wing-tail configurations in supersonic flow. Various refinement procedures ~~have been~~ were included to improve the accuracy of the results. A general purpose computer program ~~has been~~ was written for the CDC 6600. The program is capable of treating wing-tail combinations with or without vertical separation, longitudinal separation and dihedral on either surface. If a wing alone is treated, perturbation velocity components in the flow field may be found. Correlations with experimental flutter results ~~have been~~ were performed for several models tested in the low supersonic Mach number range at Cornell Aeronautical Laboratory.

The methods ~~described in this report~~ are intended to be used by airplane designers to calculate with improved accuracy, the unsteady aerodynamic loads that act on a lifting surface being propelled at supersonic speeds. The new feature of these calculations is that the aerodynamic interference between the wing and tail ~~has been~~ was taken into account. These calculations are an essential ingredient of flutter analyses and will improve the confidence level of such calculations in preventing wing-tail flutter. The general requirement for such calculations are contained in Military Specification MIL-A-8870A (USAF).

DD FORM 1 NOV 65 1473

UNCLASSIFIED
Security Classification

405108

UNCLASSIFIED

Security Classification

14. KEY WORDS	LINK A ROLE	LINK A WT	LINK B ROLE	LINK B WT	LINK C ROLE	LINK C WT
Unsteady Aerodynamics						
Aeroelasticity						
Flutter						
Supersonic Flow						
Aerodynamic Interference						

☆U.S.Government Printing Office: 1972 — 759-084/454

UNCLASSIFIED

Security Classification